Optimisation of Ligand-Directed Labelling Probes for A$_1$ Adenosine Receptors in Whole Cells: Development and Evaluation

Thesis submitted to the University of Nottingham for the degree of Doctor of Philosophy

June 2025

Chia-Yang Lin

20399328

Supervisors: Barrie Kellam

Stephen J. Hill

School of Pharmacy

University of Nottingham

Declaration

This thesis was written by the candidate as part of a four-year postgraduate research (PGR) program in the Division of Biomolecular Sciences and Medicinal Chemistry at the University of Nottingham, United Kingdom. An AI-based tool was employed to enhance the clarity of expression and correct grammatical errors. The majority of the experimental work described herein was conducted by the candidate between 2021 and 2025 at the University of Nottingham. Exceptions include the FLIM-FRET experiments, which were performed by Dr. Joelle Goulding; fluorescence-activated cell sorting (FACS), carried out by a technician from the School of Life Sciences; and LC-tandem mass spectrometry analysis, outsourced to Cambridge Centre for Proteomics. No part of this material has been previously submitted for the award of any degree.

Presentations Derived from This Thesis

Posters:

1. **8th RSC/SCI Symposium on GPCRs in Medicinal Chemistry**

5–7 October 2022, Verona, Italy

Title: Synthesis and Pharmacological Validation of New Potent and Selective Adenosine A_1-Receptor Fluorophore-Transfer Reagents

2. **XXVIII EFMC International Symposium on Medicinal Chemistry**

1–5 September 2024, Rome, Italy

Title: Optimization and Pharmacological Validation of Adenosine A_1-Receptor Fluorophore-Transfer Reagents

3. **GP2A 2025, Paul Ehrlich MedChem 2025 & COST Action OneHealthdrug**

11–13 June 2025, Nantes, France

Title: Optimisation of Ligand-Directed Covalent Labelling Probes Targeting A_1 Adenosine Receptors

Awarded Best Poster

Oral Communications:

1. **Pharmacology 2024**

10–12 December 2024, Harrogate, UK

Title: Optimising a Fluorescent Probe Capable of Covalently Transferring a Fluorophore onto the Adenosine A_1 Receptor (A_1AR)

2. **5th Annual Meeting of the IRN iGPCRnet**

7–9 July 2025, Barcelona, Spain

Title: Optimising a Fluorescent Probe Capable of Covalently Transferring a Fluorophore onto the Adenosine A_1 Receptor (A_1AR)

Publication:

Eleonora Comeo, Joëlle Goulding, <u>Chia-Yang Lin</u>, Marleen Groenen, Jeanette Woolard, Nicholas D. Kindon, Clare R. Harwood, Simon Platt, Stephen J. Briddon, Laura E. Kilpatrick, Peter J. Scammells, Stephen J. Hill*, and Barrie Kellam**. Ligand-Directed Labeling of the Adenosine A1 Receptor in Living Cells,** *J. Med. Chem.* **2024**, *67*(14), 12099–12117.

Abstract

Adenosine receptors (ARs) are widely distributed throughout the human body and exist in four subtypes: A_1, A_{2A}, A_{2B}, and A_3. The endogenous ligand adenosine modulates numerous physiological responses across various tissues and organs, including the cardiovascular system and both the central and peripheral nervous systems, through activation of these receptors. Among them, the A_1 adenosine receptor (A_1 AR) has been extensively investigated as a therapeutic target for conditions such as arrhythmia, heart failure, neuropathic pain, and diabetes. However, no A_1 AR-targeting candidate has successfully completed clinical trials and reached the market. Challenges in drug development stem not only from the complexity of the A_1 AR system but also from an incomplete understanding of its interactions with other proteins and its diverse cellular responses.

Dr. Comeo E. developed ligand-directed (LD) covalent labelling probes for A_1 AR. One probe directly transfers a sulfo-Cy5 fluorophore to A_1 AR, while the other transfers a *trans*-cyclooctene (TCO) handle. The covalent sulfo-Cy5 tag enables real-time visualisation of receptor localisation and trafficking. Additionally, protein–protein interactions involving A_1 AR can be studied using techniques such as BRET, FRET, and FCCS. The TCO handle allows broader applications *via* inverse electron demand Diels–Alder (IEDDA) reactions with tetrazine-conjugated reporters, which may include fluorophores, biotin, or radiolabels, depending on experimental design. However, both subtype selectivity and labelling efficiency require further optimisation.

This thesis presents the design, synthesis, and pharmacological evaluation of novel LD probes based on Comeo's templates. Probe **5-8**, a sulfo-Cy5 transferring LD probe, improved A_1/ A_{2A} selectivity from 5.9-fold (Comeo's original probe) to 40-fold, while maintaining selectivity over other AR subtypes. Probe **4-5**, a TCO-transferring LD probe, enhanced A_1/ A_{2B} selectivity from 60-fold to 210-fold. Parameters such as the click reaction pair, buffer or medium composition, probe concentration, and incubation time were systematically investigated to optimise labelling efficiency.

In addition to using agonist-induced internalisation to assess orthosteric binding pocket accessibility post-labelling, a BRET-based assay was conducted with probe **4-5**. FRET between the AF488 tag (introduced *via* probe **4-5** and a tetrazine-AF488), along with a red fluorescent reversible ligand **3-29** (BODIPY630/650), confirmed the availability of the orthosteric binding site. These findings were further validated using FLIM-FRET experiments.

The novel LD probes **5-8** (sulfo-Cy5) and **4-5** (TCO), with improved subtype selectivity, represent valuable tools for advancing the study of A_1 AR biology.

These tools are expected to facilitate deeper exploration of A_1 AR pharmacology and contribute to expanding our understanding of its therapeutic potential.

Acknowledgements

List of Abbreviations

ARs Adenosine receptors

AC Adenylyl cyclase

ATP Adenosine 5'-triphosphate

BEP 2-Bromo-1-ethyl pyridinium tetrafluoroborate

BODIPY 4,4-Difluoro-4-bora-3a,4a-diaza-s-indacene

BRET Bioluminescence Resonance Energy Transfer

CCPA 2-Chloro-N^6-cyclopentyladenosine

cDNA Complementary DNA

COMU (1-cyano-2-ethoxy-2- oxoethylidenaminooxy)dimethylaminomorpholino-carbenium hexafluorophosphate

Cryo-EM Cryogenic electron microscopy

Cy5 Cyanine5

DIPEA Diisopropylethylamine

DMAP 4-Dimethyl amino pyridine

DMEM Dulbecco's Modified Eagle Medium

DMTMM 4-(4,6-Dimethoxy-1,3,5-triazin-2-yl)-4-methylmorpholinium chloride

DPCPX 8-Cyclopentyl-1,3-dipropylxanthine

EDC 1-Ethyl-3-(3-dimethylaminopropyl)carbodiimide

ERK Extracellular signal-regulated kinases

ESI Electrospray ionization

FACS Fluorescence activated cell sorting

FLIM Fluorescence lifetime imaging microscopy

FRET Fluorescence Resonance Energy Transfer

GPCR G-protein coupled receptor

GRKs G-protein coupled receptor kinases

HATU *O*-(7-azabenzotriazol-1-yl)-1,1,3,3-tetramethyluronium hexa-fluorophosphate

HBSS HEPES buffered saline solution

HEK293 Human Embryonic Kidney 293 cells

HOBt Hydroxybenzotriazole

HPLC High-performance liquid chromatography

HRMS High-resolution mass spectrometry

IC$_{50}$ Half-maximal inhibitory concentration

IEDDA Inverse-electron demand Diels-Alder

K_d Dissociation constant, concentration at which half the receptors are occupied

K_i Inhibitory constant

LD Ligand-directed

LC-MS Liquid chromatography mass spectrometry

NECA 5'-*N*-ethylcarboxamide adenosine

NLuc NanoLuciferase

NMI *N*-methylimidazole

NMR Nuclear magnetic resonance

PBS Phosphate-buffered saline

PFP Pentafluoropyridine

PLC-β Phospholipase C-β

T3P Propylphosphonic anhydride

***t*-BOC** *tert*-Butyloxylcarbonyl

TCFH Chloro-*N*, *N*, *N*', *N*'-tetramethylformamidinium hexafluorophosphate

XAC Xanthine Amine Congener

Contents

Table of Figures-Chapter 1

Table of Figures-Chapter 3

Table of Figures-Chapter 4

Table of Figures-Chapter 5

Figures-Chapter 6

Table of Tables-Chapter 1

Table of Tables-Chapter 3

Table of Tables-Chapter 4

Table of Tables-Chapter 5

Chapter 1

1. General Introduction

1.1 G-Protein Coupled Receptor (GPCR)

G-protein coupled receptors (GPCRs) are transmembrane proteins that play a critical role in cellular signalling. Based on a phylogenetic analysis of the human genome, Fredriksson classified GPCRs into five main families: Glutamate (G), Rhodopsin (R), Adhesion (A), Frizzled/Taste2 (F), and Secretin (S)[1]. Members of this superfamily share a highly conserved structure composed of seven transmembrane domains connected by three extracellular and three intracellular loops. The N-terminus of GPCRs resides outside the cell, while the C-terminus remains inside (**Figure 1-1**). This unique structure, in conjunction with G-proteins, enables GPCRs to function as molecular transducers. When stimuli such as photons, hormones, or peptides activate specific GPCRs, the external signals are transmitted into intracellular signalling regulated by G-proteins, GPCR kinases (GRKs), and arrestins[2].

In the G-protein-mediate signalling pathway, activation begins with the recruitment of a heterotrimeric G-protein complex. Upon coupling with an activated GPCR, the GDP bound to the Gα subunit is exchanged for GTP, triggering dissociation of the heterotrimer. The Gα subunit then regulates downstream effectors such as adenylyl cyclase, phospholipase C, and potassium channels[2,3]. Meanwhile, the Gβγ dimer modulates other effectors, including phospholipase C β, Src kinase, calcium channels, and recruits GRKs[2,3]. Signal termination occurs through GRK-mediated phosphorylation of the GPCR, which promotes arrestin binding[4]. Arrestin binding sterically hinders further G-protein coupling, leading to receptor desensitization and facilitating its internalisation[5]. Beyond terminating G-protein signalling, arrestins also function as scaffolds for kinases such as extracellular signal-regulated kinases (ERKs) and mitogen-activated protein kinases (MAPKs)[4,6], thereby mediating signalling pathways distinct from those regulated by G-proteins (**Figure 1-2**)[7]. However, the precise mechanisms underlying arrestin-mediated signalling remain incompletely understood, with conflicting observations reported by different research groups[7–9].

GPCRs, being fragile membrane proteins, present challenges for structural analysis through traditional X-ray crystallography[10]. However, advances in electron cryo-microscopy (cryo-EM) and image processing techniques have significantly accelerated the elucidation of GPCR structures. Since the first GPCR structure was resolved using cryo-EM in 2017, the number of GPCR

structures solved *via* cryo-EM has rapidly increased, surpassing those determined by X-ray crystallography since 2019[10]. This structural information has facilitated structure-based drug discovery and virtual molecular docking experiments. The availability of more receptor structures, combined with emerging concepts such as ligand-depend biased signalling (where a ligand preferentially activates a specific signalling pathway over others, offering potential for designing ligands that enhance therapeutic effects while minimising adverse side effects[11,12]), protein-protein interactions (e.g., homodimers and heterodimers), and ligand-induced receptor rearrangements, has made GPCR research a thriving area in both academia and industry.

Several examples highlight the successful translation of novel GPCR modulation strategies into marketed drugs. Oliceridine, approved by the FDA in 2020, exemplifies the application of biased signalling mechanisms[6]. As a biased partial agonist of the μ-opioid receptor, it selectively activates the G-protein-dependent pathway to provide analgesic effects while minimising activation of the arrestin pathway, which is associated with adverse effects[13,14]. Another example is avacopan, approved by the FDA in 2021 as an adjunct therapy for anti-neutrophil cytoplasmic autoantibody-associated vasculitis (ANCA-AV)[15,16]. Avacopan acts as an allosteric modulator of the complement C5a receptor (C5aR), forming a complex with the receptor to prevent its transition to an active conformation, unlike traditional antagonists that block the orthosteric binding site[16].

To date, approximately 800 GPCRs have been identified[17], and these receptors regulate diverse physiological processes through complex signal transduction, making them highly attractive drug targets. An analysis of approved drugs (data up to February 2024) revealed that over one-quarter of marketed drugs (535 out of 2,054) target GPCRs[16]. To evaluate current trends, FDA-approved drugs from 2020 to 2024 were manually categorised. During this period, 32 new drugs targeting GPCRs were approved, representing 13% of the 246 approved drugs. GPCR-targeting drugs ranked as the fifth most common drug class approved in the last five years, maintaining a steady pace of innovation (**Figure 1-3A and B**).
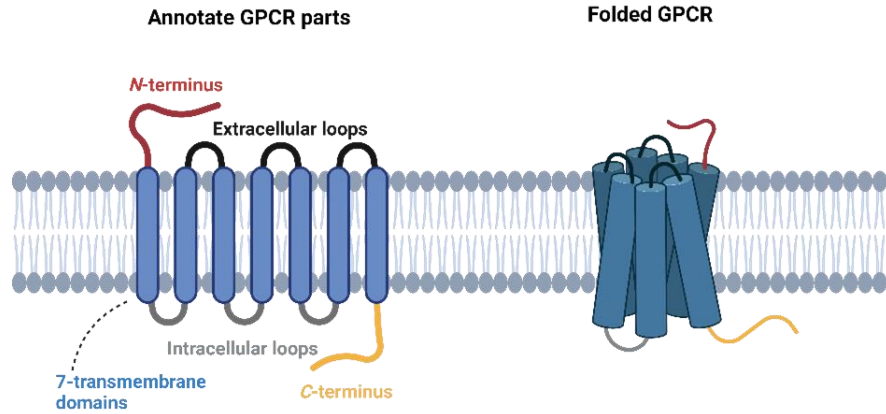
Figure 1-1. Cartoon Structure of a GPCR.
The left panel illustrates the components of the GPCR, each represented in distinct colours: red for the *N*-terminus, black for extracellular loops, grey for intracellular loops, yellow for the *C*-terminus and blue for transmembrane domains. The right panel provides a simplified depiction of the GPCR in its folded structure. Graph was generated *via* BioRender (www.BioRender.com).
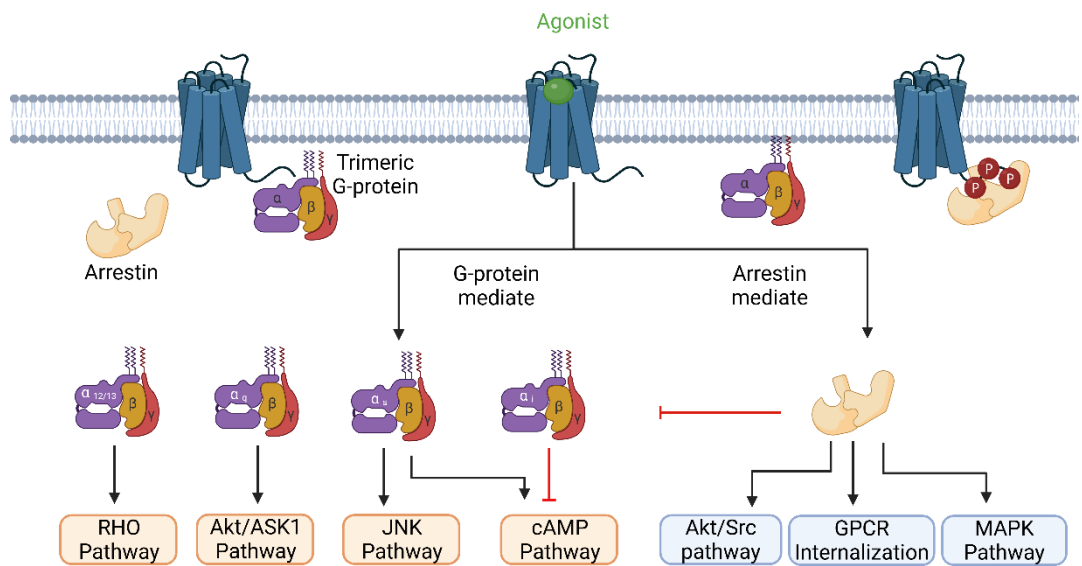
Figure 1-2. Schematic Representation of GPCR Activation Signalling Pathways *via* G-Protein and Arrestin.
The green circle represented an agonist while red circles with a white "P" indicated as phosphorylation sites. The figure was adapted from Conflitti *et al*. (2025)[16]. Graph was generated *via* BioRender (www.BioRender.com).

FDA approved drugs (2020-2024)

Biologicals (27%, N=70)
Others (23%, N=60)
Kinase (17%, N=45)
Enzyme (14%, N=36)
GPCR (12%, N=32)
Nuclear Hormone Receptors (3%, N=9)
Ion channel (2%, N=6)
Transporter (2%, N=6)

FDA approved drug 2020 to 2024

Biologicals
Enzyme
GPCR
Ion channel
Kinase
Nuclear Hormone Receptors
Others
Transporter
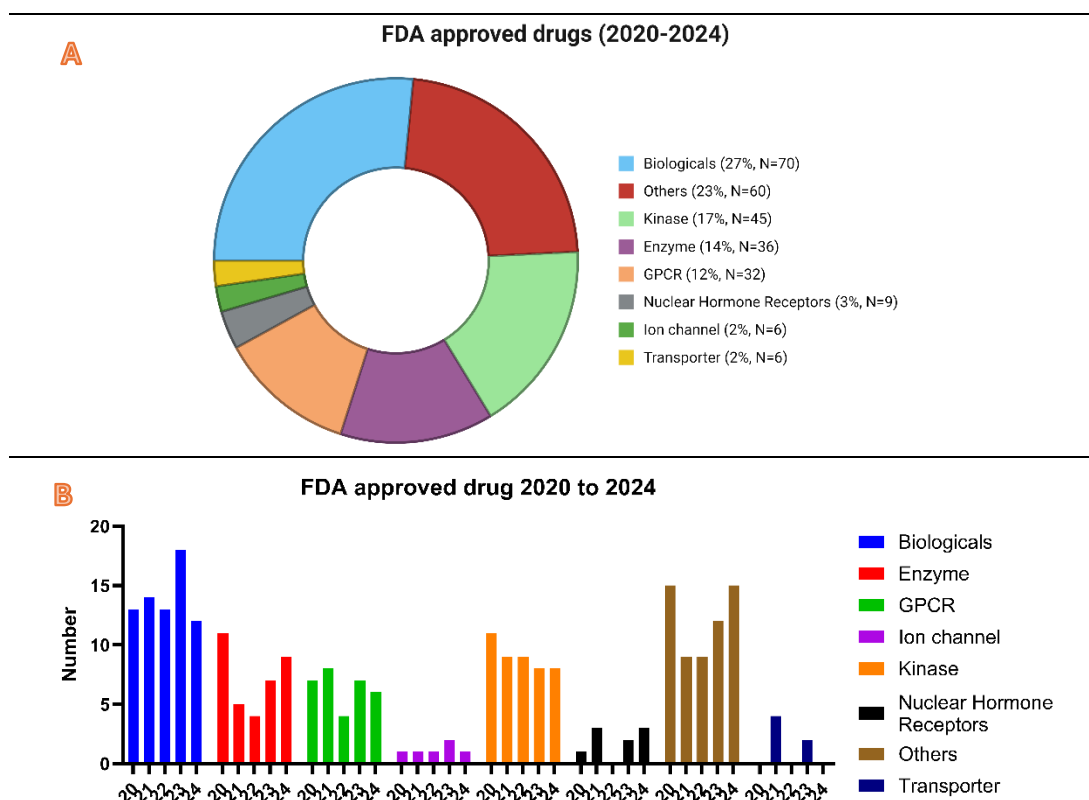
Figure 1-3. Analysis of FDA Approved Drugs in Recent 5 Years.
(**A**) The pie chart shows the percentage distribution of 246 FDA-approved drugs, categorised into eight target groups. The total count of 264 reflects cases where drugs target multiple categories. (**B**) The bar chart summarises the annual approval trends by target group. Biologicals, the largest group, manly contributed by antibody-based drugs. The antisense oligonucleotide (ASO), classified under "Others," are consistently present in the approved lists each year. The approved drug lists were downloaded from FDA website and classified into 8 categories manually. Figure part **A** was generated *via* BioRender (www.BioRender.com) while part **B** created through GraphPad Prism.

1.2 Adenosine and Adenosine Receptors (ARs)

Adenosine is a purine nucleoside consisting of adenine and ribose (**Figure 1-4**). It serves as the core scaffold and metabolite for energy-transferring molecules like ATP. Ubiquitous in the human body, adenosine mediates diverse physiological effects through the activation of adenosine receptors (ARs)[18–20]. These receptors, members of the GPCR family, are classified into four subtypes: A_1, A_{2A}, A_{2B}, and A_3[5,18–20]. The precise regulation of physiological processes by adenosine and its receptor subtypes is orchestrated by several factors, including the specific effector cascades associated with each subtype, receptor interactions (homo- and heterodimers), cell type-specific expression, and receptor affinity.

Each AR subtype is coupled to distinct signalling pathways. A_1 ARs are associated with $G_i\alpha$ and $G_o\alpha$ proteins[21], which inhibit adenylyl cyclase (AC), and modulate ion channels (K^+ and Ca^{2+})[18,20,22]. A_{2A} ARs interact with $G_s\alpha$ and $G_{olf}\alpha$ proteins[21], stimulating AC and inhibiting Ca^{2+} channels[18,20,22]. A_{2B} ARs couple with $G_s\alpha$ and $G_{q/11}\alpha$ proteins, activating both AC and PLC-β[18,20,22]. Similarly, A_3 ARs are linked to $G_i\alpha$ and $G_{q/11}\alpha$ proteins, inhibiting AC as A_1 ARs do while activating PLC-β like A_{2B} ARs[18,20,22]. These distinct pathways ensure specificity in adenosine's effects across various physiological contexts.

The affinity of AR subtypes for adenosine further refines their modulation. A_1 ARs exhibit the highest affinity, whereas A_{2B} ARs display relatively low affinity[5,20,22]. These differences play a crucial role in fine-tuning receptor activation. For example, in striatal neurons, both A_1 and A_{2A} ARs are expressed, often forming heterodimers[21]. Presynaptic A_1 ARs suppress glutamate release, while A_{2A} ARs facilitate it. Adenosine causes a biphasic glutamate release pattern *via* activating A_1 and A_{2A} ARs with concentration from 0.1 to 100 μM[21]. At low adenosine concentrations, A_1 ARs inhibit glutamate release. At higher concentrations, A_{2A} ARs become dominant, promoting glutamate release and inhibiting A_1 AR activity through A_1-A_{2A} heterodimer interactions[21]. This affinity and heterodimer-dependent switch mechanism exemplifies how adenosine can dynamically regulate physiological responses[23,24].

Receptor interactions extend the functional scope of ARs. Except for A_1-A_{2A} heterodimers, A_{2A} ARs interact with dopamine D_2 receptors (D_2R) in striatal neurons[25]. When A_{2A} ARs bind agonists or antagonists, the resulting conformational changes in the A_{2A}-D_2R complex reduce the affinity and efficacy of D_2R agonists[26]. Such receptor-receptor interactions allow adenosine to influence dopamine signalling indirectly, demonstrating the broader impact of AR systems.

Tissue-specific expression and effects further contribute to the physiological diversity of AR-mediated signalling. In the cardiovascular system (CVS), A_1 AR activation produces negative inotropic, chronotropic, and dromotropic effects[19,27], while A_{2A} AR activation enhances inotropy[27]. In the central nervous system (CNS), A_1 ARs inhibit glutamate release and regulate postsynaptic neuronal activity[19], whereas A_{2A} ARs facilitate glutamate release[21]. Both A_{2B} and A_3 ARs mediate coronary vasodilation[27]. In CNS, A_{2B} ARs activation is correlated with increasing glutamate release[28] while A_3 AR activation is linked to antinociceptive effects[29].

Through its receptor subtypes, adenosine exerts a wide range of physiological effects, driven by differences in receptor affinity, interactions between receptors, and tissue-specific expression patterns (**Table 1-1**). These versatile mechanisms underscore the therapeutic potential of ARs as targets for drug discovery.
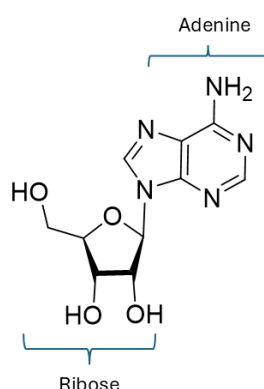
Figure 1-4. Structure of Adenosine.
Adenosine is composed of adenine and ribose. It is metabolised rapidly *in vivo* with a half-life around 10 second[22].

Table 1-1. Brief Comparison between Four Adenosine Subtypes

AR Subtype	Adenosine Affinity* (nM)[20,22]	Coupled Gα-subunit[20–22]	Receptor complex[25]	Activation	
				CNS effect	CVS effect[27]
A_1	70/ 1-10	Gi/Go	A_1-A_1, A_1-A_{2A}[21]	Decrease glutamate releasing[21]	Negative inotropic, dromotropic, and chronotropic effects
A_{2A}	150/30	Gs/Golf	A_{2A}-D_2[26], A_{2A}-A_{2A}	Increase glutamate releasing[21]	Enhance inotropy
A_{2B}	500/1000	Gs/Gq/11		Increase glutamate releasing[28]	Coronary vessel dilation
A_3	650/100	Gi/Gq/11		Alleviate pain[29]	Coronary vessel dilation

*: the adenosine affinity values were from two separate literature. The anterior one is from reference 20 while the posterior one from reference 22. The varied affinity values may result from experiment setting.

1.3 Potential of the Adenosine A_1 Receptor for Clinical Applications

A_1 ARs are abundantly expressed in the brain, spinal cord, and atria, with moderate expression in adipose tissue, liver, and kidneys, and low expression in the lungs and pancreas[22,30,31]. Their widespread distribution and ability to modulate physiological effects make A_1 ARs promising targets for drug discovery. For instance, the negative inotropic, chronotropic, and dromotropic effects mediated by A_1 ARs have been explored for arrhythmias[19,20,31]. The antidiuretic effect from A_1 ARs inhibition is investigated for heart failure (HF) treatment[32,33]. Additionally, the involvement of A_1 ARs in lipolysis and insulin secretion offers potential therapeutic avenues for dyslipidemia and type 2 diabetes mellitus (T2DM)[19,20,25,31,34]. In the central nervous system (CNS), A_1 AR stimulation is associated with pain relief, raising the prospect of developing non-narcotic analgesics[19,34].

1.3.1 A_1 AR Ligands in Cardiovascular Diseases

Adenosine modulates heart contraction strength, rate, and conduction *via* A_1 ARs and has been approved by the FDA for treating paroxysmal supraventricular tachycardia (PSVT)[34,35]. However, it may induce atrial fibrillation (AF) in approximately 15% of cases and cause side effects by activating other AR subtypes[34,35]. To minimise off-target effects, medicinal chemists have developed selective A_1 AR ligands. **Tecadenoson** and **selodenoson** (**Figure 1-5**), adenosine-based full agonists with N^6-position substitutions, were investigated for arrhythmia treatment[19,34]. Although **tecadenoson** reduced off-target effects, it was discontinued in 2009 due to a lack of clear therapeutic benefit, and **selodenoson** failed to advance beyond phase II trials[19,34,36].

A_1 AR antagonists have been evaluated for HF treatment[31]. Diuretics play a role in HF treatment for decreasing cardiac pre- and after- loads[37]. Unlike traditional diuretics, which activate tubuloglomerular feedback (TGF), A_1 AR antagonists provide diuretic effects without activating TGF and compromising glomerular filtration rate[32,37]. However, clinical trials of the xanthine-based A_1 AR antagonists **tonapofylline** (**BG9928**) and **rolofylline** (**Figure 1-5**) were terminated—the former in phase II due to sponsor decisions and the latter in phase III due to insufficient efficacy compared to placebo[25,38].

1.3.2 A_1 AR Ligands in Metabolic Diseases

A_1 ARs regulate lipolysis, insulin sensitivity, and secretion in adipose tissue, liver, skeletal muscle, and pancreatic cells[33,39]. **GR79236** (**Figure 1-5**), a selective A_1 AR agonist, inhibited lipolysis and reduced plasma non-esterified fatty acids in rats[34,40]. However, its clinical development for T2DM was hindered by dose-dependent bradycardia and hypotension resulting from cardiac A_1 AR

activation[19,34,41]. These cardiovascular side effects redirected research from full agonists to partial agonists to mitigate such issues[19,31,34].

1.3.3 A_1 AR Ligands for Pain Relief

Activation of A_1 ARs in the brain and spinal cord has demonstrated analgesic effects[42,43]. Study shows that adenosine's pain-relieving properties are absent in A_1 AR knockout mice, while morphine-induced analgesic effect is still preserved[44]. This highlights a distinct mechanism of A_1 AR agonist for analgesics compared to opioids[44]. These findings suggest that selective A_1 AR agonists could provide pain relief while avoiding opioid-related side effects. **GR79236** and **GW-493838** (**Figure 1-5**) were tested as antinociceptive agents but failed due to cardiovascular side effects and insufficient analgesic efficacy[34,41,45,46]. It was proposed that the insufficient analgesic effect may result from inadequate CNS penetration[46].

1.3.4 Challenges and Potential Resolutions for A_1 AR Ligands

Despite the extensive evaluation of A_1 AR-targeting candidates, many clinical trials have failed due to desensitisation, efficacy, and on- and off-target effects[47]. Selective A_1 AR agonists have minimised off-target effects caused by activating other adenosine receptor subtypes. However, full agonists frequently exhibit undesirable on-target cardiovascular side effects, such as bradycardia and hypotension[34,40]. Full agonists also induce tachyphylaxis, which diminishes therapeutic efficacy and limits long-term benefits[31,34].

To address these challenges, A_1 AR partial agonists, positive allosteric modulators (PAMs), and biased agonists have emerged as potential alternatives[34,41,46]. Partial agonists provide partial receptor activation, reducing receptor desensitisation and offering tissue selectivity by eliciting responses that vary based on receptor expression levels[47]. However, partial agonists face limitations such as insufficient therapeutic effects due to their partial agonism and increased on-target side effects at higher doses such as **neladenoson**[48,49](**Figure 1-5**). In clinical trial NCT002988, **neladenoson** exhibited a dose-dependent decline in renal function and limited improvement in cardiac function, suggesting that the initial hypothesis—where partial A_1 AR agonists could retain therapeutic benefits while avoiding adverse effects—may not hold true[48].

Conversely, PAMs offer improved subtype selectivity by targeting less conserved allosteric binding sites, as opposed to the orthosteric binding pockets shared across receptor subtypes[47]. PAMs enhance the affinity and/or efficacy of endogenous ligands, enabling precise activation of A_1 AR-PAM complexes in pathological tissues or organs where adenosine concentrations are elevated[47,49].

For example, **MIPS521** (**Figure 1-5**) demonstrates this approach in animal models, reducing cardiac side effects while preserving analgesic effects[50,51].

Another promising candidate is **BnOCPA** (**Figure 1-5**), an A_1 AR-biased agonist with a unique Gα coupling preference for Gob, differing from conventional agonists that activate both Goa and Gob pathways equally[50,52]. In animal studies, **BnOCPA** exhibits minimal cardiac side effects, locomotor disturbances, respiratory suppression, and sedation, while also demonstrating effective analgesic properties in rat models[52].

These promising ligands, **MIPS521** and **BnOCPA**, offer new hope in A_1 AR drug development, a field historically hindered by on-target side effects and frequent clinical trial failures, previously leading to the classification of A_1 ARs as an undruggable target[53].

A$_1$ AR full agonist

Tecadenoson **Selodenoson** **GR79236** **GW493838**

Adenosine
AR agonist

A$_1$ AR antagonist

Tonapofylline **Rolofylline** Xanthine

Neladenoson,
A$_1$ AR partial agonist

MIPS521,
A$_1$ AR PAM
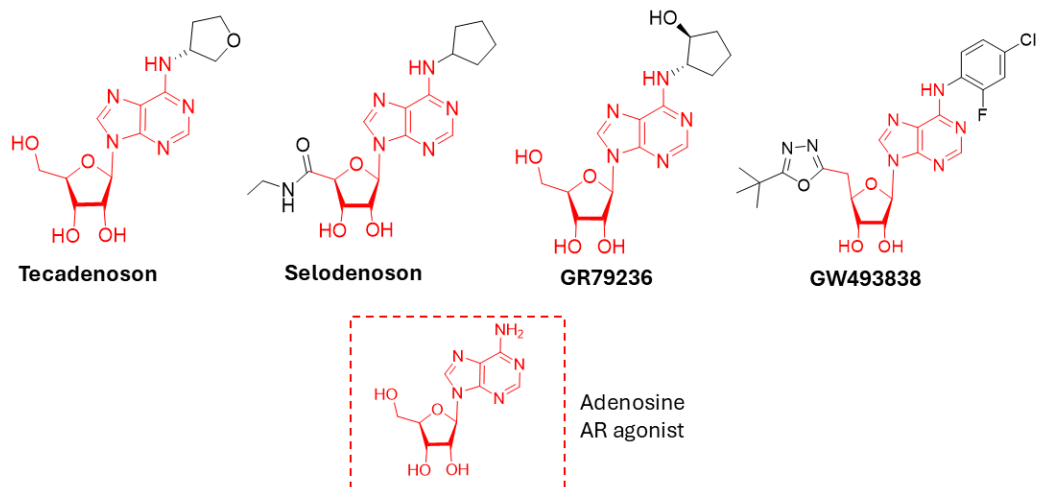
BnOCPA,
A$_1$ AR-biased agonist
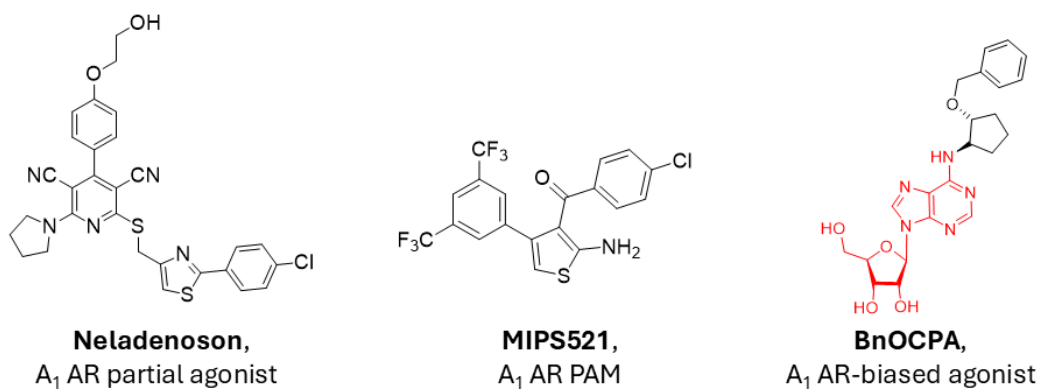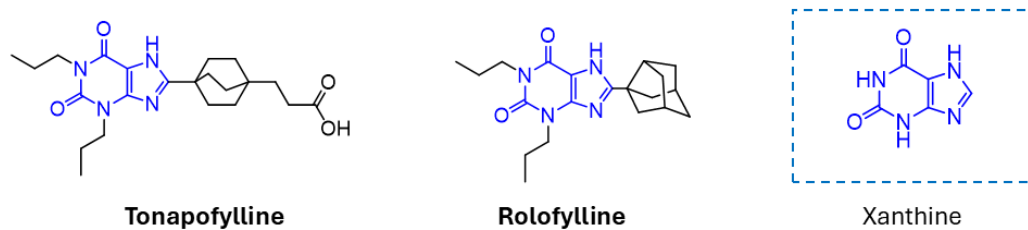
Figure 1-5. Cases of A$_1$ Full Agonist, Partial Agonist and Antagonist Failed from Clinical Trials.
Two promising ligands targeting A$_1$ARs: Positive allosteric modulator (PAM)-**MIPS521** and **BnOCPA**.

1.4 Fluorescent Probes Targeting A$_1$ ARs

Numerous tools are available for studying A$_1$ ARs, each suited to different research objectives. Over the past decades, the toolbox for labelling A$_1$ ARs has expanded to include fluorescent ligands, radioactive probes, recombinant A$_1$ ARs fused with fluorescent proteins, and antibodies. Among these, fluorescent ligands and radioactive probes are small molecules that can be synthesised in an organic chemistry lab. Radioactive probes have long been employed in pharmacological investigations for ligand-binding assessments. However, safety concerns and the complexities of handling and disposal of radioactive materials have motivated researchers to seek alternatives[54].

Fluorescent ligands offer a radiation-free option. Combined with techniques such as resonance energy transfer, advanced microscopy, flow cytometry, and high-throughput screening, fluorescent ligands have significantly broadened their applications in pharmacological studies[54,55]. These advantages have spurred interest in developing fluorescent ligands.

1.4.1 Strengths and Weaknesses of Fluorescent Ligands Compared to Radioactive Probes

The primary limitation of radioactive probes is their associated radiation hazards. Extensive safety measures must be implemented before conducting bioassays with radioactive ligands, including managing operator exposure, securing permissions for the operating area, handling waste disposal, and regulating radioactive material transport. While radioligands are widely used in receptor-ligand binding assays to determine binding affinity, safety concerns restrict their use at high concentrations, limiting their application in fragment-based drug discovery for low-affinity ligands. Furthermore, radioactive binding assays often require a separation step to distinguish receptor-bound ligands from free ligands, which complicates the process and precludes real-time assessments[55].

The scintillation proximity assay (SPA) addresses this drawback by eliminating the need for separation. SPA employs beads that emit photons only when radioactive ligands are in proximity (**Figure 1-6**)[55]. Immobilising target proteins on SPA beads ensures that emitted photons primarily originate from bound ligands[56]. Tritium- or I^{125}-labelled ligands further enhance the signal-to-noise ratio due to their short radiation range in solution, minimising activation by free ligands[56]. However, SPA has limitations. Not all target proteins retain their structure and function when immobilised on beads, and the assay is relatively costly. Despite these challenges, radioligands remain indispensable and complementary tools in pharmacological research. Firstly, they offer a distinct advantage in structural modification, as they typically retain the pharmacological properties of the parent compound with minimal alterations—such as substituting H^1 with H^3.

Secondly, radioligands emit radiation intrinsically and do not require external excitation energy. Consequently, issues such as photobleaching and donor–acceptor orientation are circumvented when employing radioligands. These advantages make radioligands a valuable method for reconfirming and validating probe affinity initially investigated using fluorescent probes.

In contrast, fluorescent ligands are safer and simpler to use in ligand-binding assays. They allow discrimination between bound and free ligands directly or indirectly without the need for separation steps[55]. Techniques such as fluorescence polarization (FP)[57], flow cytometry (FC), and resonance energy transfer (RET)[54] enable real-time assessment by measuring fluorescence and distinguishing ligand states based on polarization, quantum level or proximity (**Figure 1-7**)[58]. Studies have demonstrated that ligand affinities determined using fluorescent ligands are comparable to those obtained with radioligands[54]. Furthermore, fluorescent ligands do not face safety-related concentration limits, enabling the assessment of low-affinity ligands at high concentrations, provided solubility is not an issue.

Fluorescent ligands also enable real-time visualisation of labelled receptors and monitoring receptor dynamics using advanced microscopy[59]. However, their major limitation lies in the structural modifications required to attach fluorophores. Fluorescent ligands typically consist of a pharmacophore, a linker, and a fluorophore. The linker length and fluorophore type can significantly alter the original ligand affinity, selectivity, and biophysical properties, necessitating extensive structural optimisation[60–62].

Given their safety, broad applicability, and simplified binding assessment procedures, fluorescent ligands hold great potential for A_1 AR studies.
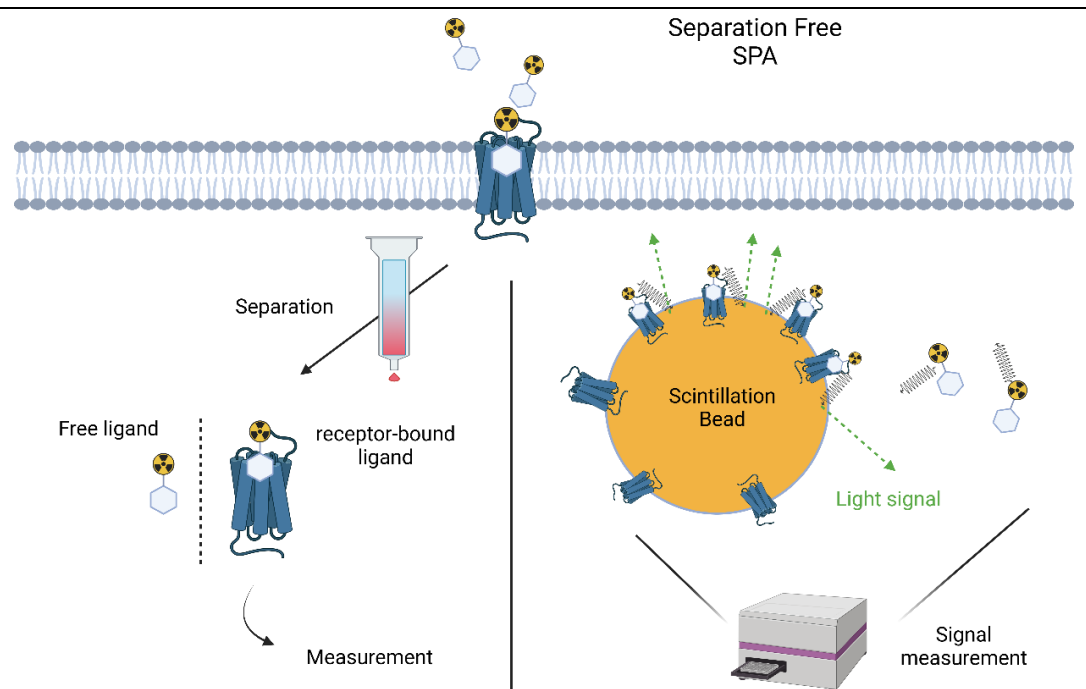
Figure 1-6. Radioactive ligand affinity assessment.
The left part shows that the separation process is needed in traditional radioligand binding assay. The right-hand part depicts the scintillation proximity assay (SPA) which directly measure photons generated from scintillation beads by receptor-bound ligands excitation. Picture was adapted from Soave *et al*. (2020)[55] and created *via* BioRender (https://BioRender.com).
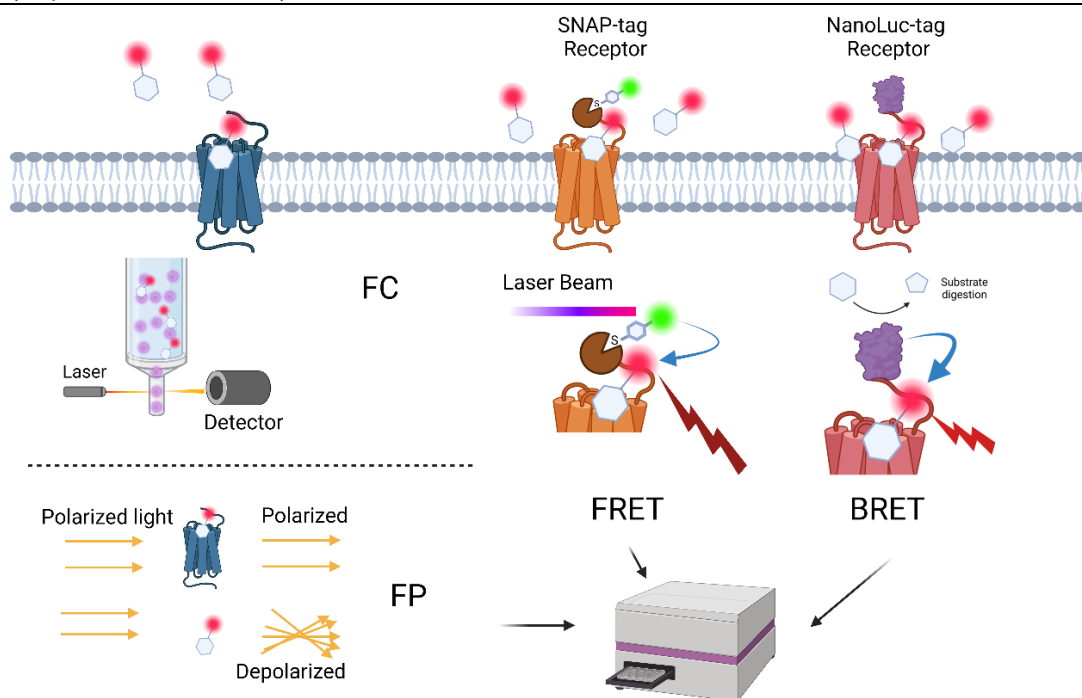
Figure 1-7. Methods of ligand affinity assessment with fluorescent ligands.
Fluorescent ligands affinity on wild type receptors can be measured *via* flow cytometry (FC) and fluorescence polarization (FP). Fluorescence resonance energy (FRET) and bioluminescence resonance energy transfer (BRET) detect fluorescence only when ligands are in proximity with tags set on receptors (Tags: fluorophore in FRET, luciferase in BRET). Therefore, FRET and BRET are employed in ligand binding assessment as they are distance sensitive. The graph was created *via* BioRender (https://BioRender.com).

1.4.2 Reversible, Agonist-Based A_1 AR Fluorescent Ligands (**Table 1-2**)

The development of A_1 AR fluorescent ligands typically begins with functionalised AR agonists or antagonists as pharmacophores. These are further modified by adding a linker for fluorophore attachment. The first reported A_1 AR fluorescent ligands in this category were ADAC-FITC and ADAC-NBD, introduced by Jacobson in 1987[63]. Both ligands, incorporating the adenosine amine congener (ADAC), exhibited nanomolar binding affinity toward A_1 ARs in bovine brain[63].

Subsequent ligands were primarily based on 5'-(*N*-ethylcarboxamido)adenosine (NECA). In 1998, Macchia synthesised a series of fluorescent ligands with varying linker lengths between NECA and dansyl fluorophores[64]. A six-carbon linker yielded the most selective ligand for fluorescence microscopy of rat cerebellar cortex[64]. However, dansyl's absorption wavelength (340 nm) limited its application due to cellular autofluorescence. To address this issue, Macchia replaced dansyl with 7-nitrobenzofurazan (NBD, absorption at 465 nm) in 2001, but the resulting ligands showed a shift in selectivity from A_1 AR to A_3 AR[65].

In 2007, Middleton developed NECA-based ligands coupled with the red-emitting fluorophore BODIPY 630/650 through varying linker lengths[66,67]. Among these, ABEA-X-BY630 demonstrated the highest A_1 AR affinity but suffered from high nonspecific cytoplasmic uptake in confocal images[60]. Later, Baker examined the effects of different fluorophores on ABEA derivatives, revealing that fluorophore and linker composition significantly influenced receptor affinity and selectivity[60]. Among the various fluorophore-conjugated ABEA derivatives, ABEA-X-BY630 stood out as a promising fluorescent probe, maintaining high A_1 AR affinity but requiring further optimisation to mitigate nonspecific cell uptake[60,68].

In 2015, Stoddart introduced ABEA-X-BY630 analogues with tripeptide linkers (Gly-Ala-Ala)[68]. Four possible combinations of D- and L-form amino acids were screened, revealing comparable potency for both A_1 and A_3 ARs[68]. Notably, the high potency of ABEA-Gly-(D)Ala-(D)Ala-X-BY630 facilitated the visualisation of A_3 AR internalisation[68].

1.4.3 Reversible, Antagonist-Based A_1 AR Fluorescent Ligands (**Table 1-3**)

In 1987, Jacobson reported XAX-FITC and XAC-(Gly3)-FITC, which displayed nanomolar binding affinity toward A_1 ARs in bovine brain[63]. Xanthine amine congener (XAC) subsequently became a widely used pharmacophore for fluorescent ligand development. In 2004, Briddon introduced XAC-X-BY630, enabling single-cell A_1 AR visualisation *via* fluorescence correlation spectroscopy and confocal microscopy[69].
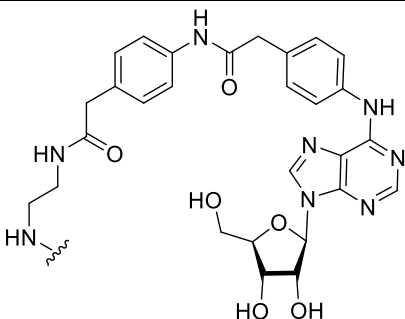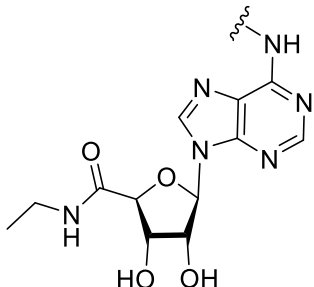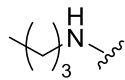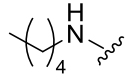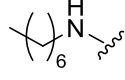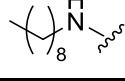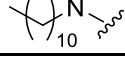
To investigate the effects of fluorophore and linker composition, Baker evaluated XAC analogues attached with various fluorophores across emission wavelengths[60]. XAC-X-BY630 retained A_1 AR affinity as XAC, whereas other derivatives showed diminished affinity[60]. Modifications to XAC-X-BY630, such as introducing a polyamide linker (e.g., **CA200645**), enhanced A_3 AR selectivity and enabled applications like fragment affinity screening[70]. Additional derivatives with dipeptide linkers, such as XAC-Ser-Tyr-X-BY630, further improved A_3 selectivity[71].
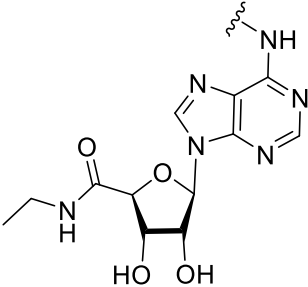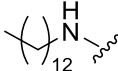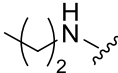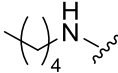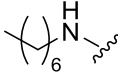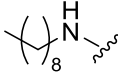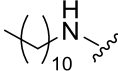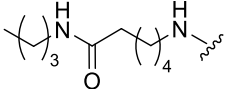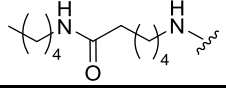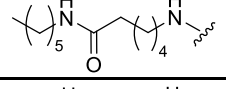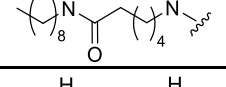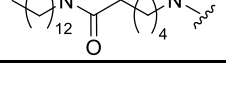
In 2021, Comeo synthesised xanthine-based fluorescent ligands, identifying **EC.44b** and **EC.46a** as subtype-selective ligands with relatively high A_1/A_3 selectivity[72]. These ligands represent advancements in antagonist-based fluorescent probe development for A_1 ARs.

FITC
Excitation: 498 nm
Emission : 517 nm

NBD
Excitation: 467 nm
Emission : 539 nm

Dansyl
Excitation: 335 nm
Emission : 518 nm

BODIPY FL
Excitation: 502 nm
Emission : 511 nm

EvoBlue 30
Excitation: 635 nm
Emission : 663 nm

BODIPY 630/650
Excitation: 625 nm
Emission : 642 nm

Texas red
Excitation: 586 nm
Emission : 603 nm

SulfoCyanine 5
Excitation: 651 nm
Emission : 670 nm
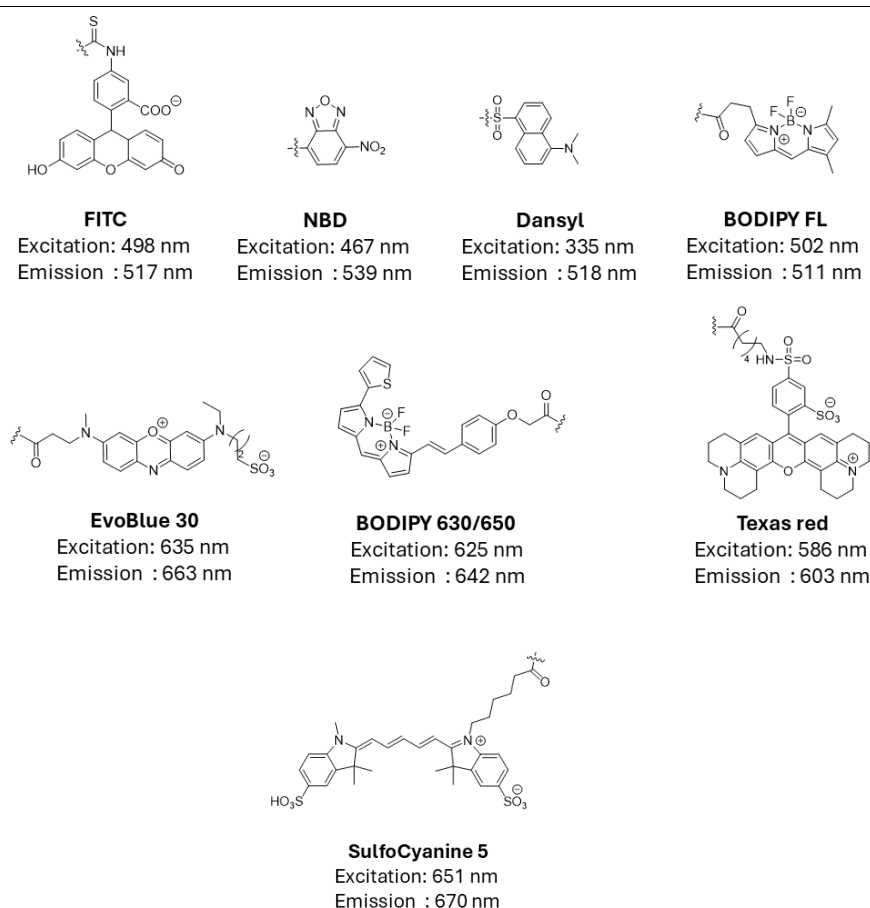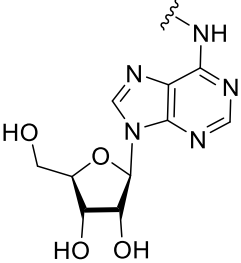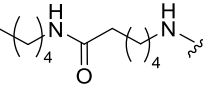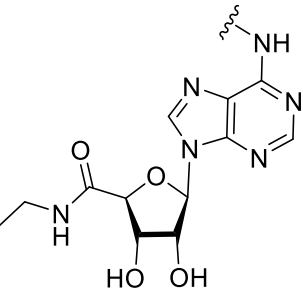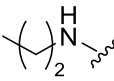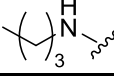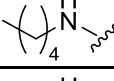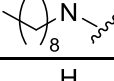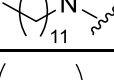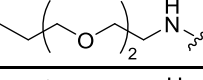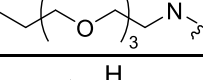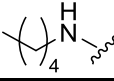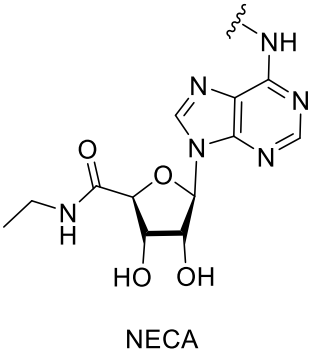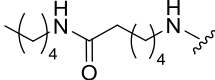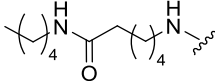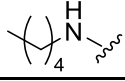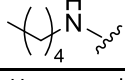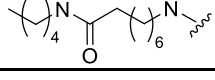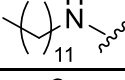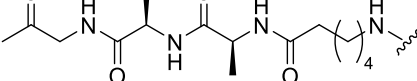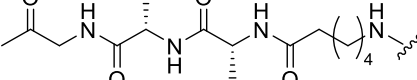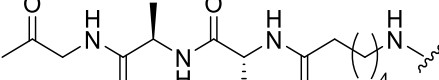
Figure 1-8. Structures and Spectrum Data of Fluorophores Attached in Ligands Targeting A_1 ARs Mention Above.
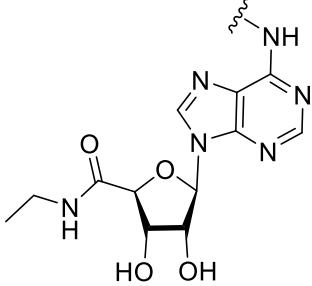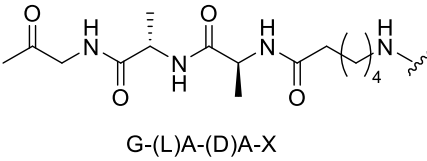
Table 1-2. Structures of agonist-based, reversible A₁ AR fluorescent ligands targeting A₁ ARs are listed in the table below. Each structure is dissected into three parts as an orthostere, a linker, and a fluorophore. (Structures of fluorophores are list in **Figure 1-8**; ligand affinity and references are listed in **Table 1-4**).

No	Compound[A]	Orthostere	Linker	Fluorophore
1-1	ADAC-FITC		-	FITC
1-2	ADAC-NBD	ADAC	-	NBD
1-3	NECA-Dansyl (n=3)			
1-4	NECA-Dansyl (n=4) [B]			
1-5	NECA-Dansyl (n=6)	NECA		Dansyl
1-6	NECA-Dansyl (n=8)			
1-7	NECA-Dansyl (n=10)			

No	Compound[A]	Orthostere	Linker	Fluorophore
1-8	NECA-Dansyl (n=12)		$\left(\ \right)_{12}$ N–H linker	Dansyl
1-9	NECA-NBD (n=2)		$\left(\ \right)_{2}$ N–H linker	
1-10	NECA-NBD (n=4)		$\left(\ \right)_{4}$ N–H linker	
1-11	NECA-NBD (n=6)		$\left(\ \right)_{6}$ N–H linker	NBD
1-12	NECA-NBD(n=8)		$\left(\ \right)_{8}$ N–H linker	
1-13	NECA-NBD (n=10)	NECA	$\left(\ \right)_{10}$ N–H linker	
1-14	AprEA-X-BY630		$\left(\ \right)_{3}$ NH–C(=O)–$\left(\ \right)_{4}$ NH linker	
1-15	ABEA-X-BY630		$\left(\ \right)_{4}$ NH–C(=O)–$\left(\ \right)_{4}$ NH linker	
1-16	APEA-X-BY630		$\left(\ \right)_{5}$ NH–C(=O)–$\left(\ \right)_{4}$ NH linker	BODIPY 630/650
1-17	AOEA-X-BY630		$\left(\ \right)_{8}$ NH–C(=O)–$\left(\ \right)_{4}$ NH linker	
1-18	ADOEA-X-BY630		$\left(\ \right)_{12}$ NH–C(=O)–$\left(\ \right)_{4}$ NH linker	

No	Compound[A]	Orthostere	Linker	Fluorophore
1-19	ABA-X-BY630	Adenosine		
1-20	NECA-BY630 (n=2)	NECA		BODIPY 630/650
1-21	NECA-BY630 (n=3)			
1-22	NECA-BY630 (n=4)			
1-23	NECA-BY630 (n=8)			
1-24	NECA-BY630 (n=11)			
1-25	NECA-BY630 (PEG, n=2)			
1-26	NECA-BY630 (PEG, n=3)			
1-27	ABEA-BY FL			BODIPY FL

No	Compound[A]	Orthostere	Linker	Fluorophore
1-28	ABEA-X-BY FL			BODIPY FL
1-29	ABEA-X-Texas red			Texas red
1-30	ABEA-Cy5			Cy5
1-31	ABEA-EvoBlue30			EvoBlue30
1-32	ABEA-AO-Dansyl			Dansyl
1-33	AUEA-Dansyl			
1-34	ABEA-G-(D)A-(D)A-X-BY630		 G-(D)A-(D)A-X	BODIPY 630/650
1-35	ABEA-G-(L)A-(L)A-X-BY630		 G-(L)A-(L)A-X	
1-36	ABEA-G-(D)A-(L)A-X-BY630		 G-(D)A-(L)A-X	

NECA

19
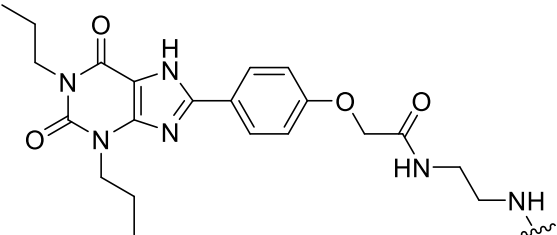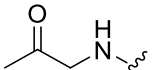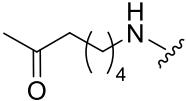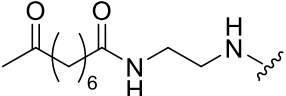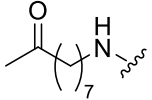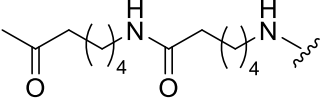
No	Compound[A]	Orthostere	Linker	Fluorophore
1-37	ABEA-G-(L)A-(D)A-X-BY630	 NECA	 G-(L)A-(D)A-X	BODIPY 630/650
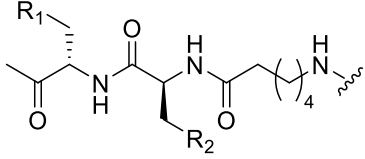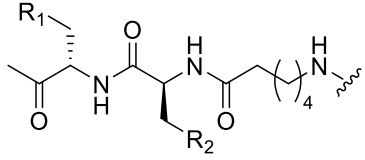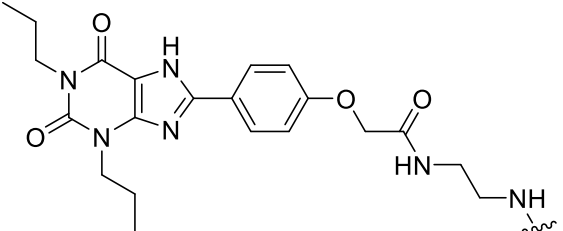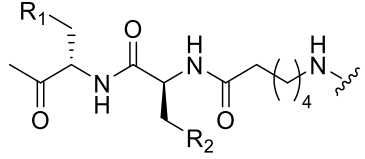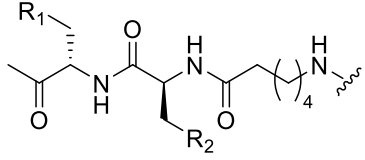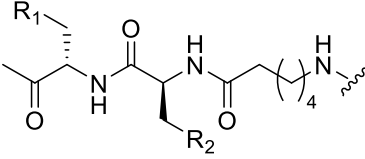
[A] abbreviation: ABEA: N^6-(4-aminobutyl)-5'-ethylamino-5'-oxo-5'-deoxyadenosine; ADAC: adenosine amine congener; ADOEA: N^6-(8-amino-3,6-dioxaoctyl)-5'-ethylamino-5'-oxo-5'-deoxyadenosine; AEAO: 8-(2-aminoethylamino)-8-oxooctanoyl; AHH: 6-(6-aminohexanamido)hexanoyl; AO: 8-aminooctanoyl; AOEA: N^6-(8-aminooctyl)-5'-ethylamino-5'-oxo-5'-deoxyadenosine; APEA: N^6-(5-aminopentyl)-5'-ethylamino-5'-oxo-5'-deoxyadenosine; APrEA: N^6-(3-aminopropyl)-5'-ethylamino-5'-oxo-5'-deoxyadenosine; AUEA: N^6-(11-aminoundecyl)-5'-ethylamino-5'-oxo-5'-deoxyadenosine; NECA: 5'-N-ethylcarboxamidoadenosine.

[B] NECA-Dansyl (n=4) = ABEA-Dansyl

Table 1-3. **Structures of antagonist-based, reversible A₁ AR fluorescent ligands targeting A₁ ARs are listed in the table below**. Each structure is dissected into three parts as an orthostere, a linker, and a fluorophore. (Structures of fluorophores are list in **Figure 1-8**; ligand affinity and references are listed in **Table 1-4**).

No	Compound[A]	Orthostere	Linker	Fluorophore
1-38	XAC-FITC		-	FITC
1-39	XAC-Gly₃-FITC		(structure)	
1-40	XAC-X-BY630		(structure)	BODIPY 630/650
1-41	XAC-X-Texas red		(structure)	Texas red
1-42	XAC-AEAO-BY FL	(structure)	(structure)	BODIPY FL
1-43	XAC-EvoBlue 30		-	EvoBlue 30
1-44	XAC-Cy5		-	Cy5
1-45	XAC-Dansyl		-	Dansyl
1-46	XAC-AO-Dansyl		(structure)	
1-47	XAC-AHH-Dansyl		(structure)	

No	Compound[A]	Orthostere	Linker	Fluorophore
1-48	CA200645		R_1=H, R_2=OH	
1-49	XAC-A-S-X-BY630		R_1=H, R_2=OH	
1-50	XAC-A-Y-X-BY630		R_1=H, R_2=Ph(4-OH)	BODIPY 630/650
1-51	XAC-N-A-X-BY630		R_1=CONH$_2$, R_2=H	
1-52	XAC-S-Y-X-BY630		R_1=OH, R_2=Ph(4-OH)	

No	Compound[A]	Orthostere	Linker	Fluorophore
1-53	XAC-S-Y-X-BYFL		R_1=OH, R_2=4-OH Ph	BODIPY FL
1-54	EC.44b			Cy5
1-55	EC.46a			BODIPY 630/650

[A] abbreviation: XAC: xanthine amine congener; EC.44b and 46a were the compound number in Comeo *et al*. (2021)[72].

Table 1-4. Affinity and selectivity of fluorescent ligands list in Table 1-2 & Table 1-3

Cpd No	pK_D or pK_i				Affinity Ratio	Ref.	Mark
	A_1	A_{2A}	A_{2B}	A_3	$A_{2A}, A_{2B}, A_3/A_1$		
1-1	8.54 (pK_i)					63	*Bovine brain A_1 AR. *Radioligand binding assay with [^{3}H] (R)-PIA
1-2	8.79 (pK_i)						
NECA	5.3-8.2 / -	6.9-8.7 / -	5.7-6.9 / -	7.5-8.4 / -		IUPHAR/BPS	
1-3	7.38 (pK_i)	5.37 (pK_i)		5.74 (pK_i)	A_2/A_1:102; A_3/A_1:43	64	*Rat cortical-A_1, measured with [^{3}H]-CHA *Rat striatal-A_2, measured with [^{3}H]-CHA *Rat testis membrane-A_3, measured with [^{3}H] (R)-PIA. *Cpd 1-5 showed highest A_1 AR affinity in this series and maintained good selectivity.
1-4	7.15 (pK_i)	5.02 (pK_i)		5.70 (pK_i)	A_2/A_1:135; A_3/A_1:29		
1-5	7.57 (pK_i)	5.37 (pK_i)		5.44 (pK_i)	A_2/A_1:159; A_3/A_1:133		
1-6	6.95 (pK_i)	< 4 (pK_i)		6.60 (pK_i)	A_2/A_1: >90; A_3/A_1:2		
1-7	6.63 (pK_i)	< 4 (pK_i)		5.96 (pK_i)	A_2/A_1:>42; A_3/A_1:4.7		
1-8	5.47 (pK_i)	< 4 (pK_i)		5.60 (pK_i)	A_2/A_1:>3; A_3/A_1:0.7		
1-9	< 4 (pK_i)	5.17 (pK_i)		7.25 (pK_i)	A_2/A_1:< 0.67; A_3/A_1:0.005	65	*Human cortical membrane-A_1, measured with [^{3}H]-DPCPX
1-10	< 4 (pK_i)	< 4 (pK_i)		6.42 (pK_i)	A_2/A_1: 1; A_3/A_1:0.04		

1-11	< 4 (pK_i)	5.22 (pK_i)	7.63 (pK_i)	A$_2$/A$_1$:< 0.61; A$_3$/A$_1$:0.002	*Human striatal membrane-A$_2$, measured with [^{3}H]-CGS21680
1-12	5.46 (pK_i)	5.29 (pK_i)	8.13 (pK_i)	A$_2$/A$_1$:1.47; A$_3$/A$_1$:0.002	*Human striatal membrane-A$_2$, measured with [^{3}H]-CGS21680
1-13	5.20 (pK_i)	5.21 (pK_i)	7.55 (pK_i)	A$_2$/A$_1$:0.96; A$_3$/A$_1$:0.004	*hA$_3$ AR expressed in CHO cells, measured with [^{125}I]-AB-MECA. *Selectivity shifted from A$_1$ to A$_3$ AR when danyl was swapped by NBD.
1-14	6.61 (pK_D)				*hA$_1$, A$_{2A}$, A$_{2B}$, and A$_3$ ARs were expressed in CHO cells respectively. *A$_1$ AR measured with [^{3}H]-DPCPX. *1-15 showed the highest A$_1$ affinity in this study ***1-16**,**1-17** affinity can't be defined below 10 μM.
1-15	6.80 (pK_D)				
1-16	-			66	
1-17	-				
1-18	6.19 (pK_D)			60	As **1-27** to **1-33**
1-19	6.65 (pK_D)			66	Measurement was same as 1-14
1-20	6.44 (pK_i)				*hA$_1$ AR expressed in CHO cells, affinity was
1-21	6.38 (pK_i)			67	
1-22	6.58 (pK_i)				

1-23						measured with [³H]-DPCPX.
1-24						
1-25					67	*Binding affinity data was not provided in reference.
1-26						
1-27	< 4 (pK_D)					*hA$_1$ AR expressed in CHO cells, affinity was measured with [³H]-DPCPX.
1-28						
1-29						
1-30	< 4 (pK_D)				60	*Swapping BY630 in **1-15** with different fluorophores reduce A$_1$ AR binding affinity.
1-31						
1-32	< 4 (pK_D)					
1-33	4.97 (pK_D)					
1-34	6.17 (pK_D)					
1-35					68, 74	*Affinity was measured in NLuc-hA$_1$ AR.
1-36						
1-37						
XAC	7.5	8.4-9.0	6.9-8.8	7.0-7.4	IUPHAR/BPS	
1-38	8.03 (pK_i)				63	*Bovine brain A$_1$ AR. *Radioligand binding assay with [³H] (*R*)-PIA
1-39	7.78 (pK_i)					
1-40	7.42 (pK_D)				60	*Radioligand binding assay with [³H]-DPCPX.
1-41	5.72 (pK_D)					
1-42	< 4 (pK_D)					

1-43	5.27 (pK_D)					
1-44	5.59 (pK_D)					
1-45	6.71 (pK_D)					
1-46	6.91 (pK_D)					
1-47	6.87 (pK_D)					
1-48	7.9 (pK_D)	7.56 (pK_D)	8.05 (pK_D)	7.55 (pK_D)	A_{2A}/A_1: 2.47; A_{2B}/A_1:0.83; A_3/A_1:2.35	Measured on my own	*Affinity was measured *via* BRET. *NLuc-hA$_1$, hA$_{2B}$, and hA$_3$ ARs were expressed by HEK G cells. *NLuc-hA$_{2A}$ ARs were transiently expressed by HEK T cells.
1-49	8.39 (pK_D)			9.29 (pK_i)	A_3/A_1: 0.13		*hA$_1$ and hA$_3$ ARs were expressed in CHO cells. *A$_1$ affinity was measured *via* [^{3}H]-DPCPX. *A$_3$ affinity measured by antagonising agonist-stimulated responses. *The series showed selectivity on A$_3$ ARs.
1-50	7.62 (pK_D)			8.41 (pK_i)	A_3/A_1: 0.16	71	
1-51	7.82 (pK_D)			8.58 (pK_i)	A_3/A_1: 0.17		
1-52	7.62 (pK_D)			9.12 (pK_i)	A_3/A_1: 0.03		
1-53	6.50 (pK_D)			7.96 (pK_i)	A_3/A_1: 0.03		
1-54	7.35 (pK_D)	< 6 (pK_D)	< 6 (pK_D)	< 6 (pK_D)	A_{2A}/A_1: > 22.4; A_{2B}/A_1: > 22.4; A_3/A_1:> 22.4	72	*Ligand affinity was assessed with HEKG cells expressing NLuc-hA$_1$, hA$_{2A}$, hA$_{2B}$, or hA$_3$ ARs *via* BRET.
1-55	8.50 (pK_D)	7.30 (pK_D)	7.26 (pK_D)	7.23 (pK_D)	A_{2A}/A_1: 15.8; A_{2B}/A_1:17.4; A_3/A_1:18.6		

1.5 Covalent Labelling of A_1 ARs with Fluorescent tags

Over the past three decades, numerous fluorescent ligands have been developed for A_1 ARs[73], enabling investigations at the single-cell level using confocal microscopy[66,72,74], exploration of protein-protein interactions[75], and assessment of non-fluorescent ligand binding affinity[70,76,77]. However, these reversible fluorescent ligands are unsuitable for long-term studies due to ligand dissociation from receptors. Additionally, they occupy the orthosteric binding pocket, limiting the observation of receptor activity induced by non-fluorescent ligands. Another concern is their potential for off-target labelling of other adenosine receptor subtypes due to a narrow selectivity window. Therefore, a highly selective covalent labelling method for A_1 ARs is needed to expand the toolkit for A_1 AR research.

1.5.1 Covalent Labelling of Engineered A_1 ARs

Several methods enable the covalent labelling of a protein of interest (POI) using engineered cell models. Since its introduction in eukaryotic cells in 1994, fluorescent proteins (e.g., GFP) have been extensively applied in cell biology research[78]. GFP, consisting of 238 amino acids (~27 kDa)[79], can be fused to a POI[80], facilitating studies of protein localisation, interactions, and translocation. Various fluorescent proteins with distinct spectroscopic properties are available, allowing flexible experimental designs[80].

An alternative approach is the use of self-labelling protein tags, which rely on enzyme-mediated covalent labelling. Human O^6-alkylguanine-DNA alkyltransferase (hAGT) recognizes O^6-alkylated benzyl guanine (BG) derivatives, transferring the alkyl moiety onto itself for DNA repair[80,81]. This mechanism has been harnessed to develop self-labelling tags such as SNAP-tag and CLIP-tag, which specifically react with BG and O^2-benzyl cytosine derivatives, respectively, allowing fluorophore attachment (**Figure 1-9**)[80–82]. Other self-labelling tags include the bacterial dehalogenase-derived Halo-tag[83], fungal-derived Cutinase-tag[84], beta-lactamase-tag, purple bacterial photoactive yellow protein (PYP)-tag[85], and E. coli dihydrofolate reductase (eDHFR)-tag[86]. These tags provide high specificity, versatile fluorophore selection, and rapid labelling, making them valuable tools in cell biology and pharmacology.

Non-enzymatic peptide-based tags also facilitate covalent labelling. In 2007, Hamachi and colleagues introduced the Cys-(Ala)6-(Asp)4 peptide tag (CA6D4 tag), where tetraaspartate directs Zn(II)-Dpa-Tyr probes to the POI, and the cysteine residue undergoes proximity-driven nucleophilic substitution for covalent labelling (**Figure 1-9**)[87].

While covalent labelling techniques offer advantages such as stability during long-term studies and compatibility with ligand binding assessments, they require genetic modifications, limiting their applicability to native cells[88].

Additionally, concerns have been raised regarding the potential interference of large tags with the natural behaviour of POIs[88].
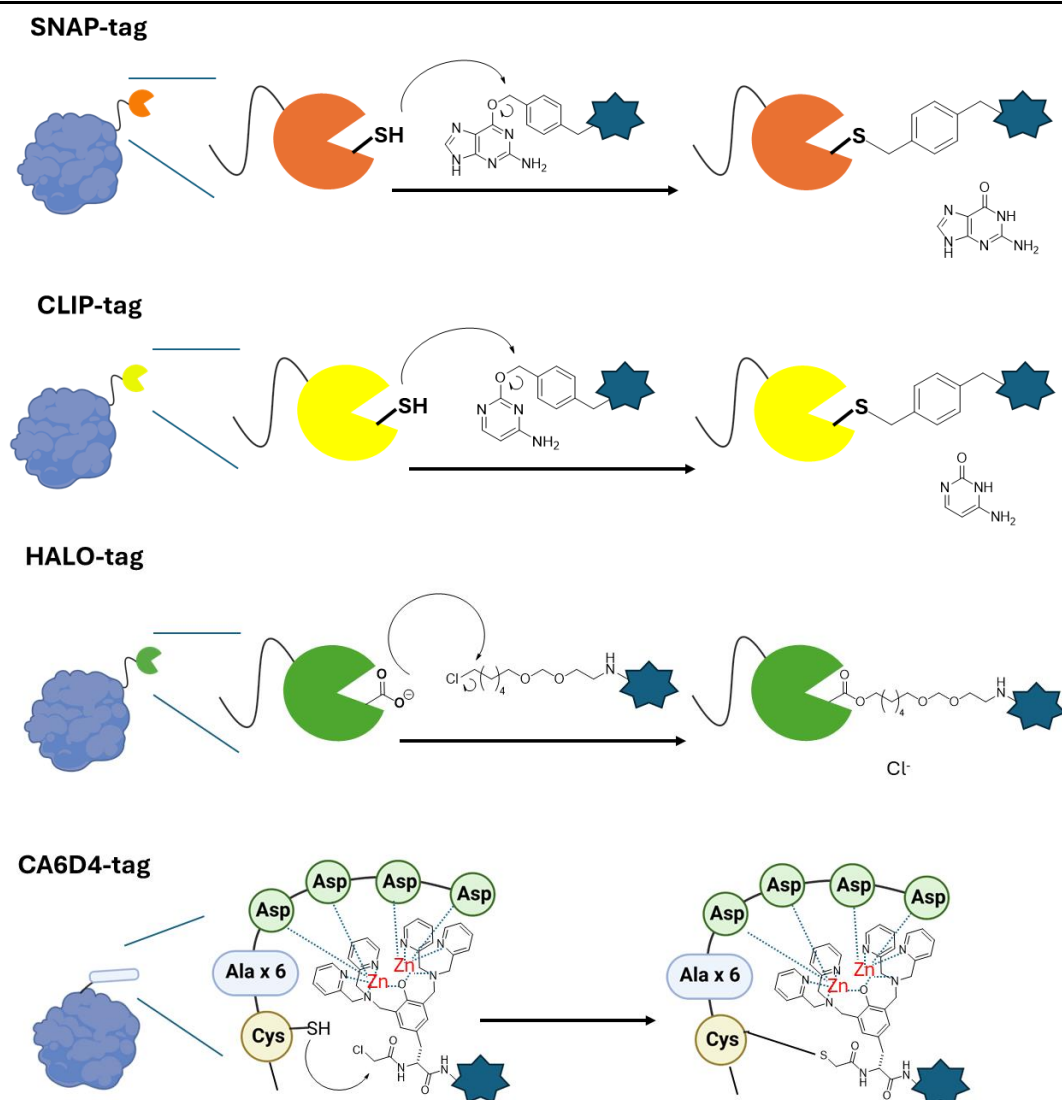
Figure 1-9. The Mechanism of Self-Labelling Protein Tags and the CA6D4 Short Peptide Tag involves Tagging Target Proteins.
The SNAP tag forms a covalent bond with an O^6-benzylguanine-incorporated substrate *via* a cysteine residue, while the CLIP tag similarly binds an O^2-cytosine-incorporated substrate through cysteine. HALO tags, on the other hand, interact with chloroalkane substrates. The CA6D4 tag chelates a Zn(II)-Dpa-Tyr probe, facilitating the formation of a covalent bond between cysteine and the Zn(II)-Dpa-Tyr probe. Pictures modified from Nonaka *et al*. (2007)[87] and Amaike *et al*. (2017)[88]. The elements used in the graph were generated *via* BioRender (www.BioRender.com).

1.5.2 Ligand-Directed (LD) Covalent Labelling Probes

Covalently tagging endogenous proteins in native cells *via* chemical reactions provides a powerful strategy for POI investigation. However, achieving specificity in a complex cellular environment with low POI expression is challenging. Efficient reactions must occur under mild physiological conditions with optimal kinetics.

LD probes address these challenges by incorporating three components: an orthostere for POI binding, a reactive moiety for covalent attachment, and a transferable cargo. Pharmacophore with high selectivity ensures POI targeting, while the reactive moiety, positioned near nucleophilic amino acids, facilitates a pseudo-intramolecular reaction to enhance reaction rates and cargo transfer[89].

1.5.2.1 Reactive Moiety Used in LD Probes

To develop an effective LD probe, a reactive moiety capable of efficiently transferring cargo under physiological conditions while maintaining stability in aqueous environments is critical[88,89]. Several reactive moieties have been incorporated into LD probes in the literature (**Figure 1-10**).

In 2009, Hamachi's group introduced a tosyl-based LD probe (LDT), which successfully transferred fluorophores, biotin, and ^{19}F tags onto carbonic anhydrase (CA) in purified protein samples, human red blood cells, and mouse blood (both *in vitro* and *in vivo*)[90]. SDS-PAGE analysis with fluorescent scanning confirmed CA-specific labelling, which was further validated through selective labelling in protein mixtures and competitive inhibition studies[90]. However, LDT probes suffered from slow reaction rates and low labelling efficiency, limiting their broader application.

To address these limitations, Hamachi's group introduced acyl imidazole (LDAI) as a reactive moiety in 2012 and compared its performance with LDT[91]. In a study involving folate receptor-targeting probes, western blotting and fluorescence imaging demonstrated that LDAI exhibited superior labelling efficiency[91]. Subsequently, in 2015, Hamachi's group introduced dibromophenyl benzoate (BB) as a new reactive moiety[92]. Fenical's group had previously used phenyl ester (PE) to label actin covalently[93]. To enhance the reaction rate of LDPE, Hamachi's group optimised phenyl ring substitutions, balancing reactivity and stability. Their findings showed that *ortho*-dibromophenyl benzoate provided superior labelling efficiency compared to other derivatives, such as *ortho*-dichlorophenyl benzoate and *ortho*-nitrophenyl benzoate, as well as LDAI[92]. The study also highlighted the impact of linker length on labelling yield, reaction rate, and LDBB stability[92]. Initially, a tetrafluorophenyl benzoate moiety was proposed due to its high electron withdrawing effect, but its instability prevented successful purification[92].

In 2018, Hamachi's group expanded LD probe chemistry by introducing *N*-sulfonyl pyridone (SP) and *N*-acyl-*N*-alkyl-sulfonamide (NASA) as new reactive moieties. LDSP exhibited rapid and specific CA labelling, outperforming LDT and LDAI in analogous systems[94]. Furthermore, LDSP-conjugated fluorophores enabled fluorescence resonance energy transfer (FRET) studies with reversible CA-fluorescent probe interactions in human breast cancer cells (MCF7)[94].

Meanwhile, LDNASA optimisation focused on selecting the best electron-withdrawing group for enhancing labelling efficiency. Among cyano, 4-nitrophenyl, and 2,4-dinitrophenyl groups, cyano proved the most effective, achieving the highest labelling efficiency on FKBP12[95]. Kinetic analysis further confirmed that LDNASA labelling rates for FKBP12 and eDHFR surpassed those of LDBB and LDAI, reaching levels comparable to self-labelling enzyme tags (e.g., SNAP and CLIP) and the fastest click reaction pairs, such as tetrazine and *trans*-cyclooctene[95].

Benzotriazole (BTA) was introduced as the reactive moiety by Wu's group in 2022[96]. FKBP12, GRAMD1A, and CA were labelled using probes incorporating BTA as the reactive moiety, and their validation was performed *via* mass spectrometry, in-gel fluorescent scanning, and confocal imaging[96]. The study also highlighted that the LDBTA labelling reaction proceeded at a faster rate compared to LDNASA, as evidenced by the kinetic investigation of FKBP12 labelling with two probes incorporating either LDNASA or LDBTA[96].

Tosyl[97], acyl imidazole[98], dibromophenyl benzoate[92], *N*-sulfonyl pyridone[99], *N*-acyl-*N*-alkyl-sulfonamide[95,99] and benzotriazole[96] have all been demonstrated as effective LD probe reactive moieties, successfully tagging proteins of interest in live cells. Variations in labelling speed, efficiency, and physicochemical properties provide a versatile toolkit for designing LD probes tailored to specific protein targets.
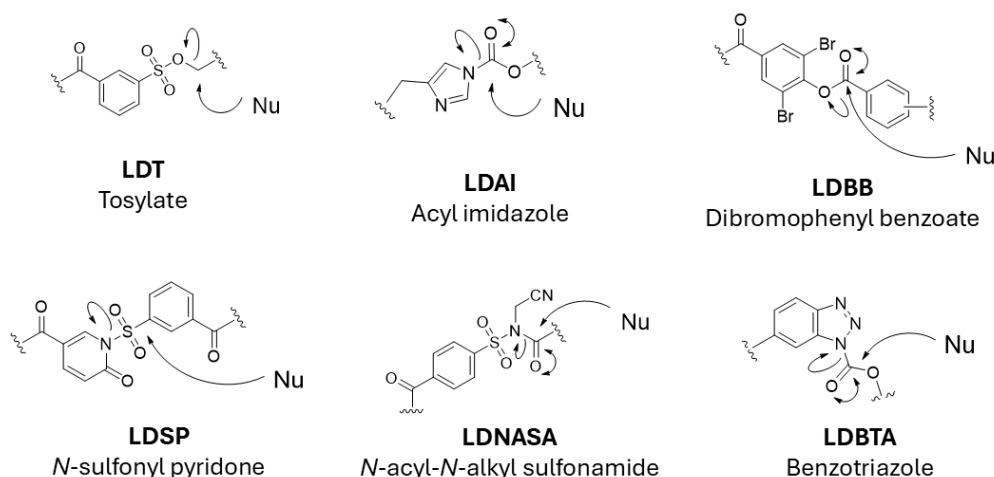
Figure 1-10. Structures of LD Reactive Moiety and the Mechanism of Nucleophilic Substitution.

1.5.2.2 LD Probes for Click Reaction Handle Transfer

Click reactions are a class of highly efficient and selective chemical reactions used to covalently link two moieties. The concept was introduced to enable universal and reliable chemical synthesis with simple operational procedures. Since the early 2000s, several click reaction pairs have been developed and widely applied in medicinal chemistry, peptide synthesis, polymer chemistry, and radiochemistry[100]. Click chemistry has also been extensively utilised for biomolecular labelling. The first biological application was reported by Saxon and Bertozzi in 2000[101], who demonstrated cell surface engineering by treating cells with azidosugars, which were incorporated into glycoconjugates *via* metabolism[101]. The azide tag was then used to attach a biosensor through a click reaction, showcasing the potential of click chemistry in biological research[101]. However, executing a click reaction on a POI requires pre-installing a click reaction handle. Previous approaches relied on metabolically incorporating azidosugars[102] or azido amino acids[103] into target proteins, a process requiring several days. LD probes, which covalently transfer cargo onto POIs, offer a solution by rapidly installing a click reaction handle.

Once the click reaction handle is established *via* an LD probe, the next consideration is selecting an appropriate click reaction pair. The following four commonly used click reactions have been employed in biomolecular labelling:

Staudinger Ligation: This reaction was first employed by Bertozzi's group to attach biosensors to cell surfaces[101] and mucin-type *O*-linked glycoproteins[102]. Staudinger ligation occurs between an azide and a phosphine equipped with an electrophilic trap. The phosphine reacts with the azide to form an iminophosphorane intermediate, which releases N_2 and undergoes an intramolecular cyclisation to yield an oxazaphosphetane, ultimately hydrolysing into a phosphine oxide-containing amide in an aqueous environment[104] (**Figure 1-11**). Staudinger ligation can be categorised into traceless and non-traceless forms, depending on whether a cleavable linker is present between the electrophilic trap and phosphine[104]. The traceless variant yields labelling products without residual phosphine oxide. While biocompatible and selective, Staudinger ligation suffers from slow reaction kinetics and phosphine oxidation, limiting its applications[104].

Cu(I)-Catalysed Azide-Alkyne Click Chemistry (CuAAC): 1,2,3-Triazoles can be synthesised *via* 1,3-dipolar cycloaddition between an azide and an alkyne. However, the reaction is slow and yields regioisomeric products. The introduction of Cu(I) as a catalyst significantly accelerates the reaction and gives regioselective product[105] (**Figure 1-11**). CuAAC offers faster kinetics than Staudinger ligation but requires reducing agents to generate Cu(I) from Cu(II) salt

and prevent Cu(I) oxidation[106]. The oxidative byproducts of reductants and copper ions are cytotoxic, necessitating careful optimisation of copper concentrations, incubation times, catalyst ligands, and quenching agents[106]. Despite these limitations, CuAAC remains a preferred choice for cellular experiments due to its rapid kinetics[107].

Strain-Promoted Azide-Alkyne Cycloaddition (SPAAC): To circumvent Cu toxicity, Carolyn's group developed SPAAC, which employs strained cyclooctynes instead of linear alkynes to enhance reaction rates[108] (**Figure 1-11**). Further kinetic improvements were achieved by introducing electrophiles or fusing biphenyl rings to increase ring strain, yielding reagents such as 4-dibenzocyclooctynol (DIBO) and aza-dibenzocyclooctynes (DIBAC)[107]. However, the increased size and lipophilicity of these modifications hinder biomolecule incorporation and lead to non-specific protein binding[109]. To address this, bicyclo[6.1.0]nonyne (BCN) was developed, exhibiting ~100-fold higher reactivity than cyclooctyne without significantly increasing lipophilicity[109].

Inverse Electron Demand Diels-Alder Reaction (IEDDA): 1,2,4,5-Tetrazines (dienes) react with alkenes *via* IEDDA, forming a cycloadduct and eliminating N_2 gas[110] (**Figure 1-11**). IEDDA is the fastest click reaction among those discussed and is widely adopted for biomolecular labeling. The reaction rate depends on the diene and alkene partners, with *trans*-cyclooctene (TCO) frequently employed due to its low activation energy[107]. Electron-withdrawing groups on tetrazines enhance reaction kinetics, while electron-donating groups have the opposite effect[111]. Despite its advantages, TCO isomerisation and tetrazine stability must be considered in experimental designs[111].

Nontraceless Staudinger Ligation

Iminophosphorane
(ylide form)

Oxazaphosphetane

Phosphine oxide
Incorporated amide

Iminophosphorane
(ylene form)
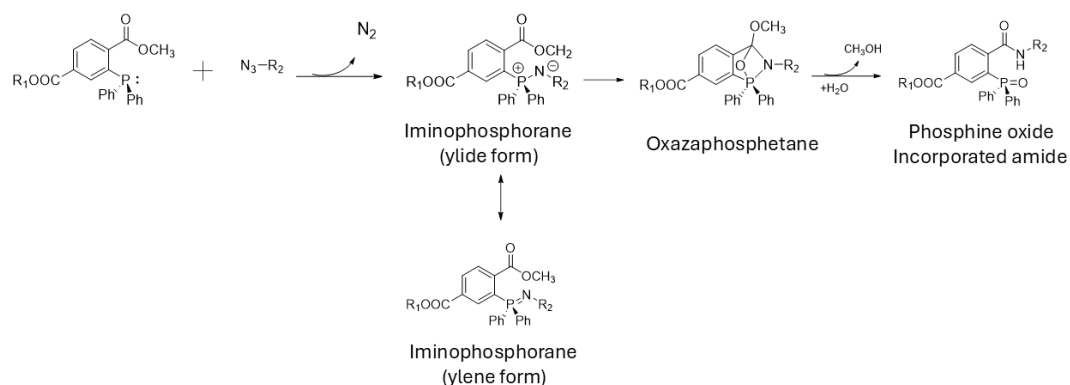
Traceless Staudinger Ligation
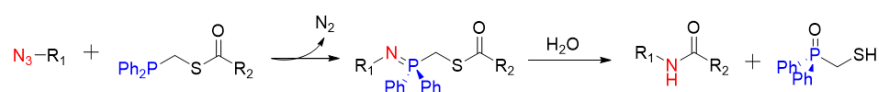
Cu(I)-Catalyzed Azide-Alkyne Click Chemistry (CuAAC)
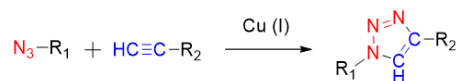
Strain-Promoted Azide-Alkyne Cycloaddition (SPAAC)

Alkynes with
higher reaction rate

DIBO

DIBAC

BCN
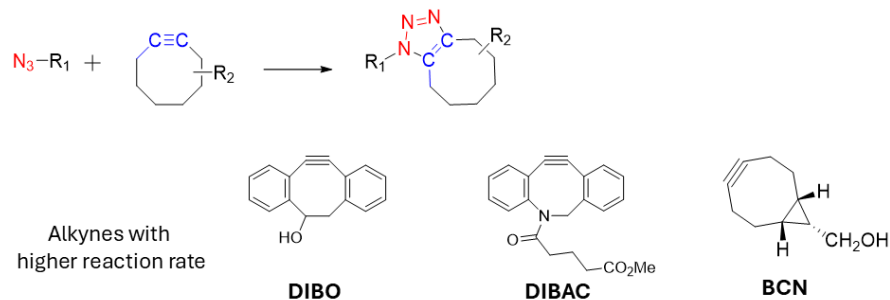
Inverse Electron Demand Diels-Alder Reaction (IEDDA)
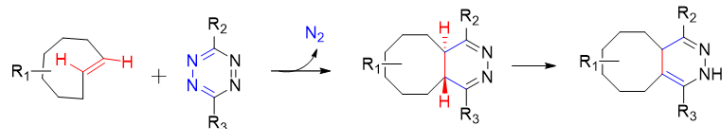
Figure 1-11. List of Click Reaction Applied in Biomolecular Investigation.
The picture depicts how two molecules conjugate together through corresponding click reactions. Reaction mechanism was adopted from Bednarek *et al*. (2020)[104] and Bird *et al*. (2021)[107].

1.5.2.3 Covalent Labelling of A_1 ARs with Small Molecular Probes

Beerkens reported an affinity-based probe, **LUF7909** (**Figure 1-12**), which demonstrated the ability to introduce an alkyne handle onto A_1 ARs *via* a covalent bond formed between its sulfonyl fluoride moiety and an amino acid residue of A_1 AR[112]. The alkyne handles subsequently enabled click chemistry reactions with biosensors, such as biotin or fluorophores, *via* CuAAC[112]. The covalent tagging strategy facilitated wash-resistant labelling and pull-down experiments for proteomics analysis, broadening the scope of A_1 AR investigations. However, **LUF7909** occupied the A_1 AR orthosteric binding site, hindering further functional analyses with other ligands.

In 2024, Comeo reported two successful LD probes (compounds **1-56** and **1-57**, **Figure 1-12**) for covalently labelling A_1 ARs[74]. Compound **1-56** directly transferred a SulfoCy5 fluorophore onto A_1 ARs in both native cells (dorsal root ganglion neurons) and overexpressing HEK293G and HEK293T cells[74]. Meanwhile, compound **1-57** installed a TCO click handle on A_1 ARs, enabling subsequent labelling with methyl tetrazine-SulfoCy5 *via* IEDDA click chemistry[74]. Both probes utilised a 2-fluorophenyl ester as the reactive moiety, first introduced in LD probes targeting A_{2A} ARs in 2020[113].

In a personal conversation, Dr. Nicholas Kindon described his design of a 2-fluorophenyl ester to achieve covalent labelling of A_{2A} ARs. By analysing the docking structure of the A_{2A} antagonist ZM241385 with A_{2A} AR (PDB: 4EIY), he identified lysine residues (K150 and K153) proximal to ZM241385's phenol group (**Figure 1-13**). Functionalising this phenol into a phenyl ester may allow site-specific amide bond formation. To enhance reactivity while preserving structural integrity, fluorine was chosen as an electron-withdrawing substituent. The resulting compound successfully labelled A_{2A} ARs[113]. Inspired by this strategy, Comeo successfully applied the 2-fluorophenyl ester approach to LD probes for A_1 ARs labelling.
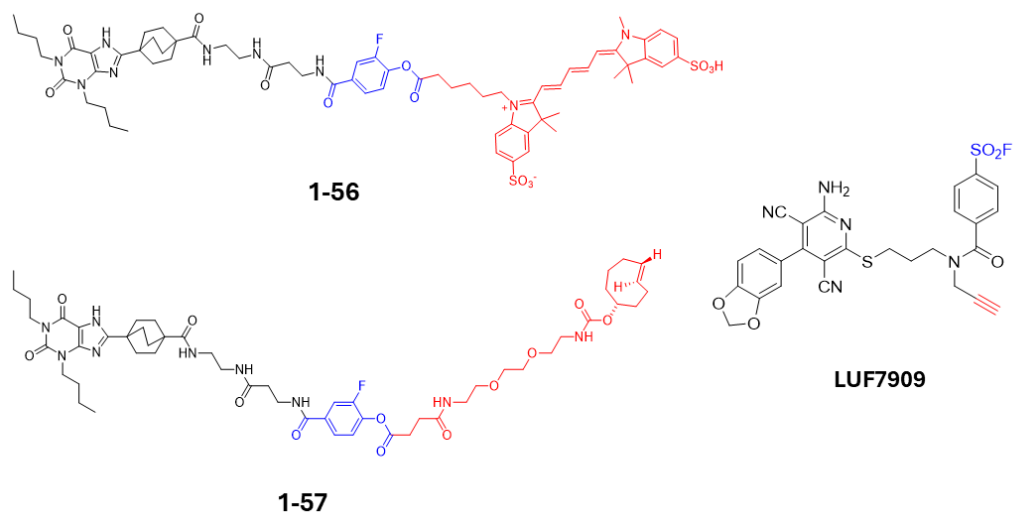
Figure 1-12. Structures of compounds 1-56, 1-57, and LUF7909.
In **1-56** and **1-57**, the 2-fluorophenyl ester (blue) serves as the reactive moiety, while the red-highlighted regions represent transferred cargos—SulfoCy5 for **1-56** and a TCO (click reaction handle) for **1-57**. **LUF7909** covalently binds to A_1 ARs *via* its sulfonyl fluoride moiety (blue), with the alkyne functionality enabling CuAAC conjugation to a desired biosensor.

ZM241385 docking with A_{2A} AR (PDB:4EIY)
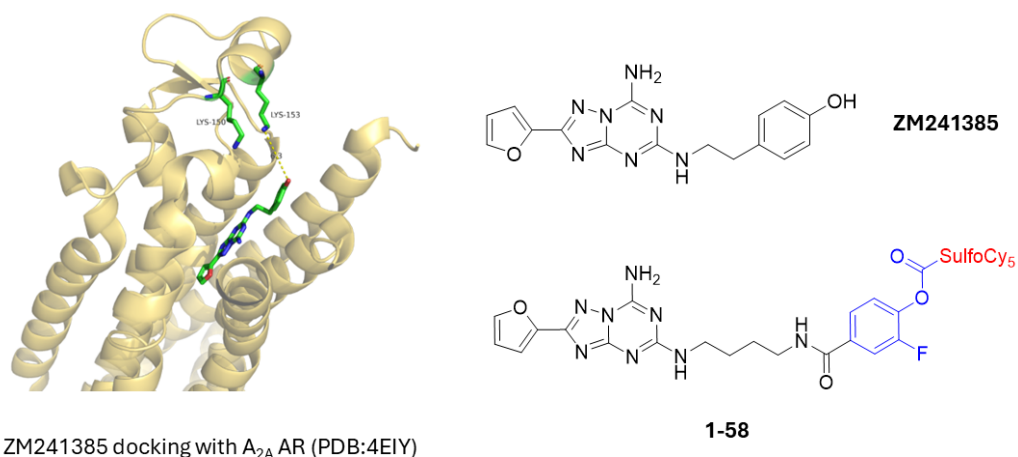
Figure 1-13. Inspiration of 2-fluorophenyl ester Design.
The 2-fluorophenyl ester, inspired by the docking results of ZM241385 with the A_{2A} AR (PDB: 4EIY), was incorporated as the reactive moiety (blue moiety) into the ZM241385-based labelling probe (**1-58**). This probe successfully labelled A_{2A} ARs[113].

1.6 Thesis Aim

A_1 AR agonists and antagonists have been investigated in clinical trials owing to their therapeutic potential. **Neladenoson bialanate**, a partial A_1 AR agonist, was evaluated for the treatment of heart failure (NCT03098979)[114]. Additionally, the selective A_1 AR antagonists **SLV320** and **tonapofylline** were studied for their natriuretic effects in patients with acute heart failure while aiming to preserve renal function (NCT00744341 for **SLV320**[115]; NCT00709865 and NCT00745316 for **tonapofylline**[116]). However, many candidates failed in clinical trials due to on-target side effects resulting from the widespread distribution of A_1 ARs, off-target effects caused by promiscuous signalling, or insufficient therapeutic efficacy. Despite decades of research, the complexities of A_1 AR signalling and protein-protein interactions remain incompletely understood. A tool to visualise endogenous A_1 ARs in real-time and monitor their interactions in native cells would greatly aid further investigations. Comeo's LD probes (compounds **1-56** and **1-57**) successfully covalently labelled A_1 ARs while preserving receptor internalisation following agonist treatment. However, compound **1-56** exhibited selectivity issues between A_1 and A_{2A} ARs, raising concerns about off-target labelling. In contrast, compound **1-57** showed improved A_1 AR selectivity but with lower labelling efficiency. The first objective of this project was to enhance compound **1-56**'s selectivity through structural modifications. The second goal was to optimise compound **1-57**'s affinity and selectivity for A_1 ARs. Finally, this study aimed to improve A_1 AR labelling efficiency through LD probe design and click reaction strategies, with the goal of identifying additional LD probes for A_1 AR tagging.

Chapter 2. Experimental Methods

2.1 Pharmacology

2.1.1 Experiment Materials, Reagents, and Cell Models

2.1.1.1 Materials

6-well plates were purchased from Corning Costar (Corning Incorporated, Corning, NY, USA). Tissue culture flasks (T25, T75, and T175) were acquired from SARSTEDT (SARSTEDT AG & Co. KG, Germany). 96-well plates (white plates, F-bottom, clear bottom; black plates, F-bottom, fluotrac, Med. binding) were supplied by Greiner Bio-One (Greiner Bio-One GmbH, Germany). µ-Slide 8-well plates with glass bottoms for cell imaging studies were obtained from Ibidi (Ibidi GmbH, Germany).

2.1.1.2 Reagents

Dulbecco's Modified Eagle's Medium (DMEM) with phenol red (D6546), DMEM without phenol red (D1145), and phosphate-buffered saline (PBS) were purchased from Sigma Chemicals (Pool, Dorset, UK). Foetal calf serum (FCS) was acquired from PAA Laboratories (Teddington, Middlesex, UK). Geneticin (G418) and Penicillin Streptomycin (Pen/Strep) were obtained from Life Technologies (Paisley, UK). Optimem, MOPS SDS Running Buffer (20X), NUPAGE® LDS sample buffer (4X), PageRuler Prestained Protein Ladder, NuPAGE™ 4-12% Bis-Tris gel (1.0mm X 10 well), and Laury maltose neopentyl glycol (LMNG) were purchased from Thermo Fisher Scientific (USA). SNAP-surface® Alexa Fluor® 488 and 647 were acquired from New England Biolabs (Hitchin, UK). Methyl tetrazine SulfoCyanine5 was purchased from Lumiprobe (Germany). Tetrazine SulfoCyanine 5 and Tetrazine AF488 were obtained from BroadPharm (San Diego, CA, USA). Adenosine receptor ligands: PSB-603, MRS1220, ZM241385, and DPCPX were sourced from Tocris Bioscience (Bristol, UK). Other reagents were acquired from Sigma-Aldrich (UK), analytical quality.

2.1.1.3 Cell Line

Human embryonic kidney (HEK) 293 cells stably expressing NanoLuc-A_1 (human), NanoLuc-A_{2B} (human), and NanoLuc-A_3 (human) were generated as previously described in Stoddart *et al*. (2015)[77] and Comeo *et al*. (2020)[117]. TwinStrep-SNAP-A_1 (human) ARs stably expressed by HEK239G cells were generated by Dr. Simon Platt and described in Comeo *et al*. (2024)[74]. TwinStrep-SNAP-A_{2A} (human) ARs stably expressed by the HEK TRex system were generated as described by Stoddart *et al*. (2020)[113]. HEK 293 cells stably expressing HiBiT-A_1 ARs were generated by Dr. Mark Soave, as described in Soave *et al*. (2020)[118]. HEK293T cells were purchased from ATCC. HEK293 cells expressing the GloSensor cAMP

biosensor (HEKG) were obtained from Promega (Southampton, UK). All cells were maintained in DMEM containing 10% FCS and 4 mM L-glutamine at 37°C in a humidified atmosphere with air/CO_2 (19:1).

2.1.1.4 Transiently Transfected Cell Line and Maintenance

HEK293T cells were transiently transfected with NanoLuc-A_{2A} (human) ARs, NanoLuc-A_1 (human) ARs, and SNAP-A_1 (human) ARs cDNA plasmids respectively for ligand affinity assessment towards A_{2A} ARs, orthosteric binding site assessments (BRET), post-LD probe labelling A_1 AR binding affinity assessment, and confocal imaging. For 96-well plate experiments, HEK293T cells at approximately 80% confluence in T75 flasks were split and seeded into 6-well plates with 40-50k cells per well in 2 mL on Day 1. On Day 2, cDNA (250 ng) corresponding to the experimental receptor was mixed with Fugene (1:3 ratio) and Optimem to a total volume of 100 µL, incubated for 10 minutes at room temperature, then added to one well of the 6-well plate. On Day 3, transfected HEK293T cells were collected and seeded into 96-well plates at 30-35k cells per well. On Day 4, cells were ready for experiments. For FLIM and confocal imaging, HEK293T cells at approximately 80% confluence in T75 flasks were split and seeded into 8-well plates with 7-12k cells per well in 300 µL on Day 1. On Day 2, cDNA (300 ng) was mixed with Fugene (1:4 ratio) and Optimem to a total volume of 11 µL, incubated for 10 minutes at room temperature, then added to one well of the 8-well plate. On Day 3, cells were ready for experiments. All cells were maintained in DMEM containing 10% FCS and 4 mM L-glutamine at 37°C in a humidified atmosphere with air/CO_2 (19:1).

Prior to cell seeding, both 8-well and 96-well plates were coated with poly-D-lysine. A poly-D-lysine solution was prepared at a concentration of 10 µg/mL in PBS and subsequently filtered through a 0.2 µm membrane filter. The solution was then applied to the wells—50 µL per well for 96-well plates and 300 µL per well for 8-well plates—and incubated for 30 minutes under a fume hood. Following incubation, the poly-D-lysine solution was aspirated, and the wells were rinsed once with DMEM supplemented with 10% FCS prior to cell seeding.

2.1.2 Ligand Binding Assessment

2.1.2.1 Nano-BRET Based Saturation Binding Assay

Ligands tagged with a fluorophore were assessed for their binding affinity *via* a Nano-BRET based saturation binding assay. HEK293T cells stably expressing hA_1 AR with a NanoLuciferase (NLuc) tag on the *N*-terminus were used to investigate ligand binding affinity towards A_1 AR. HEK293T cells stably expressing NLuc-hA_1 ARs reached approximately 80% confluence in T75 flasks, were split, and seeded into 96-well plates with 30-35k cells per well in 100 µL media. The next day, the media in the 96-well plates were aspirated and refilled with HEPES buffered

saline solution (HBSS: 145 mmol/L NaCl, 5 mmol/L KCl, 1.7 mmol/L CaCl$_2$, 1 mmol/L MgSO$_4$, 10 mmol/L HEPES, 2 mmol/L sodium pyruvate, 1.5 mmol/L NaHCO$_3$, 10 mmol/L D-glucose, pH 7.4) - 90 µL in total binding wells and 80 µL HBSS along with 10 µL of 10 µM DPCPX in non-specific binding (NSB) wells. Cells were incubated at 37°C in humidified air for 30 minutes. After incubation, test ligands prepared at concentrations from 0 to 5 µM were added to corresponding concentration rows (10 µL/well). After an hour of incubation at 37°C in humidified air for equilibrium, furimazine (Promega) diluted 40 times in HBSS was added to each well (10 µL) and incubated for 5 minutes at 37°C in humidified air for equilibrium. The plate was read on a PHERAstar FS plate reader (BMG Labtech) at 37°C. Emissions were read at 460 nm (80 nm bandpass; donor NanoLuc emission) and >610 nm (long pass; fluorescent probe emission) for the SulfoCy5- or BODIPY-630/650-labelled probe. A$_{2A}$, A$_{2B}$, and A$_3$ AR binding affinity assessments followed similar procedures as A$_1$ AR. Plates with cells expressing corresponding NLuc-AR subtypes were prepared, and NSB was defined by cells preincubated with 1 µM of selective antagonists (ZM241385 for A$_{2A}$, PSB603 for A$_{2B}$, and MRS1220 for A$_3$). 250 ng of NLuc-hA$_{2A}$ AR cDNA was used for transient transfection in a 6-well plate for cell preparation.

2.1.2.2 Nano-BRET Based Competition Binding Assay

This assay measured the binding affinity of probe **4-5**. HEK293T cells stably expressing NLuc-hA$_1$ ARs were used to investigate ligand binding affinity towards A$_1$ AR. On the experiment day, the media in the 96-well plate was aspirated and refilled with 50 µL of 30 nM CA200645 (prepared in HBSS) in each well. Subsequently, 50 µL of probe **4-5** (experiment set) and 50 µL of DPCPX (control) prepared at concentrations from 0 to 20 µM in HBSS were added to the corresponding rows and columns. After an hour of incubation at 37°C in humidified air for equilibrium, furimazine (Promega) diluted 40 times in HBSS was added to each well (10 µL) and incubated for 5 minutes at 37°C in humidified air for equilibrium. The plate was read on a PHERAstar FS plate reader (BMG Labtech) at 37°C. Emissions were read at 460 nm (80 nm bandpass; donor NanoLuc emission) and >610 nm (long pass; fluorescent probe emission) for CA200645. A$_{2A}$, A$_{2B}$, and A$_3$ AR binding affinity assessments followed similar procedures as A$_1$ AR. Plates with cells expressing corresponding NLuc-AR subtypes were prepared, and control was done with selective antagonists (ZM241385 for A$_{2A}$, PSB603 for A$_{2B}$, and MRS1220 for A$_3$). CA200645 at a concentration of 15 nM was employed as the fluorescent ligand in competition binding assays across four AR subtypes. 250 ng of NLuc-hA$_{2A}$ AR cDNA was used for transient transfection in a 6-well plate for cell preparation.

2.1.3 Dissociation Assay (Preliminary Covalent Labelling Assessment)

HEK293T cells stably expressing NLuc-hA$_1$ ARs were seeded in 96-well white plates with 30-35k cells per well a day before the experiment. On the experiment day, the media was aspirated, and cells were incubated under three conditions: total binding wells incubated with 90 μL of test probes only, non-specific binding (NSB) wells incubated with 90 μL of test probes and 10 μM DPCPX simultaneously, and an experiment set incubated with 90 μL of test probes only during the incubation stage. Cells were incubated in a humidified atmosphere at 37°C for 1 hour and 45 minutes. Furimazine (Promega) diluted 40 times with HBSS was added to each well (10 μL/well). A 15-minute equilibrium was carried out in the incubator at 37°C. At the end of incubation, the plate was read on a PHERAstar FS plate reader (BMG Labtech) at 37°C. Emissions were read at 460 nm (80 nm bandpass; donor NanoLuc emission) and >610 nm (long pass; fluorescent probe emission). The basal BRET measurement proceeded with a 5-minute kinetic reading (30 seconds per reading). Subsequently, 10 μL of HBSS was manually added to the total binding and NSB wells, while 10 μL of 100 μM DPCPX was added to the experimental wells. All additions were completed within 45 seconds. The plate was then continuously read at 30-second intervals for a further 60 minutes at 37 °C. The concentrations of tested ligands was as follows: 250 nM for probes **3-15**, **3-16**, **3-21**, **3-22**, and **3-29**, and 100 nM for probes **3-33** and **CA200645,** all prepared in HBSS. For the A$_{2A}$ dissociation assay, HEK293T cells transiently transfected with 250 ng NLuc-hA$_{2A}$ cDNA were collected from 6-well plates and seeded into white 96-well plates at 30-33k cells per well a day before the experiment. DPCPX was replaced with ZM241385. The remaining experimental steps were the same as those for the A$_1$ dissociation assay.

The incubation was performed in an incubator at 37°C with humidified air.

2.1.4 In-Gel Fluorescent Scan

2.1.4.1 A$_1$ AR Labelling

HEK293G cells stably expressing TwinStrep-SNAP-tagged A$_1$ adenosine receptors (TS-SNAP-A$_1$ ARs) were cultured in T175 flasks and used at 80–90% confluence, depending on the experimental design. The TwinStrep (TS) tag, located at the *N*-terminus of the A$_1$ AR, facilitates receptor extraction from solubilised cell lysates due to its high affinity for Strep-Tactin®, a streptavidin variant immobilised on magnetic beads. Upon incubation with the beads, TS-tagged A$_1$ ARs selectively bind to Strep-Tactin, enabling their separation from other cellular proteins using a magnetic separator. The bound receptors were subsequently eluted using biotin, which exhibits a higher binding affinity for Strep-Tactin than the TS tag.

The SNAP tag was employed for fluorescent labelling using SNAP-Surface Alexa Fluor 647 (AF647). This tag forms a covalent bond with its substrate, allowing for specific and stable labelling of the receptor. The fluorescent signal from the SNAP-AF647 conjugate served as a positive control in in-gel fluorescence scanning.

Probe **3-15**, **3-29**, **3-33**, **3-34** Labelling

For negative and positive controls, the media in T175 flasks was aspirated and refilled with 10 mL of DMEM-D6546 (with phenol red, Sigma-Aldrich) and 400 nM of SNAP-surface AF647 in 10 mL of DMEM-D6546. For experimental sets, a concentration of 10 times the A_1 K_d was prepared for each tested probe in DMEM-D6546 and incubated with cells in T175 flasks. Each T175 flask labelled with different conditions was followed by a 2-hour incubation at 37°C in humidified air/CO_2 (19:1 ratio).

Probe **5-8** Labelling

For negative and positive controls, the media in T175 flasks was aspirated and refilled with 10 mL of DMEM-D1145 (without phenol red, Sigma-Aldrich) and 50 nM of SNAP-surface AF647 in 10 mL of DMEM-D1145, followed by a 1-hour incubation at 37°C in humidified air/CO_2 (19:1 ratio). For experimental sets, 4 nM of probe **5-8** in 10 mL of DMEM-D1145 replaced the media in T175 flasks, followed by a 1-hour incubation under the same conditions as control sets. For antagonist intervention sets, cells were preincubated with 30 nM of DPCPX in 10 mL of DMEM-D1145 for 30 minutes. The DMEM-D1145 in T175 flasks was aspirated and refilled with 4 nM of probe **5-8** and 30 nM of DPCPX in 10 mL of DMEM-D1145, followed by another 1-hour incubation. For selectivity enhancement sets, cells were preincubated with 10 nM of ZM241385 in 10 mL of DMEM-D1145 for 30 minutes. The DMEM-D1145 in T175 flasks was aspirated and refilled with 4 nM of probe **5-8** and 10 nM of ZM241385 in 10 mL of DMEM-D1145, followed by another 1-hour incubation.

Probe **4-5** Labelling

Positive and negative control sets were the same as in the probe **5-8** experiment. For experimental sets, 200 nM of probe **4-5** in 10 mL of DMEM-D1145 replaced the media in T175 flasks, followed by a 1-hour incubation. After an hour, the media was aspirated, and cells were gently washed with warm PBS twice. 500 nM of Tetrazine-sulfoCy5 in 10 mL of DMEM-D1145 was added to probe **4-5** prelabelled cells for an additional 1-hour incubation. For antagonist intervention sets, cells were preincubated with 10 μM of DPCPX in 10 mL of DMEM-D1145 for 30 minutes. The DMEM-D1145 in T175 flasks was aspirated and refilled with 200 nM of probe **4-5** and 10 μM of DPCPX in 10 mL of DMEM-D1145, followed by another 1-hour incubation. After an hour, the media was aspirated, and cells

were gently washed with warm PBS twice, followed by a 1-hour incubation with 500 nM of Tetrazine-sulfoCy5 in 10 mL of DMEM-D1145. All incubations were conducted under the same conditions as control sets.

2.1.4.2 A_{2A} AR Labelling

20 µL of tetracycline (1 mg/mL) was added to HEK T-Rex cells maintained in T175 flasks at 50-70% confluence to induce TS-SNAP-A_{2A} AR expression. The next day, the cells were ready for labelling.

Probe **5-8** Labelling in Highly Expressed TS-SNAP-A_{2A} AR System

For negative and positive controls, the media in T175 flasks was aspirated and refilled with 10 mL of DMEM-D1145 and 50 nM of SNAP-surface AF647 in 10 mL of DMEM-D1145, followed by a 1-hour incubation at 37°C in humidified air/CO_2 (19:1 ratio). For experimental sets, 4 nM of probe **5-8** in 10 mL of DMEM-D1145 replaced the media in T175 flasks, followed by a 1-hour incubation. For ZM241385 blocking A_{2A} AR sets, cells were preincubated with 10 nM of ZM241385 in 10 mL of DMEM-D1145 for 30 minutes. The SFM in T175 flasks was aspirated and refilled with 4 nM of probe **5-8** and 10 nM of ZM241385 in 10 mL of DMEM-D1145, followed by another 1-hour incubation. All incubations were conducted under the same conditions as control sets.

At the end of incubation, the media was aspirated, and cells were gently washed with 5 mL of PBS twice. 5 mL of enzyme-free cell dissociation solution (Sigma-Aldrich) was added to T175 flasks, and cells were detached for 1-2 minutes. Cells were washed off with 5 mL of PBS and centrifuged at 1,000xRCF for 5 minutes. The supernatant was discarded, and the cell pellet was ready for solubilisation or stored in a -80°C freezer until use.

2.1.4.3 Solubilisation

A_1 AR Solubilisation

Cell pellets were thawed on ice (if stored at -80°C), weighed, and resuspended in solubilisation buffer (0.5% (w/v) Lauryl Maltose Neopentyl Glycol (LMNG) (Thermo Fisher Scientific, UK), 0.01% (w/v) Cholesteryl Hemisuccinate Tris salt (Anatrace, OH, USA), 20 mM HEPES, 10% (v/v) glycerol, 150 mM NaCl, complete protease inhibitors (Roche, UK), pH 7.5) at a ratio of 1:10 (w/v) of cell pellet to solubilisation buffer. Resuspended cells were solubilised for 2 hours on a DigiRoller 6 roller (SLS, UK) at 80 RPM and 4°C. Samples were centrifuged at 16,000 x g for 20 minutes at room temperature.

A_{2A} AR Solubilisation

Cell pellets were thawed on ice (if stored at -80°C), weighed, and resuspended in solubilisation buffer (1% n-Dodecyl β-D-maltoside (DDM) (Sigma Aldrich, UK), 20 mM HEPES, 10% (v/v) glycerol, 150 mM NaCl, complete protease inhibitors

(Roche, UK), pH 7.5) at a ratio of 1:10 (w/v) of cell pellet to solubilisation buffer. Resuspended cells were solubilised for 2 hours on a DigiRoller 6 roller (SLS, UK) at 80 RPM and 4°C. Samples were centrifuged at 16,000 x g for 20 minutes at room temperature.

2.1.4.4 Receptor Extraction

20 µL of MagStrep "type3" XT magnetic beads (IBA, Göttingen, Germany) were added to a new amber microcentrifuge tube and washed with 200 µL of receptor-paired solubilisation buffer twice. The same amount of supernatant from centrifuged solubilised cells for the same batch experiment was added into separate amber microcentrifuge tubes. These tubes were then fixed on a head-to-head shaker overnight for receptor extraction in the cold room. The next day, the supernatant was removed from the beads using a magnetic separator, and the beads were washed with 200 µL of receptor-paired solubilisation buffer twice. The beads were then resuspended with 30 µL of elution buffer (1:9 solution of 10x buffer BXT (commercial biotin solution for twin-strep tag elution, IBA) and solubilised buffer) and fixed on a head-to-head shaker for 4 hours in a cold room. The supernatant containing the preliminary purified extracted receptor was transferred to a new amber microcentrifuge tube *via* the magnetic separator.

2.1.4.5 SDS-PAGE Gel Electrophoresis and In-Gel Fluorescent Scan

30 µL of samples containing extracted receptors were mixed with 10 µL NuPAGE™ LDS sample buffer and resolved on a NuPAGE™ 4–12% Bis-Tris 1.0 mm × 10 well gel using NuPAGE™ MOPS SDS running buffer (TS-SNAP-A_1 AR labelling positive control sample loading 20 µL, TS-SNAP-A_{2A} AR labelling positive control sample diluted 50 times and loaded 10 µL, all other conditions loaded the whole sample 40 µL). Gels were run for 50 minutes at 200 V. Samples were not boiled and no reductant was added prior to gel electrophoresis. 5 µL PageRuler™ Prestained Protein Ladder was used as the marker. Gels were scanned on an Amersham Typhoon imaging system (GE Healthcare Life Sciences, Pittsburgh, PA) using Fluorstage and Cy5 670BP30 filter sets with PMT set to auto and pixel size set to 200 µm. After acquiring Cy5 scan images, the gel was stained with Instant® Coomassie Protein Stain (Abcam) 10 mL overnight. The next day, the gel was washed with Milli-Q water twice to remove excess dye and scanned with the Typhoon imaging system using Fluorstage and IRlong 825BP30 with PMT set to auto and pixel size set to 200 µm.

2.1.5 Confocal Microscopy

2.1.5.1 Membrane A_1 AR Labelling

HEK293T cells transiently expressing SNAP-hA_1 ARs in an 8-well plate were utilised in this experiment. The cells were prepared as described in the **2.1.1.4 Transfection Section** with 300 ng SNAP-hA_1 AR cDNA per well. On the day of the

experiment, the media was aspirated, and the cells were incubated with 200 μL of 250 nM SNAP-surface® AF488 for 30 minutes. Subsequently, the media was removed, and the cells were washed once with warm DMEM. Experiment wells received 180 μL DMEM, while the antagonist control set received 160 μL DMEM along with 20 μL of 100 μM DPCPX (final concentration of DPCPX in the well was 10 μM). The plate was incubated for 30 minutes. For probe **3-15** labelling assessment, 20 μL of 1 μM probe **3-15** was added to all wells for a 2-hour final incubation. For probe **4-5** labelling assessment, 20 μL of 1 μM probe **4-5** was added to all wells for a 2-hour incubation. After 2 hours, the media was removed, and the cells were washed twice with warm DMEM, followed by a final incubation with 200 μL of 1 μM Tet-SulfoCy5 (or Methyl-Tet-SulfoCy5, depends on the aim of experiment) for 15 minutes. For probe **5-8** labelling assessment, 20 μL of 400 nM probe **5-8** was added to all wells for a 2-hour incubation. At the end of the incubation, the media was removed, the cells were washed twice with warm PBS, fixed with 4% paraformaldehyde (Sigma-Aldrich) at room temperature for 20 minutes, washed again with PBS, and filled with 350 μL of PBS. The sample was then ready for image collection. All reagents were prepared in DMEM, and incubation was performed in an incubator at 37°C in a humidified atmosphere with air/CO_2 (19:1 ratio).

Fixed cell imaging was conducted using a Zeiss LSM 710 laser scanning confocal microscope fitted with a Zeiss C-Apochromat 40x 1.2 NA water immersion objective. A 633 nm HeNe laser was employed for the excitation of the SulfoCy5 fluorophore, and a 488/561/633 dichroic was used for emission detection between 638 and 759 nm. A 488 nm HeNe laser was used to excite AF488, and emission was detected between 492 and 534 nm. The pinhole diameter (1 Airy Unit; 1.1 μm optical slice), laser power, and gain were kept constant in all experiments. Images were acquired at 16-bit depth, 1024x1024 pixel resolution with a line averaging of 2 and a pixel dwell time of 3.14 μs. Images were processed in Zeiss ZEN 3.9 (blue edition), and linear adjustments to brightness and contrast were applied equally across all images. To obtain membrane intensity values, regions of interest were manually drawn around cell membranes and measured *via* FIJI (ImageJ) version 2.16.0 software.

2.1.5.2 Agonist-Induced A_1 AR Internalisation Observation

The cells and labelling procedures for this experiment were the same as those described in the "**2.1.5.1 Membrane A_1 AR Labelling**" section. Once the final labelling stage was completed, the media were aspirated, and the cells were washed twice with warm DMEM to remove excess labelling reagents. The cells were then incubated with 200 μL of DMEM or 10 μM 2-Chloro-N^6-cyclopentyladenosine (CCPA) for 2 hours. At the end of the treatment, the media were removed from the plate. The cells were washed twice with warm PBS, fixed

with 4% paraformaldehyde (Sigma-Aldrich) at room temperature for 20 minutes, washed again with PBS, and filled with 350 μL of PBS. The sample was then ready for image collection. All reagents were prepared in DMEM, and incubation was performed in an incubator at 37°C in a humidified atmosphere with air/CO_2 (19:1 ratio).

Fixed cell imaging was performed using a Zeiss LSM 710 laser scanning confocal microscope with the same settings as mentioned in the "**2.1.5.1 Membrane A$_1$ AR Labelling**" section. Images were processed in Zeiss ZEN 3.9 (blue edition), and linear adjustments to brightness and contrast were applied equally across all images. To obtain intracellular intensity, regions of interest were manually drawn around the intracellular area and measured *via* FIJI (ImageJ) version 2.16.0 software.

2.1.6 Investigation of Probe **3-22** Precise A$_1$ AR Labelling Position *via* Point-Mutation A$_1$ AR Model

cDNA Constructs

The wild-type NLuc-hA$_1$ AR cDNA construct was originally generated by Dr Stoddart and is described in Stoddart *et al*. (2015)[77]. Mutant NLuc-hA$_1$ AR cDNA constructs were synthesised and obtained from GenScript (USA). All constructs were cloned into the pcDNA3.1(+) vector containing a neomycin resistance cassette. In the mutant constructs, the signal peptide (derived from 5-HT$_{3A}$) and the NanoLuc (NLuc) tag were identical to those in the wild-type construct.

Site-directed mutagenesis was used to introduce specific point mutations into the A$_1$ AR sequence. The single-point mutations included lysine-to-alanine substitutions at positions K168A, K173A, and K265A. A double mutant was generated by substituting both K168 and K173 with alanine, while the triple mutant included substitutions at K168, K173, and K265.

Transformation

Competent *Escherichia coli* DH5α cells (Thermo Fisher Scientific) were used for plasmid transformation. A 50 μL aliquot of DH5α cells was thawed on ice, and 25 μL was mixed with 1 μL of reconstituted mutant NLuc-hA$_1$ AR cDNA (prepared in nuclease-free water according to GenScript's recommendations). The mixture was incubated on ice for 30 minutes, followed by heat shock at 42 °C for 30 seconds. The cells were then cooled on ice for 5 minutes and transferred to a 1.5 mL microcentrifuge tube containing 250 μL of LB broth. The suspension was incubated at 37 °C with shaking at 225 rpm for 1 hour. Following incubation, the transformation mixture was spread onto LB agar plates containing 50 μg/mL ampicillin. Plates were inverted and incubated overnight at 37 °C.

cDNA Amplification

Following overnight incubation, a single colony was selected and inoculated into 5 mL of LB broth containing 50 µg/mL ampicillin in a 20 mL universal tube. The culture was incubated at 37 °C with shaking at 225 rpm for 6 hours. Subsequently, the culture was transferred into a 500 mL flask containing 200 mL of LB broth with 50 µg/mL ampicillin and incubated overnight under the same conditions.

cDNA Extraction

The bacterial culture was centrifuged at 40,000 × g for 30 minutes at 4 °C to pellet the cells. Plasmid DNA was extracted and purified from the pellet using a commercial Maxiprep kit (PureYield™ Plasmid Maxiprep System, Promega), following the manufacturer's protocol.

Sanger Sequencing

The identity and integrity of the mutant NLuc-hA$_1$ AR cDNA constructs were confirmed by Sanger sequencing. Sequencing was performed using a T7P forward primer (5' TAATACGACTCACTATAGGG 3') and a BGH reverse primer (5' TAGAAGGCACAGTCGAGG 3'). The sequencing was carried out by Mr. Matthew Carlile (School of Life Sciences technician). Sequence data were analysed and aligned using Benchling (www. Benchling.com) to confirm the presence of the intended mutations.

2.1.6.1 Binding Affinity Characterisation of Ligands to Wild-Type and Mutated NLuc-A$_1$ ARs

Five mutated NLuc-hA$_1$ AR constructs were amplified, purified in-house and confirmed by Sanger sequencing. These included three single-point mutations (K168A, K173A, and K265A), one double mutation (K168A/K173A), and one triple mutation (K168A/K173A/K265A). HEK293T cells were transiently transfected with either the mutated or wild-type NLuc-hA$_1$ AR cDNA, following the protocol outlined in **Section 2.1.1.4**. Transfected cells were seeded into white 96-well plates at a density of 30–35k cells per well one day prior to the experiment. On the day of the assay, a NanoBRET-based saturation binding experiment (**Section 2.1.2.1**) was conducted using the mutated and wild-type receptors, with probe **3-22** (LD probe) and probe **3-29** (a reversible fluorescent ligand) employed to determine the respective dissociation constants (K_d values).

The incubation was performed in an incubator at 37°C with humidified air.

2.1.6.2 Assessing Labelling Reversibility by DPCPX Displacement

HEK293T cells expressing mutated NLuc-hA$_1$ AR cDNA and wild-type NLuc-hA$_1$ AR cDNA were prepared following the transient transfection protocol in **Section 2.1.1.4**. Cells were seeded in 96-well white plates at 30-35k cells per well one

day before the experiment. On the day of the experiment, cells were treated under three conditions. In the first condition, cells were incubated with 100 nM of the test ligand for one hour, washed with warm HBSS once, and incubated with HBSS for another hour. In the second condition, cells were preincubated with 10 μM DPCPX for 30 minutes followed by an hour of incubation with 100 nM of the test ligand. Cells were then washed once and incubated with warm HBSS for another hour. In the third condition, cells were incubated with 100 nM of the test ligand for one hour, washed with warm HBSS once, and incubated with 10 μM DPCPX for another hour. At the end of the incubation, furimazine (Promega) diluted 40 times with HBSS was added to each well (10 μL per well). The plate was read on a PHERAstar FS plate reader (BMG Labtech) at 37°C after 5 minutes of equilibrium. Emissions were measured at 460 nm (80 nm bandpass; donor NanoLuc emission) and >610 nm (long pass; fluorescent probe emission) for the SulfoCy5- or BODIPY630/650-labelled probe.

The incubation was performed in an incubator at 37°C with humidified air.

2.1.6.3 Assessing A_{2A} Bystander Effects

The assessment followed the same protocol as in **Section 2.1.6.2** but utilised A_{2A} knock-out HEK293 cells (generated by Dr. Simon Platt) for transient transfection with mutated and wild-type NLuc-hA_1 AR cDNA.

2.1.7 Association Kinetic Assay

HEK293T cells stably expressing NLuc-hA_1 ARs were seeded in 96-well white plates at 30-35k cells per well one day before the experiment. On the day of the experiment, the media was aspirated, and cells were incubated with 80 μL of HBSS or 70 μL HBSS with 10 μL of 100 μM DPCPX (defined non-specific binding) for 30 minutes. Furimazine (Promega), diluted 40 times with HBSS, was added to each well (10 μL per well) and equilibrated for 10 minutes. At the end of the incubation, the plate was read on a PHERAstar FS plate reader (BMG Labtech) at 37°C. Emissions were measured at 460 nm (80 nm bandpass; donor NanoLuc emission) and >610 nm (long pass; fluorescent probe emission). The basal BRET measurement proceeded with a 5-minute kinetic reading (30 seconds per reading). Probe **3-29**, prepared in HBSS at concentrations of 4 μM, 2 μM, and 1 μM, was added manually (10 μL per well) within 45 seconds. The plate was read every 30 seconds for 60 minutes at 37°C.

The incubation was performed in an incubator at 37°C with humidified air.

2.1.8 Probe **4-5** Labelling Condition Optimisation

2.1.8.1 Click Reaction Incubation Time Assessment

HEK293T cells stably expressing NLuc-hA$_1$ ARs were seeded in 96-well black plates at 30-35k cells per well one day before the experiment. On the day of the experiment, the media was aspirated, and cells were washed once with warm PBS. Cells were then incubated with 250 nM of probe **4-5** or **1-56** (control) prepared in DMEM-D6546 for 3 hours. At the end of the first labelling stage, cells were washed twice with warm DMEM-D6546 and refilled with DMEM-D6546. Methyl-tetrazine SulfoCy5 (MTCy5) at 1 µM, prepared in DMEM-D6546, was added to cells pre-labelled with probe **4-5** at various time points (immediately, 1 hr, 2 hr, 2.5 hr, and 2 hr 45 min). Fifteen minutes after the last MTCy5 solution replacement, cells were washed twice with PBS and filled with HBSS. The plate was read on a Clariostar (BMG, Germany) at 37°C with an excitation wavelength of 610 nm (30 nm bandpass) and an emission wavelength of 675 nm (50 nm bandpass).

The incubation was performed in an incubator at 37°C with humidified air, maintaining an air/CO$_2$ ratio of 19:1.

2.1.8.2 Evaluation of Methyl-Tetrazine-SulfoCy5 Labelling Without Preincubation with Probe **4-5**

HEK293T cells transiently transfected with SNAP-hA$_1$ ARs, following the protocol in **Section 2.1.1.4**, were seeded in an 8-well plate one day before the experiment. On the day of the experiment, the media was removed, and cells were incubated with 1 µM Methyl-tetrazine-SulfoCy5 for different periods of time (5, 15, 30, and 60 minutes). After incubation, cells were washed twice with PBS, fixed with 4% paraformaldehyde (Sigma-Aldrich), washed once with PBS, and refilled with PBS. The plate was then ready for confocal imaging.

The incubation was performed in an incubator at 37°C with humidified air, maintaining an air/CO$_2$ ratio of 19:1.

Fixed cell imaging was performed using a Zeiss LSM 710 laser scanning confocal microscope fitted with a Zeiss C-Apochromat 40×/1.2 NA water immersion objective. A 633 nm HeNe laser was used for the excitation of the SulfoCy5 fluorophore, and a 488/561/633 dichroic was used for emission detection between 638 and 759 nm. The pinhole diameter (1 Airy Unit; 1.1 µm optical slice), laser power, and gain were kept constant in all experiments. Images were acquired at 16-bit depth, 1024×1024-pixel resolution with a line averaging of 2 and a pixel dwell time of 3.14 µs. Images were processed in Zeiss ZEN 3.9 (blue edition), and linear adjustments to brightness and contrast were applied equally across all images.

2.1.8.3 Probe **4-5** Incubation Period Investigation

Eight-well plates seeded with HEK293T cells transiently expressing SNAP-hA$_1$ ARs followed the protocol in **Section 2.1.1.4**. On the day of the experiment, the media was removed, and cells were labelled with SNAP-surface® AF488 at 250 nM prepared in DMEM-D6546 for 30 minutes. Cells were then washed once with warm DMEM-D6546, followed by 100 nM of probe **4-5** labelling with different incubation periods (30, 60, and 120 minutes) in the presence or absence of a 30-minute preincubation with DPCPX. Cells were washed twice with warm DMEM-D6546 and incubated with 1 μM Methyl-tetrazine-SulfoCy5 for either 5 or 10 minutes (as stated in **Chapter 4**, **Figure 4-7** legend). Cells were washed twice with PBS, fixed with 4% paraformaldehyde (Sigma-Aldrich), washed once with PBS, and refilled with PBS. The plate was then ready for confocal imaging. The confocal imaging study followed the same protocol as in **Section 2.1.5.1**.

The incubation was performed in an incubator at 37°C with humidified air, maintaining an air/CO$_2$ ratio of 19:1.

2.1.8.4 Phase 2 Labelling Reagent Selection

Eight-well plates seeded with HEK293T cells transiently expressing SNAP-hA$_1$ ARs followed the protocol in **Section 2.1.1.4**. On the day of the experiment, the media was removed, and cells were labelled with SNAP-surface® AF488 at 250 nM prepared in DMEM-D6546 for 30 minutes. Cells were then washed once with warm DMEM-D6546, followed by 100 nM of probe **4-5** labelling for 2 hours in the presence or absence of a 30-minute preincubation with 10 μM DPCPX. Cells were washed twice with warm DMEM-D6546 and incubated under one of the following conditions: 1 or 10 μM Methyl-tetrazine-SulfoCy5 or Tetrazine-SulfoCy5 for 15 minutes. Cells were then washed twice with PBS, fixed with 4% paraformaldehyde (Sigma-Aldrich), washed once with PBS, and refilled with PBS. The plate was then ready for confocal imaging. The confocal imaging study followed the same protocol as in **Section 2.1.5.1**.

The incubation was performed in an incubator at 37°C with humidified air, maintaining an air/CO$_2$ ratio of 19:1.

2.1.8.5 Labelling Media Selection Assessment

Eight-well plates seeded with HEK293T cells transiently expressing SNAP-hA$_1$ ARs followed the protocol in **Section 2.1.1.4**. On the day of the experiment, the media was removed, and cells were labelled with SNAP-surface® AF488 at 250 nM prepared in DMEM-D1145 for 30 minutes. Cells were washed once with the tested media, followed by a 2-hour incubation with probe **4-5**, two washes with the tested media, and a 15-minute incubation with methyl-tetrazine-SulfoCy5 (MTCy5). Probe **4-5** at 100 nM and MTCy5 at 1 μM were prepared in the following tested media: DMEM with phenol red (DMEM-D6546), DMEM without phenol red

(DMEM-D1145), or HBSS. At the end of the incubation, cells were washed twice with PBS, fixed with 4% paraformaldehyde (Sigma-Aldrich), washed once with PBS, and refilled with PBS. The plate was then ready for confocal imaging. The confocal imaging study followed the same protocol as in **Section 2.1.5.1**.

DMEM as media, the incubation was performed in an incubator at 37°C with humidified air, maintaining an air/CO_2 ratio of 19:1.

HBSS as media, the incubation was performed in an incubator at 37°C with humidified air.

2.1.9 Orthosteric Binding Pocket Availability Assessment

2.1.9.1 BRET-Based Analysis

HEK293T cells transiently expressing NLuc-hA$_1$ ARs in 96-well white plates were prepared following the protocol in **Section 2.1.1.4**. On the day of the experiment, the media was removed, and cells were washed twice with warm HBSS. Cells were then incubated with or without 250 nM of probe **4-5** in HBSS for 1 hour, followed by two washes with HBSS, and incubated with or without 500 nM Tetrazine-AF488 in HBSS for 1 hour. Cells were then washed twice with HBSS and incubated with 100 nM of probe **3-29** in the presence or absence of a 30-minute preincubation with 1 μM DPCPX for one hour. Furimazine (Promega), diluted 40 times with HBSS, was added to each well (10 μL per well) followed by a 5-minute equilibrium. The plate was read on a PHERAstar FSX plate reader (BMG Labtech) at 37°C. For red BRET measurement, emissions were read at 450 nm (80 nm bandpass; donor NanoLuc emission) and >610 nm (long pass; fluorescent probe **3-29** emission). For green BRET measurement, emissions were read at 475 nm (30 nm bandpass; donor NanoLuc emission) and at 535 nm (30 nm bandpass; AF488 tag emission).

The incubation was performed in an incubator at 37°C with humidified air.

2.1.9.2 FLIM-FRET Analysis

Eight-well plates seeded with HEK293T cells transiently expressing NLuc-hA$_1$ ARs followed the protocol in **Section 2.1.1.4**. On the day of the experiment, the media was removed, and cells were incubated with 250 nM of probe **4-5** in HBSS for 1 hour. Cells were then washed twice with HBSS and labelled with 500 nM of Tetrazine-AF488 in HBSS for one hour. After two washes with HBSS, cells were treated under four conditions. The first condition involved incubation with HBSS for one hour. The second condition involved incubation with 100 nM of probe **3-29** in HBSS for one hour. The third condition involved incubation with 10 μM DPCPX in HBSS for one hour. The fourth condition involved incubation with 100 nM of probe **3-29** in HBSS in the presence of a 30-minute preincubation with 10

µM DPCPX for one hour. The plate was then ready for FLIM measurement, which was performed by Dr. Joelle Goulding.

The incubation was performed in an incubator at 37°C with humidified air.

Fluorescence lifetime images were captured using a PicoQuant MicroTime200 microscope on an Olympus IX 83 body equipped with a HydraHarp400 TCSPC unit and a 60x water objective, 1.2 NA. Samples were excited with 485 nm and 638 nm pulsed interleaved lasers (40 MHz), and signals were collected through a 485/640 dichroic onto two SPAD detectors with either 535/50 or 690/70 bandpass emission filters. Twenty frames of 256×256 pixels were captured at a 10 µs pixel dwell time before being analysed within Symphotime64 software. The average amplitude-weighted fluorescence lifetime of the donor was calculated from five independent experiments (three of which involved incubation with 10 µM DPCPX), with three replicate fluorescence lifetime images analysed per experiment.

2.1.10 Orthosteric Binding Pocket Accessibility Test *via* HiBiT and LgBiT Complementation Assay

HEK293 cells stably expressing HiBiT-hA$_1$ ARs (**Section 2.1.1.3**) were seeded in a 96-well white plate at a density of 30-35 thousand cells per well one day prior to the experiment. On the day of the experiment, the media was removed, and the cells were incubated with DMEM-D6546 or 500 nM of probe **3-15** in DMEM-D6546 for one hour. The cells were then washed twice with warm HBSS and incubated with 50 µL of HBSS or 20 nM DPCPX (prepared in HBSS) for 30 minutes. Subsequently, 50 µL of 5'- (*N*-Ethylcarboxamido)adenosine (NECA) prepared in HBSS at concentrations ranging from 20 nM to 200 µM was added to the corresponding wells, and the plate was incubated for 2 hours. Purified LgBiT (Promega) diluted with HBSS was then added to each well to a final concentration of 10 nM, and the cells were incubated for 15 minutes. Luminescence was measured using the PHERAstar FS plate reader (BMG Labtech) with the LUMPlus module at 37°C.

Incubation conditions:

Cells in DMEM-D6546: incubated at 37°C under humidified air with an air/CO$_2$ ratio of 19:1.

Cells in HBSS: incubated at 37°C under humidified air.

2.1.11 Sorting Cells with Higher TS-SNAP-hA$_1$AR Expression *via* FACS

HEK293G cells stably expressing TS-SNAP-hA$_1$ ARs were maintained in DMEM-D6546 supplemented with 10% FCS in a T75 flask. When the cells reached

approximately 80% confluence, the flask was prepared for labelling. The media was aspirated, and the cells were incubated with or without (control) 50 nM SNAP-surface® AF647 in 10 mL DMEM-D6546 for 30 minutes. Following incubation, the media was removed, and the cells were gently washed twice with warm PBS. The cells were detached using enzyme-free cell detachment solution (Sigma-Aldrich) and centrifuged at 1,000 rmp for 5 minutes. The supernatant was discarded, and the cell pellet was resuspended in FACS buffer (1 mM Ethylenediaminetetraacetic acid (EDTA), 25 mM HEPES, 1% Bovine serum albumin (BSA) in PBS, filtered prior to application) to achieve a cell density of approximately 5-10 × 10^6 cells/mL. Samples were sorted by Nicola Croxall (flow cytometry technical specialist). The cells were separated into two groups: cells with AF647 signal and cells with the top 25% AF647 intensity signal. The separated cells were seeded in T25 flasks and maintained in DMEM-D6546 (containing 10% FCS, 1% Pen/Strep, and 1 mg/mL G418) in an incubator with a humidified atmosphere and an air/CO_2 ratio of 19:1. Antibiotic media was used to maintain the cells for one week to prevent infection.

2.1.12 Cell Membrane Preparation

Two cell pellets collected from 85-95% confluence T175 flasks were thawed on ice and resuspended in 5 mL of PBS. The two cell suspensions were combined into one universal tube (20 mL). The cell suspension was homogenised using a handheld electric homogeniser (IKA T10 Ultra Turrax homogeniser) with 10 bursts of 2 seconds each at 22,000 rpm. The homogenised cells were centrifuged at 1,500 rpm for 20 minutes at 4°C to remove unbroken cells and nuclei. The supernatant was transferred to a clean centrifuge tube (suitable for high-speed centrifugation) and further centrifuged at 40,000 g for 30 minutes at 4°C. The resulting pellet, which consisted of cell membranes, was ready for the solubilisation process.

2.1.13 Data Analysis

Data were represented as mean ± SEM (or SD, as annotated in each table or figure legend) of *n* experiments performed in triplicate. The *n* referred to the number of separate experiments. An independent experiment meant cells were from a separate flask with freshly diluted reagent solution throughout the entire experiment. The data were presented and analysed using Prism software (GraphPad Prism 10 version 10.4.1, San Diego, CA) and Excel.

NanoBRET Saturation Binding Assay

Total and non-specific binding curves were fit simultaneously with the following equation:

$$\text{BRET ratio} = \frac{Bmax\ [B]}{B+(Kd)} + M\ (B) + C$$

Where $Bmax$ is the maximal specific binding, $[B]$ is the concentration of fluorescent ligand in nM, K_d is the equilibrium dissociation constant in nM, M is the slope of the non-specific binding set, and C is the Y-intercept of the non-specific binding set.

NanoBRET Competition Binding Assay

Competition binding curves were fit with the following equation:

$$\text{BRET ratio} = Bottom + \frac{(Top-bottom)}{1+10^{(x-LogIC50)}}$$

Where Bottom refers to the BRET ratio measured following incubation with 10 µM of a subtype-selective antagonist, representing non-specific binding. Top denotes the total binding BRET ratio obtained with 15 nM CA200645 across all four AR subtypes. X is the concentration of non-fluorescent ligand (either probe **4-5** or adenosine subtype selective antagonist), while $LogIC_{50}$ corresponds to the logarithm of the concentration of the non-fluorescent ligand required to displace 50% of CA200645 specific binding.

K_i values of non-fluorescent ligands were calculated by fitting corresponding IC_{50} values in the Cheng-Prusoff equation:

$$K_i = \frac{IC50}{1+\frac{L}{Kd}}$$

Where L is the CA200645 concentration in nM and K_d is the CA200645 dissociation constant (15 nM for A_1, 30 nM for A_{2A}, 10 nM for A_{2B}, and 30 nM for A_3 AR, which were obtained through NanoBRET saturation binding assay with 4 independent experiments conducted in triplicate, data present in **Chapter 3 Table 3-5**).

Association Assay

BRET signals obtained at each concentration of probe **3–29** were baseline-corrected by subtracting the non-specific binding signal, defined as the BRET ratio measured in the presence of 10 µM DPCPX. The resulting specific binding values, plotted against the corresponding time points, were fitted to a one-phase association model using the following equation:

$$\text{Specific binding BRET} = Bmax\ (1-e)^{-Kon(obs)*t}$$

Where $Bmax$ is the highest specific binding value, $K_{on(obs)}$ is the observed-on rate constant of specific probe concentration with units as the reciprocal of minutes, and t is the time in minutes.

$K_{on(obs)}$ values acquired from three different probe **3-29** concentrations were plotted against the probe concentrations. A linear regression was fit to the data to determine the K_{on} and K_{off} parameters:

$$Y = mX + b$$

Where Y is the $K_{on(obs)}$, the slope m is K_{on}, X is the concentration of probe **3-29**, and the constant b is K_{off}.

NanoBit complementation assay

EC$_{50}$ Determination

The potency of NECA to internalise HiBiT-A$_1$ AR on the cell membrane expressed by HEK293 cells was determined by fitting the data into a one-site concentration-response curve using the following equation:

$$\text{HiBiT-A}_1 \text{ AR on the membrane\%} = 100 - \frac{100[x]^n}{[x]^n + EC50^n}$$

Where $[x]$ is the concentration of NECA, n is the Hill slope coefficient, and the EC_{50} is the concentration of NECA required to internalise 50% of HiBit-A$_1$ ARs.

DPCPX pK_b

In the presence of 10 nM DPCPX, the concentration of NECA required to achieve the same level of HiBiT-A$_1$ AR internalisation was shifted compared to its absence. By fitting the data into the Gaddum equation, the dissociation constant K_b for DPCPX was determined:

$$\text{Log (DR-1)} = \text{Log }[B] - \log K_b$$

Where DR (dose ratio) is the ratio of NECA needed to achieve the same internalisation effect in the presence or absence of DPCPX, $[B]$. K_b is the equilibrium dissociation constant of DPCPX.

2.2 Chemistry

2.2.1 Materials

Chemicals and solvents (analytic and HPLC grade) were acquired from commercial suppliers without further purification. SulfoCyanine5 NHS ester and SulfoCyanine5 free acid were purchased from Lumiprobe (Germany). *Trans-*cyclooctene-NHS (TCO-NHS) ester was obtained from Jena Biosciences (Germany).

2.2.2 Chromatography

Thin-layer chromatography (TLC) was used to monitor reaction status, with TLC plates being commercial products (Merk Kieselgel 60 F). Visualisation of TLC was performed under UV light at 254 nm.

Purification *via* automated flash column chromatography was carried out using an Interchim Puriflash 4100 system (PF4100-250) coupled to a dual-wavelength DAD UV detector (200-600 nm) with silica high performance (HP) 50 µm 12 g cartridges. Methods were designed and executed using Interchim Flash (ver: V5.1c.09) software. Compounds were purified at a flow rate of 20 mL/min with a gradient program mentioned in each compound synthesis section.

Reverse-phase high performance liquid chromatography (RP-HPLC) was conducted using a Waters 515 LC system with a Waters 996 photodiode array detector at wavelengths between 190 and 800 nm. Spectra were analysed using Millennium 32 software. Compounds purified through RP-HPLC were processed with either a Phenomenex Onyx™ Monolithic semipreparative C18 column (CH0-7878, 100 mm × 10 mm) at a flow rate of 10 mL/min or a semipreparative YMC-Pack C8 column (150 mm × 10 mm × 5 µm) at a flow rate of 4 mL/min using a gradient method from 30% to 95% solvent B over 12 minutes and 16 minutes, respectively (solvent A = 0.1% formic acid in H_2O, solvent B = 0.1% formic acid in MeCN). Compound purity analysis was performed with either a YMC-Pack C8 analytic column (150 mm × 4.6 mm × 5 µm) or a Phenomenex Onyx™ Monolithic C18 analytic column (CH0-7643, 100 mm × 4.6 mm) at a flow rate of 1 mL/min using a gradient method from 5% to 95% solvent B over 20 minutes (solvent A = 0.1% formic acid in H_2O, solvent B = 0.1% formic acid in MeCN). Final products presented a single peak in RP-HPLC accompanied by photodiode array spectra and were over 95% pure.

2.2.3 Nuclear Magnetic Resonance Spectroscopy

NMR spectra were acquired using a Bruker-AV 400. ^{1}H NMR spectra were recorded at 400.13 MHz, and ^{13}C NMR spectra were recorded at 101.62 MHz. All ^{13}C NMR spectra were ^{1}H broadband decoupled. Deuterium solvents used in

NMR analysis (reference peaks listed) were $CDCl_3$ (δ H = 7.26 ppm, δ C = 77.16 ppm) purchased from Cambridge Isotope Laboratories Inc., $MeOD_4$ (δ H = 3.34 ppm, δ C = 49.86 ppm), Acetone-d_6 (δ H = 2.05 ppm, δ C = 29.84, 206.26 ppm), and DMSO-d_6 (δ H = 2.5 ppm, δ C = 40.45 ppm) supplied by Sigma-Aldrich (UK). Chemical shifts (δ) were recorded in parts per million (ppm), and coupling constants were recorded in Hz. Signal splitting patterns were depicted using the following abbreviations: singlet (s), doublet (d), triplet (t), quadruplet (q), pentet (p), broad (br), doublet of doublets (dd), double doublet of doublets (ddd), double triplet of doublets (dtd), and multiplet (m). Software Mnova 14.2.2 was used to analyse NMR data.

2.2.4 Mass Spectroscopy

Preliminary low-resolution mass spectra (LRMS) data were acquired using a Shimadzu UFLCXR LC-MS system coupled with an Applied Biosystems API2000, visualised at 254 nm (channel 1) and 220 nm (channel 2). LC-MS was performed at a flow rate of 0.5 mL/min over a specific period with a Phenomenex Gemini-NX C18 110A column (50 mm × 2 mm × 3 µm). The running buffers were as follows: buffer A, 0.1% formic acid in H_2O; buffer B, 0.1% formic acid in MeCN. **Method A** analysed samples with a gradient method of solvent B from 5% to 95% and back to 5% over 5 minutes. **Method B** analysed samples with a gradient method of solvent B from 5% to 95% and back to 5% over 13 minutes. High-resolution mass spectra (HRMS) were acquired using a Bruker microTOF mass spectrometer by electrospray ionisation operating in negative or positive ion mode.

2.2.5 Molecular Docking Simulation

Congeners were docked with A_1 and A_{2A} ARs using Schrodinger Maestrolab (version 14.3.129). Congener structures were drawn in ChemDraw, saved as .sdf files, and uploaded into Schrodinger Maestrolab. The A_1 AR (PDB ID: 5EUN) and A_{2A} AR (PDB ID: 4EIY) structures were downloaded from the PDB website. Ligand and protein preparations were performed using Maestrolab before docking experiments. Docking grids were defined using DU172 and ZM241385 as the binding centres for A_1 and A_{2A} ARs, respectively. Congeners were then docked with the prepared grids, and docking scores were generated in the results table. Docking scores represented the free energy of the ligand-receptor complex, with lower values indicating a more stable complex.

2.2.6 Stability Assessment

2.2.6.1 24-hour Assessment

Probe **3-16**, **3-22**, and **3-29**

Analysis was conducted *via* RP-HPLC using a YMC-Pack C8 analytic column (150 mm × 4.6 mm × 5 µm) at a flow rate of 1 mL/min with a gradient method from 5%

to 95% solvent B over 20 minutes (solvent A = 0.1% formic acid in H_2O, solvent B = 0.1% formic acid in MeCN). The machine, detector, and analytic software were as mentioned in **Section 2.2.2**. Control samples were prepared as DMSO diluted in HBSS with the same ratio as in the experimental sets. In the experimental sets, probes were first aliquoted with DMSO and then diluted with HBSS (probe **3-16**: 1.76 mM, probe **3-22**: 1.2 mM, and probe **3-29**: 1.24 mM). After sample preparation, 20 µL of the tested sample was injected into the RP-HPLC system for analysis and defined as time 0. The vial with remaining sample was placed on a heat block preheated to 37°C without light exposure. Analysis was performed after incubation for 1, 3, 5, and 24 (or 25) hours respectively.

Probe **5-8**

Analysis was conducted *via* RP-HPLC using a Phenomenex Onyx™ Monolithic C18 analytic column (CH0-7643, 100 mm × 4.6 mm) at a flow rate of 1 mL/min with a gradient method from 5% to 95% solvent B over 20 minutes (solvent A = 0.1% formic acid in H_2O, solvent B = 0.1% formic acid in MeCN). The machine, detector, and analytic software were as mentioned in **Section 2.2.2**. Control samples were prepared as DMSO diluted in HBSS with the same ratio as in the experimental sets. In the experimental set, probes were first aliquoted with DMSO and then diluted with HBSS to a final concentration of 1.2 mM. Caffeine at 2 mM served as the internal standard for both control and experimental sets. After sample preparation, 20 µL of the tested sample was injected into the RP-HPLC system for analysis and defined as time 0. The vail with remaining sample was placed on a heat block preheated to 37°C without light exposure. Analysis was performed after incubation for 1, 3, 5, and 24 hours. Analysis was ceased if there was no intact probe **5-8** detected.

Different incubation media were used with the same procedures, replacing HBSS with DMEM with phenol red (DMEM-D6546), DMEM without phenol red (DMEM-D1145), and DMEM-D6546 with 10% FCS. Control samples were prepared with DMSO and the corresponding tested media.

2.2.6.2 Long-term Storage Purity Analysis

Analysis was conducted *via* RP-HPLC using a YMC-Pack C8 analytic column (150 mm × 4.6 mm × 5 µm) at a flow rate of 1 mL/min with a gradient method from 5% to 95% solvent B over 20 minutes (solvent A = 0.1% formic acid in H_2O, solvent B = 0.1% formic acid in MeCN). The machine, detector, and analytic software were as mentioned in **Section 2.2.2**. The control sample was commercial DMSO. For experimental sets, samples were aliquoted in DMSO at 1 mM and stored in a -20°C freezer (probes **3-15**, **3-16**, **3-21**, and **3-22** were stored for over one year, while probe **3-29** was stored for 3 months). On the experiment day, samples were

taken out from the freezer and thawed completely at room temperature before submitting 20 µL of each sample to RP-HPLC analysis.

2.2.6.3 DMSO Aliquoted Probe **5-8** Stability Assessment

Analysis was conducted *via* RP-HPLC using a Phenomenex Onyx™ Monolithic C18 analytic column (CH0-7643, 100 mm × 4.6 mm) at a flow rate of 1 mL/min with a gradient method from 5% to 95% solvent B over 20 minutes (solvent A = 0.1% formic acid in H_2O, solvent B = 0.1% formic acid in MeCN). The machine, detector, and analytic software were as mentioned in **Section 2.2.2**. The control was prepared as DMSO aliquoted caffeine at 2 mM and dispensed into amber microcentrifuge tubes, each containing 20 µL. For the experimental set, probe **5-8** was aliquoted with DMSO and mixed with DMSO aliquoted caffeine to achieve final concentrations of 1 mM and 2 mM, respectively. The stock solution was dispensed into amber microcentrifuge tubes, each containing 20 µL. One analysis was conducted immediately after dispensing and was defined as week 0. Both control and probe **5-8** were analysed weekly by taking microcentrifuge tubes from the freezer and thawing them at room temperature for 20 minutes before injection.

2.2.7 General Procedure

A: COMU Facilitated Amide Coupling

A solution of the respective carboxylic acid (1.0 eq) in anhydrous DMF (2 mL) was stirred with DIPEA (1.1 eq) and COMU (1.1 eq) for 5 minutes. Then, a solution of the respective amine (1 eq) in anhydrous DMF (3 mL) was added to the activated carboxylic acid mixture, and the reaction was stirred for 30-60 minutes at room temperature. LC-MS was used to monitor the progress of the reaction. Upon completion, iced water (50 mL) was added to the mixture. If the product precipitated, it was collected by filtration. If no precipitation occurred, the mixture was extracted with EtOAc. The collected EtOAc extract was washed sequentially with 1 M $HCl_{(aq)}$, saturated $NaHCO_{3(aq)}$, and brine. The washed EtOAc solution was dried over anhydrous $MgSO_4$, filtered, and evaporated under reduced pressure. Finally, the resulting residue was purified using automated flash column chromatography.

B: Phenyl Ester Synthesis

A solution of the respective carboxylic acid (1.0 eq) in anhydrous DMF (0.5 mL) was stirred with DIPEA (2 drops) and 2-bromo-1-ethyl-pyridinium tetrafluoroborate (BEP) (1 eq) for 5 minutes. Then, a solution of the respective phenol (1 eq) in anhydrous DMF (0.5 mL) was added to the activated carboxylic acid mixture, and the reaction was left overnight in a cupboard at room temperature. LC-MS was used to monitor the reaction progress. Upon completion, DMF was removed under reduced pressure. The residue was

reconstituted with 0.5 mL of MeCN and 1 mL of H$_2$O. The target compound was purified and collected *via* semi-preparative RP-HPLC. The collected fraction was concentrated and lyophilised to afford the desired product.

C: *t*-Boc Deprotection

t-Boc-protected amine was dissolved in 4 M HCl/dioxane (4 mL, 0.5 mL for 1 mg scale reaction) and stirred for 20-60 minutes at room temperature. The reaction was monitored by TLC and LC-MS. The acidic solvent was removed under reduced pressure. The HCl salt of the desired amine was obtained and used in the next step without further purification.

2.2.8 Compound Synthesis and Characterisation
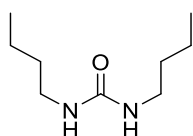
1,3-Dibutylurea (**3-4**). Butylamine (7.7 mL, 77.8 mmol, 1.1 eq) was dissolved in anhydrous THF (20 mL) and cooled to 0°C in an ice bath. Butyl isocyanate (**3-3**) (8 mL, 69.7 mmol, 1 eq) was then added to the mixture, and the ice bath was removed. The solution was stirred at room temperature for 4 hours. Evaporation of the solvent yielded the product **3-4** as a white solid (11.7 g, 67.3 mmol, yield = 97%).

¹H NMR (DMSO-*d₆*) δ 5.71 (t, *J* = 4Hz, 2H), 2.96 (td, *J* = 8, 4 Hz, 4H), 1.37-1.21 (m, 8H), 0.87 (t, *J* = 8 Hz, 6H).

¹³C NMR (DMSO-*d₆*) δ 158.6, 39.4, 32.7, 20.0, 14.2.
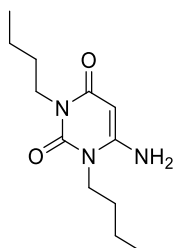
6-Amino-1,3-dibutylpyrimidine-2,4(1*H*,3*H*)-dione (**3-5**). Compound **3-4** (6 g, 34.8 mmol, 1 eq) was reacted with cyanoacetic acid (3.3 g, 38.3 mmol, 1.1 eq) in Ac$_2$O (20 mL). The mixture was heated to 85°C and stirred for 2 hours. The mixture was then concentrated to dryness with a water bath set at 80°C until a brown syrup appeared. 4 mL of water was added to the brown syrup, followed by concentration. This process was repeated three times to remove as much Ac$_2$O as possible. 10 mL of water was added to the final concentrated syrup and basified with 70% NaOH$_{(aq)}$. The precipitate formed during the basification stage and was recrystallised from hot EtOH/H$_2$O to yield fine pale-yellow crystals, compound **3-5** (7.12 g, 29.8 mmol, yield = 86%).

LC-MS *m/z* calcd. for $C_{12}H_{21}N_3O_2$ [M-H$^+$] 240.17; found 240.1, t_R = 2.56 min, **Section 2.2.4, Method A**.

^{1}H NMR (DMSO-d_6) δ 6.75 (s, 2H), 4.64 (s, 1H), 3.76 (t, *J* = 7.6 Hz, 2H), 3.69 (t, *J* = 7.6 Hz, 2H), 1.51-1.39 (m, 4H), 1.32-1.18 (m, 4H), 0.88 (t, *J* = 8 Hz, 3H), 0.86 (t, *J* = 8Hz, 3H).

^{13}C NMR (DMSO-d_6) δ 161.6, 154.7, 151.7, 75.6, 41.95, 39.92, 30.19, 30.14, 20.09, 19.72, 14.19, 14.15.
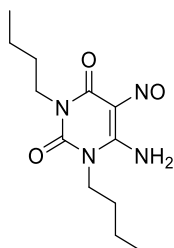
6-Amino-5-nitroso-1,3-dipropylpyrimidine-2,4(1*H***,3***H***)-dione** (**3-6**). Compound **3-5** (4.78 g, 20 mmol, 1 eq) was dissolved in 50% acetic acid (50 mL). The resulting mixture was heated to 65°C to form a clear yellow solution. NaNO$_2$ (1.65 g, 24 mmol, 1.2 eq) was added to the solution portion-wise. After the addition of NaNO$_2$, a pink solid and a purple (or deep pink) solution were obtained. The reaction mixture was stirred at room temperature for 1 hour. The pink precipitate was then filtered, washed with iced water, and dried in an oven overnight to give pure compound **3-6** as a pink solid (4 g, 14.9 mmol, yield = 75%).

LC-MS *m/z* calcd. for $C_{12}H_{20}N_4O_3$ [M-H$^+$] 269.16; found 268.9, t_R = 2.63 min, **Section 2.2.4, Method A**.

^{1}H NMR (DMSO-d_6) δ 13.13 (s, 1H), 9.17 (s, 1H), 3.89 (t, *J* = 7.2 Hz, 2H), 3.82 (t, *J* = 7.6 Hz, 2H), 1.61-1.53 (m, 2H), 1.52-1.45 (m, 2H), 1.38-1.26 (m, 4H), 0.91 (t, *J* = 7.2 Hz, 3H), 0.88 (t, *J* = 7.2 Hz, 3H).

^{13}C NMR (DMSO-d_6) δ 160.4, 149.5, 145.9, 139.5, 41.4, 41.1, 29.9, 28.9, 20.1, 19.7, 14.2, 14.1.
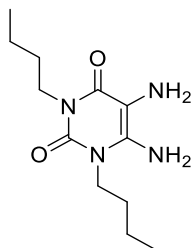
5,6-Diamino-1,3-dibutylpyrimidine-2,4(1*H***,3***H***)-dione** (**3-7**). 25 mL of 12% NH$_4$OH was added to a round-bottom flask containing compound **3-6** (0.7 g, 2.61 mmol, 1 eq). The mixture was heated to 80°C, and sodium dithionite was added portion-wise. The mixture was stirred continuously until the solution

became clear. Once the clear solution appeared, it was cooled to room temperature. The solution was then extracted with DCM (25 mL, 4 times). The combined DCM layers were dried over anhydrous Na_2SO_4, filtered, and evaporated to yield **3-7** as a brown sticky oil (0.63 g, 2.47 mmol, yield = 95%).

LC-MS *m/z* calcd. for $C_{12}H_{22}N_4O_2$ [M-H$^+$] 255.18; found 254.9, t_R = 2.17 min, **Section 2.2.4, Method A**.

^{1}H NMR (DMSO-d_6) δ 6.14 (s, 2H), 3.82 (t, 1H, *J* = 7.58), 3.76 (d, *J* = 7.32 Hz, 2H), 2.89 (s, 2H), 1.57-1.41 (m, 4H), 1.27 (h, *J* = 7.53 Hz, 2H), 1.23 (h, *J* = 7.25 Hz, 2H), 0.88 (t, *J* = 7.48 Hz, 3H), 0.86 (t, *J* = 7.24 Hz, 3H).

^{13}C NMR (DMSO-d_6) δ 158.8, 149.4, 144.2, 95.9, 41.4, 40.2, 29.9, 29.7, 19.6, 19.3, 13.72, 13.7.
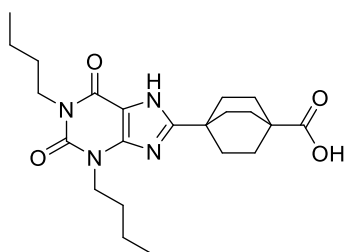
4-(1,3-Dibutyl-2,6-dioxo-2,3,6,7-tetrahydro-1*H*-purin-8-yl)bicyclo[2.2.2]octane-1-carboxylic acid (3-8).

Coupling Reaction: COMU (1.07 g, 2.5 mmol, 1.1 eq), 4-(methoxycarbonyl)bicyclo[2.2.2]octane-1-carboxylic acid (0.48 g, 2.27 mmol, 1 eq), and DIPEA (0.87 mL, 5 mmol, 2.2 eq) were dissolved in anhydrous DMF (5 mL). The mixture was stirred at room temperature for 5 minutes and then transferred to another round-bottom flask containing fresh compound **3-7** (0.847 g, 2.5 mmol, 1.1 eq). The reaction was monitored by LC-MS. Once the reaction was complete, 60 mL of water was added to the mixture. EtOAc was used to extract the mixture three times, and the collected EtOAc layer was washed with 1M HCl, saturated $NaHCO_{3(aq)}$, and brine, respectively. The organic solvent was then dried over anhydrous Na_2SO_4, filtered, and evaporated to yield a red crude.

Cyclisation:
1M KOH (5 mL, 5 mmol, 2.2 eq) and isopropyl alcohol (IPA, 5 mL) were added to the red crude. The mixture was refluxed at 91°C for 2 hours. The mixture was then cooled to room temperature and evaporated to remove IPA. The resulting residue was extracted with EtOAc once. The water layer was transferred to a flask and acidified to pH 3-4 by adding concentrated HCl. The yellow precipitate was filtered, dried in an oven overnight, and yielded compound **3-8** (0.668 g, 1.6 mmol, yield = 70%).

LC-MS *m/z* calcd. for $C_{22}H_{32}N_4O_4$ [M-H⁺] 417.25; found 417.4, t_R = 3.0 min, **Section 2.2.4, Method A**.

¹H NMR (DMSO-*d₆*) δ 12.93 (s, 1H), 12.09 (s, 1H), 3.96 (t, *J* = 7.2 Hz, 2H), 3.86 (t, *J* = 7.3 Hz, 2H), 1.96-1.83 (m, 6H), 1.81-1.72 (m, 6H), 1.63 (p, *J* = 7.2 Hz, 2H), 1.5 (p, *J* = 6.8 Hz, 2H), 1.27 (h, *J* = 7.4 Hz, 4H), 0.90 (t, *J* = 7.32 Hz, 3H), 0.88 (t, *J* = 7.56 Hz, 3H).

¹³C NMR (DMSO-*d₆*) δ 178.9, 160.6, 154.4, 151, 147.8, 106.9, 42.8, 38.2, 33.6, 30.1, 30.0, 29.86, 28.1, 27.9, 20.1, 19.7, 14.2, 14.0.
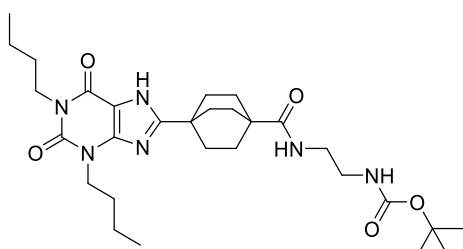
***tert*-Butyl (2-(4-(1,3-dibutyl-2,6-dioxo-2,3,6,7-tetrahydro-1*H*-purin-8-yl)bicyclo[2.2.2]octane-1-carboxamido)ethyl)carbamate (3-9)**. Compound **3-8** (624.8 mg, 1.5 mmol, 1 eq) and commercial *tert*-butyl (2-aminoethyl)carbamate (264.4 mg, 1.65 mmol, 1.1 eq) were subjected to the procedure outlined in **Section 2.2.7 General Procedure A**. The reaction progress was monitored by LC-MS. Upon completion of the reaction, 50 mL of iced water was added to the mixture, resulting in the formation of a precipitate. The precipitate was filtered and dried in an oven overnight, yielding compound **3-9** (789.4 mg, 1.43 mmol, yield = 95%).

LC-MS *m/z* calcd. for $C_{29}H_{48}N_7O_4$ [M-H⁺] 559.38; found 559.3, t_R = 2.97 min, **Section 2.2.4, Method A**.

¹H NMR (DMSO-*d₆*) δ 12.92 (s, 1H), 7.38 (t, *J* = 5.5 Hz, 1H), 6.79 (t, *J* = 5.8 Hz, 1H), 3.96 (t, *J* = 7.2 Hz, 2H), 3.86 (t, *J* = 7.2 Hz, 2H), 3.06 (q, *J* = 6.2 Hz, 2H), 2.97 (q, *J* = 6.3 Hz, 2H), 1.89-1.84 (m, 6H), 1.74-1.70 (m, 6H), 1.63 (p, *J* = 7.8 Hz, 2H), 1.5 (p, *J* = 7.5 Hz, 2H), 1.38 (s, 9H), 1.27 (h, *J* = 7.4 Hz, 4H), 0.90 (t, *J* = 7.32 Hz, 3H), 0.89 (t, *J* = 7.52 Hz, 3H).

¹³C NMR (MeOD-*d₄*) δ 180.5, 162.19, 158.8, 156.0, 152.8, 149.4, 108.4, 80.1, 44.2, 42.1, 41.3, 40.7, 40.1, 34.9, 31.24, 31.21, 31.0, 29.2, 28.8, 21.2, 20.8, 14.2, 14.1.
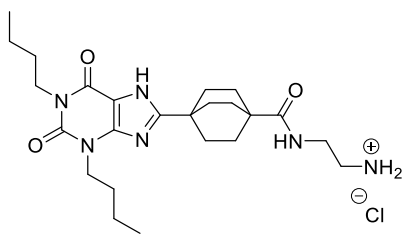
N-(2-aminoethyl)-4-(1,3-dibutyl-2,6-dioxo-2,3,6,7-tetrahydro-1_H_-purin-8-yl)bicyclo[2.2.2]octane-1-carboxamide hydrochloride salt (3-10). Compound **3-9** (294 mg, 0.49 mmol, 1 eq) was subjected to the procedure outlined in **Section 2.2.7 General Procedure C**. The reaction progress was monitored by LC-MS. Once the _t_-Boc group was removed, the mixture was evaporated to yield the crude compound **3-10** for the next step without further purification.
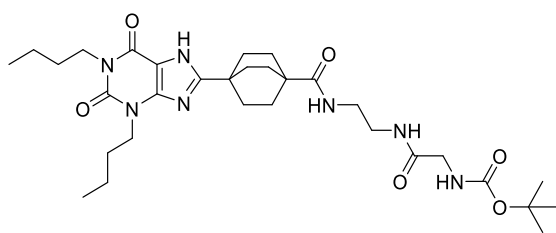
tert-Butyl (2-((2-(4-(1,3-dibutyl-2,6-dioxo-2,3,6,7-tetrahydro-1_H_-purin-8-yl)bicyclo[2.2.2]octane-1-carboxamido)ethyl)amino)-2-oxoethyl)carbamate (3-11). The crude compound **3-10**, obtained from the _t_-Boc deprotection of compound **3-9** (294 mg, 0.49 mmol, 1 eq), was reacted with Boc-Glycine (151 mg, 0.86 mmol, 1.76 eq) following the procedure outlined in **Section 2.2.7 General Procedure A**. The reaction progress was monitored by LC-MS. Upon completion of the reaction, no precipitate formed when iced water was added to the mixture. The mixture was then purified using automated flash column chromatography (gradient MeOH:DCM from 3:97 to 10:90, 15 CV), yielding compound **3-11** (213 mg, 0.35 mmol, yield = 71%).

LC-MS _m/z_ calcd. for $C_{31}H_{49}N_7O_6$ [M-H$^+$] 616.38; found 616.2, t_R = 2.95 min, **Section 2.2.4, Method A**.

¹H NMR (MeOD-_d₄_) δ 4.11 (t, _J_ = 7.3 Hz, 2H), 3.99 (t, _J_ = 7.5 Hz, 2H), 3.7 (s, 2H), 2.03-1.99 (m, 6H), 1.92-1.88 (m, 6H), 1.74 (p, _J_ = 7.2 Hz, 2H), 1.62 (p, _J_ = 7.6 Hz, 2H), 1.48 (s, 9H), 1.37 (h, _J_ = 7.64 Hz, 2H), 1.37 (h, _J_ = 7.44 Hz, 2H), 0.97 (t, _J_ = 6.88 Hz, 3H), 0.96 (t, _J_ = 7.68 Hz, 3H).

¹³C NMR (MeOD-_d₄_) δ 179.1, 171.8, 160.8, 157.1, 154.6, 151.4, 148.07, 106.8, 79.3, 43.4, 42.8, 40.8, 39.2, 38.7, 38.6, 33.5, 29.84, 29.81, 29.4, 27.8, 27.3, 19.7, 19.4, 12.8, 12.7.

N-(2-(2-aminoacetamido)ethyl)-4-(1,3-dibutyl-2,6-dioxo-2,3,6,7-tetrahydro-1H-purin-8-yl)bicyclo[2.2.2]octane-1-carboxamide hydrochloride salt (3-12). Compound **3-11** (100 mg, 0.16 mmol, 1 eq) was subjected to the procedure outlined in **Section 2.2.7 General Procedure C**. The reaction progress was monitored by LC-MS. Once the *t*-Boc group was removed, the mixture was evaporated to yield the crude compound **3-12** for the next step without further purification.
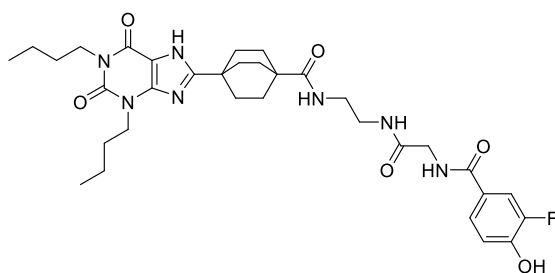
4-(1,3-Dibutyl-2,6-dioxo-2,3,6,7-tetrahydro-1H-purin-8-yl)-N-(2-(2-(3-fluoro-4-hydroxybenzamido)acetamido)ethyl)bicyclo[2.2.2]octane-1-carboxamide (3-13). The crude compound **3-12**, obtained from the *t*-Boc deprotection of compound **3-11** (100 mg, 0.16 mmol, 1 eq), was reacted with 3-fluoro-4-hydroxybenzoic acid (27.5 mg, 0.176 mmol, 1.1 eq) following the procedure outlined in **Section 2.2.7 General Procedure A**. The reaction mixture was heated to 90°C and stirred overnight. The reaction progress was monitored by LC-MS. Upon completion, no precipitate formed when iced water was added to the mixture. The mixture was then purified using automated flash column chromatography (gradient MeOH:DCM from 5:95 to 10:90, 19 CV), yielding compound **3-13** (48.7 mg, 0.07 mmol, yield = 47%).

LC-MS *m/z* calcd. for $C_{33}H_{44}FN_7O_6$ [M-H$^+$] 654.34; found 654.1, t_R = 2.74 min, **Section 2.2.4, Method A**.

^{1}H NMR (DMSO-d_6) δ 12.9 (bs, 1H), 10.49 (bs, 1H), 8.61 (t, *J* = 5.88 Hz, 1H), 7.92 (t, *J* = 5.5 Hz, 1H), 7.69 (dd, *J* = 12.3, 2.2 Hz, 1H), 7.59 (dd, *J* = 8.44, 2.3 Hz, 1H), 7.43 (t, *J* = 5.24 Hz, 1H), 7.00 (t, *J* = 8.6 Hz, 1H), 3.96 (t, *J* = 7.14 Hz, 2H), 3.85 (t, *J* = 7.4 Hz, 2H), 3.8 (d, *J* = 5.84 Hz, 2H), 3.12 (s, 4H), 1.90-1.82 (m, 6H), 1.77-1.68 (m, 6H), 1.63 (p, *J* = 7.27 Hz, 2H), 1.5 (p, *J* = 7.42 Hz, 2H), 1.27 (h, *J* = 7.4 Hz, 4H), 0.89 (t, *J* = 7.48 Hz, 3H), 0.88 (t, *J* = 7.48 Hz, 3H).

^{13}C NMR (MeOD-d_4) δ 180.7, 172.6, 169.1, 162.2, 156.0, 152.8, 152.5 (d, *J* = 240.17 Hz), 150.1 (d, *J* = 13.12 Hz), 149.4 , 126.3 (d, *J* = 5.47 Hz, 125.5 (d, *J* = 3.42

Hz), 118.4 (d, J = 3 Hz), 116.6 (d, J = 20 Hz), 108.2, 44.3, 44.2, 42.1, 40.6, 40.5, 40.0, 34.9, 31.21 , 31.18, 31.0, 29.1, 21.1, 20.8, 14.2, 14.1.
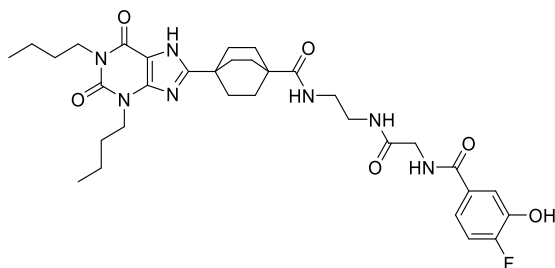
4-(1,3-Dibutyl-2,6-dioxo-2,3,6,7-tetrahydro-1H-purin-8-yl)-N-(2-(2-(4-fluoro-3-hydroxybenzamido)acetamido)ethyl)bicyclo[2.2.2]octane-1-carboxamide (3-14). The crude compound **3-12**, obtained from the t-Boc deprotection of compound **3-11** (100 mg, 0.16 mmol, 1 eq), was reacted with 4-fluoro-3-hydroxybenzoic acid (25.6 mg, 0.164 mmol, 1.01 eq) following the procedure outlined in **Section 2.2.7 General Procedure A**. The reaction mixture was heated to 90°C and stirred overnight. The reaction progress was monitored by LC-MS. Upon completion, no precipitate formed when iced water was added to the mixture. The mixture was then purified using automated flash column chromatography (gradient MeOH:DCM from 5:95 to 10:90, 19 CV), yielding compound **3-14** (39 mg, 0.059 mmol, yield = 37%).

LC-MS m/z calcd. for $C_{33}H_{44}FN_7O_6$ [M-H$^+$] 654.34; found 654.2, t_R = 2.76 min, **Section 2.2.4, Method A**.

^{1}H NMR (MeOD-d_4) δ 7.49 (dd, J = 8.44, 2.2 Hz, 1H), 7.37 (ddd, J = 8.5, 4.28, 2.3 Hz, 1H), 7.13 (dd, J = 10.74, 8.4 Hz, 1H), 4.09 (t, J = 7.28 Hz, 2H), 3,97 (s, 2H), 3.96 (t, J = 7.52 Hz, 2H), 3.32 (s, 4H), 2.01-1.81 (m, 12H), 1.71 (p, J = 7.4 Hz, 2H), 1.6 (p, J = 7.54 Hz, 2H), 1.37 (h, J = 7.48 Hz, 2H), 1.36 (h, J = 7.32 Hz, 2H), 0.97 (t, J = 7.36 Hz, 3H), 0.96 (t, J = 7.24 Hz, 3H).

^{13}C NMR (MeOD-d_4) δ 180.7, 172.5, 169.6, 162.2, 156.0, 155.3 (d, J = 245.2 Hz), 152.8, 149.4, 146.4 (d, J = 13.27 Hz), 131.7, 120.3 (d, J = 7.2 Hz), 118.6 (d, J = 4.17 Hz), 116.87 (d, J = 19.33 Hz), 108.2, 44.3, 44.2, 42.1, 40.5, 40.3, 40.1, 34.9, 31.23, 31.21, 30.99, 29.2, 21.2 , 20.8, 14.2, 14.1.
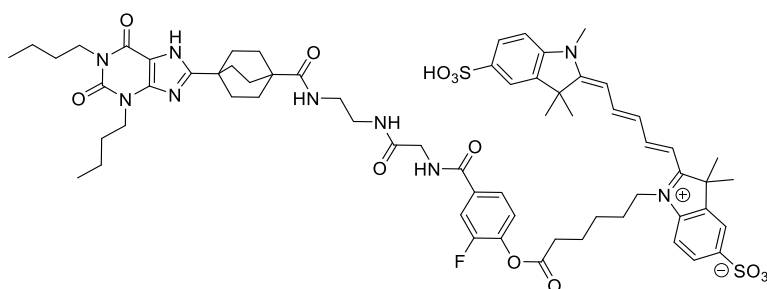
1-(6-(4-((2-((2-(4-(1,3-Dibutyl-2,6-dioxo-2,3,6,7-tetrahydro-1*H*-purin-8-yl)bicyclo[2.2.2]octane-1-carboxamido)ethyl)amino)-2-oxoethyl)carbamoyl)-2-fluorophenoxy)-6-oxohexyl)-3,3-dimethyl-2-((1*E*,3*E*)-5-((*E*)-1,3,3-trimethyl-5-sulfoindolin-2-ylidene)penta-1,3-dien-1-yl)-3*H*-indol-1-ium-5-sulfonate (3-15). Compound **3-13** (1 mg, 1.53 µmol, 1 eq) was reacted with SulfoCyanine 5 carboxylic acid (1.06 mg, 1.55 µmol, 1 eq) following the procedure outlined in **Section 2.2.7 General Procedure B**, yielding the final product **3-15** (0.9 mg, 0.7 µmol, yield = 46%).

HR-MS (TOF-ESI, negative) calcd. **m/z** for $C_{65}H_{79}FN_9O_{13}S_2$ [M-H$^-$] 1,276.522827, found 1,276.5226, error within 2.4 ppm; for $C_{65}H_{78}FN_9O_{13}S_2$ [M-2H^{2-}] 637.757775, found 637.7588, error within 2.4 ppm; **Section 2.2.4**.

Purity: 98.25%, measured by RP-HPLC with a YMC-Pack C8 analytic column (150 mm × 4.6 mm × 5 µm) mentioned in **Section 2.2.2**.

	Name	Retention Time (min)	Purity1 Angle	Purity1 Threshold	PDA Match1 Spect. Name	PDA Match1 Angle	PDA Match1 Threshold	PDA Match1 Lib. Name	Area (µV*sec)	% Area	Height (µV)	Int Type	Amount	Units	Peak Type	Peak Codes
1		2.989							209103	0.87	26121	BB			Unknown	
2		4.172							212671	0.88	20731	bb			Unknown	
3		17.152							23726401	98.25	1169309	bb			Unknown	
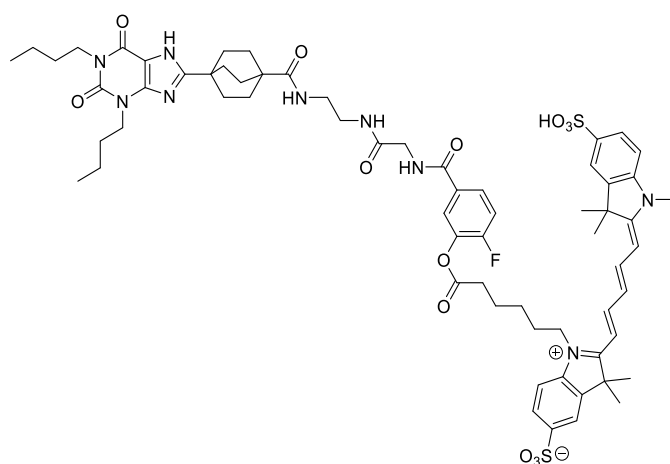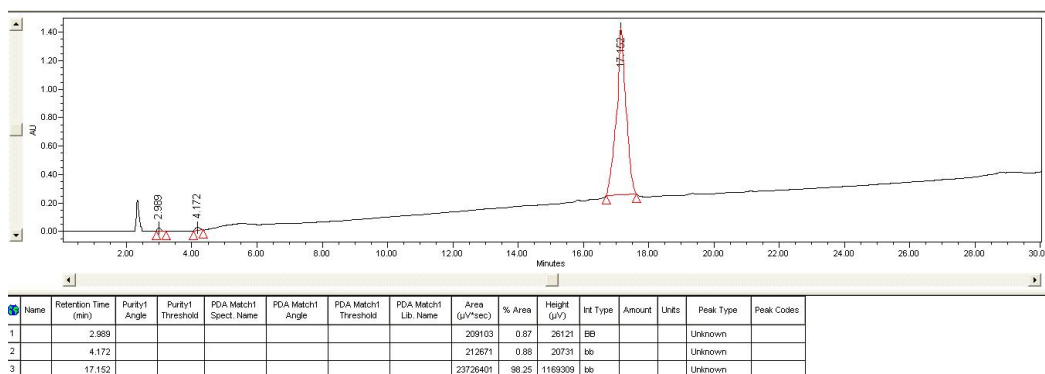
1-(6-(5-((2-((2-(4-(1,3-Dibutyl-2,6-dioxo-2,3,6,7-tetrahydro-1*H*-purin-8-yl)bicyclo[2.2.2]octane-1-carboxamido)ethyl)amino)-2-oxoethyl)carbamoyl)-2-fluorophenoxy)-6-oxohexyl)-3,3-dimethyl-2-((1*E*,3*E*)-5-((*E*)-1,3,3-trimethyl-5-sulfoindolin-2-ylidene)penta-1,3-dien-1-yl)-3*H*-indol-1-ium-5-sulfonate (3-16). Compound **3-14** (1 mg, 1.53 µmol, 1 eq) was reacted with SulfoCyanine 5 carboxylic acid (1.03 mg, 1.51 µmol, 1 eq) following the procedure outlined in **Section 2.2.7 General Procedure B**, yielding the final product **3-16** (1.15 mg, 0.89 µmol, yield = 59%).

HR-MS (TOF-ESI, negative) calcd. **_m/z_** for $C_{65}H_{79}FN_9O_{13}S_2$ [M-H$^-$] 1,276.522827, found 1,276.534, error (8 ppm) within 10 ppm; for $C_{65}H_{78}FN_9O_{13}S_2$ [M-2H^{2-}] 637.757775, found 637.7582, error within 2.4 ppm; **Section 2.2.4**.

Sample-ID	paxcl4_CYL-A1-016	Lab	C13
Submitter	Chia-Yang Lin (paxcl4)	Supervisor	Barrie Kellam (pazbk)
Analysis Name	paxcl4_CYL-A1-016_625937_33_01_1091 20.d	Acquisition Date	1/21/2022 5:28:47 PM
Ionisation Mode	ESI Negative	Instrument	Bruker MicroTOF

-MS, 0.7-0.9min #59-75

Expected ions not found!

-MS, 0.7-0.9min #59-75

2- 637.7582
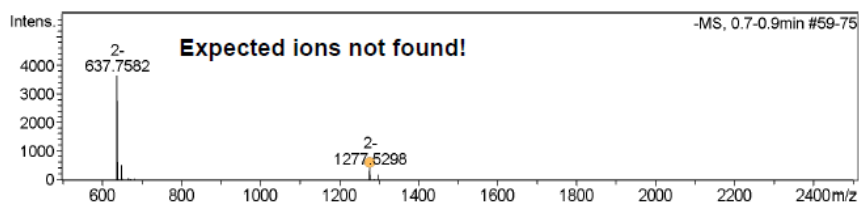
2- 1277.5298

#	m/z	I %
1	637.7582	100.0
2	638.2600	75.6
3	638.7610	40.7
4	639.2644	17.2
5	639.7701	6.0
6	648.7461	14.3
7	649.2518	10.4
8	649.7559	6.0
9	650.2648	1.2
10	666.7423	1.7
11	667.2376	1.5
12	682.7352	1.2
13	1276.5340	8.5
14	1277.0306	9.3
15	1277.5298	11.5
16	1277.8467	1.2
17	1278.0469	5.0
18	1278.5428	4.2
19	1298.5263	4.7
20	1299.5069	5.1

Generate Molecular Formula Parameters

Charge	Tolerance	sigma limit	H/C Ratio	Electron Conf.	Nitrogen Rule	Chrom.BackGround	Calibration
-1	6 ppm	0.08	3 - 0	both	false	false	TRUE

Expected Formula	C65 H80 F1 N9 O13 S2	**Adduct(s):**	H, radical

Note: Sigma fits < 0.05 indicates high probability of correct MF

Purity: 99.5%, measured by RP-HPLC with a YMC-Pack C8 analytic column (150 mm × 4.6 mm × 5 µm) mentioned in **Section 2.2.2**.

	Name	Retention Time (min)	Purity1 Angle	Purity1 Threshold	PDA Match1 Spect. Name	PDA Match1 Angle	PDA Match1 Threshold	PDA Match1 Lib. Name	Area (µV*sec)	% Area	Height (µV)	Int Type	Amount	Units	Peak Type	Peak Codes
1		18.257							9437647	99.50	464823	BB			Unknown	
2		20.446							47844	0.50	4106	bb			Unknown	
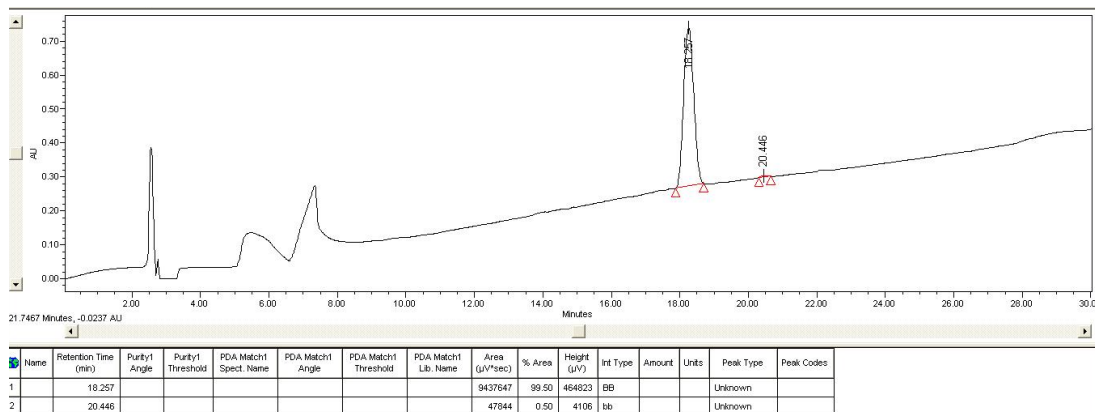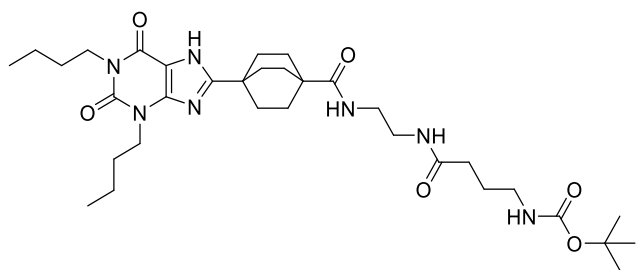
***tert*-Butyl (4-((2-(4-(1,3-dibutyl-2,6-dioxo-2,3,6,7-tetrahydro-1*H*-purin-8-yl)bicyclo[2.2.2]octane-1-carboxamido)ethyl)amino)-4-oxobutyl)carbamate (3-17).** The crude compound **3-10**, obtained from the *t*-Boc deprotection of compound **3-9** (274 mg, 0.49 mmol, 1 eq), was reacted with Boc-γ-aminobutyric acid (120 mg, 0.59 mmol, 1.2 eq) following the procedure outlined in **Section 2.2.7 General Procedure A**. The reaction progress was monitored by LC-MS. Upon completion, 20 mL of iced water was added to the mixture, resulting in the formation of a precipitate. The yellow precipitate was collected *via* gravity filtration and dried in an oven overnight, yielding compound **3-17** (247.8 mg, 0.38 mmol, yield = 78%).

LC-MS *m/z* calcd. for $C_{33}H_{53}N_7O_6$ [M-H$^+$] 644.41; found 644.4, t_R = 2.95 min, **Section 2.2.4, Method A**.

^{1}H NMR (DMSO-d_6) δ 12.9 (s, 1H), 7.79 (t, *J* = 5.6 Hz, 1H), 7.42 (t, *J* = 5.5 Hz, 1H), 6.79 (t, *J* = 5.24 Hz, 1H), 3.96 (t, *J* = 7.2 Hz, 2H), 3.86 (t, *J* = 7.4 Hz, 2H), 3.08 (t, *J* = 2.6 Hz, 4H), 2.89 (q, *J* = 7 Hz, 2H), 2.03 (t, *J* = 7.5 Hz, 2H), 1.88-1.84 (m, 6H), 1.74-1.70 (m, 6H), 1.61 (m, *J* = 7.3, 1.65 Hz, 4H), 1.5 (p, *J* = 7.8 Hz, 2H), 1.36 (s, 9H), 1.27 (h, *J* = 7.5 Hz, 4H), 0.90 (t, *J* = 7.44 Hz, 3H), 0.88 (t, *J* = 7.24 Hz, 3H).

^{13}C NMR (MeOD-d_4) δ 180.5, 176.1, 162.2, 158.6, 155.9, 152.8, 149.4, 108.2, 79.9, 44.2, 42.1, 40.9, 40.7, 40.1 39.9, 34.9, 34.3, 31.23, 31.21, 31.0, 29.2, 28.8, 27.3, 21.6, 20.8, 14.18, 14.12.
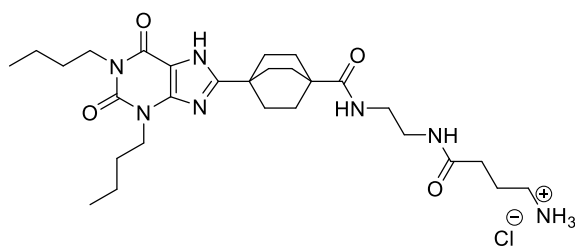
***N*-(2-(4-aminobutanamido)ethyl)-4-(1,3-dibutyl-2,6-dioxo-2,3,6,7-tetrahydro-1*H*-purin-8-yl)bicyclo[2.2.2]octane-1-carboxamide hydrochloride salt (3-18)**. Compound **3-17** (100 mg, 0.155 mmol, 1 eq) was subjected to the procedure outlined in **Section 2.2.7 General Procedure C**. The reaction progress was monitored by LC-MS. Once the *t*-Boc group was removed, the mixture was evaporated to yield the crude compound **3-18** for the next step without further purification.
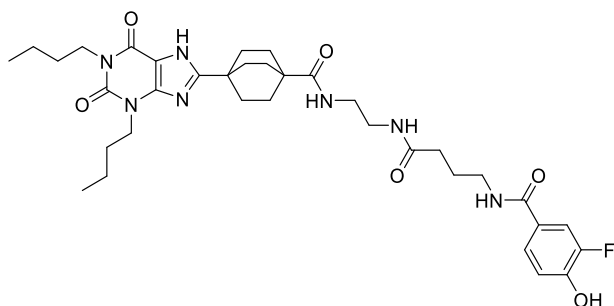
4-(1,3-Dibutyl-2,6-dioxo-2,3,6,7-tetrahydro-1*H*-purin-8-yl)-*N*-(2-(4-(3-fluoro-4-hydroxybenzamido)butanamido)ethyl)bicyclo[2.2.2]octane-1-carboxamide (**3-19**). The crude compound **3-18**, obtained from the *t*-Boc deprotection of compound **3-17** (100 mg, 0.155 mmol, 1 eq), was reacted with 3-fluoro-4-hydroxybenzoic acid (24.5 mg, 0.156 mmol, 1.01 eq) following the procedure outlined in **Section 2.2.7 General Procedure A**. The reaction mixture was heated to 90°C and stirred overnight. The reaction progress was monitored by LC-MS. Upon completion, no precipitate formed when iced water was added to the mixture. The mixture was then purified using automated flash column chromatography (gradient MeOH:DCM from 5:95 to 10:90, 19 CV), yielding compound **3-19** (40 mg, 0.058 mmol, yield = 38%).

LC-MS *m/z* calcd. for $C_{35}H_{48}FN_7O_6$ [M-H$^+$] 682.37; found 682.2, t_R = 2.75 min, **Section 2.2.4, Method A**.

^{1}H NMR (MeOD-*d*$_4$) δ 7.58 (dd, *J* = 11.98, 2.16 Hz, 1H), 6.95 (t, *J* = 8.52 Hz, 1H), 7.52 (dd, *J* = 8.69, 2.19 Hz, 1H), 4.09 (t, *J* = 7.3 Hz, 2H), 3.97 (t, *J* = 7.5 Hz, 2H), 3.38 (t, J = 6.84 Hz, 2H), 3.29 (s, 4H), 2.27 (t, *J* = 7.4 Hz, 2H), 2.02-1.85 (m, 14H), 1.72 (p, *J* = 7.48 Hz, 2H), 1.60 (p, *J* = 7.5 Hz, 2H), 1.37 (h, *J* = 7.3 Hz, 4H), 0.97 (t, *J* = 7.44 Hz, 3H), 0.96 (t, *J* = 7.44 Hz, 3H).

^{13}C NMR (MeOD-*d*$_4$) δ 180.5, 176.1, 168.8, 162.1, 155.9, 152.34 (d, *J* = 239.8 Hz), 152.7, 149.8, 149.5 (d, *J* = 22.59 Hz), 127.0 (d, *J* = 5.5 Hz), 125.1 (d, *J* = 5.4 Hz), 118.4 (d, *J* = 2.9 Hz), 116.3 (d, *J* = 19.7 Hz), 108.2, 44.2, 42.13, 40.62, 40.35, 40.08, 40.0, 34.8, 34.4, 31.2, 31.17, 30.96, 29.18, 26.76, 21.1, 20.8, 14.17, 14.11.
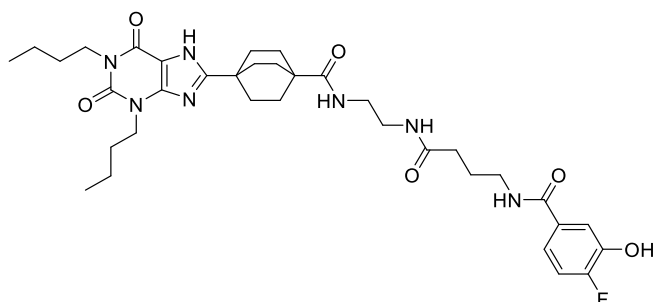
4-(1,3-Dibutyl-2,6-dioxo-2,3,6,7-tetrahydro-1*H*-purin-8-yl)-*N*-(2-(4-(4-fluoro-3-hydroxybenzamido)butanamido)ethyl)bicyclo[2.2.2]octane-1-carboxamide

71

(3-20). Crude compound **3-18**, obtained from **3-17** (100 mg, 0.155 mmol, 1 eq) *via* *t*-Boc deprotection, was reacted with 4-fluoro-3-hydroxybenzoic acid (24.5 mg, 0.156 mmol, 1.01 eq) according to **Section 2.2.7 General Procedure A**. The reaction mixture was heated to 90°C and stirred overnight. Progress of the reaction was monitored using LC-MS. Upon completion, no precipitate formed when iced water was added to the mixture. The mixture was then purified using automated flash column chromatography (gradient MeOH:DCM from 5:95 to 10:90, 19 column volumes), yielding compound **3-20** (51.5 mg, 0.076 mmol, 49%).

LC-MS *m/z* calcd. for $C_{35}H_{48}FN_7O_6$ [M-H$^+$] 682.37; found 682.2, t_R = 2.75 min, **Section 2.2.4, Method A**.

^{1}H NMR (MeOD-*d*$_4$) δ 7.43 (dd, *J* = 8.44, 2.1 Hz, 1H), 7.30 (ddd, *J* = 8.5, 4.22, 2.26 Hz, 1H), 7.12 (dd, *J* = 10.76, 8.56 Hz, 1H), 4.1 (t, *J* = 7.28 Hz, 2H), 3.99 (t, *J* = 7.5 Hz, 2H), 3.41 (t, *J* = 6.9 Hz, 2H), 3.31 (s, 4H), 2.00-1.86 (m, 14H), 1.73 (p, *J* = 7.42 Hz, 2H), 1.62 (p, *J* = 7.54 Hz, 2H), 1.38 (h, *J* = 7.2 Hz, 4H), 0.98 (t, *J* = 7.32 Hz, 3H), 0.97 (t, *J* = 7.36 Hz, 3H).

^{13}C NMR (MeOD-*d*$_4$) δ 180.5, 176.1, 169.4, 162.13, 156.0, 155.0 (d, *J* = 244.5 Hz), 152.8, 149.4, 146.4 (d, *J* = 13.27 Hz), 132.4, 119.9 (d, *J* = 7.21 Hz), 118.3 (d, *J* = 3.79 Hz), 116.8 (d, *J* = 19.33 Hz), 108.2, 44.2, 42.1, 40.7, 40.4, 40.1, 40.0, 34.9, 34.5, 31.23, 31.20 , 30.98, 29.2, 26.7, 21.2, 20.8, 14.18, 14.11.
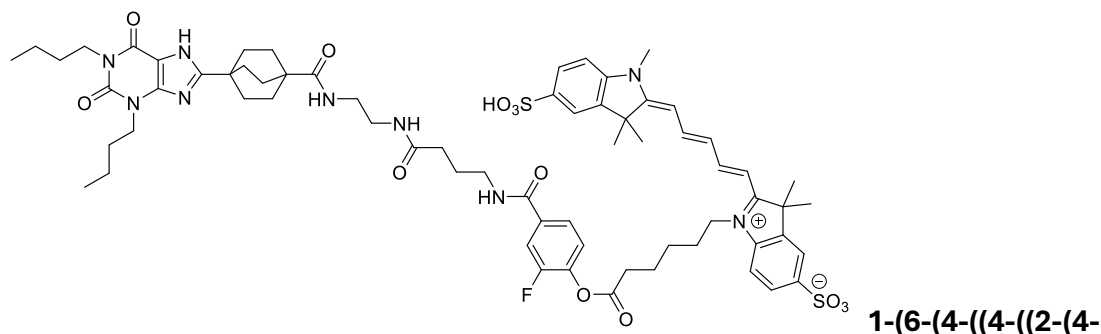
1-(6-(4-((4-((2-(4-(1,3-Dibutyl-2,6-dioxo-2,3,6,7-tetrahydro-1*H*-purin-8-yl)bicyclo[2.2.2]octane-1-carboxamido)ethyl)amino)-4-oxobutyl)carbamoyl)-2-fluorophenoxy)-6-oxohexyl)-3,3-dimethyl-2-((1*E*,3*E*)-5-((*E*)-1,3,3-trimethyl-5-sulfoindolin-2-ylidene)penta-1,3-dien-1-yl)-3*H*-indol-1-ium-5-sulfonate (3-21). Compound **3-19** (1 mg, 1.467 µmol, 1 eq) was reacted with SulfoCyanine 5 carboxylic acid (0.975 mg, 1.467 µmol, 1 eq) following the conditions described in **Section 2.2.7 General Procedure B**. The reaction yielded compound **3-21** with a mass of 1.34 mg (1.025 µmol), corresponding to a yield of 70%.

HR-MS (TOF-ESI, negative) calcd. *m/z* for $C_{67}H_{83}FN_9O_{13}S_2$ [M-H$^-$] 1,304.554127, found 1304.5632, error (7 ppm) within 10 ppm; for $C_{65}H_{82}FN_9O_{13}S_2$ [M-2H^{2-}] 651.773425, found 651.7739, error within 2.4 ppm; **Section 2.2.4**.

Purity: 96.85%, measured by RP-HPLC with a YMC-Pack C8 analytic column (150 mm × 4.6 mm × 5 μm) mentioned in **Section 2.2.2**.

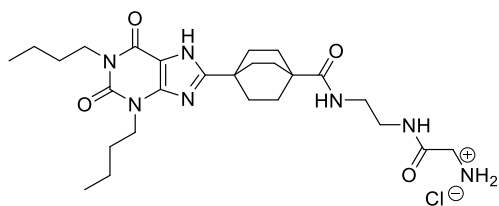**1-(6-(5-((4-((2-(4-(1,3-Dibutyl-2,6-dioxo-2,3,6,7-tetrahydro-1*H*-purin-8-yl)bicyclo[2.2.2]octane-1-carboxamido)ethyl)amino)-4-oxobutyl)carbamoyl)-2-fluorophenoxy)-6-oxohexyl)-3,3-dimethyl-2-((1*E*,3*E*)-5-((*E*)-1,3,3-trimethyl-5-sulfoindolin-2-ylidene)penta-1,3-dien-1-yl)-3*H*-indol-1-ium-5-sulfonate (3-22)**. Compound **3-20** (1 mg, 1.467 µmol, 1 eq) was reacted with SulfoCyanine 5 carboxylic acid (1.01 mg, 1.483 µmol, 1 eq) following the conditions described in **Section 2.2.7 General Procedure B**. The reaction yielded compound **3-22** with a mass of 1.18 mg (0.94 µmol), corresponding to a yield of 62%.

HR-MS (TOF-ESI, negative) calcd. ***m/z*** for $C_{67}H_{83}FN_9O_{13}S_2$ [M-H$^-$] 1,304.554127, found 1304.5668, error (9 ppm) within 10 ppm; for $C_{65}H_{82}FN_9O_{13}S_2$ [M-2H^{2-}] 651.773425, found 651.7724, error within 2.4 ppm; **Section 2.2.4**.

Mass Spectrometry
Analytical Services
School of Chemistry

The University of Nottingham

Sample-ID	paxcl4_CYL-A1-14	Lab	C13
Submitter	Chia-Yang Lin (paxcl4)	Supervisor	Barrie Kellam (pazbk)
Analysis Name	paxcl4_CYL-A1-14_625936_32_01_10911 9.d	Acquisition Date	1/21/2022 5:26:18 PM
onisation Mode	ESI Negative	Instrument	Bruker MicroTOF

-MS, 0.7-0.9min #59-75

Expected ions not found!
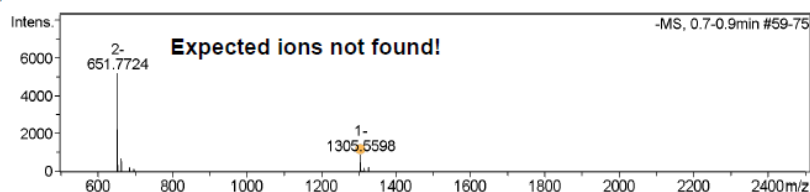
#	m/z	I %
1	651.7724	100.0
2	652.2751	79.0
3	652.7753	42.7
4	653.2778	17.4
5	653.7811	6.9
6	662.7633	13.1
7	663.2672	10.7
8	663.7632	6.2
9	685.7684	3.9
10	686.2707	3.3
11	696.7598	2.7
12	1304.5668	10.3
13	1305.0606	14.3
14	1305.5598	17.3
15	1306.0598	9.0
16	1306.5697	6.7
17	1316.0398	3.5
18	1316.5682	3.2
19	1326.5413	4.2
20	1327.5543	4.5

Generate Molecular Formula Parameters

Charge	Tolerance	sigma limit	H/C Ratio	Electron Conf.	Nitrogen Rule	Chrom.BackGround	Calibration
-1	6 ppm	0.08	3 - 0	both	false	false	TRUE

Expected Formula	C67 H84 F1 N9 O13 S2	**Adduct(s):**	H, radical

Note: Sigma fits < 0.05 indicates high probability of correct MF

Purity: 96.46%, measured by RP-HPLC with a YMC-Pack C8 analytic column (150 mm × 4.6 mm × 5 μm) mentioned in **Section 2.2.2**.

19.0725 Minutes, 0.2335 AU

	Name	Retention Time (min)	Purity1 Angle	Purity1 Threshold	PDA Match1 Spect. Name	PDA Match1 Angle	PDA Match1 Threshold	PDA Match1 Lib. Name	Area (μV*sec)	% Area	Height (μV)	Int Type	Amount	Units	Peak Type	Peak Codes
1		3.013							425113	2.11	51754	Bb			Unknown	
2		5.028							175989	0.87	7109	bb			Unknown	I08
3		16.084							111175	0.55	16914	bb			Unknown	
4		17.062							19426171	96.46	654102	bB			Unknown	
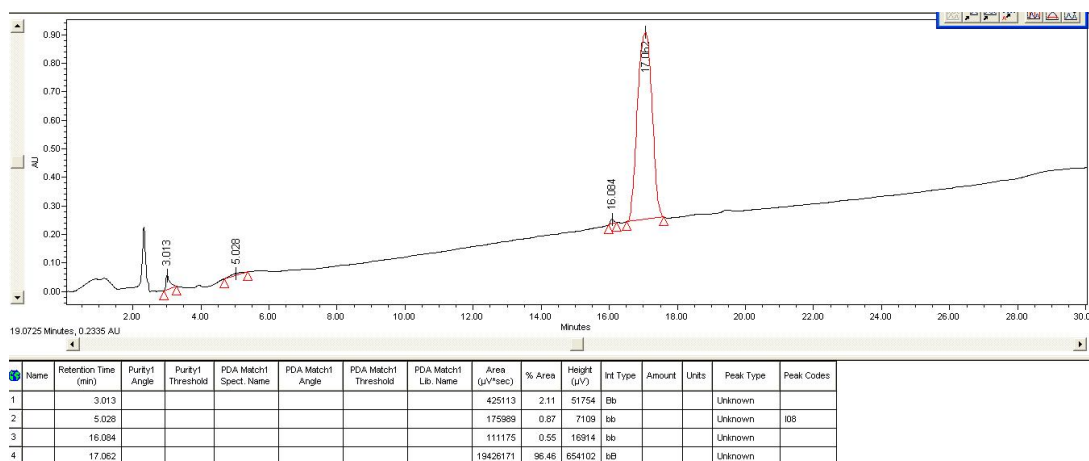
***tert*-Butyl (3-((2-(4-(1,3-dibutyl-2,6-dioxo-2,3,6,7-tetrahydro-1*H*-purin-8-yl)bicyclo[2.2.2]octane-1-carboxamido)ethyl)amino)-3-oxopropyl)carbamate (3-23)**. Crude compound **3-10**, obtained from the *t*-Boc deprotection of compound **3-9** (274 mg, 0.49 mmol, 1 eq), was reacted with *N*-Boc β-alanine (112 mg, 0.59 mmol, 1.2 eq) following the conditions described in **Section 2.2.7 General Procedure A**. The reaction progress was monitored by LC-MS. Upon completion, the reaction mixture was worked up as no precipitate formed when iced water was added. Purification was performed using automated flash column chromatography (gradient MeOH:DCM from 2:98 to 10:90, 19 CV), yielding compound **3-23** (280 mg, 0.44 mmol) with a yield of 91%.

LC-MS *m/z* calcd. for $C_{32}H_{51}N_7O_6$ [M-H$^+$] 630.397; found 630.3, t_R = 2.80 min, **Section 2.2.4, Method A**.

^{1}H NMR (MeOD-*d$_4$*): δ 4.11 (t, *J* = 7.2 Hz, 2H), 3.99 (t, *J* = 7.6 Hz, 2H), 3.30 (s, 4H), 2.37 (t, *J* = 6.7 Hz, 2H), 2.04-1.97 (m, 6H), 1.96-1.86 (m, 6H), 1.74 (p, *J* = 7.2 Hz, 2H), 1.62 (p, *J* = 7.6 Hz, 2H), 1.45 (s, 9H), 1.36 (m, 4H), 0.97 (t, *J* = 8 Hz, 3H), 0.96 (t, *J* = 7.36 Hz, 3H).

^{13}C NMR (MeOD-*d$_4$*): δ 179.08, 173.12, 160.79, 156.94, 154.59, 151.42, 148.07, 106.82, 78.75, 42.81, 40.74, 40.75, 39.17, 38.73, 38.62, 36.73, 36.16, 33.54, 29.84, 29.82, 29.63, 27.83, 27.36, 19.76, 19.44, 12.78, 12.72.
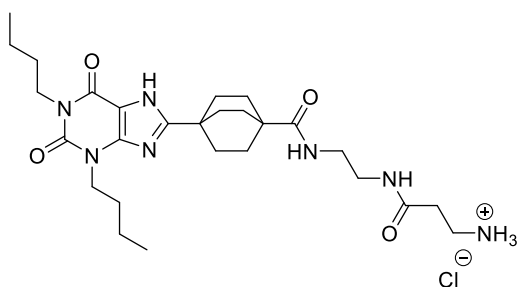
***N*-(2-(3-aminopropanamido)ethyl)-4-(1,3-dibutyl-2,6-dioxo-2,3,6,7-tetrahydro-1*H*-purin-8-yl)bicyclo[2.2.2]octane-1-carboxamide hydrochloride salt (3-24)**. Compound **3-23** (200 mg, 0.32 mmol, 1 eq) was subjected to the conditions described in **Section 2.2.7 General Procedure C**. The reaction progress was monitored by LC-MS. Upon removal of the *t*-Boc group, the mixture was evaporated to yield the

crude compound **3-24**, which was used in the next step without further purification.
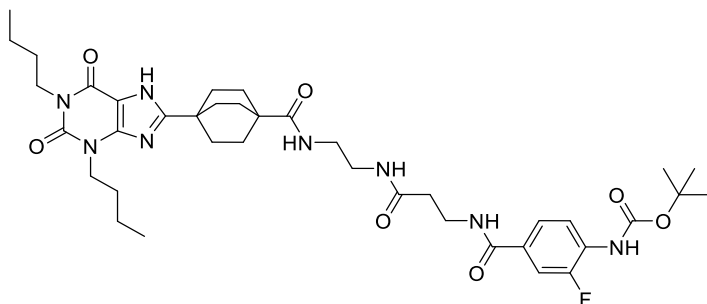
tert-Butyl (4-((3-((2-(4-(1,3-dibutyl-2,6-dioxo-2,3,6,7-tetrahydro-1H-purin-8-yl)bicyclo[2.2.2]octane-1-carboxamido)ethyl)amino)-3-oxopropyl)carbamoyl)-2-fluorophenyl)carbamate (3-25). Crude compound **3-24**, obtained from the *t*-Boc deprotection of compound **3-23** (200 mg, 0.32 mmol, 1 eq), was reacted with compound **3-32** (97 mg, 0.38 mmol, 1.2 eq) following the conditions described in **Section 2.2.7 General Procedure A**. The reaction mixture was heated to 80°C and stirred overnight. The reaction progress was monitored by LC-MS. Upon completion, the reaction mixture was worked up as no precipitate formed when iced water was added. Purification was performed using automated flash column chromatography (gradient MeOH:DCM from 2:98 to 10:90, 17 CV), yielding compound **3-25** (175 mg, 0.228 mmol) with a yield of 71%.

LC-MS *m/z* calcd. for $C_{39}H_{55}FN_8O_7$ [M-H$^+$] 767.425; found 767.2, t_R = 2.87 min, **Section 2.2.4, Method A**.

^{1}H NMR (MeOD-*d₄*): δ 8.06 (t, *J* = 8.8 Hz, 1H), 7.63 (m, 2H), 4.12 (t, *J* = 7.3 Hz, 2H-), 3.99 (t, *J* = 7.3 Hz, 2H), 3.65 (t, *J* = 6.7 Hz, 2H), 3.31 (s, 4H), 2.52 (t, *J* = 6.7 Hz, 2H), 2-1.96 (m, 6H), 1.88-1.83 (m, 6H), 1.74 (p, *J* = 7.4 Hz, 2H), 1.62 (p, *J* = 7.7 Hz, 2H), 1.53 (s, 9H), 1.39 (m, 4H), 0.97 (t, *J* = 7.32 Hz, 3H), 0.96 (t, *J* = 7.44 Hz, 3H).

^{13}C NMR (MeOD-*d₄*): δ 178.54, 172.96, 166.15, 160.54, 156.14, 155.33, 152.01, 151.37 (d, *J*=243.4 Hz), 148.66, 130.18 (d, *J*=10.3 Hz), 128.54 (d, *J*=6.1 Hz), 123.26 (d, *J*=2.5 Hz), 119.15, 114.09 (d, *J*=20.7 Hz), 106.88, 81.68, 43.42, 41.43, 40.23, 40, 38.94, 36.40, 35.86, 33.63, 30.24, 30.12, 29.94, 28.36, 28.22, 20.29, 19.91, 13.88, 13.77.

N-(2-(3-(4-amino-3-fluorobenzamido)propanamido)ethyl)-4-(1,3-dibutyl-2,6-dioxo-2,3,6,7-tetrahydro-1H-purin-8-yl)bicyclo[2.2.2]octane-1-carboxamide hydrochloride salt (3-26). Compound **3-25** (60 mg, 78 µmol, 1 eq) was subjected to the conditions described in **Section 2.2.7 General Procedure C**. The reaction progress was monitored by LC-MS. Upon removal of the *t*-Boc group, the mixture was evaporated to yield the crude compound **3-26**, which was used in the next step without further purification.
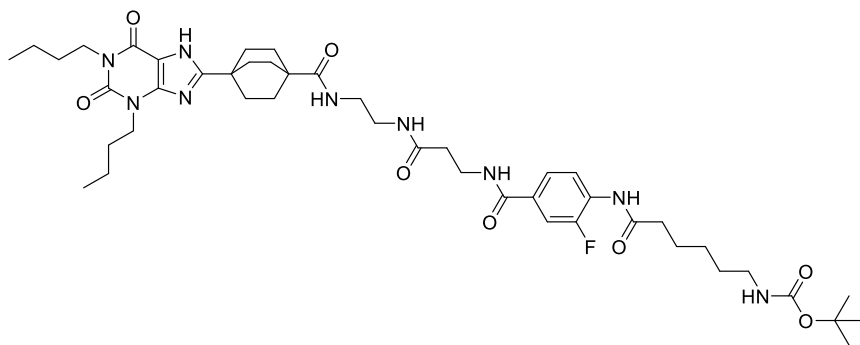
***tert*-Butyl (6-((4-((3-((2-(4-(1,3-dibutyl-2,6-dioxo-2,3,6,7-tetrahydro-1H-purin-8-yl)bicyclo[2.2.2]octane-1-carboxamido)ethyl)amino)-3-oxopropyl)carbamoyl)-2-fluorophenyl)amino)-6-oxohexyl)carbamate (3-27)**. Crude compound **3-26**, obtained from the *t*-Boc deprotection of compound **3-25** (60 mg, 78 µmol, 1 eq), was reacted with Boc-E-Acp-OH (20.7 mg, 89.7 µmol, 1.15 eq), propylphosphonic anhydride (T3P, 0.16 mL, 269.1 µmol, 3.45 eq), and DIPEA (78 µL, 448.5 µmol, 5.75 eq) in DCM. The reaction mixture was heated to 80°C and stirred for 19 hours. The reaction progress was monitored by LC-MS. Upon completion, the reaction mixture was worked up as no precipitate formed when iced water was added. Purification was performed using automated flash column chromatography (gradient EtOAc:Cyclohexane from 25:75 to 100:0, 20 CV; followed by gradient MeOH:DCM from 10:90 to 20:80, 10 CV), yielding compound **3-27** (3.7 mg, 4.2 µmol) with a yield of 5%.

LC-MS *m/z* calcd. for $C_{45}H_{66}FN_9O_8$ [M-H$^+$] 880.51; found 879.9, t_R = 2.85 min, **Section 2.2.4, Method A**.

^{1}H NMR (MeOD-*d₄*): δ 8.14 (t, *J* = 7.8 Hz, 1H), 7.68-7.60 (m, 2H), 4.09 (t, *J* = 7 Hz, 2H), 3.97 (t, *J* = 7.5 Hz), 3.64 (t, *J* = 7.1 Hz, 2H), 3.29 (s, 4H), 3.04 (t, *J* = 7.3 Hz, 2H),

2.50 (t, *J* = 7.3 Hz), 2.45 (t, *J* = 7.9 Hz, 2H), 2-1.91 (m, 6H), 1.88-1.81 (m, 6H), 1.71 (m, 4H), 1.60 (p, *J* = 7.8 Hz), 1.50 (p, *J* = 7.3 Hz), 1.42 (s, 9H), 1.40-1.28 (m, 6H), 0.97 (t, *J* = 7.36 Hz, 3H), 0,96 (t, *J* = 7.36 Hz, 3H).

¹³C NMR (101 MHz, MeOD-*d₄*): *δ* 180.49, 174.91, 174.41, 168.20, 162.18, 158.56, 155.98, 155.72, 152.81, 149.46, 132.07, 130.2 (d, *J* = 11.4 Hz), 124.34 (d, *J* = 3.3 Hz), 124.27, 115.50 (d, *J* = 21.7 Hz), 108.21, 79.81, 49.64, 44.22, 42.15, 41.17, 40.58, 40.17, 40.10, 37.78, 37.43, 36.87, 34.91, 31.25, 31.22, 30.98, 30.71, 29.20, 28.78, 27.41, 26.37, 21.16, 20.84, 14.19, 14.12.
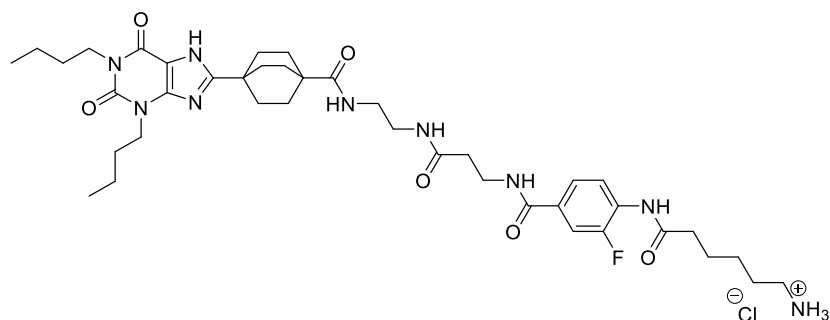
***N*-(2-(3-(4-(6-aminohexanamido)-3-fluorobenzamido)propanamido)ethyl)-4-(1,3-dibutyl-2,6-dioxo-2,3,6,7-tetrahydro-1*H*-purin-8-yl)bicyclo[2.2.2]octane-1-carboxamide hydrochloride salt** (**3-28**). Compound **3-27** (3.5 mg, 4 µmol, 1 eq) was subjected to the conditions described in **Section 2.2.7 General Procedure C**. The reaction progress was monitored by LC-MS. Upon removal of the *t*-Boc group, the mixture was evaporated to yield the crude compound **3-28**, which was used in the next step without further purification.
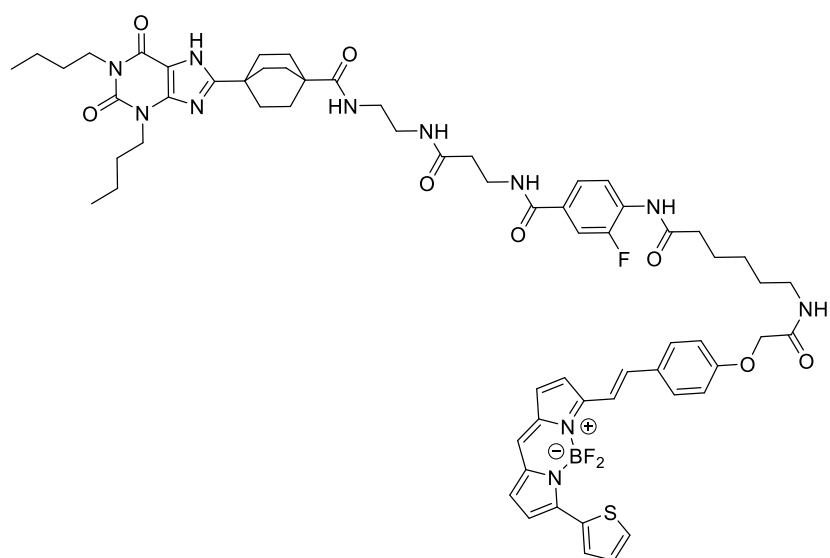
(***E***)-4-(1,3-dibutyl-2,6-dioxo-2,3,6,7-tetrahydro-1*H*-purin-8-yl)-*N*-(2-(3-(4-(6-(2-(4-(2-(5,5-difluoro-7-(thiophen-2-yl)-5*H*-4λ⁴,5λ⁴-dipyrrolo[1,2-c:2',1'-*f*][1,3,2]diazaborinin-3-yl)vinyl)phenoxy)acetamido)hexanamido)-3-fluorobenzamido)propanamido)ethyl)bicyclo[2.2.2]octane-1-carboxamide**

(**3-29**). Crude compound **3-28** (3.5 mg, 4 µmol, 1 eq), obtained from *t*-Boc deprotection, was coupled with BODIPY630/650 carboxylic acid (1.8 mg, 4 µmol, 1 eq) using 2-bromo-1-ethyl-pyridinium tetrafluoroborate (BEP, 1.1 mg, 4 µmol, 1 eq) and DIPEA (6 drops) in DMF (0.7 mL). The reaction was carried out at room temperature in the dark. After an overnight reaction, DMF was removed by rotary evaporation. The residue was reconstituted with MeCN and MeOH. Further purification was performed using RP-HPLC with a semipreparative YMC-Pack C8 column (150 mm × 10 mm × 5 µm). The collected fraction was concentrated and lyophilised to give a blue fluffy solid, compound **3-29** (1.7 mg, 1.4 µmol) with a yield of 35%.

HR-MS (TOF-ESI, negative) calcd. ***m/z*** for $C_{63}H_{72}BF_3N_{11}O_8S$ [M-H⁻] 1,210.53367, found 1,210.5365, error within 2.4 ppm; **Section 2.2.4**.

HR-MS (TOF-ESI, positive) calcd. *m/z* for $C_{63}H_{73}BF_3N_{11}O_8SNa$ $[M+Na^+]$ 1,234.53017, found 1,234.5284, error within 2.4 ppm; **Section 2.2.4**.

Sample-ID	pczlo_paxcl4_CYL-25-CNL_070323	Lab	C13
Submitter	Lola Ogunyemi (pczlo)	Supervisor	Z_NO SUPERVISOR z_NO SUPERVISOR
Analysis Name	pczlo_paxcl4_CYL-25-CNL_070323__42_01_43720.d	Acquisition Date	08/03/2023 14:16:51
Ionisation Mode	ESI Positive	Instrument	Bruker MicroTOF
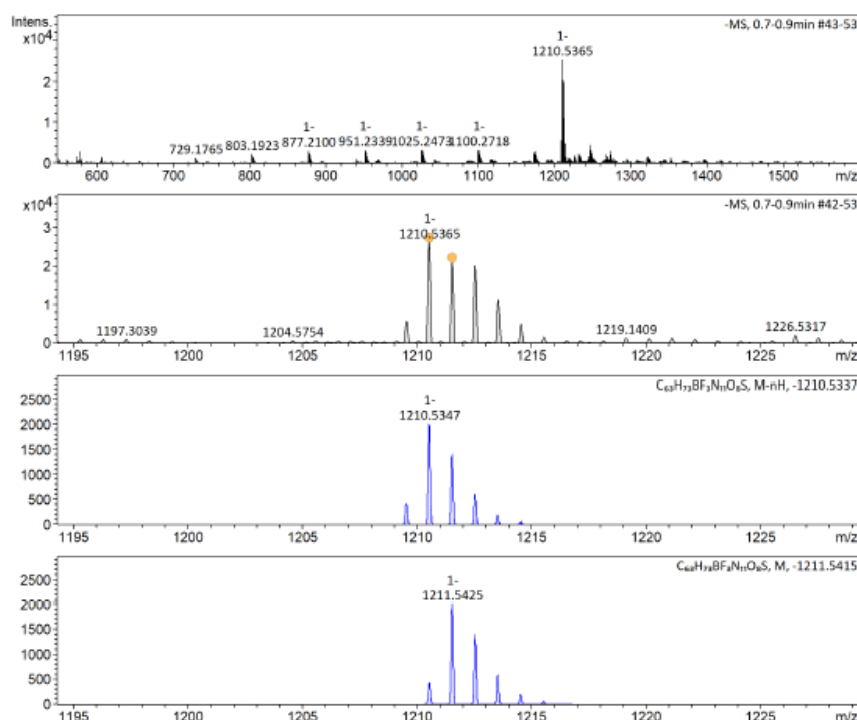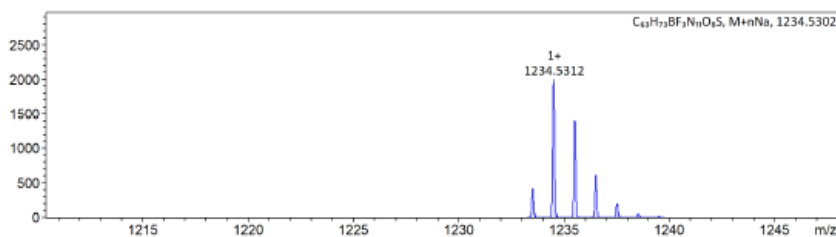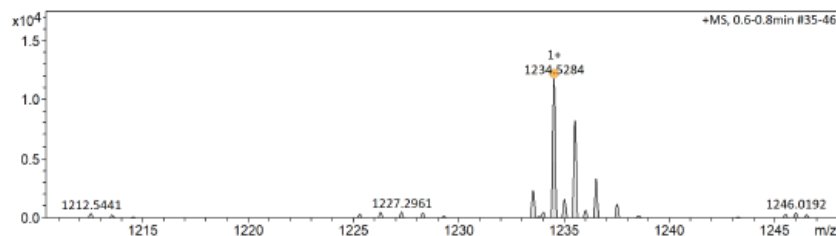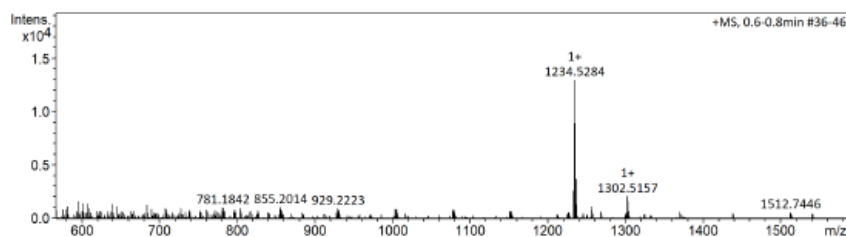
Meas. m/z	#	Ion Formula	Score	m/z	err [mDa]	err [ppm]	mSigma
1234.528419	1	C63H73BF3N11NaO8S	100.00	1234.530165	1.7	1.4	9.4

Note: Sigma fits < 0.05 indicates high probability of correct MF

Purity: 96.69%, measured by RP-HPLC with a YMC-Pack C8 analytic column (150 mm × 4.6 mm × 5 µm) mentioned in **Section 2.2.2**.

Peak#	Ret. Time	Area	Height	Mark	Conc.	Unit	ID#	Name	Area%
1	27.313	629913	20870	M	0.000				3.309
2	29.035	18405452	1185066	M	0.000				96.691
Total		19035365	1205937						100.000
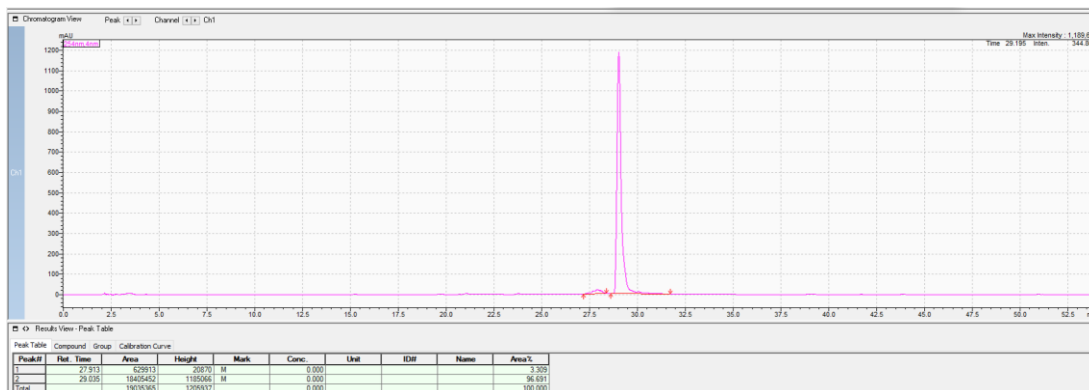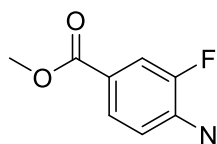
Methyl 4-amino-3-fluorobenzoate (3-31). Compound **3-30** (0.8 g, 4 mmol, 1 eq) and Pd/C (0.08 g, 0.1 eq) were added into 10 mL of MeOH. Two balloons of H_2 were purged into the flask, and the mixture was stirred at room temperature for 1.5 hours. The reaction progress was monitored by TLC. The mixture was filtered through a celite cake, and the cake was washed several times with MeOH. The collected MeOH was evaporated to yield compound **3-31** (0.54 g, 3.19 mmol) with a yield of 78%.

LC-MS *m/z* calcd. for $C_8H_9FNO_2$ [M-H$^+$] 170.05; found 170.1, t_R = 2.55 min, **Section 2.2.4, Method A**.

^{1}H NMR (DMSO-d_6): δ 7.53 (dd, *J* = 8.44, 2.02 Hz, 1H), 7.48 (dd, *J* = 12.24, 2.02 Hz, 1H), 6.78 (t, *J* = 8.64 Hz, 1H), 6.07 (s, 2H), 3.76 (s, 3H).

^{13}C NMR (DMSO-d_6): δ 166.09, 149.61 (d, *J* = 236.14 Hz), 142.23 (d, *J* = 12.89 Hz), 127.29 (d, *J* = 2.6Hz), 116.43 (d, *J* = 6.06 Hz), 116.10 (d, *J* = 19.33 Hz), 115.23 (d, *J* = 4.93 Hz), 52.0.
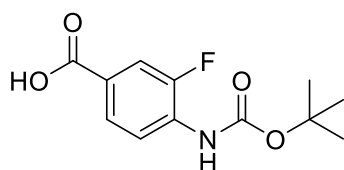
4-((*tert*-Butoxycarbonyl)amino)-3-fluorobenzoic acid (3-32). Compound **3-31** (845.8 mg, 5 mmol, 1 eq), DMAP (61 mg, 0.5 mmol, 0.1 eq), and Boc$_2$O (6.55 g, 30 mmol, 6 eq) were dissolved in THF (50 mL). The mixture was refluxed overnight. THF was removed *via* rotary evaporation. The residue, along with K_2CO_3 (2 g, 15 mmol, 3 eq), was dissolved in MeOH (50 mL) and refluxed for an additional 3 hours. After cooling to room temperature, MeOH was removed *via* rotary evaporation. The residue was reconstituted with EtOAc and extracted with water. The collected EtOAc solution was washed twice with 2 N HCl, followed by saturated NaHCO$_{3(aq)}$ and brine. The organic solution was evaporated, and the crude product was used for the next reaction.

The crude product and 2 M NaOH (25 mL) were dissolved in 50 mL of a MeOH/THF (1:1) mixture. The mixture was stirred at room temperature for 5.5 hours. The organic solvent was removed *via* rotary evaporation. The residue in water was extracted with EtOAc. The collected aqueous portion was acidified with 2 N HCl to afford a white precipitate. The precipitate was collected *via* filtration and dried in an oven, yielding compound **3-32** (0.98 g, 3.85 mmol) with a yield of 64%.

LC-MS *m/z* calcd. for $C_{12}H_{14}FNO_4$ [M-H⁺] 255.09; found 256.1, t_R = 2.73 min, **Section 2.2.4, Method A**.

¹H NMR (DMSO-*d₆*): δ 13.03 (s, 1H), 9.36 (s, 1H), 7.90 (t, *J* = 8.2 Hz, 1H), 7.72 (dd, *J* = 8.57, 1.88 Hz, 1H), 7.65 (dd, *J* = 11.45, 1.88 Hz, 1H), 1.48 (s, 9H).

¹³C NMR (DMSO-*d₆*): δ 166.55 (d, *J* = 2.53 Hz), 153, 152.8 (d, *J* = 246.08 Hz), 131.66 (d, *J* = 11.39 Hz), 126.61 (d, *J* = 6.09 Hz), 126.19 (d, *J* = 3.28 Hz), 122.48, 116.49 (d, *J* = 20.8 Hz), 80.52, 28.43.
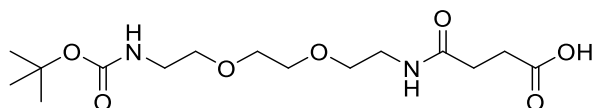
2,2-Dimethyl-4,15-dioxo-3,8,11-trioxa-5,14-diazaoctadecan-18-oic acid (4-2). Commercially available *tert*-butyl (2-(2-(2-aminoethoxy)ethoxy)ethyl)carbamate (**4-1**) (218 mg, 0.87 mmol, 1 eq) was dissolved in $CHCl_3$ (7 mL) and cooled to 0°C in an ice bath. Succinic anhydride (87.6 mg, 0.87 mmol, 1 eq) was added to the cooled solution of **4-1**, and the mixture was allowed to stir for 10 minutes. The ice bath was then removed, and the reaction was continued for 1 hour. $CHCl_3$ was evaporated under reduced pressure, and the crude product was purified using automated flash column chromatography (gradient MeOH:DCM from 1:99 to 10:90, 23 CV), yielding compound **4-2** (111 mg, 0.32 mmol) with a yield of 36%.

¹H NMR (400 MHz, CDCl₃-*d*) δ 7.44 (s, 1H, NH), 6.94 (s, 1H, NH), 3.62 (s, 4H), 3.54 (p, *J* = 4.9 Hz, 4H), 3.45 (q, *J* = 5.1 Hz, 2H), 3.32 (q, *J* = 5.2 Hz, 2H), 2.70-2.64 (t, *J* = 5.8 Hz, 2H), 2.5 (t, *J* = 5.6 Hz, 2H), 1.45 (s, 9H).

¹³C NMR (101 MHz, CDCl₃-*d*) δ 177.64, 173.13, 158.15, 81.26, 77.36, 70.44, 70.35, 69.73, 41.73, 39.45, 31.64, 30.44, 28.50.
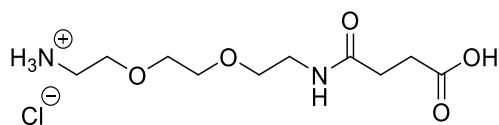
4-((2-(2-(2-Aminoethoxy)ethoxy)ethyl)amino)-4-oxobutanoic acid hydrochloride salt (4-3). Compound **4-2** (38.28 mg, 110 μmol, 1.1 eq) underwent *t*-Boc deprotection following the conditions described in **Section 2.2.7 General Procedure C**. The reaction progress was monitored by LC-MS. Upon removal of the *t*-Boc group, the mixture was evaporated to yield the crude compound **4-3**, which was used in the next step without further purification.
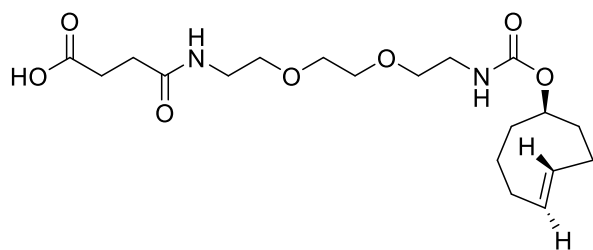
(*R*,*E*)-1-(cyclooct-4-en-1-yloxy)-1,12-dioxo-5,8-dioxa-2,11-diazapentadecan-15-oic acid (4-4). Crude compound **4-3**, derived from the *t*-Boc deprotection of compound **4-2** (38.28 mg, 110 µmol, 1.1 eq), was coupled with TCO-NHS ester (26.73 mg, 100 µmol, 1 eq) in the presence of DIPEA (0.2 mL) and DMF (1 mL). The reaction was allowed to proceed at room temperature overnight. Milli-Q water (15 mL) was then added to the mixture. The solution was basified with triethylamine (TEA) and extracted twice with EtOAc. The aqueous fraction was acidified with 6% acetic acid (to pH 3-4) and extracted three times with DCM. The collected DCM fraction was dried over anhydrous Na_2SO_4, filtered, and evaporated to dryness. The crude product was further purified using automated flash column chromatography (gradient MeOH:DCM from 2:98 to 10:90, 25 CV), yielding compound **4-4** (25.2 mg, 63 µmol) with a yield of 63%.

^{1}H NMR (400 MHz, MeOD-d_4) δ 5.60 (ddd, *J* = 15.2, 9.1, 5.2 Hz, 1H), 5.48 (ddd, *J* = 15.7, 10.7, 3.5 Hz, 1H), 4.37-4.25 (m, 1H), 3.61 (s, 4H), 3.57-3.48 (m, 4H), 3.36 (t, *J* = 5.5 Hz, 2H), 3.26 (t, *J* = 5.7 Hz, 2H), 2.59 (t, *J* = 7 Hz, 2H), 2.48 (t, *J* = 6.9 Hz, 2H), 2.39-2.25 (m, 3H), 2.02-1.86 (m, 4H), 1.79-1.65 (m, 2H), 1.63-1.55 (m, 1 H).

^{13}C NMR (101 MHz, MeOD-d_4) δ 176.17, 174.74, 158.63, 135.98, 133.80, 81.79, 71.30, 71.28, 71.04, 70.59, 42.19, 41.55, 40.40, 39.64, 35.19, 33.48, 32.12, 31.53, 30.29.
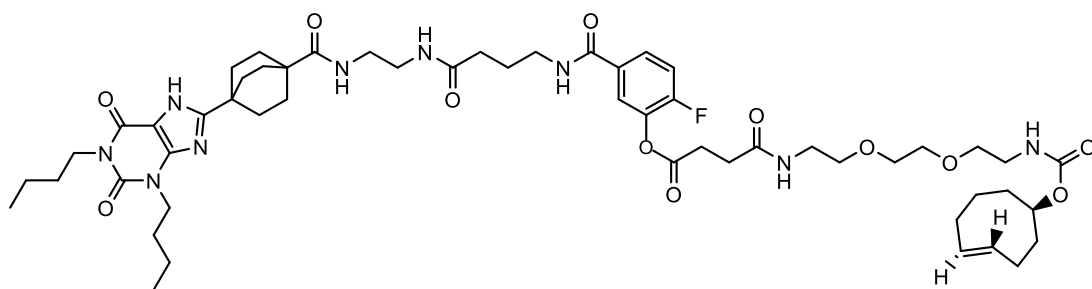
5-((4-((2-(4-(1,3-Dibutyl-2,6-dioxo-2,3,6,7-tetrahydro-1*H*-purin-8-yl)bicyclo[2.2.2]octane-1-carboxamido)ethyl)amino)-4-oxobutyl)carbamoyl)-2-fluorophenyl (*R*,*E*)-1-(cyclooct-4-en-1-yloxy)-1,12-dioxo-5,8-dioxa-2,11-diazapentadecan-15-oate (4-5). Compound **3-20** (1.71 mg, 2.51 µmol, 1.07 eq) and compound **4-4** (0.94 mg, 2.35 µmol, 1 eq) were reacted following the conditions described in **Section 2.2.7 General Procedure B**. The crude product was purified using RP-HPLC with a semipreparative YMC-

Pack C8 column (150 mm × 10 mm × 5 µm). The collected fraction was concentrated and lyophilised to give a white fluffy solid, compound **4-5** (1.24 mg, 1.16 µmol) with a yield of 49%.

^{1}H NMR (400 MHz, CDCl$_3$-d_3) δ 11.26 (s, 1H), 8.07 (s, 1H), 7.76-7.70 (m, 1H), 7.67 (d, J = 7.1 Hz, 1H), 7.31 (s, 1H), 7.21 (t, J = 9.0 Hz, 1H), 6.89 (s, 1H), 6.67 (s, 1H), 6.46 (s, 1H), 5.60-5.51 (m, 1H), 5.51-5.42 (m, 1H), 5.14 (s, 1H), 4.33 (s, 1H), 4.09 (t, J = 7.4 Hz, 2H), 4.00 (t, J = 7.6 Hz, 2H), 3.71-3.15 (m, 18H), 2.97 (s, 2H), 2.67 (t, J = 6.6 Hz, 2H), 2.41-2.25 (m, 5H), 1.92 (dd, J = 10.8, 4.9 Hz, 13H), 1.86-1.52 (m, 17H), 1.45-1.29 (m, 5H), 0.96 (t, J = 7.32 Hz, 3Hz), 0.93 (t, J = 7.32 Hz, 3H).

^{13}C NMR (101 MHz, CDCl$_3$-d_3) δ 178.70, 174.21, 170.93, 168.61, 166.21, 163.16, 156.43 (d, J = 213.5 Hz), 151.33, 148.74, 138.14, 135.05, 133.11, 126.47, 123.36, 116.98 (d, J = 20.2 Hz), 106.83, 77.36, 43.52, 41.29, 39.94, 39.02, 38.81, 34.41, 34.06, 33.72, 32.67, 31.11, 30.36, 30.29, 30.04, 29.28, 28.41, 25.22, 20.40, 20.07, 14.01, 13.92.

HRMS (TOF ESI, positive) calcd. for $C_{54}H_{78}FN_9O_{12}$ [M+H]$^+$: 1064.582674; found 1064.5834, error within 2.4 ppm, **Section 2.2.4**.

+MS, 0.7-0.9min #41-52

+MS, 0.7-0.9min #41-52

Intens. x10^4

1+ 1064.5834

2128.6609

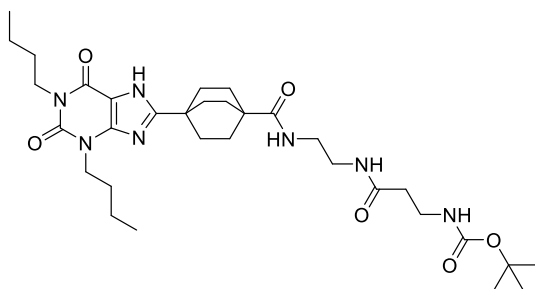| #	m/z	I %
1	532.7953	4.3
2	533.2962	3.0
3	551.7684	2.9
4	552.2695	2.0
5	559.7555	2.1
6	1064.5834	100.0
7	1065.5843	64.5
8	1066.5888	21.4
9	1067.5829	6.0
10	1083.5524	2.0
11	1084.0547	2.5
12	1086.5583	9.3
13	1087.5588	6.0
14	1088.5694	2.2
15	1091.5481	2.0
16	1092.0437	2.4
17	2127.6705	3.7
18	2128.6609	6.8
19	2129.6364	4.8
20	2130.6322	2.0

Generate Molecular Formula Parameters

Charge	Tolerance	sigma limit	H/C Ratio	Electron Conf.	Nitrogen Rule	Chrom.BackGround	Calibration
+1	6 ppm	0.08	3 - 0	both	false	false	TRUE

Expected Formula C54 H78 F1 N9 O12   **Adduct(s):** H, Na, NH4, C3H5N2, radical

#	meas. m/z	theo. m/z	|Err|[ppm]	Sigma	Formula	Adduct	Adduct Mass
1	1 064.5834	1 064.5827	0.70	0.0089	C54H79FN9O12	M+H	1.0078
1	1 086.5583	1 086.5646	5.90	0.0127	C54H78FN9NaO12	M+Na	22.9898

Note: Sigma fits < 0.05 indicates high probability of correct MF

Purity: 97.67%, measured by RP-HPLC with a YMC-Pack C8 analytic column (150 mm × 4.6 mm × 5 μm) mentioned in **Section 2.2.2**.


	Name	Retention Time (min)	Purity1 Angle	Purity1 Threshold	PDA Match1 Spect. Name	PDA Match1 Angle	PDA Match1 Threshold	PDA Match1 Lib. Name	Area (μV*sec)	% Area	Height (μV)	Int Type	Amount	Units	Peak Type	Peak
1		19.476							20498735	97.67	2557791	bb			Unknown	
2		19.813							488027	2.33	84356	bb			Unknown	
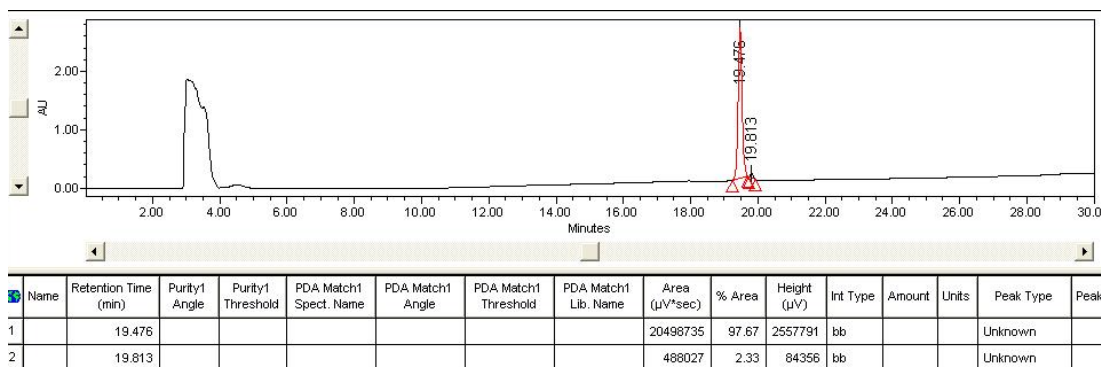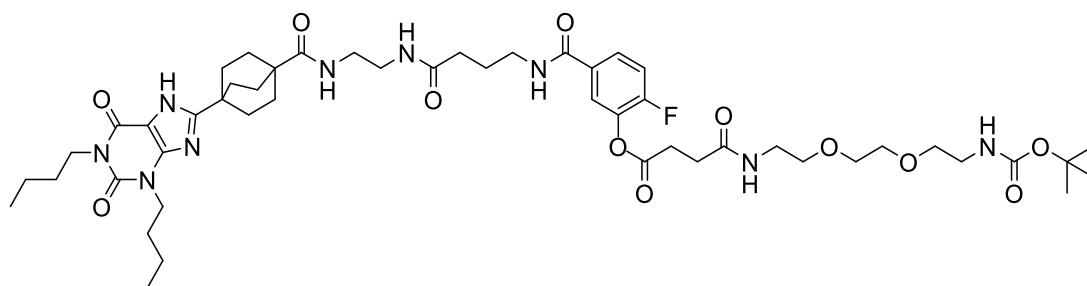
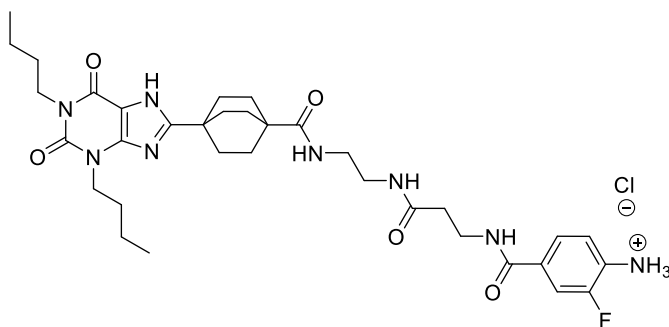**5-((4-((2-(4-(1,3-Dibutyl-2,6-dioxo-2,3,6,7-tetrahydro-1*H*-purin-8-yl)bicyclo[2.2.2]octane-1-carboxamido)ethyl)amino)-4-oxobutyl)carbamoyl)-2-fluorophenyl 2,2-dimethyl-4,15-dioxo-3,8,11-trioxa-5,14-diazaoctadecan-18-oate (5-1).** Compound **3-20** (10 mg, 14.7 µmol, 1 eq) and compound **4-2** (5.12 mg, 14.7 µmol, 1 eq) were reacted following the conditions described in **Section 2.2.7 General Procedure B**. The crude product was purified using RP-HPLC with a Phenomenex Onyx™ Monolithic semipreparative C18 column (CH0-7878, 100 mm × 10 mm). The collected fraction was concentrated and lyophilised to yield a white fluffy solid (5.6 mg, 5.5 µmol) with a yield of 37%.

LC-MS *m/z* calcd. for $C_{50}H_{74}FN_9O_{12}$ [M-H$^+$] 1012.55; found 1012.5, t_R = 6.75 min, **Section 2.2.4 Method B**.

^{1}H NMR (400 MHz, Acetone-*d*$_6$) δ 8.16 (t, *J* = 5.8 Hz, 1H), 7.86 (ddd, *J* = 8.4, 4.5, 2.1 Hz, 1H), 7.79 (dd, *J* = 7.4, 2.3 Hz, 1H), 7.44 (s, 1H), 7.35 (t, *J* = 9.2 Hz, 2H), 7.18 (s, 1H), 5.92 (s, 1H), 4.06 (t, *J* = 7.2 Hz, 2H), 3.93 (t, *J* = 7.4 Hz, 2H), 3.55 (s, 4H), 3.52 (t, *J* = 5.6 Hz, 2H), 3.48 (t, *J* = 5.8 Hz, 2H), 3.44 (q, *J* = 6.4 Hz, 2H), 3.38 (q, *J* = 5.6 Hz, 2H), 3.30 (s, 4H), 3.21 (q, *J* = 5.8 Hz, 2H), 2.93 (t, *J* = 6.7 Hz, 2 H), 2.66 (t, *J* = 6.7 Hz, 2H), 2.28 (t, *J* = 6.9 Hz, 2H), 2.02-1.86 (m, 14H), 1.72 (p, *J* = 7.4 Hz, 2H), 1.57 (p, *J* = 7.4 Hz, 2H), 1.40 (s, 9H), 1.33 (dt, *J*=15.3, 7.4 Hz, 4H), 0.95 (t, *J* = 7.72 Hz, 3H), 0.92 (t, *J* = 7.0 Hz, 3H).

^{13}C NMR (101 MHz, Acetone-*d*$_6$) δ 177.86, 173.86, 171.71, 171.21, 165.85, 161.12, 155.05, 151.89, 148.87, 139.03, 131.56 (d, *J*=287.6Hz), 127.18 (d, *J*=8.1 Hz), 124.47, 118.81, 117.20 (d, *J*=19.3 Hz), 107.50, 87.94, 79.16, 70.95, 70.87, 70.64, 70.44, 43.43, 41.28, 41.07, 40.76, 40.11, 40.10, 40.06, 39.50, 34.52, 34.07, 30.98, 30.93, 30.84, 30.79, 29.01, 28.64, 26.22, 20.80, 20.48, 14.16, 14.07.
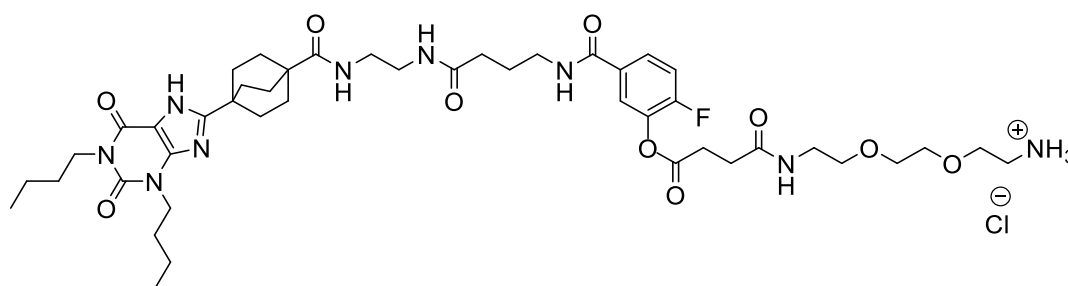
5-((4-((2-(4-(1,3-Dibutyl-2,6-dioxo-2,3,6,7-tetrahydro-1*H*-purin-8-yl)bicyclo[2.2.2]octane-1-carboxamido)ethyl)amino)-4-oxobutyl)carbamoyl)-2-fluorophenyl   **4-((2-(2-(2-aminoethoxy)ethoxy)ethyl)amino)-4-oxobutanoate hydrochloride salt (5-2).**
Compound **5-1** (2.24 mg, 2 µmol) was subjected to the reaction described in **Section 2.2.7 General Procedure C** for *t*-Boc deprotection**.** The reaction progress was monitored by LC-MS. Upon removal of the *t*-Boc group, the mixture was evaporated to yield the crude compound **5-2**, which was used in the next step without further purification.
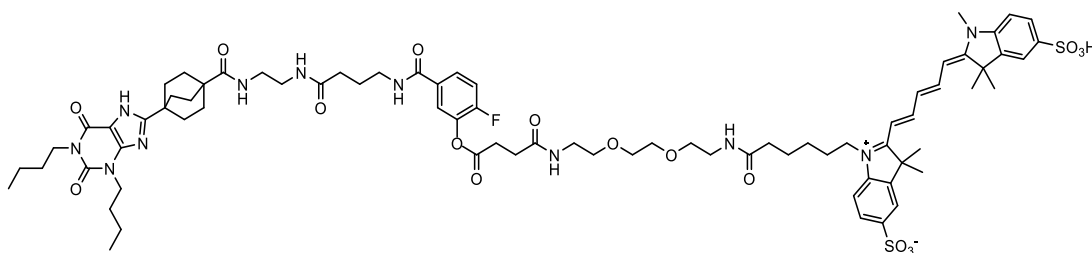
1-(1-(5-((4-((2-(4-(1,3-Dibutyl-2,6-dioxo-2,3,6,7-tetrahydro-1*H*-purin-8-yl)bicyclo[2.2.2]octane-1-carboxamido)ethyl)amino)-4-oxobutyl)carbamoyl)-2-fluorophenoxy)-1,4,15-trioxo-8,11-dioxa-5,14-diazaicosan-20-yl)-3,3-dimethyl-2-((1*E*,3*E*)-5-((*E*)-1,3,3-trimethyl-5-sulfoindolin-2-ylidene)penta-1,3-dien-1-yl)-3*H*-indol-1-ium-5-sulfonate (5-3).
Crude compound **5-2**, obtained from the *t*-Boc deprotection of compound **5-1** (2.24 mg, 2 µmol, 1 eq), was coupled with SulfoCy5 NHS ester (1.62 mg, 2.08 µmol, 1.04 eq) in the presence of 5 drops of DIPEA in DMF at room temperature for 1 hour. DMF was removed *via* high-vacuum rotary evaporation. The crude product was reconstituted with Milli-Q water (0.8 mL) and MeCN (0.6 mL). The mixture was then purified using RP-HPLC with a Phenomenex Onyx™ Monolithic semipreparative C18 column (CH0-7878, 100 mm × 10 mm). The collected fraction was concentrated and lyophilised to give a blue fluffy solid, compound **5-3** (1.34 mg, 0.87 µmol) with a yield of 43%.

HRMS (TOF ESI, negative) calcd. for $C_{77}H_{102}FN_{11}O_{17}S_2$ [M]$^-$: 1535.688609; found 1535.6881, error within 2.4 ppm, **Section 2.2.4**.

Mass Spectrometry
Analytical Services
School of Chemistry

The University of Nottingham

Sample-ID	paxcl4_CYL-30_150724	Lab	C13
Submitter	Chia-Yang Lin (paxcl4)	Supervisor	Barrie Kellam (pazbk)
Analysis Name	paxcl4_CYL-30_150724_670308_8_01_14 7959.d	Acquisition Date	7/15/2024 2:46:40 PM
onisation Mode	ESI Negative	Instrument	Bruker MicroTOF

MS, 0.7-0.9min #31-37

Expected ions not found!

-MS, 0.7-0.9min #31-37
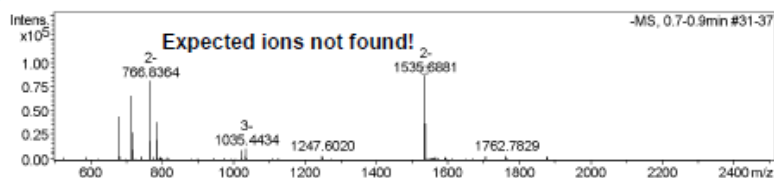
#	m/z	I %
1	680.3595	50.7
2	681.3622	20.9
3	716.3357	75.8
4	717.3391	31.2
5	718.3353	30.0
6	766.8364	94.0
7	767.3386	82.4
8	767.8390	49.4
9	768.3392	21.4
10	784.8253	44.1
11	785.3273	38.5
12	785.8268	36.0
13	786.3263	22.4
14	1035.4434	12.0
15	1534.6951	45.8
16	1535.2211	51.4
17	1535.6881	100.0
18	1536.1753	46.0
19	1536.6891	42.3
20	1537.1794	11.8

Generate Molecular Formula Parameters

Charge	Tolerance	sigma limit	H/C Ratio	Electron Conf.	Nitrogen Rule	Chrom.BackGround	Calibration
-1	6 ppm	0.08	3 - 0	both	false	false	TRUE

Expected Formula   C77 H102 F1 N11 O17 S2   **Adduct(s):**   H, radical

Purity: **> 99%,** measured by RP-HPLC with a Phenomenex Onyx™ Monolithic analytic C18 column (CH0-7643, 100 mm × 4.6 mm) mentioned in **Section 2.2.2**.
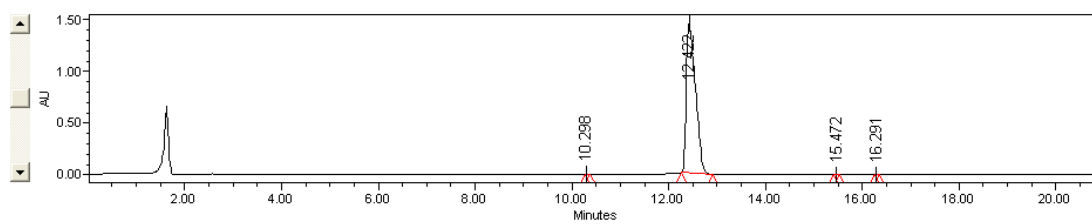
	Name	Retention Time (min)	Purity1 Angle	Purity1 Threshold	PDA Match1 Spect. Name	PDA Match1 Angle	PDA Match1 Threshold	PDA Match1 Lib. Name	Area (µV*sec)	% Area	Height (µV)	Int Type	Amount	Units	Peak Type
1		10.298							7535	0.04	1302	bb			Unknown
2		12.422							19046749	99.94	1465727	bb			Unknown
3		15.472							2178	0.01	516	bb			Unknown
4		16.291							2049	0.01	542	bb			Unknown
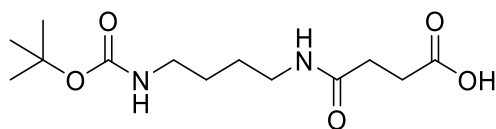
4-((4-((*tert*-Butoxycarbonyl)amino)butyl)amino)-4-oxobutanoic acid (5-5). Commercially available *tert*-butyl (4-aminobutyl)carbamate (**5-4**, 124.1 mg, 0.66 mmol, 1.2 eq) was dissolved in $CHCl_3$ (7 mL) and cooled to 0°C in an ice bath. Succinic anhydride (55 mg, 0.55 mmol, 1 eq) and DIPEA (52 µL, 0.3 mmol) were added to the cooled solution of **5-4**, and the mixture was allowed to stir for 10 minutes. The ice bath was then removed, and the reaction was continued for 1 hour. $CHCl_3$ was evaporated under reduced pressure, and the crude product was dissolved in EtOAc, followed by extraction with saturated $NaHCO_3$ solution three times. The aqueous layer was collected and acidified with 2 N HCl solution (pH 4-5). The aqueous solution was extracted three times with EtOAc. The organic fraction was collected, dried over anhydrous Na_2SO_4, filtered, and evaporated to give compound **5-5** as a white solid (116.3 mg, 0.4 mmol) with a yield of 73%.

¹H NMR (400 MHz, DMSO-*d₆*) δ 12.24 (s, 1H), 7.80 (t, *J* = 5.6 Hz, 1H), 6.78 (s, *J* = 5.7 Hz, 1H), 3.00 (q, *J* = 5.8 Hz, 2H), 2.88 (q, *J* = 6.3 Hz, 2H), 2.40 (t, *J* = 7.0 Hz, 2H), 2.28 (t, *J* = 7.0 Hz, 2H), 1.37 (s, 9H), 1.35-1.31 (m, 4H).

¹³C NMR (101 MHz, DMSO-*d₆*) δ 173.87, 170.71, 155.59, 77.34, 38.27, 30.01, 29.20, 28.29, 26.97, 26.54
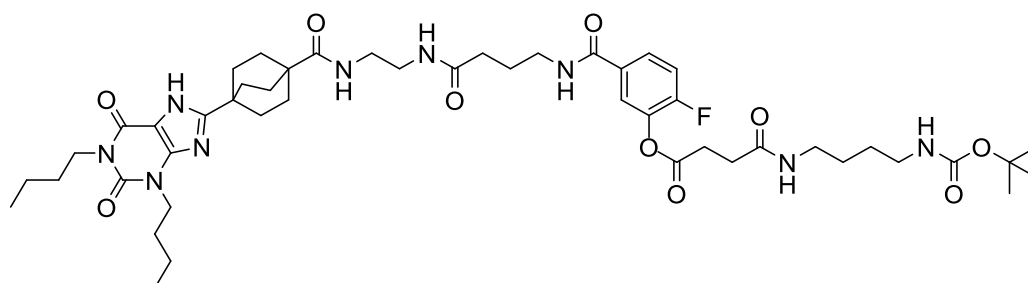
5-((4-((2-(4-(1,3-Dibutyl-2,6-dioxo-2,3,6,7-tetrahydro-1*H*-purin-8-yl)bicyclo[2.2.2]octane-1-carboxamido)ethyl)amino)-4-oxobutyl)carbamoyl)-2-fluorophenyl 4-((4-((*tert*-butoxycarbonyl)amino)butyl)amino)-4-oxobutanoate (5-6). Compound **3-20** (10 mg, 14.7 µmol, 1 eq) and compound **5-5** (4.44 mg, 15.4 µmol, 1.05 eq) were reacted following the conditions described in **Section 2.2.7 General Procedure B**. The crude product was purified using RP-HPLC with a Phenomenex Onyx™ Monolithic semipreparative C18 column (CH0-7878, 100 mm × 10 mm). The collected fraction was concentrated and lyophilised to give a white fluffy solid, compound **5-6**, (7.78 mg, 8.17 µmol) with a yield of 56%.

LC-MS *m/z* calcd. for $C_{48}H_{70}FN_9O_{10}$ [M-H⁺] 952.53; found 952.5, t_R = 6.99 min, **Section 2.2.2 Method B**.

¹H NMR (400 MHz, Acetone-*d₆*) δ 11.89 (s, 1H), 8.16 (t, *J* = 5.7 Hz, 1H), 7.86 (ddt, *J* = 8.5, 4.3, 1.8 Hz, 1H), 7.79 (dt, *J* = 7.7, 1.9 Hz, 1H), 7.45 (s, 1H), 7.39-7.24 (m, 2H), 7.19 (s, 1H), 5.96 (s, 1H), 4.06 (t, *J* = 7.2 Hz, 2H), 3.93 (t, *J* = 7.4 Hz, 2H), 3.44 (q, *J* = 6.3 Hz, 2H), 3.31 (d, *J* = 3.8 Hz, 4H), 3.24 (q, *J* = 6.2 Hz, 2H), 3.06 (q, *J* = 6.2 Hz, 2H), 2.92 (t, *J* = 6.7 Hz, 2H), 2.64 (t, *J* = 6.7 Hz, 2H), 2.29 (t, *J* = 6.8 Hz, 2H), 2.03-1.98 (m, 6H), 1.95-1.84 (m, 8H), 1.77-1.67 (m, 2H), 1.62-1.53 (m, 2H), 1.51 (s, 4H), 1.36 (m, 13 Hz), 0.95 (t, *J* = 9.2 Hz, 3H), 0.92 (t, *J* = 7.6 Hz, 3H).

¹³C NMR (101 MHz, Acetone-*d₆*) δ 177.87, 173.86, 171.53, 171.23, 165.87, 161.12, 158.87, 158.03, 155.89 (d, J = 169.5 Hz), 155.53, 151.89, 148.86, 138.98 (d, *J* = 13.0 Hz), 132.99, 127.14 (d, *J* = 8.1 Hz), 124.5, 117.2 (d, *J* = 19.5 Hz), 78.34, 43.43, 41.28, 40.77, 40.14, 40.11, 39.73, 39.50, 34.52, 34.09, 30.98, 30.93, 30.87, 30.85, 30.59, 30.47, 29.03, 28.67, 28.24, 27.67, 26.24, 20.81, 20.29, 14.16, 14.07.
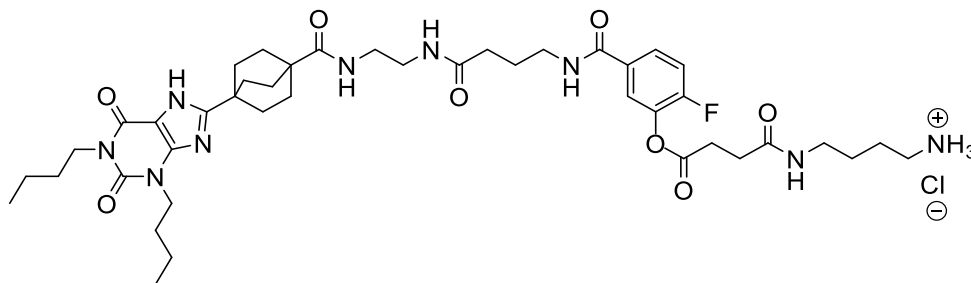
5-((4-((2-(4-(1,3-Dibutyl-2,6-dioxo-2,3,6,7-tetrahydro-1*H*-purin-8-yl)bicyclo[2.2.2]octane-1-carboxamido)ethyl)amino)-4-oxobutyl)carbamoyl)-2-fluorophenyl 4-((4-aminobutyl)amino)-4-oxobutanoate hydrochloride salt (5-7). Compound **5-6** (2.2 mg, 2.3 μmol) was synthesised using the conditions described in **Section 2.2.7 General Procedure C**. The reaction progress was monitored by LC-MS. Upon removal of the *t*-Boc group, the mixture was evaporated to yield the crude compound **5-7**, which was used in the next step without further purification.
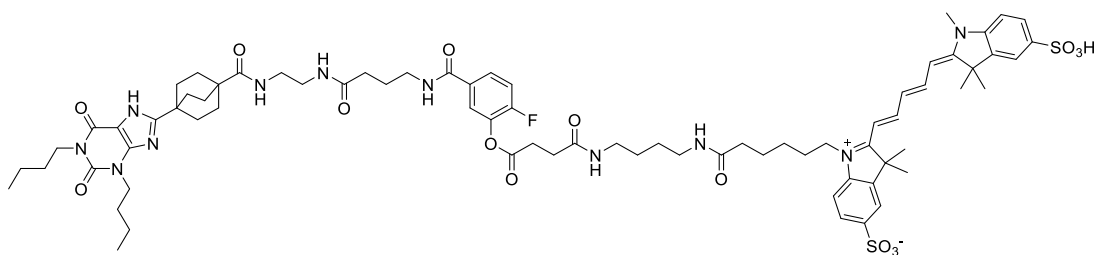
1-(6-((4-(4-(5-((4-((2-(4-(1,3-Dibutyl-2,6-dioxo-2,3,6,7-tetrahydro-1*H*-purin-8-yl)bicyclo[2.2.2]octane-1-carboxamido)ethyl)amino)-4-oxobutyl)carbamoyl)-2-fluorophenoxy)-4-oxobutanamido)butyl)amino)-6-oxohexyl)-3,3-dimethyl-2-((1*E*,3*E*)-5-((*E*)-1,3,3-trimethyl-5-sulfoindolin-2-ylidene)penta-1,3-dien-1-yl)-3*H*-indol-1-ium-5-sulfonate (5-8). Crude compound **5-7**, obtained from the *t*-Boc deprotection of compound **5-6** (2.2 mg, 2.3 μmol, 1 eq), was coupled with SulfoCy5 NHS ester (2 mg, 2.56 μmol, 1.1 eq) in the presence of 5 drops of DIPEA in DMF at room temperature for 1 hour. DMF was removed *via* high-vacuum rotary evaporation. The crude product was reconstituted with Milli-Q water (0.8 mL) and MeCN (0.6 mL). The mixture was then purified using RP-HPLC with a Phenomenex Onyx™ Monolithic semipreparative C18 column (CH0-7878, 100 mm × 10 mm). The collected fraction was concentrated and lyophilised to give a blue fluffy solid, compound **5-8,** (2.38 mg, 1.6 μmol) with a yield of 70%.

HRMS (TOF ESI, negative) calcd. for $C_{75}H_{98}FN_{11}O_{15}S_2$ [M]$^-$: 1475.66748; found 1475.6699, error within 2.4 ppm, **Section 2.2.4**.

Sample-ID	paxcl4_CYL-33_010724	Lab	C13
Submitter	Chia-Yang Lin (paxcl4)	Supervisor	Barrie Kellam (pazbk)
Analysis Name	paxcl4_CYL-33_010724_669817_19_01_1 47568.d	Acquisition Date	7/1/2024 3:00:13 PM
Ionisation Mode	ESI Negative	Instrument	Bruker MicroTOF

-MS, 0.7-0.9min #31-37

Expected ions not found!
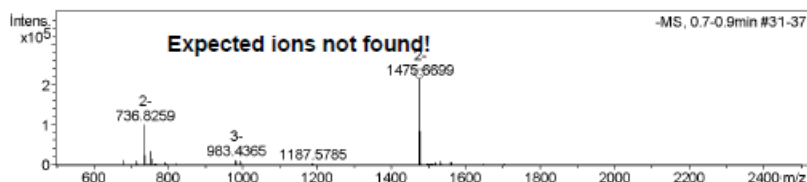
#	m/z	I %
1	680.3591	6.1
2	716.3349	5.6
3	736.8259	46.8
4	737.3270	42.7
5	737.8280	25.6
6	738.3290	11.3
7	754.8149	15.8
8	755.3164	13.6
9	755.8152	13.0
10	756.3154	7.8
11	983.1035	5.9
12	983.4365	6.3
13	983.7720	4.5
14	1474.6754	45.7
15	1475.1979	54.7
16	1475.6699	100.0
17	1476.1593	45.3
18	1476.6715	39.3
19	1477.1602	11.1
20	1477.6780	8.7

Generate Molecular Formula Parameters

Charge	Tolerance	sigma limit	H/C Ratio	Electron Conf.	Nitrogen Rule	Chrom.BackGround	Calibration
-1	6 ppm	0.08	3 - 0	both	false	false	TRUE

Expected Formula C75 H98 F1 N11 O15 S2   **Adduct(s):** H, radical

Purity: **> 99%,** measured by RP-HPLC with a Phenomenex Onyx™ Monolithic analytic C18 column (CH0-7643, 100 mm × 4.6 mm) mentioned in **Section 2.2.2**.
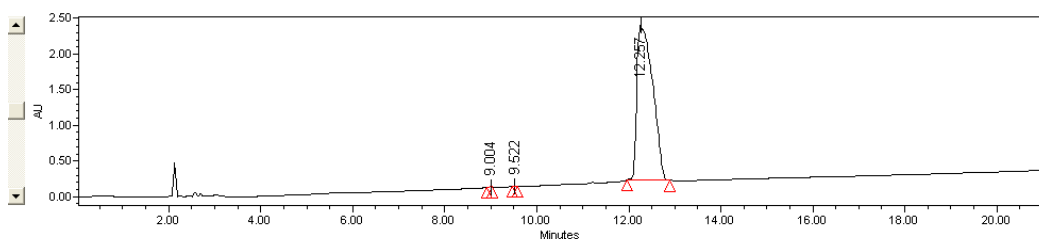
	Name	Retention Time (min)	Purity1 Angle	Purity1 Threshold	PDA Match1 Spect. Name	PDA Match1 Angle	PDA Match1 Threshold	PDA Match1 Lib. Name	Area (µV*sec)	% Area	Height (µV)	Int Type	Amount	Units	Peak Type	Peak Code
1		9.004							27134	0.05	6608	bb			Unknown	
2		9.522							22328	0.04	4858	bb			Unknown	
3		12.257							51589293	99.90	2166651	bb			Unknown	

Chapter 3. Optimisation, Synthesis, and Pharmacological Evaluation of a Novel Ligand-Directed Labelling Probe Targeting A$_1$ Adenosine Receptors

Brief Introduction

Reversible fluorescent ligands were first applied in life science related investigations as they offered direct visual observation of target proteins[117], alongside extended applications in combination with various techniques (e.g. BRET[55,119] and FRET[120]) and equipment (e.g. flow cytometry for cell sorting[121] and plate reader for high-throughput screening[70]). Most importantly, they are free from radioactivity. However, reversible fluorescent ligands are limited in prolonged biomolecule real time observations due to dissociation issues. Methods for covalently labelled biomolecules offer solutions to the prolonged observation demands. Covalent tagging a protein of interest (POI) can be done *via* fluorescent protein tags or self-labelling protein tags in conjunction with corresponding substrates[88,122]. These methods provide valuable ways to investigate POI but genetic interventions are inevitable and the sizes of protein tags are much larger than small molecules.

Tagging POI with small molecules through chemical reaction is a potential resolution for the demand for POIs covalently lablelled without genetic work[89,96]. Irreversible fluorescent ligands are comprised of a fluorophore, an orthostere for recognising and engaging the POI, and a moiety forming covalent link with the POI[123]. For example, Taliani *et al*. (2010) reported an NBD-tethering probe which irreversibly labelled the 18kDa translocator protein *via* an electrophilic isothiocyanato group[124]. The irreversible fluorescent labelling can be done *via* separate steps as well. For example, Beerkens *et al*. (2022) covalently labelled the A$_1$ AR with LUF7909 (see **Chapter 1**, **Figure 1-12**) through a sulfonyl fluoride moiety[112]. An azide attached reporter was then cyclised with the LUF7909 alkyne moiety through a copper catalysed click reaction[112]. However, the orthosteric binding pocket of the POI was blocked after this labelling approach, which limited follow-on functional assays with the tagged POI[88,96]. Alternative ligand-directed (LD) covalently labelling probes offered the covalent labelling outcome but did not interfere with the accessibility of the orthosteric binding pocket[113]. In theory, an ideal LD probe would specifically bind to the POI and transfer its cargo (fluorophore, biotin, or click reaction handle) onto the POI through a proximity driven reaction between the reactive linker moiety and a nucleophilic amino residue on the POI (**Figure 3-1**)[88,89,96]. LD probes provided covalent labelling

approaches without genetic work and kept ligand accessibility to the post labelled POI thereby enabling wider biomolecule investigation (e.g. trafficking[125] or response after agonist stimulation[74]).
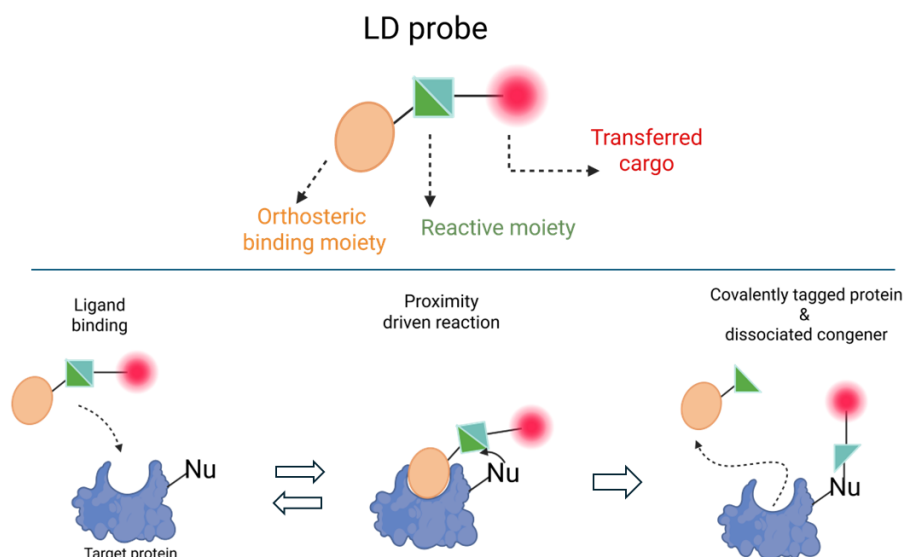
Figure 3-1. Ideal Ligand-Directed (LD) Covalent Labelling Probe.
An ideal LD probe requires specific binding to the target protein in a crowded, multi-component environment. After ligand binding to the target protein, a proximity-driven nucleophilic reaction occurs between the reactive moiety and a nucleophilic amino residue (Nu), transferring the cargo moiety onto the target protein. Finally, the remaining ligand part (congener) dissociates from the binding pocket, resulting in the covalently tagged target protein.

Aim of the project

To label a POI in live cells, the specificity of LD probes was paramount to avoid off-target labelling[88,96]. Comeo *et al*. (2024) developed LD probe (**1-56**) directly transferring sulfocyanine 5 (SulfoCy5) onto A_1 ARs[74]. Probe **1-56** exhibited nanomolar binding affinity towards A_1 ARs and was demonstrated to covalently label overexpressed A_1 ARs in transiently transfected HEK293T cells and endogenous A_1 ARs in dorsal root ganglion cells[74]. However, its selectivity between the A_1 and A_{2A} ARs was only six-fold, which raised a concern of off-target labelling especially in A_1/A_{2A} co-expressing systems[74]. The aim of the work embodied within this chapter was to improve **1-56** AR subtype selectivity profile through structure modification followed by a series of pharmacological investigation to characterise newly synthesised **1-56** analogues.

The orthostere in **1-56** was derived from **Tonopofylline** (**3-1**) and its analogue (**3-2**) (**Figure 3-2**)[72], both of which were A_1 AR-selective antagonists with nanomolar binding affinity for hA_1 AR[126] (

Table 3-*1*). The modification of the *N*-alkyl chain from *n*-propyl (in **3-1** and **3-2**) to *n*-butyl (in **1-56**) was guided by crystal structure data, which revealed that the A_1 AR possessed a deeper orthosteric binding pocket than the A_{2A} AR[127]. This modification aimed to enhance subtype selectivity for A_1 over A_{2A} ARs through *N*-alkyl chain elongation. However, the selectivity of **1-56** was found to be even lower than that of probe **3-1** (

Table 3-*1*).

Several studies have demonstrated that generating a fluorescent ligand by attaching a fluorophore to an orthosteric ligand can significantly alter the latter's binding affinity and receptor selectivity[60,92,128]. To maintain probe **1-56** high affinity for hA$_1$ AR, the orthosteric moiety remained unchanged to keep its protein ligand interactions with the orthosteric binding pocket. For confocal imaging quality, a fluorophore with high water solubility (to minimise membrane non-specific binding) and a red-shifted emission wavelength (to avoid cell autofluorescence) was preferred[72,129]. SulfoCy5 was preserved as the fluorescent moiety for its desirable water solubility and red-shifted emission properties[129]. Consequently, a fine-tuning on the linker region was an applicable option for optimising **1-56** AR subtype affinity.

3-1
Toponafylline

3-2
Toponafylline analogue

1-56
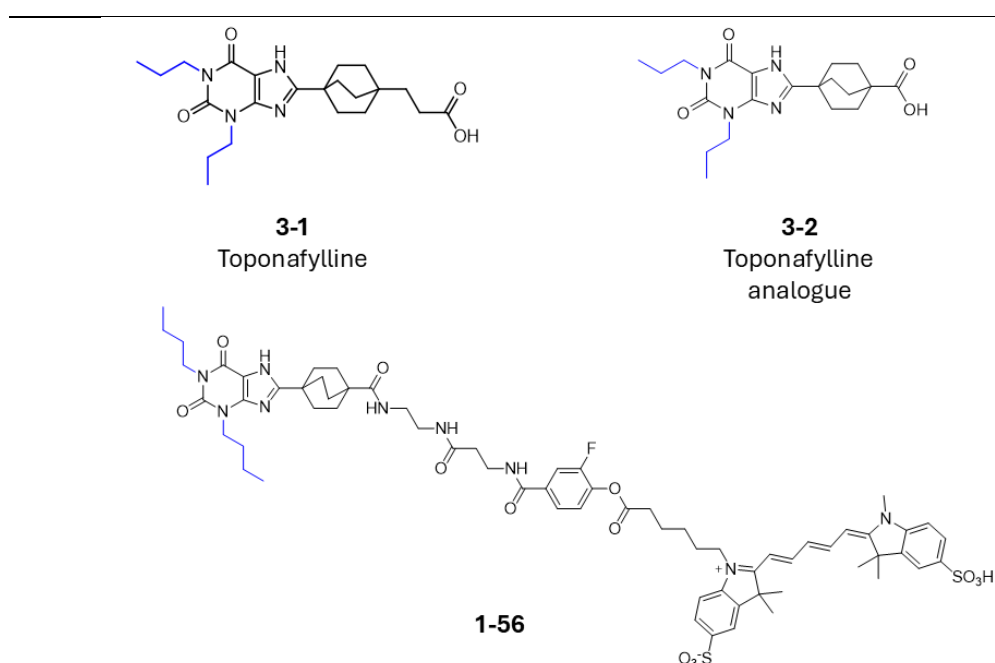
Figure 3-2. Structure of 1-56, toponafylline (3-1), and its analogue (3-2).
In **1-56**, the carboxylic acid of **3-2** was functionalised into an amide to facilitate linker attachment. Both **3-1** and **3-2** share n-propyl substituents on nitrogens, whereas **1-56** features n-butyl groups (highlighted in blue).

Table 3-1. Adenosine receptors subtype affinity and affinity ratio

Compound	K_d (nM), K_i (nM) or % of specific radioligand binding [a]				Ratio	
	hA_1	hA_{2A}	hA_{2B}	hA_3	hA_{2A}/A_1	hA_{2B}/A_1
3-1 [b]	7.4	6110	90	>1000	915	12
3-2 [b]	33	1070	48%	100%	32	-- [e]
1-56 [c]	45.5	267.9	> 250 [d]	> 250 [d]	5.89	> 5.5 [f]

a. **Radioligand Binding Percentage**[126,130]: Measured by incubating 1 μM of the tested compound with radioligand [A_{2B}: 0.5 nM ^{125}I-3-(4-aminobenzyl)-8-phenyloxyacetate-1-propyl-xanthine; A_3: 0.6 nM ^{125}I-aminobenzyladenosine (^{125}I-ABA)] compared to the corresponding vehicle set. High radioligand binding percentage indicated poor antagonist activity, while low radioligand binding percentage indicated effective displacement of the radioligand.

b. K_i **(nM) and Specific Radioligand Binding Percentages**: Values obtained from Kiesman *et al.* (2006)[126].

c. K_d **(nM)**: Represented the mean from five replicate saturation assays. Saturation binding assays were conducted using HEK293T cells stably expressing nanoluciferase (NLuc)-tagged A_1 at the *N*-terminus. HEK293G cells stably NLuc-tagged A_{2B}, and A_3 receptors at the *N*-terminus. A_{2A} ARs with *N*-terminal NLuc tags were transiently expressed in HEK293T cells.

d. **Binding Observations**: Total binding presented as a flat line parallel with nonspecific binding from 0 to 500 nM. Therefore, the K_d value was larger than 250 nM. Exact value was not determined as higher concentrations were not tested.

e. **Ratio Calculation**: Not possible due to differences in affinity measurement methods.

f. A_{2B}/A_1 **Selectivity:** As A_{2B} effective specific binding was not observed below 500 nM while A_{2A} was saturated below 500 nM, A_{2B}/A_1 selectivity was a minor issue compared to A_{2A}/A_1, even though the ratio in A_{2B}/A_1 was lower than A_{2A}/A_1.

3.1 Design of **1-56** Derivatives

As mentioned previously, modifications to the linker moiety (highlighted in green in **Figure 3-3**) were explored as the primary strategy for optimising **1-56**. First, β-alanine was replaced with either γ-aminobutyric acid (GABA) or glycine. Secondly, the substitution position of the 2-fluorophenyl ring was considered, leading to the design of a *meta*-2-fluorophenyl ester analogue. These two modifications resulted in four proposed analogues (**Figure 3-3**). Adjustments to the linker length by one carbon unit and altering the phenyl ring substitution position represent minor structural refinements that minimise interference with the pharmacophoric elements interacting with the A_1 AR orthosteric binding pocket. At the same time, these modifications may enhance subtype-selective labelling or improve tagging efficiency by altering the spatial positioning of the reactive moiety.
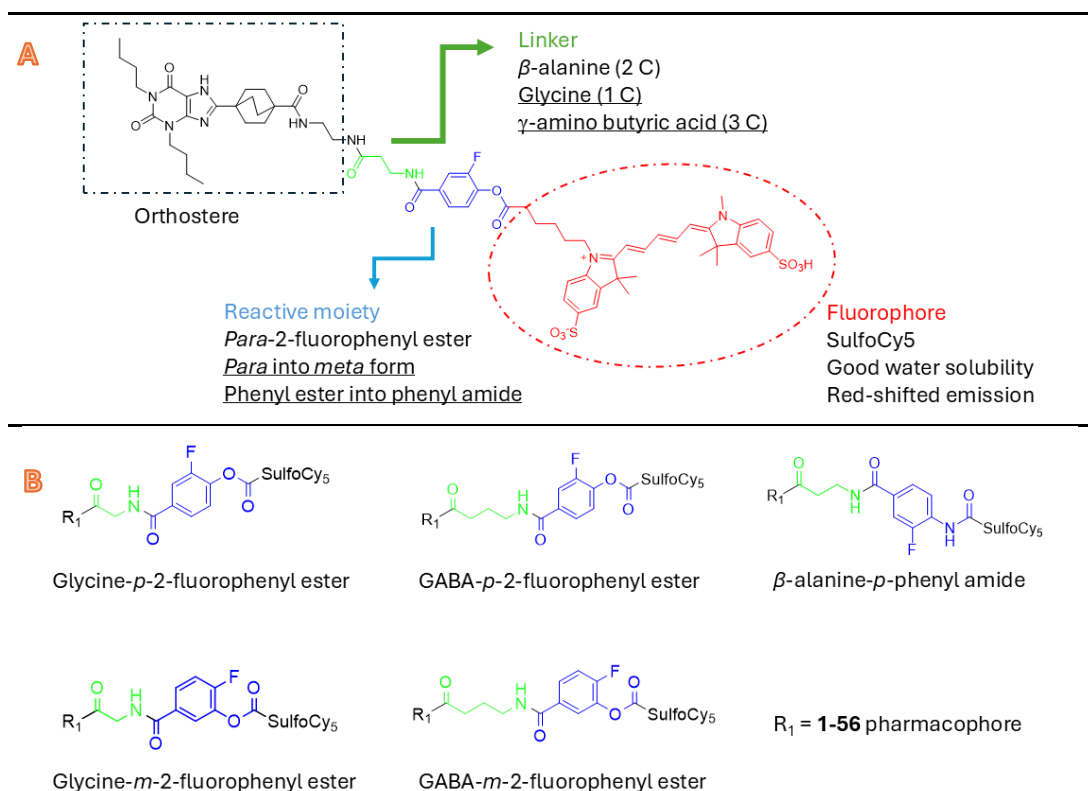
Figure 3-3. Structural Modification Plan.
(**A**) Structural modulation components in probe **1-56**. The black-dotted frame highlights the orthostere incorporated into **1-56**, serving as the warhead to target A_1 ARs. The linker, highlighted in green, is the primary tuning element, designed to be replaced with either glycine or GABA. The p-2-fluorophenyl ester in **1-56** (shown in blue) was modified into m-2-fluorophenyl ester in attempt to optimise A_1 AR selectivity and affinity. Additionally, a β-alanine-p-phenyl amide modification was considered to evaluate the critical role of the phenyl ester in cargo transfer. SulfoCy5, depicted in red, is a fluorophore with high water solubility and an emission wavelength that minimises interference from cellular autofluorescence. (**B**) Five analogues of **1-56** were designed based on the structural modifications outlined in (**A**).

3.2 Result and discussion

3.2.1 Chemistry

3.2.1.1Ligand docking simulation

Preliminary assessment was conducted using molecular docking simulations (experimental details are described in **Chapter 2, Section 2.2.5**). Initial docking experiments using the full LD fluorescent probes were unsuccessful due to their large size, which prevented them from fitting into the binding pocket. The basic Schrödinger Maestro docking settings compressed the entire molecule into the binding pocket. However, the LD fluorescent ligand was designed to extend the reactive moiety and fluorophore away from the binding pocket *via* the linker. Consequently, the reactive moiety had the opportunity to react with nucleophilic residues away from the binding pocket, minimising the possibility of the transferred fluorophore obstructing access to the binding pocket. Docking studies were subsequently performed using congeners of the LD fluorescent probes, where the interacting part engaged with the receptor binding pocket as an alternative approach (**Figure 3-4**). As shown in **Table 3-2**, congeners with a glycine linker exhibited docking scores (the predicted free energy of ligand-receptor complex) similar to **1-56** for both A_1 and A_{2A} ARs. In contrast, congeners incorporating GABA displayed significantly lower docking scores for A_{2A} ARs compared to A_1 ARs, suggesting improved selectivity for A_1 ARs. Given the potential impact of fluorophore attachment on binding affinity and selectivity, all four LD fluorescent probe analogues were advanced to the synthesis pipeline. Additionally, an analogue incorporating a phenyl amide in place of the phenyl ester was designed as a non-reactive ligand for comparison with LD probes.

Table 3-2. Congeners' docking score

Linker	X	Y	Docking score	
			A₁	A₂A
β-Alanine	OH	F	-11.747	-10.998
Glycine	OH	F	-9.314	-10.619
	F	OH	-11.204	-9.102
GABA	OH	F	-10.191	-4.972
	F	OH	-12.248	-7.187

The molecular docking simulations were performed using Schrodinger Maestro. PDB-5EUN was used as the A₁ AR model, and PDB-4EIY as the A₂A AR model. Before proceeding with ligand docking, congeners and receptors were processed using LigandPrep and ReceptorPrep. Congener binding positions were defined as DU172 in A₁ AR and ZM241385 in A₂A AR. The docking score represented the calculated free energy of the ligand-receptor complex, with a lower docking score indicating a more stable complex.

Conger with *p*-phenol (X=OH, Y=F)
with *m*-phenol (X=F, Y=OH)

A
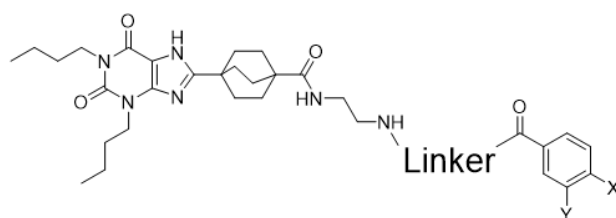
β-Alanine-Para-phenol
A₁ AR- 5EUN
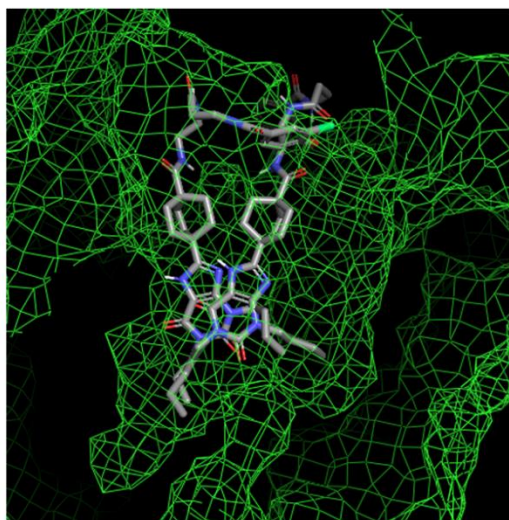
β-Alanine-Para-phenol
A₂A AR- 4EIY

B
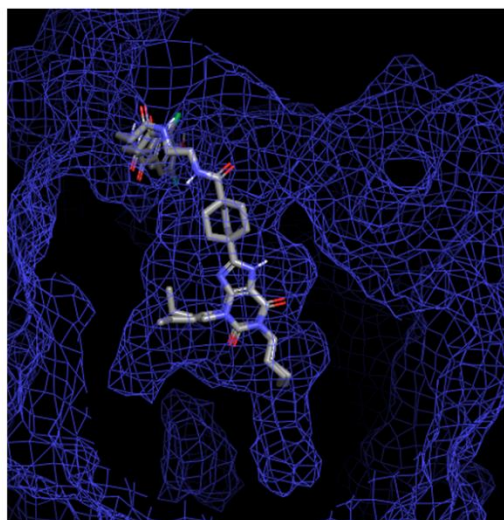
Glycine-Para-phenol
A$_1$ AR- 5EUN
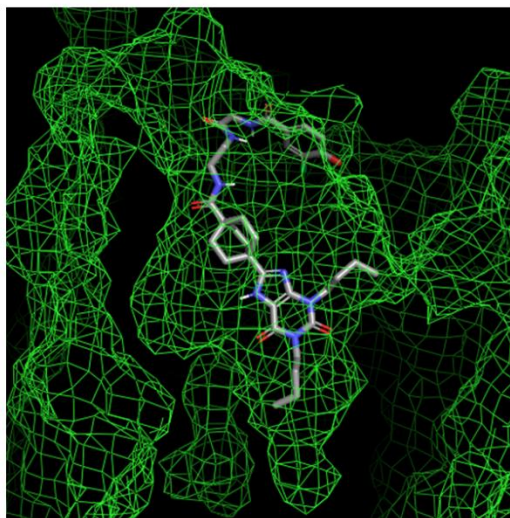
Glycine-Para-phenol
A$_{2A}$ AR- 4EIY

C
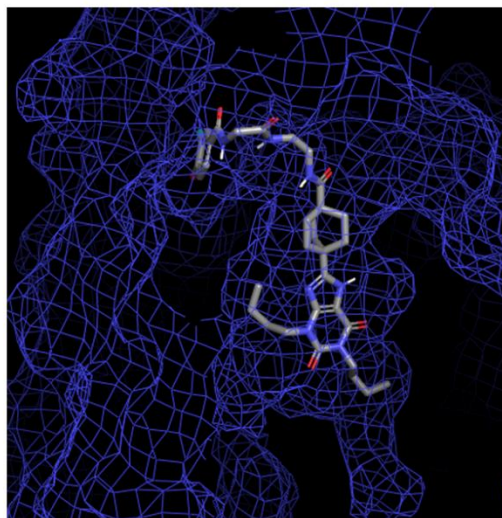
Glycine-Meta-phenol
A$_1$ AR- 5EUN
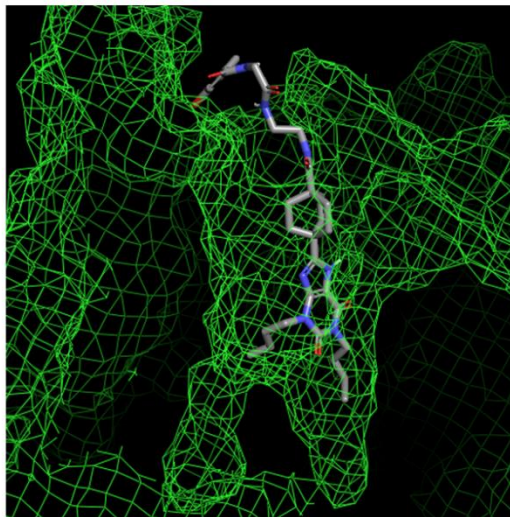
Glycine-Meta-phenol
A$_{2A}$ AR- 4EIY
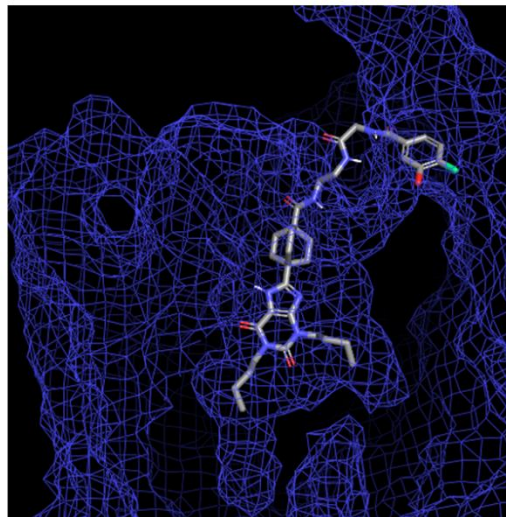
D

GABA-Para-phenol
A$_1$ AR- 5EUN
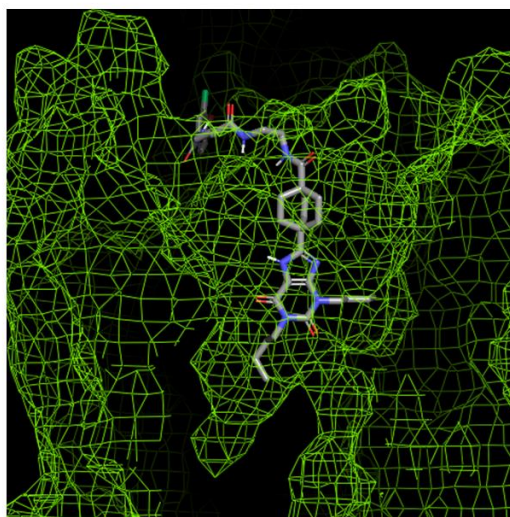
GABA-Para-phenol
A$_{2A}$ AR- 4EIY
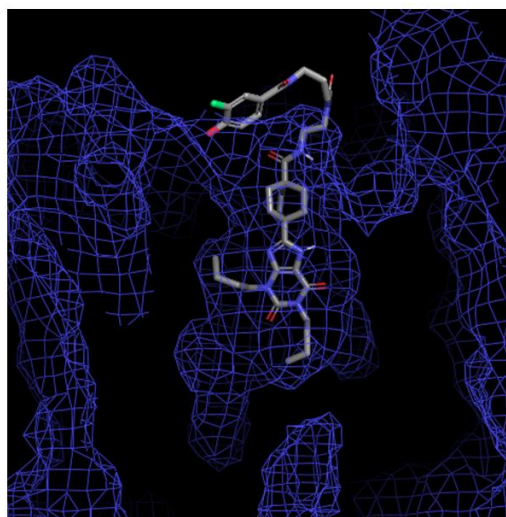
GABA-Meta-phenol
A₁ AR- 5EUN
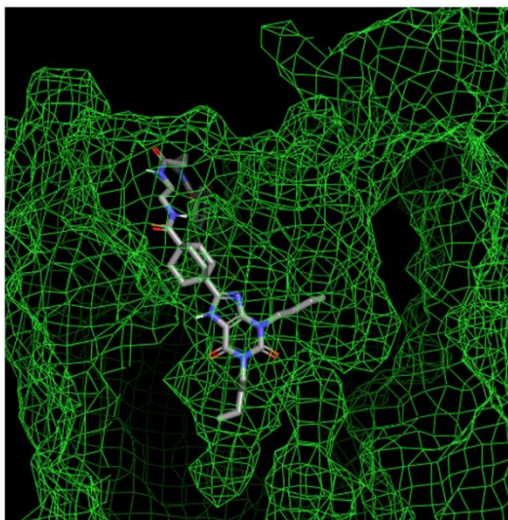
GABA-Meta-phenol
A₂A AR- 4EIY
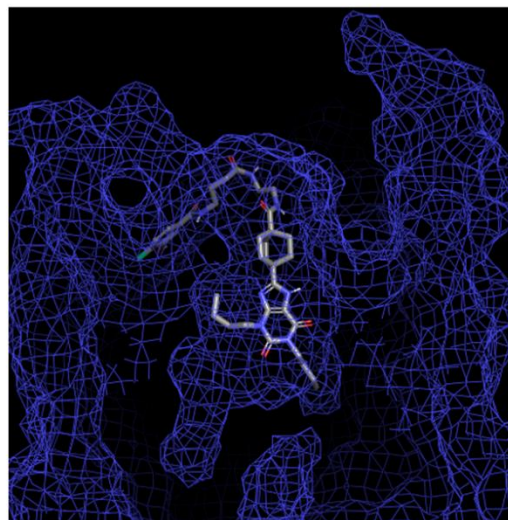
Figure 3-4. Docking Poses of Congeners in A₁ AR (green) and A₂A AR (blue). Docking simulations were performed using Schrödinger Glide, with PDB structures 5EUN and 4EIY representing the A₁ and A₂A ARs, respectively. Receptors are displayed in mesh style, while ligands are shown in stick representation. Images were rendered using PyMOL. All congeners share the same orthosteric binding moiety, with variations in linker structure and phenyl ring substitution position. Docking scores are summarised in **Table 3-2**.

- **Set A**: *β-Alanine-para-phenyl ester congener*. Both butyl chains extend into the deep binding pockets of A₁ and A₂A ARs without exhibiting unnatural torsion. This may explain why elongation of the alkyl side chain does not enhance subtype selectivity between A₁ and A₂A ARs for this congener.
- **Set B**: *Glycine-para-phenol congener*. One butyl chain projects into the pocket cave, while the other remains in the main binding region. Consequently, docking scores show no significant difference between A₁ and A₂A ARs.
- **Set C**: *Glycine-meta-phenol congener*. Both butyl chains extend into the deep binding pockets of A₁ and A₂A ARs, resulting in comparable docking scores.
- **Set D**: *GABA-para-phenol congener*. In A₁ AR, one butyl chain occupies the main pocket while the other extends into the deep cavity. In contrast, both chains fail to reach the deep pockets in A₂A AR, potentially accounting for the greater docking score disparity between the two receptors.
- **Set E**: *GABA-meta-phenol congener*. In A₁ AR, additional space accommodates both butyl chains, whereas in A₂A AR, the chains do not penetrate the deep binding pockets. This spatial allowance in A₁ AR may contribute to the increased stability of the receptor–congener complex compared to A₂A AR.

Scheme 3-1. Fluorescent ligands synthesis (glycine linker) [a]
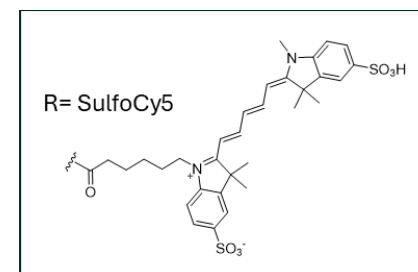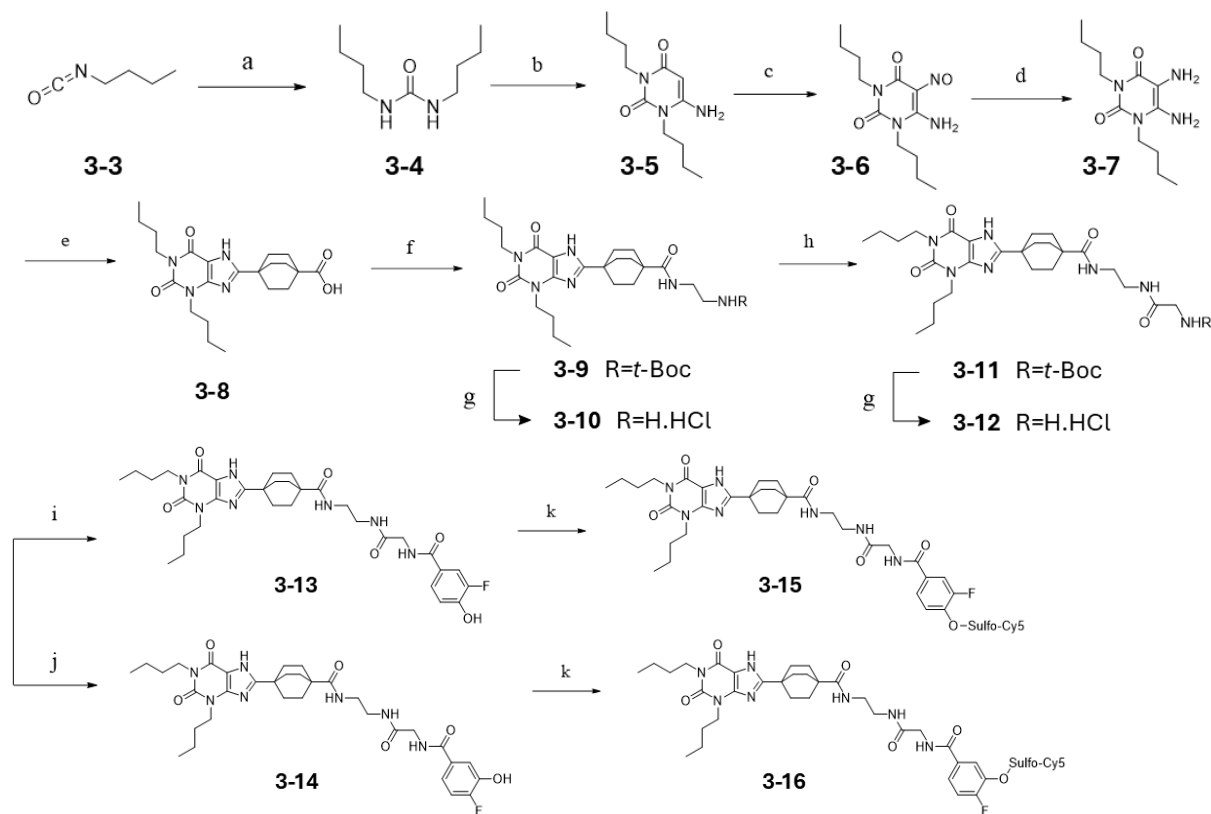
[a] Reagents and conditions: a) butylamine, THF, rt, 4 h, 97%; b) cyanoacetic acid, Ac_2O, 85°C, 2 hr, 86%; c) $NaNO_2$, 50% AcOH, 65°C, 1 hr, 75%; d) $Na_2S_2O_4$, 12.5% NH_4OH_{aq}, 80°C, 30 min, 95%; e) 1: COMU, DIPEA, 4-(methoxycarbonyl)bicyclo[2.2.2]octane-1-carboxylic acid, DMF, rt, 20 min; 2: 1M KOH, IPA, 91°C, 2hr, 70%; f) COMU, DIPEA, *tert*-butyl (2-aminoethyl)carbamate, DMF, rt, 20 min, 95%; g) 4 N HCl in dioxane, rt, 1 hr; h) Boc-glycine, COMU, DIPEA, DMF, 3 hr, 71%; i) 3-fluoro-4-hydroxybenzoic acid, COMU, DIPEA, DMF, 90°C, overnight, 47%; j) 4-fluoro-3-hydroxybenzoic acid, COMU, DIPEA, DMF, 90°C, overnight, 37%; k) Sulfo-Cy5 free acid, BEP, DIPEA, DMF, rt, avoid light, overnight, 46% (**3-15**), 59% (**3-16**).

Scheme 3-2. Fluorescent ligands synthesis (GABA linker) [a]

3-9 R=t-Boc
3-10 R=H.HCl

3-17 R=t-Boc
3-18 R=H.HCl

3-19

3-20

3-22

3-21
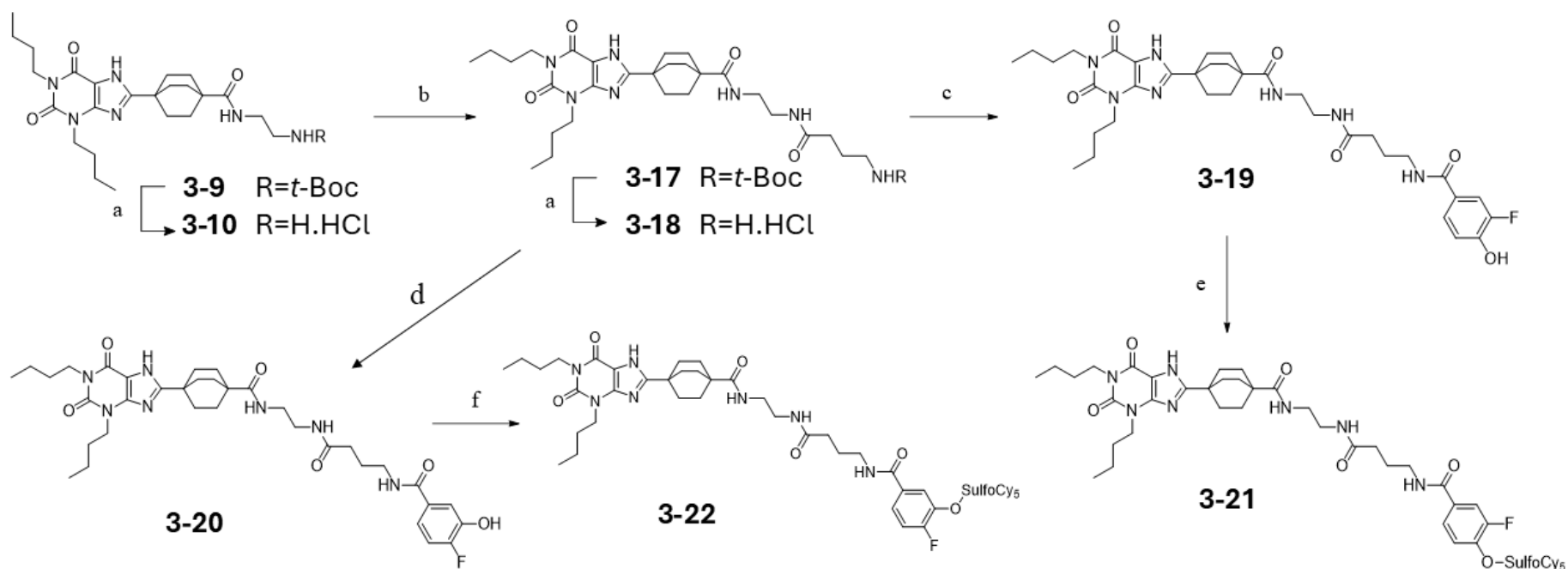
[a] Reagents and conditions: a) 4 N HCl in dioxane, rt, 1 hr; b) Boc-γ-aminobutyric acid, COMU, DIPEA, DMF, 2 hr, 78%; c) 3-fluoro-4-hydroxybenzoic acid, COMU, DIPEA, DMF, 90°C, overnight, 38%; d) 4-fluoro-3-hydroxybenzoic acid, COMU, DIPEA, DMF, 90°C, overnight, 49%; e) Sulfo-Cy5 free acid, BEP, DIPEA, DMF, rt, avoid light, overnight, 70%; f) Sulfo-Cy5 free acid, BEP, DIPEA, DMF, rt, avoid light, overnight, 62%.

Scheme 3-3. Analogues of 1-56 with 2-fluorophenyl amide
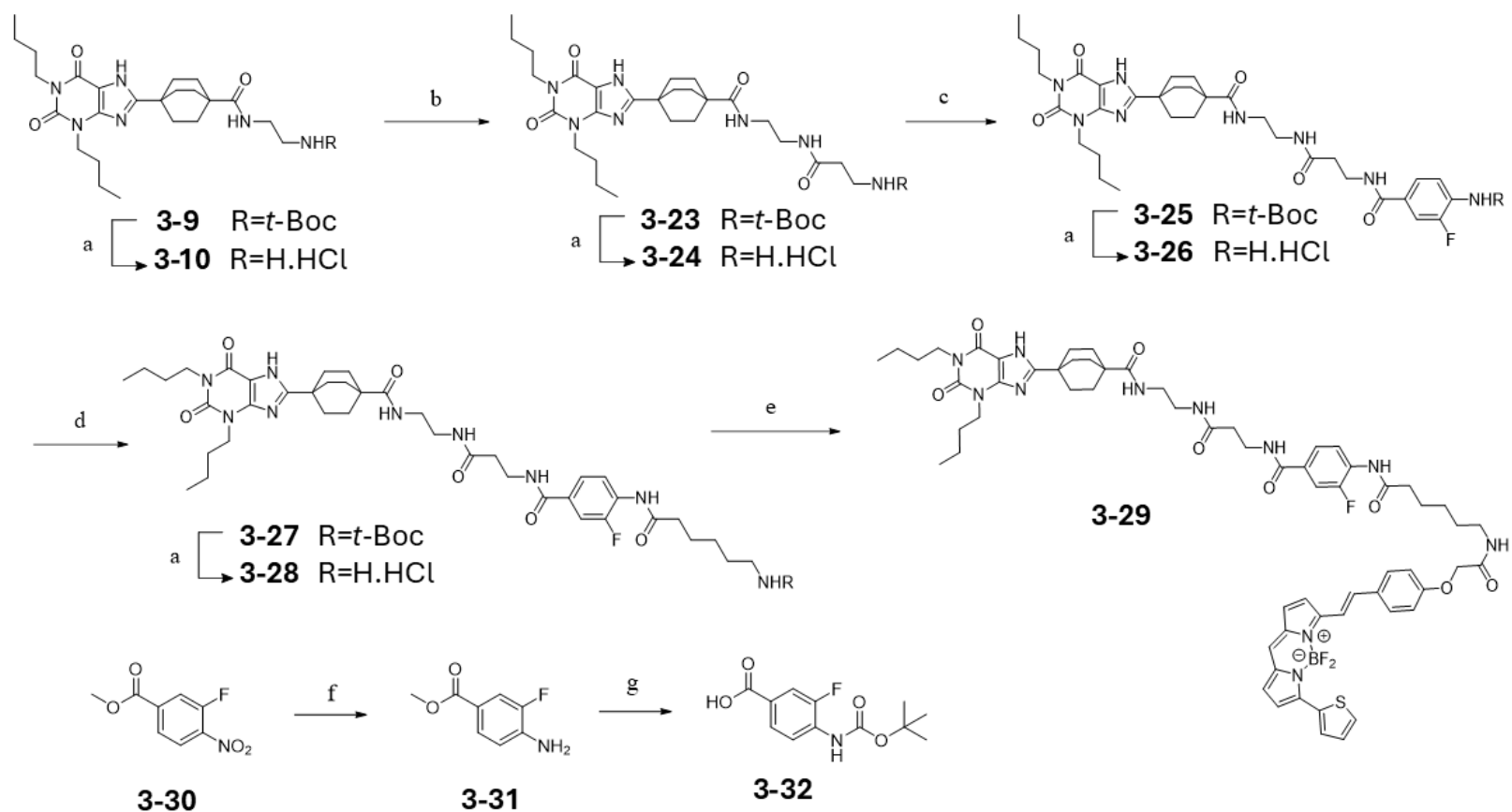
3-9 R=*t*-Boc
3-10 R=H.HCl

3-23 R=*t*-Boc
3-24 R=H.HCl

3-25 R=*t*-Boc
3-26 R=H.HCl

3-27 R=*t*-Boc
3-28 R=H.HCl

3-29

3-30

3-31

3-32

[a] Reagents and conditions: a) 4N HCl in dioxane, rt, 1 hr; b) *N*-Boc *β*-alanine, COMU, DIPEA, DMF, rt, 5 hr, 91%; c) 4-((*tert*-butoxycarbonyl)amino)-3-fluorobenzoic acid (**3-32**), COMU, DIPEA, DMF, 80°C, overnight, 71%; d) T3P, DIPEA, Boc-E-ACP-OH, DCM, 80°C, 19 hr, 5%; e) BODIPY630/650 carboxylic acid, BEP, DIPEA, rt, overnight, 35%; f) Pd/C, H₂, MeOH, rt, 1.5 hr, 78%; g) 1. DMAP, Boc₂O, THF, reflux, overnight; 2. K₂CO₃, MeOH, reflux, 3 hr; 3. 2M NaOH, MeOH/THF, rt, 5.5 hr, 64%

3.2.1.2 Synthesis

3.2.1.2.1 Analogues of 1-56 with 2-Fluorophenyl Ester Moiety

The synthesis of five **1-56** analogues is outlined in **Scheme 3-1**, **3-2**, and **3-3**. **Scheme 3-1** illustrates the synthesis of **1-56** analogues incorporating a glycine linker. All synthetic methods were adapted from Comeo *et al.* (2024)[74] with minor modifications (full experimental details are described in **Chapter 2**, **Section 2.2.8**).

The synthesis of **3-15** began with the nucleophilic addition of *n*-butylamine to commercially available butyl isocyanate (**3-3**), yielding symmetrical urea **3-4**. This reaction was conducted in THF at ambient temperature, and the product, 1,3-dibutylurea (**3-4**), was obtained by evaporating the reaction mixture after a 4-hour reaction. Subsequently, cyanoacetic acid was added to **3-4** in acetic anhydride (Ac$_2$O) at 85°C for 2 hours, producing pyrimidine-2,4-dione (**3-5**) in high yield. In this step, cyanoacetic acid was activated by Ac$_2$O, facilitating double nucleophilic addition of **3-4** to form the desired heterocycle. Excess Ac$_2$O was removed under reduced pressure, the remaining portion was hydrolysed with water. The aqueous solution was basified with 70% NaOH$_{(aq)}$, and crude **3-5** was purified by recrystallisation from ethanol-water.

To introduce an amine group at the C-5 position, **3-5** was nitrosylated with sodium nitrite to form **3-6**, followed by reduction with sodium dithionite to yield **3-7**. Compound **3-8** was obtained through a two-step process: activation of 4-(methoxycarbonyl)bicyclo[2.2.2]octane-1-carboxylic acid (bicyclic acid) with COMU and DIPEA in DMF, followed by coupling with **3-7**. Dehydrative cyclisation of the amide intermediate was performed using the mixture of 1M KOH$_{(aq)}$ and isopropanol (IPA) under reflux for 2 hours. The reaction mixture was cooled, IPA was evaporated, and the residue was acidified with HCl to precipitate xanthine carboxylic acid **3-8**.

Scheme 3-4. Synthesis flow of compound 3-4 to 3-8
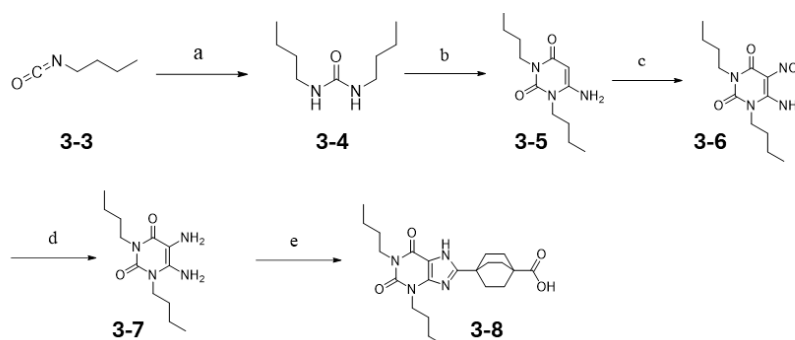
[a] Reagents and conditions: a) butylamine, THF, rt, 4 h, 97%; b) cyanoacetic acid, Ac$_2$O, 85°C, 2 hr, 86%; c) NaNO$_2$, 50% AcOH, 65°C, 1 hr, 75%; d) Na$_2$S$_2$O$_4$, 12.5% NH$_4$OH$_{aq}$, 80°C, 30 min, 95%; e) 1: COMU, DIPEA, 4-(methoxycarbonyl)bicyclo[2.2.2]octane-1-carboxylic acid, DMF, rt, 20 min; 2: 1M KOH, IPA, 91°C, 2hr, 70%;

Compound **3-8** was further modified by conjugating *t*-Boc-protected ethylenediamine *via* COMU coupling in DMF, yielding **3-9**. The glycine linker was introduced by tethering *t*-Boc-glycine to **3-10** (deprotected **3-9**) *via* a similar COMU coupling procedure, with purification *via* automated flash column chromatography. The critical 2-fluorophenyl ester moiety of **3-15** was formed by coupling 3-fluoro-4-hydroxybenzoic acid with **3-12** (deprotected **3-11**) using COMU and DIPEA in DMF at 90°C overnight, yielding **3-13**. This step required precise reactant ratios to minimise ester side product formation, which degraded under continuous heating, favoring the formation of the desired product.

The final step involved conjugation of Sulfo-Cy5 fluorophore to **3-13** using BEP to activate Sulfo-Cy5 carboxylic acid, facilitating acylation. The reaction was performed in a light-protected environment overnight, and the fluorescent ligand **3-15** was purified *via* semi-preparative HPLC.

Scheme 3-5. Synthesis flow of compound 3-8 to 3-15
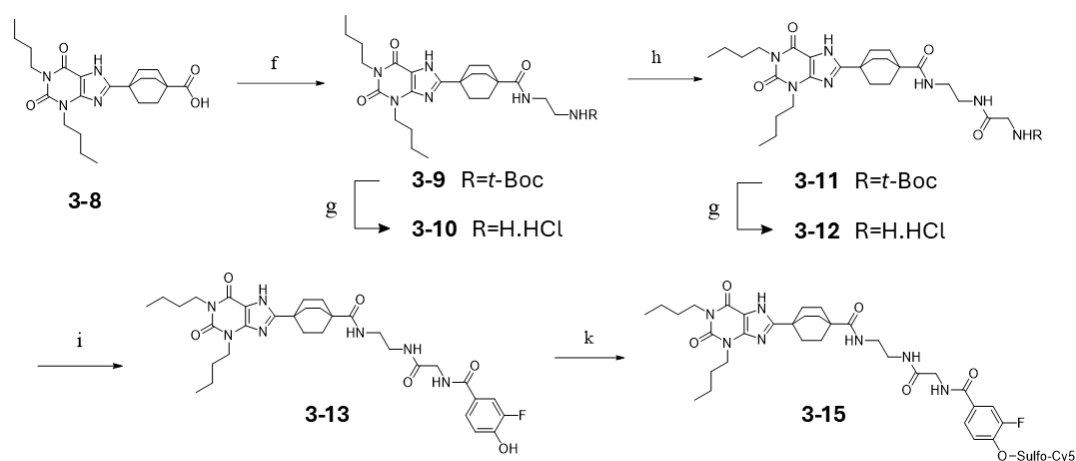
^{a} Reagents and conditions: f) COMU, DIPEA, *tert*-butyl (2-aminoethyl)carbamate, DMF, rt, 20 min, 95%; g) 4 N HCl in dioxane, rt, 1 hr; h) Boc-glycine, COMU, DIPEA, DMF, 3 hr, 71%; i) 3-fluoro-4-hydroxybenzoic acid, COMU, DIPEA, DMF, 90°C, overnight, 47%; k) Sulfo-Cy5 free acid, BEP, DIPEA, DMF, rt, avoid light, overnight, 46% (**3-15**).

Compounds **3-16**, **3-21**, and **3-22**, featuring variations in linker structures (glycine or γ-aminobutyric acid) and fluorophenyl ester positions, were synthesised using the same methodology (**Scheme 3-1** and **3-2**).

3.2.1.2.2 Analogues of **1-56** with 2-Fluorophenyl Amide

The synthesis of compound **3-29** is depicted in **Scheme 3-3**. The synthesis began with the coupling of **3-10** with *t*-Boc-protected β-alanine using COMU and DIPEA in DMF, followed by purification *via* automated flash column chromatography to yield **3-23**. The same coupling procedure was applied to **3-24** (deprotected **3-23**) and 4-((*tert*-butoxycarbonyl)amino)-3-fluorobenzoic acid (**3-32**), yielding **3-25**. Subsequently, 6-((*tert*-butoxycarbonyl)amino)hexanoic acid was coupled to **3-26**

(deprotected **3-25**) using propylphosphonic anhydride (T3P)[131] in DCM under reflux for 19 hours, affording **3-27** after flash chromatography purification.

The final step involved fluorophore attachment. BODIPY-630/650 carboxylic acid was conjugated to **3-28** (deprotected **3-27**) *via* BEP activation in DMF overnight, followed by semi-preparative HPLC purification to afford the fluorescent ligand **3-29**.

Scheme 3-6. Synthesis of probe 3-29
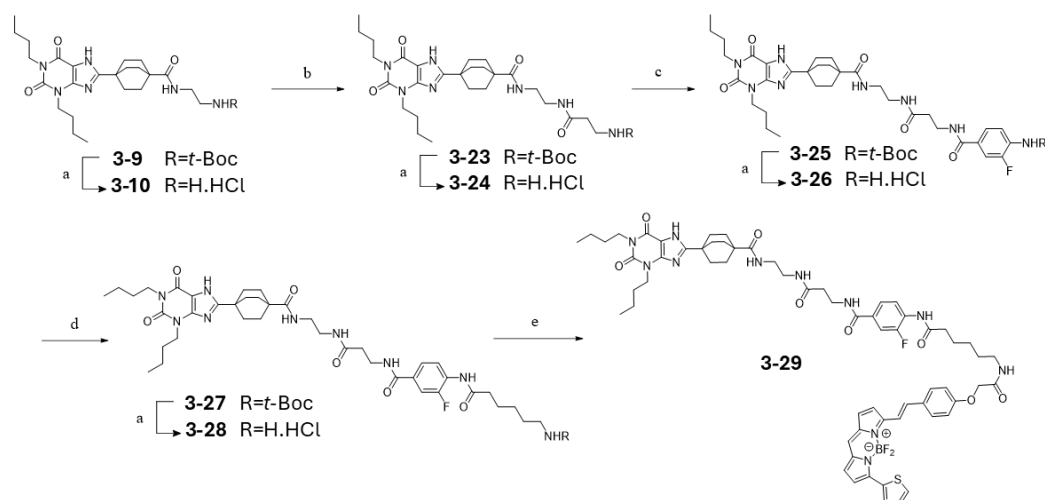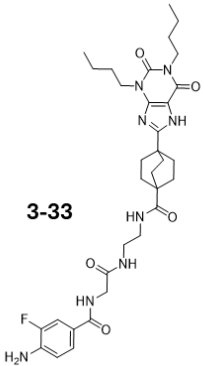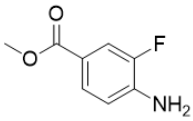
a Reagents and conditions: a) 4N HCl in dioxane, rt, 1 hr; b) *N*-Boc *β*-alanine, COMU, DIPEA, DMF, rt, 5 hr, 91%; c) 4-((*tert*-butoxycarbonyl)amino)-3-fluorobenzoic acid (**3-32**), COMU, DIPEA, DMF, 80°C, overnight, 71%; d) T3P, DIPEA, Boc-E-ACP-OH, DCM, 80°C, 19 hr, 5%; e) BODIPY630/650 carboxylic acid, BEP, DIPEA, rt, overnight, 35%; f) Pd/C, H$_2$, MeOH, rt, 1.5 hr, 78%;

Initially, a phenyl amide analogue of **3-15** was planned. However, attempts to couple **3-33** with Sulfo-Cy5 free acid failed with various coupling conditions (**Table 3-3**), likely due to the weak nucleophilicity of the aniline, which was further diminished by the electron-withdrawing fluorine and benzamide moieties. Additionally, Sulfo-Cy5 was unstable at high temperatures, restricting reaction conditions to temperature below 35°C. To conserve the expensive Sulfo-Cy5 free acid and the laboriously synthesised **3-33**, biotin and **3-31** were used as alternative carboxylic acid and aniline in the amide coupling to determine applicable conditions. However, these reactions also failed. As a compromise, **3-29**, incorporating BODIPY-630/650, was synthesised. **3-26** was first coupled with *t*-Boc-protected 6-aminohexanoic acid, allowing the coupling reaction to proceed under heating conditions. Despite this, coupling attempts failed.
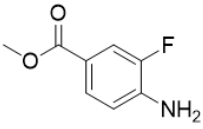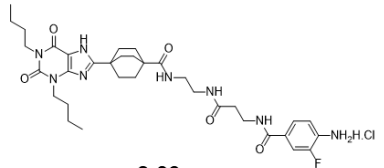
Several coupling reagents and conditions were tested, including BEP[132], HOBt[133], EDC, TCFH[134], and PFP[135], but none succeeded (**Table 3-4**). The only effective reagent was T3P, albeit with low yield. T3P not only activated hexanoic acid but also facilitated coupling through phosphorus-oxygen bond formation, potentially explaining its success where other reagents failed.

Table 3-3. Investigating Coupling Condition for Generating a Phenyl Amide Analogue of 3-15

Entry	Aniline	Coupling reagent	Base	Carboxylic acid	Solvent	Temp/time	Result (product)
1		COMU (1.1eq)	DIPEA (0.1 mL)	SulfoCy5	DMF	rt/overnight	X
2		BEP (1.1 eq)	DIPEA (0.1 mL)	SulfoCy5	DMF	rt/overnight	X
3		BEP (1.1 eq)	DIPEA (0.1 mL)	SulfoCy5	MeCN	rt/overnight	X
4		BEP (1.1 eq)	NMI (0.1 mL)	SulfoCy5	DMF	rt/overnight	trace
5		BEP (1.1 eq)	NMI (0.1 mL)	Biotin	MeCN	rt/overnight	X
6	**3-33**	(COCl)$_2$ (0.1 mL)	NMI (0.3 mL)	Biotin	DCM/DMF	rt/overnight	X
7		(COCl)$_2$ (0.1 mL)	DMAP (0.3 mg)	Biotin	MeCN	rt/overnight	trace
8		HATU (2 eq)	DIPEA (2 drops)	Biotin	DMF	rt/overnight	X
9		EDC.HCl (2 eq)	DMAP (2.2 eq)	Biotin	DMF	rt/overnight	X
10		PFP (1.1 eq)	DIPEA (2 eq)	Biotin	MeCN	rt/overnight	X
11		BEP (1.1 eq)	NMI (0.1 mL)	Biotin	MeCN	rt/overnight	X
12		(COCl)$_2$ (1.2 eq)	DIPEA (0.1 mL)	Biotin	DMF	rt/overnight	X
13		(COCl)$_2$ (3.0 eq)	NMI (0.3 mg)	Biotin	DCM	rt/overnight	trace
14		IBCF (1.1 eq)	DIPEA (3 eq)	Biotin	DCM	rt/overnight	trace
15		HATU (2 eq)	DIPEA (2 drops)	Biotin	DMF	rt/overnight	X
16		(COCl)$_2$ (1.2 eq)	DMAP (2.2 eq)	SulfoCy5	DMF/DCM	rt/overnight	X
17	**3-31**	EDC.HCl (1eq), DMAP (1 eq), HOBt (0.1 eq)	DIPEA (3drops)	Biotin	MeCN	rt/ 40 hr	X
18		TCFH (1.2 eq)	NMI (3.5 eq)	Biotin	MeCN	rt/ 24 hr	X
19		TCFH (1.2 eq)	NMI (3.5 eq)	Biotin	DMF	rt/ 20 hr	X
20	**3-31**, NaH	COMU (1.1eq)	DIPEA (0.1 mL)	Biotin	DMF	rt/overnight	X

Trace: LC/MS detected a small peak with strong starting material peaks (inefficient coupling). X: product peak was not found in LC/MS spectrum.

Table 3-4. **Investigating Coupling Condition for Generating a Phenyl Amide Probe**

Entry	Aniline	Coupling reagent	Base	Carboxylic acid	Solvent	Temp/time	Result (product)
1		TCFH (1.2 eq)	NMI (3.5 eq)		MeCN	80°C/ 21 hr	X
2		PFP (1.1 eq)	DIPEA (2 eq)		MeCN	80°C/ 21 hr	Side product
3		TCFH (1.2 eq)	NMI (3.5 eq)		DMF	110°C/ 20 hr	X
4	**3-31**	PFP (1.1 eq)	DIPEA (2 eq)	*t*-Boc 6-aminohexanoic acid	DMF	110°C/ 20 hr	Side product
5		EDC.HCl (1eq), DMAP- (1 eq), HOBt (0.1 eq)	DIPEA (3drops)		DMF	110°C/ 20 hr	Side product
6		T3P (3 eq)	DIPEA (5 eq)		DCM	Reflux/ 19 hr	O
7	**3-26**	T3P (3 eq)	DIPEA (5 eq)		DCM	Reflux/ 19 hr	O

X: Product peak wasn't found in LC/MS spectrum. O: Desire product peak was found in LC/MS spectrum.

3.2.1.3 Ligand Stability (24-Hour in HBSS, 3-Month Investigation)

LD fluorescent probes are designed to covalently transfer fluorophores by reacting with nucleophilic amino residues on target proteins. Efficient labelling is critical for biomolecular investigations, necessitating a balance between probe reactivity and stability[88,89]. To enhance labelling efficiency, LD probes incorporate an electrophilic moiety as the reactive site; however, in aqueous cellular environments, this moiety may interact with other nucleophiles (e.g., water or amino acids), leading to probe decomposition.

To assess probe stability under physiological conditions, LD probes (**3-16**, **3-22**, and **3-29**) were incubated in HEPES Buffered Saline Solution (HBSS) at 37°C, and their integrity was analysed *via* HPLC (**Figure 3-5**) (full experimental details are described in **Chapter 2**, **Section 2.2.6.1**). After 5 hours, **3-16** and **3-22** remained >95% intact, while their stability began to decline below 90% after 25 hours. In contrast, **3-29** remained stable after 24 hours. These results confirm that LD probes remain intact beyond the intended labelling duration, supporting their application in A_1 AR labelling with live cells. Notably, **3-29**'s superior stability suggests that the 2-fluorophenyl ester is susceptible to degradation, whereas its amide variant remains unsurprisingly resistant to hydrolysis.

Additionally, probe stability in DMSO stock solutions stored at −20°C was evaluated *via* HPLC. Four **1-56** LD probe analogues exhibited varying degrees of degradation over one-year storage, with all showing purity below 95% (**Figure 3-6**). In contrast, **3-29** remained intact after three months. These findings indicate that my LD probes are unsuitable for long-term storage in DMSO at −20°C. Therefore, storing probes in powder form and dispensing small amount (0.1– 0.2 mg per vial) are recommended to minimise probe degradation and excess aliquot preparation from each vial.

3-16

Stability_HBSS 37°C

MW: 1278.52

	Cy5	Congener	**3-16**	other
Retention time	7.6 min	10 min	10.7 min	
T 0	-	0.58%	97%	2.42%
T 1hr	-	0.76%	97%	2.24%
T 3hr	-	1.73%	97.57%	0.70%
T 5hr	-	1.94%	97.65%	0.41%
T 25hr	0.63%	9.14%	90.23%	0
Purity check after synthesis: 99.5%				

3-16 1.76 mM
0.45 mg dissolved in
40 μL of DMSO + 160 μL of HBSS

3-16
HPLC
spectra

3-22

MW: 1306.58

Stability_HBSS 37°C
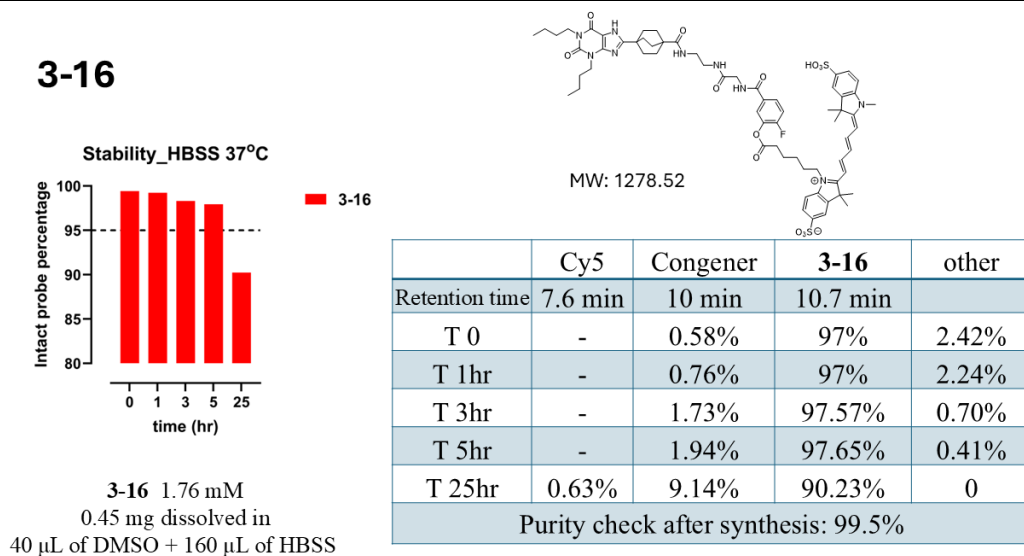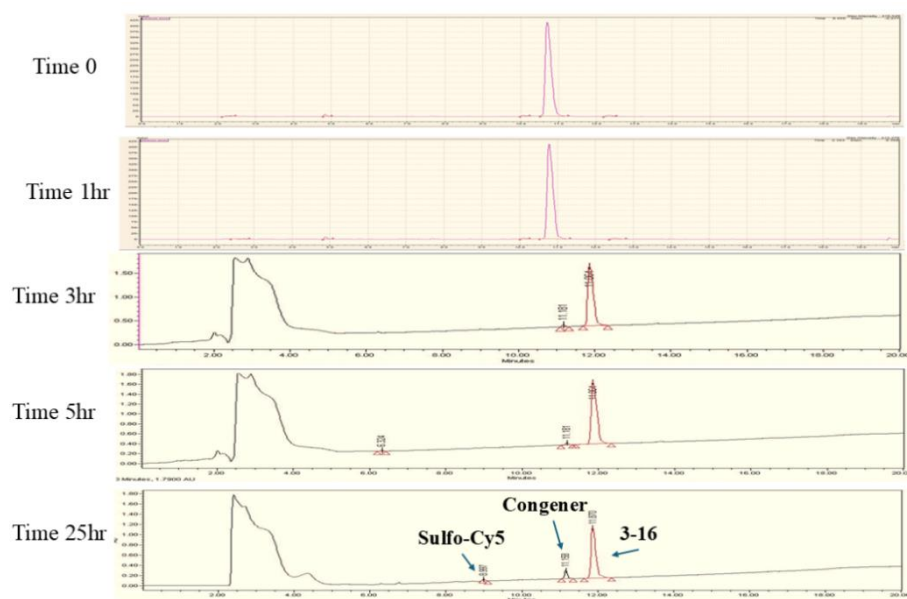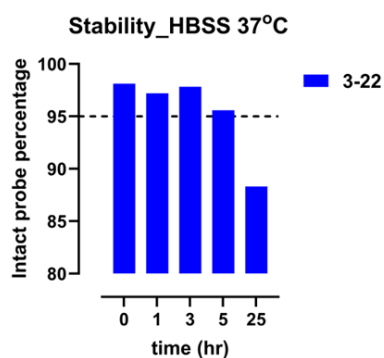
3-22 1.2 mM
0.24 mg dissolved in
30 μL of DMSO + 120 μL of HBSS
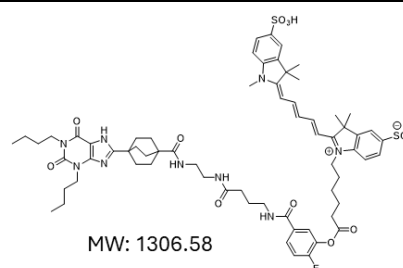
	Cy5	Congener	**3-22**
Retention time	9.2 min	11.4 min	12.1 min
T 0	-	1.88%	98.12%
T 1hr	-	2.80%	97.2%
T 3hr	-	2.18%	97.82%
T 5hr	0.66%	3.76%	95.58%
T 25hr	2.19%	9.5%	88.3%
Purity check after synthesis: 99.5%			

3-22
HPLC
spectra

3-29

Stability_HBSS 37°C

MW: 1212.21

3-29 1.24 mM
0.21 mg dissolved in
60 μL of DMSO + 80 μL of HBSS
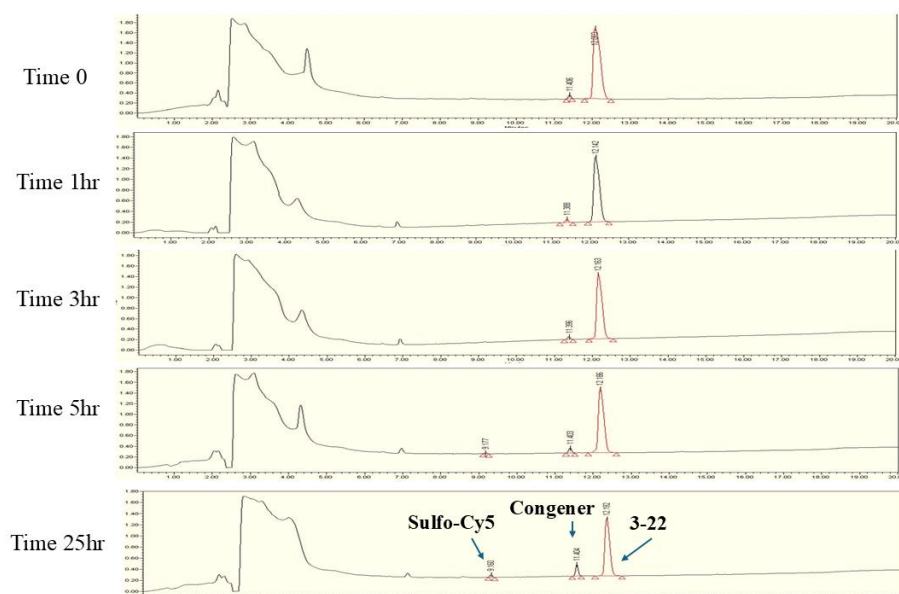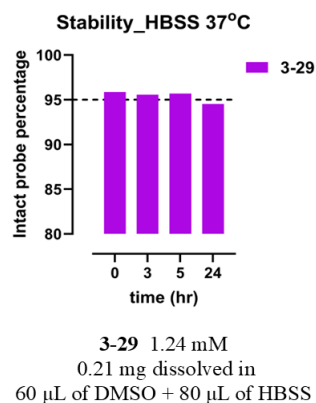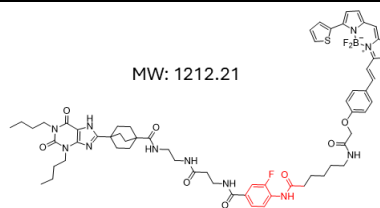
	Congener	**3-29**	other
Retention time	13.8 min	14.1 min	
T 0	3.39%	95.85%	0.76%
T 1hr	-	-	-
T 3hr	4.43%	95.57%	
T 5hr	3.58%	95.7%	0.72%
T 24hr	5.47%	94.53%	
Purity check after synthesis: 99.5%			

3-29 HPLC spectra

Time 0

Time 3hr

Time 5hr

Time 24h
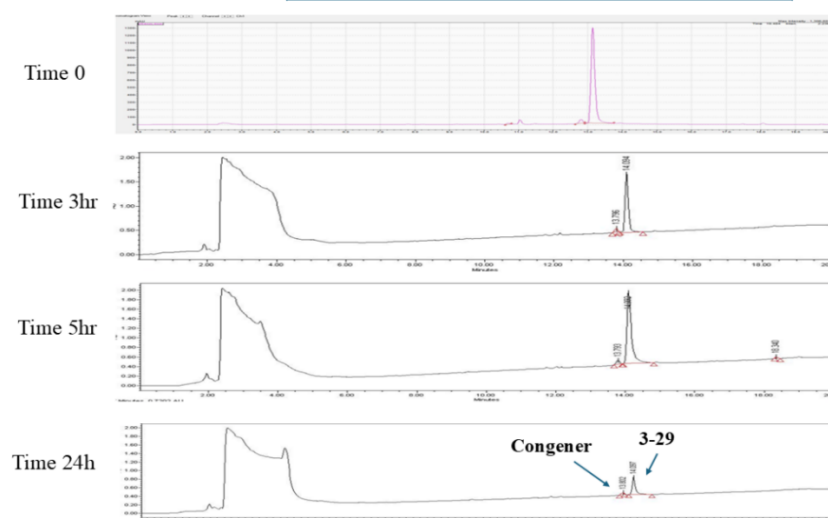
Figure 3-5. Stability Assessment of Probes in HBSS at 37°C.
Probes **3-16**, **3-22**, and **3-29** were incubated in HBSS at 37°C, and samples were collected at 0, 1, 3, 5, and 25 hours to evaluate probe integrity using HPLC. The figure presents each probe's HPLC spectra, a bar chart depicting the remaining percentage of the parent probe, and tables summarising the percentages of the fluorophore, congener, and parent probe.

Purity of Aliquoted Probes
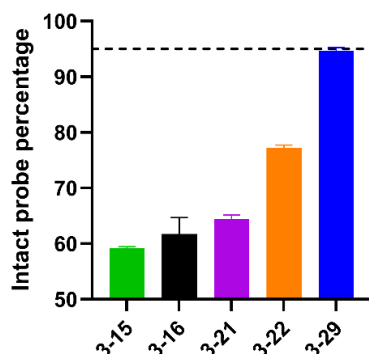
Figure 3-6. Stability of DMSO-Aliquoted Probe Stocks After Long-Term Storage at -20°C.
LD probes (**3-15**, **3-16**, **3-21**, and **3-22**) were stored for over one year, while **3-29** was stored for over three months. HPLC analysis was performed to assess the remaining probe content. The four LD probes exhibited varying degrees of decomposition over long-term storage, leading to a decline in purity. In contrast, **3-29** retained approximately 95% purity after three months, possibly due to the shorter storage duration or the enhanced stability conferred by replacing the phenyl ester with a phenyl amide.

3.2.2 Pharmacology

Bioluminescence resonance energy transfer (BRET) is the primary technique utilised in the described experiments used to evaluate our newly synthesised probes. This method relies on two key components: a donor and an acceptor. The donor, a luciferase enzyme, oxidises its substrate (e.g. furimazine for Nanoluciferase, coelenterazine for Renilla luciferase)[119,136], to generate luminescence, which, in turn, excites the fluorescent acceptor, leading to light emission. BRET occurs when the donor and acceptor meet specific criteria, including proximity, orientation, and spectral overlap[119,120,137] (**Figure 3-7**). Typically, the donor and acceptor must be within 10 nm of each other, as this distance constraint ensures efficient energy transfer[119,137]. Additionally, an appropriate orientation between the donor and acceptor is essential, as perpendicular alignment minimises energy transfer efficiency[119,138]. Lastly, the donor's emission spectrum must overlap with the acceptor's absorption spectrum[119,137]. Due to its stringent distance dependency, BRET serves as a powerful tool for studying protein-protein interactions, conformational changes, and ligand-receptor binding.

Nanoluc luciferase (NLuc), an engineered enzyme derived from the deep-sea shrimp *Oplophorus gracilirostris*, offers several advantages over conventional luciferases such as Renilla (Rluc, 36 kDa) and Firefly (Fluc, 61 kDa)[136]. NLuc is significantly smaller (19 kDa), exhibits greater stability across varying temperature and pH conditions, and produces a stable, high-intensity luminescence with a relatively narrow emission spectrum[136]. These properties enhance the sensitivity of NanoBRET and improve the signal-to-noise ratio[119,137] (**Figure 3-8**). Moreover, NLuc's smaller size facilitates improved protein trafficking to the cell membrane compared to RLuc8[77], a mutant of RLuc. In Stoddart *et al*. (2015)[77], microscope images revealed that β2 adrenergic receptors (β$_2$ARs) with NLuc tag at the *N*-terminus properly trafficked to the cell membrane, whereas β$_2$ARs with Rluc8 tag at the *N*-terminus failed to do so and aggregated inside the cell. NLuc broadened the BRET application to G protein-coupled receptors (GPCRs) without impairing receptor trafficking. NanoBRET has been widely employed as a reliable tool for assessing ligand binding affinities in GPCRs, including β$_2$ARs, A$_1$ ARs, and A$_3$ ARs[77]. Notably, ligand dissociation constants (K_d) measured *via* NanoBRET closely align with those obtained using radioligand binding assays[58,77,119]. Given its robustness and the advantage of avoiding radiation-related safety concerns, NanoBRET was selected as the primary method for ligand binding assessments in this study.

Criteria for BRET

1. Proximity

Luciferase   Fluorescent partner

2. Orientation

3. Spectral overlap
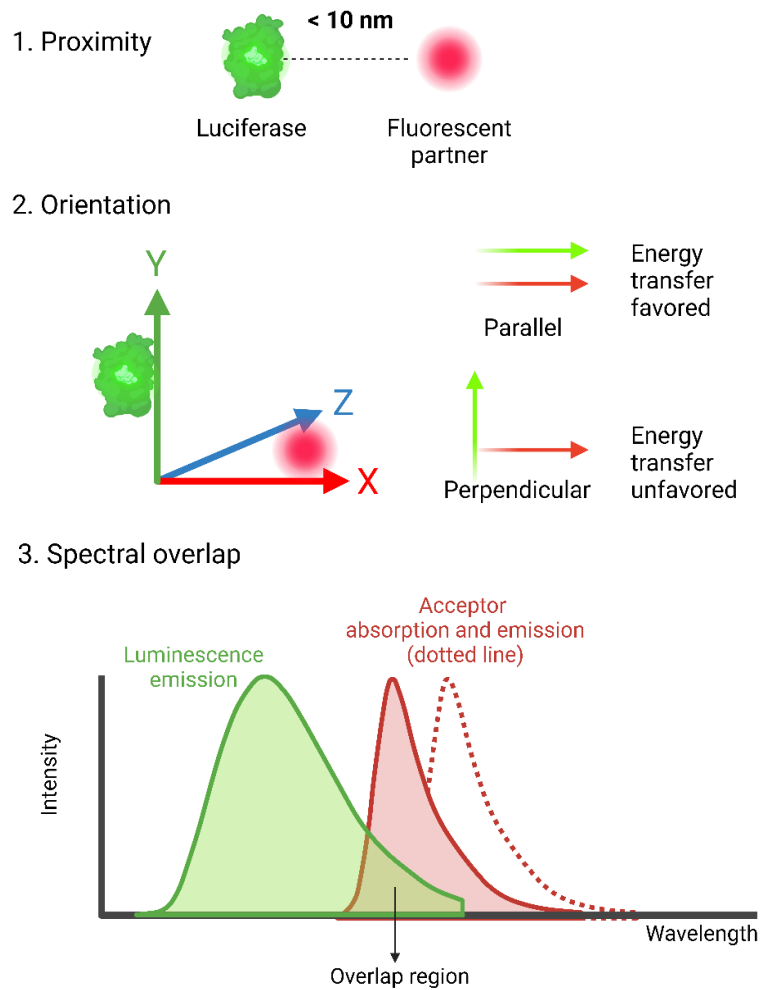
Figure 3-7. Key Criteria for Bioluminescence Resonance Energy Transfer (BRET)[119,120,137]. BRET efficiency is governed by three primary factors. First, the luciferase (donor) and fluorescent acceptor must be in close proximity (within 10 nm) to facilitate energy transfer. Second, the relative orientation of the donor and acceptor is crucial, as dipole-dipole interactions mediate energy transfer; parallel alignment is favorable, whereas perpendicular orientation is less efficient. Finally, spectral overlap between the donor's luminescence emission and the acceptor's absorption spectrum is essential to ensure effective excitation of the fluorescent acceptor. These conditions collectively enable efficient BRET. The graph was created in BioRender (www.biorender.com).

NanoLuciferase

Higher pH and temperature tolerability compared to Rluc

Small size (19 kDa)

minimise protein trafficking impact

O_2

CO_2

Furimazine

Furimamide

Brighter and stable luminescence
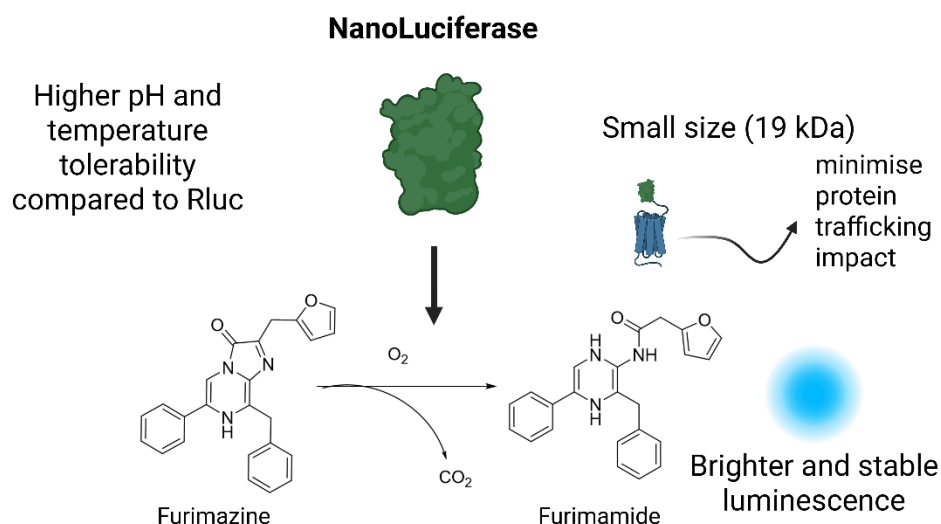
Figure 3-8. Advantages of Nanoluciferase (NLuc).
Nanoluciferase (NLuc) is an engineered luciferase, with a molecular weight of 19 kDa, significantly smaller than RLuc (36 kDa) and FLuc (61 kDa)[136]. Its reduced size minimises interference with receptor trafficking, as demonstrated by Stoddart[77] in studies involving β2-adreno receptors, where NLuc showed less impact compared to the RLuc8 tag. Additionally, NLuc exhibits enhanced stability across a broader range of temperatures and pH conditions compared to FLuc[136]. The combination of NLuc with its substrate, furimazine, produces brighter and more stable luminescence than previous luciferase systems, making NLuc a highly suitable choice for BRET assays[119]. The graph was created in BioRender (www.biorender.com).

3.2.2.1 Adenosine Receptors Subtype Affinity Screening

Before assessing AR subtype affinity, the purity of five probes was verified *via* HPLC, ensuring >95% purity, and their molecular weights were confirmed using high-resolution mass spectrometry (HRMS) with a mass error below 10 ppm (corresponding spectra can be found in **Chapter 2**, **Section 2.2.8**). The initial pharmacological evaluation focused on binding affinity toward A_1 ARs, measured through a BRET-based saturation binding assay. HEK293T cells stably expressing A_1 ARs with NLuc tags at their *N*-terminus served as the cell model for the BRET assay (full experimental details are described in **Chapter 2**, **Section 2.1.2.1**). In the assay, cells were incubated with increasing concentrations of the test ligand (0–500 nM), while non-specific binding was defined using 1 µM DPCPX, an A_1 AR-selective antagonist[5,118] (**Figure 3-9**). Following a one-hour incubation to allow ligand-binding equilibrium, the NLuc substrate furimazine was added, and the BRET signal was measured after five minutes using a plate reader. In addition to the five newly synthesised probes, **CA200645** (**1-48**), a known pan-AR fluorescent ligand[70,139,140], was tested as a reference. Saturation binding assays revealed that all tested probes exhibited nanomolar binding affinity toward NLuc-A_1 ARs (**Figure 3-10**). Structural modifications were well tolerated, as demonstrated by the preserved binding affinity of **1-56**.
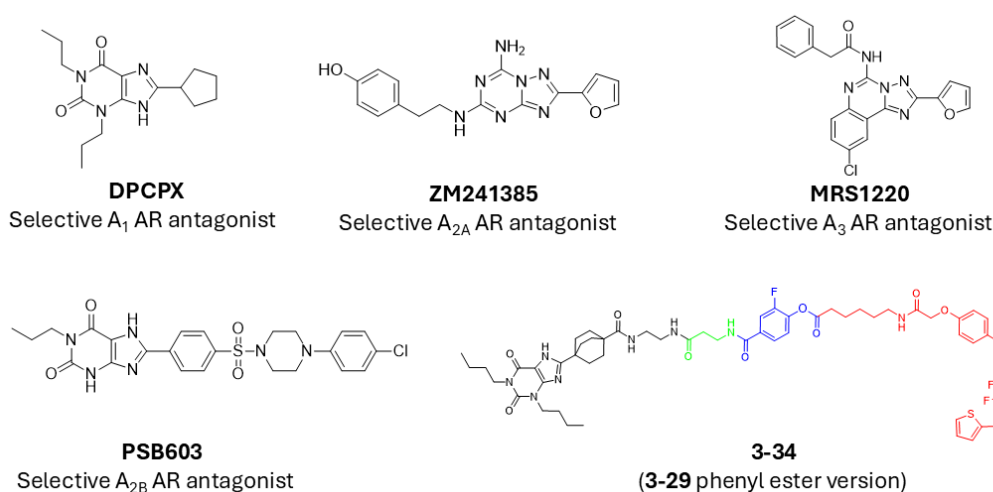
Figure 3-9. Adenosine receptor (AR) subtype-selective antagonists and an LD probe delivering BODIPY-630/650, synthesised by Comeo.
These AR subtype-selective antagonists were used to assess non-specific binding in the corresponding saturation binding assays. Compound **3-34**, an LD probe synthesised by Comeo, was designed to deliver BODIPY-630/650 to A_1 ARs. Compound **3-29**, a phenyl amide analogue of **3-34**, was designed to investigate the role of the 2-fluorophenyl ester in covalent cargo transfer.
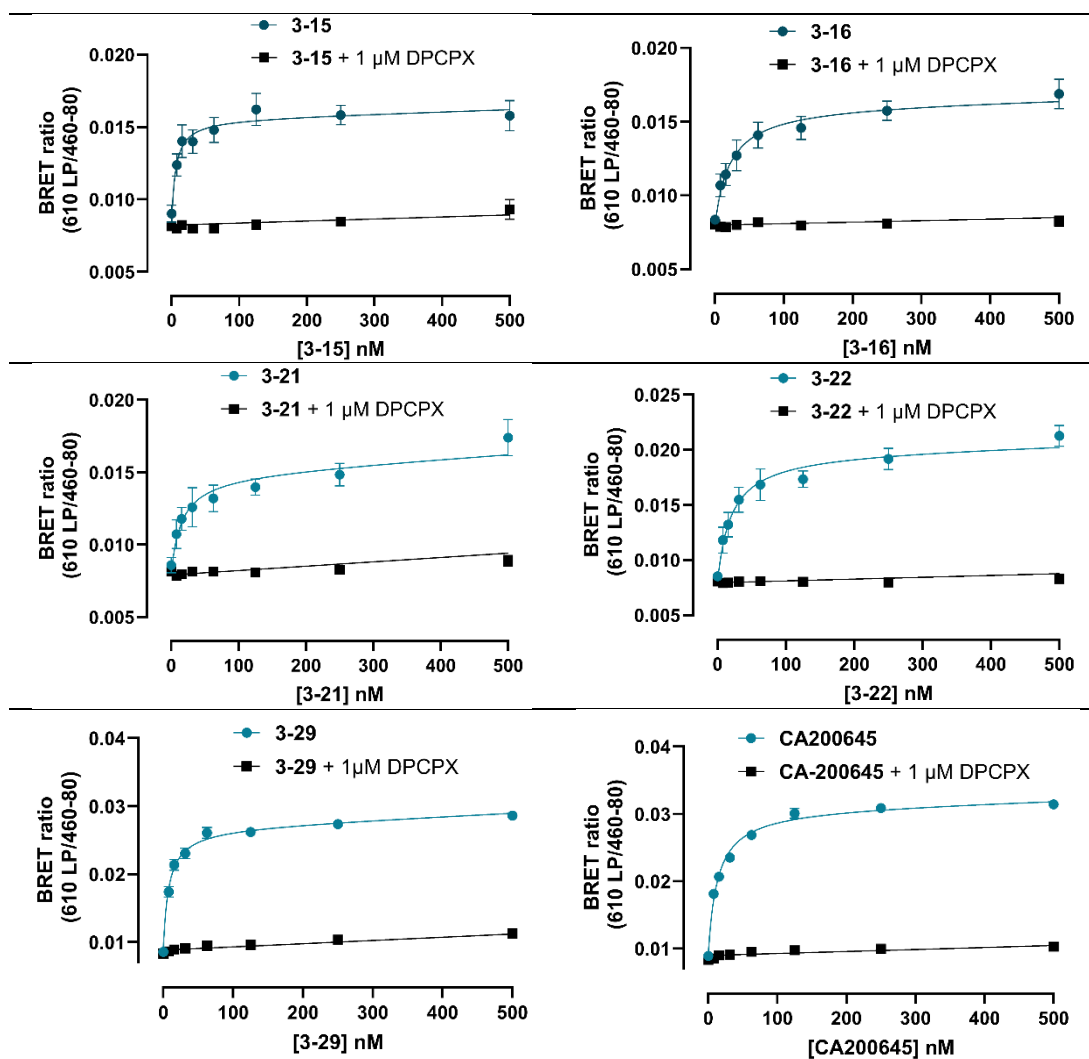
Figure 3-10. Total and non-specific binding graphs for NLuc-hA$_1$ ARs as the cell model. The x-axis represents ligand concentration (nM), while the y-axis shows the BRET ratio, calculated as the signal above 610 nm divided by the signal from 420–500 nm. All six tested probes exhibited high affinity for NLuc-hA$_1$ ARs. Compounds **3-15**, **3-16**, **3-21**, and **3-22** showed lower Bmax values compared to **3-29** and **CA200645**. This difference may be attributed to the attached fluorophore, as **3-29** and **CA200645** were labelled with BODIPY-630/650, whereas the other four probes carried SulfoCy5. Among the SulfoCy5-labelled ligands, **3-22** exhibited the highest Bmax, while **3-15** demonstrated the highest binding affinity. Data represent the mean ± SEM from five independent experiments (four for **CA200645**), with three technical replicates per concentration. Ligand concentrations ranged from 0 to 500 nM. Non-specific binding was assessed by preincubating cells with 1 µM DPCPX for 30 minutes before adding the test ligands.

Following confirmation of A_1 AR binding, we assessed ligand affinity for the remaining three AR subtypes to evaluate potential selectivity shifts. The same methodology was applied to different cell models: HEK293G cells stably expressing NLuc-A_{2B} or NLuc-A_3 ARs were used to study A_{2B} and A_3 AR binding, while HEK293T cells transiently transfected with NLuc-A_{2A} ARs were used for A_{2A} AR binding assessment. Ligand concentrations ranged from 0 to 500 nM, with non-specific binding determined by preincubation with 1 µM subtype-selective antagonists (**ZM241385** for A_{2A}, **PSB603** for A_{2B}, and **MRS1220** for A_3 ARs, **Figure 3-9**). One-site specific binding curves for all four AR subtypes are shown in **Figure 3-11**.
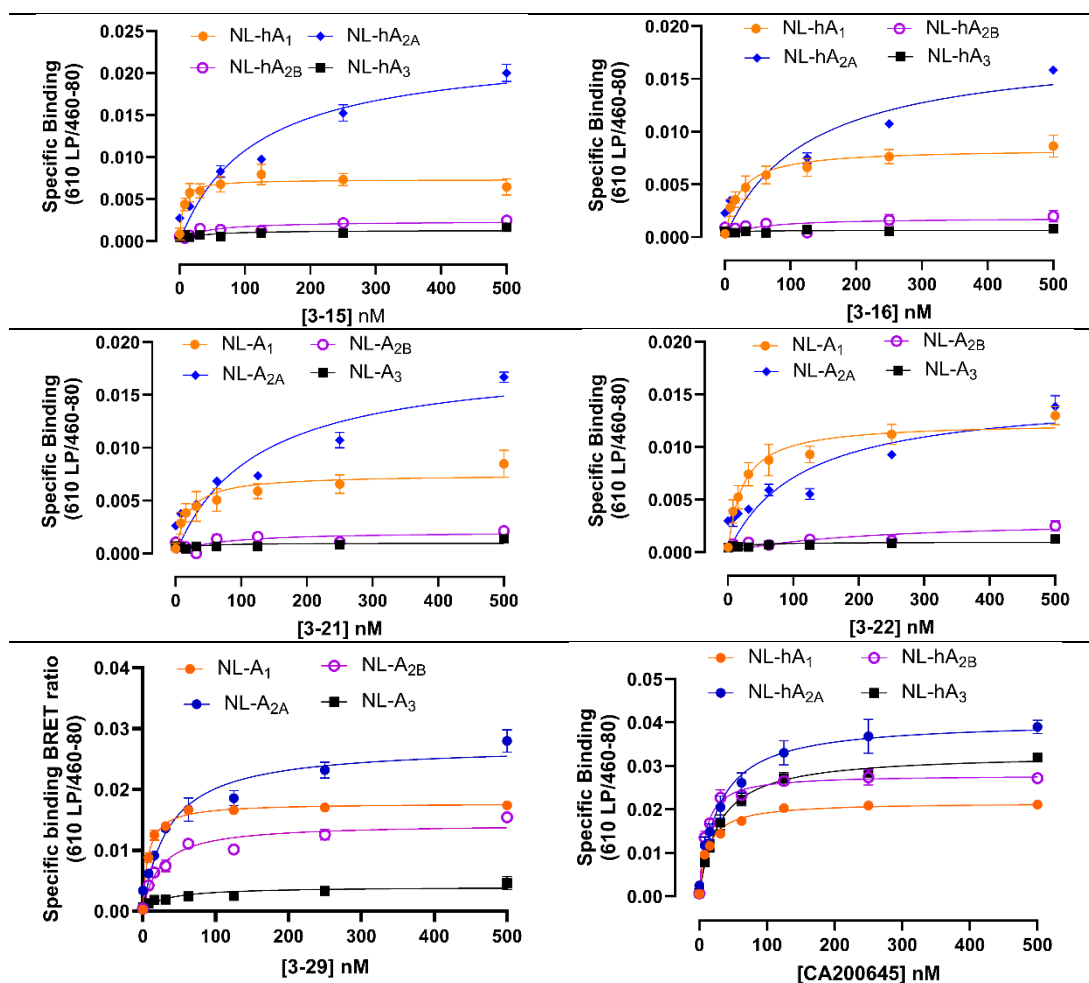
Figure 3-11. Specific binding of five novel probes and CA200645 to the four AR subtypes. The x-axis represents the probe concentration used for incubation, while the y-axis indicates ligand-specific binding, calculated by subtracting non-specific binding from total binding. Non-specific binding was determined by preincubating cells with 1 µM of a selective antagonist (DPCPX for A_1, ZM241385 for A_{2A}, PSB603 for A_{2B}, and MRS1220 for A_3 ARs) for 30 minutes. Four LD probes (**3-15**, **3-16**, 3-**21**, and **3-22**) exhibited binding to A_1 and A_{2A} ARs, while **3-29** showed binding to A_1, A_{2A}, and A_{2B} ARs. The reference ligand, **CA200645**, displayed pan-adenosine subtype binding, consistent with its known characteristics. NLuc-A_{2A} AR screening was conducted using transiently transfected HEK293T cells. NLuc-A_1 ARs were stably expressed by HEK293T cells whereas the NLuc-A_{2B} and NLuc-A_3 ARs were expressed in HEK293G stable cell lines. Data represent the mean ± SEM from five independent saturation experiments (four for **CA200645**), each performed in triplicate.

Table 3-5. Summary of Tested Probes Apparent pK_d and Reversible Probe's pK_d on Four Adenosine Subtype Receptors

Ligand	Structure information			Mean pK_d ± SEM				hA$_{2A}$ K_d/hA$_1$ K_d
	Linker	Phenyl-ester	Fluorophore	NLuc-hA$_1$	NLuc-hA$_{2A}$	NLuc-hA$_{2B}$	NLuc-hA$_3$	
3-15[a]	Glycine	*para*	Sulfo-Cy5	8.24 ± 0.19	6.81 ± 0.04	< 6.60[d]	< 6.60[d]	18.9
3-16[a]	Glycine	*meta*	Sulfo-Cy5	7.61 ± 0.13	6.62 ± 0.09	< 6.60[d]	< 6.60[d]	9.3
3-21[a]	GABA	*para*	Sulfo-Cy5	7.65 ± 0.23	6.57 ± 0.05	< 6.60[d]	< 6.60[d]	8.2
3-22[a]	GABA	*meta*	Sulfo-Cy5	7.66 ± 0.17	6.45 ± 0.09	< 6.60[d]	< 6.60[d]	13.6
1-56[a]	β-alanine	*para*	Sulfo-Cy5	7.40 ± 0.12	6.76 ± 0.22	< 6.60[d]	< 6.60[d]	5.9
3-29[b]	β-alanine	*para*-amide	BODIPY630/650	8.11 ± 0.04	7.48 ± 0.07	7.68 ± 0.07	< 6.60[d]	4.4
3-34[a]	β-alanine	*para*	BODIPY630/650	8.52 ± 0.10	7.70 ± 0.07	7.03 ± 0.20	< 6.60[d]	6.3
CA200645[b]	Polyamide[c]	-	BODIPY630/650	7.88 ± 0.03	7.52 ± 0.08	7.99 ± 0.09	7.53 ± 0.08	2.5

All data represent the mean ± SEM from five repeated saturation experiments (four for **CA200645**) performed in triplicate. Nonspecific binding was defined by preincubating cells with 1 μM of a specific antagonist (DPCPX for A$_1$, ZM241385 for A$_{2A}$, PSB603 for A$_{2B}$, and MRS1220 for A$_3$ ARs) for 30 minutes. NLuc-hA$_1$ ARs were stably expressed by HEK293T cells while hA$_{2B}$, and hA$_3$ ARs were expressed by HEK293G stable cell lines. NLuc-hA$_{2A}$ AR was expressed by transiently transfected HEK293T cells with the NLuc-hA$_{2A}$ AR plasmid.

a: LD probes with the reactive phenyl ester structure.

b: A reversible ligand.

c: β-alanine coupled with 5-aminopentanoic acid

d: Saturation was not reached at 500 nM. Additionally, the total binding was represented by a flat line, parallel to the non-specific binding. Therefore, its K_d must be greater than 250 nM, which converted to a pK_d of 6.60.

Four **1-56** LD probe analogues displayed similar subtype selectivity, demonstrating strong binding to A_1 ARs, moderate affinity for A_{2A} ARs, and no detectable binding to A_{2B} or A_3 ARs at concentrations below 500 nM. In contrast, probe **3-29** exhibited binding to A_1, A_{2A}, and A_{2B} ARs, suggesting that the additional A_{2B} AR affinity may be attributed to the BODIPY-630/650 fluorophore, a pattern previously observed in the Comeo-synthesised compound **3-34** (**Figure 3-9**). As expected, **CA200645** displayed pan-AR binding across all four subtypes, consistent with its known characteristics. **Table 3-5** summarises the AR subtype affinity screening results for the five novel probes, two Comeo-synthesised probes, and **CA200645**. Compared to **1-56**, the four novel LD probes (**3-15**, **3-16**, **3-21**, and **3-22**) exhibited slightly enhanced selectivity between A_1 and A_{2A} ARs, with the highest selectivity ratio (A_{2A} K_d / A_1 K_d) reaching 18. Importantly, these probes maintained strong A_1 affinity while showing no detectable binding to A_{2B} and A_3 ARs at concentrations below 500 nM.

3.2.2.2 Assessing the Covalent Transfer of Fluorophores onto ARs

Previous assessments characterised the AR subtype binding ability of four newly synthesised LD analogues, revealing a binding pattern consistent with the lead compound (**1-56**) but with improved selectivity for A_1/A_{2A} ARs. To further investigate their binding properties, a BRET-based dissociation assay was conducted to determine whether the BRET signal would remain stable following antagonist treatment, indicating covalent fluorophore transfer onto A_1 ARs. In contrast, a decrease in BRET signal after antagonist treatment would suggest a reversible interaction. **CA200645**, a known reversible ligand, was included as a control (full experimental details are described in **Chapter 2**, **Section 2.1.3**).

To optimise labelling efficiency, ligand concentrations were selected based on saturation binding assays: 250 nM for **3-15**, **3-16**, **3-21**, **3-22**, and **3-29**, and 100 nM for **CA200645** and **3-34**. HEK293T cells stably expressing NLuc-A_1 ARs were incubated with the test ligands for two hours, followed by the addition of furimazine. An initial five-minute reading was performed to confirm signal stability before DPCPX addition, after which a 60-minute kinetic measurement (recorded every 30 seconds) was initiated. As shown in **Figure 3-12**, the experimental data aligned with the hypothesis: the BRET signal from LD probes remained stable, suggesting covalent fluorophore transfer, while the signal from reversible ligands declined to baseline following antagonist treatment. The dissociation results for **3-29** and **3-34** confirmed our previous assumption that the 2-fluorophenyl ester moiety is essential for cargo transfer. Specifically, **3-29**, which contains a 2-fluorophenyl amide group, exhibited the same reversible binding behaviour as **CA200645**, whereas **3-34** retained its BRET signal following antagonist treatment, indicating successful fluorophore transfer. The relatively lower BRET signal observed for **3-34** may be attributed to the transferred BODIPY-630/650 fluorophore, which could adopt a different orientation relative to NLuc compared to SulfoCy5.
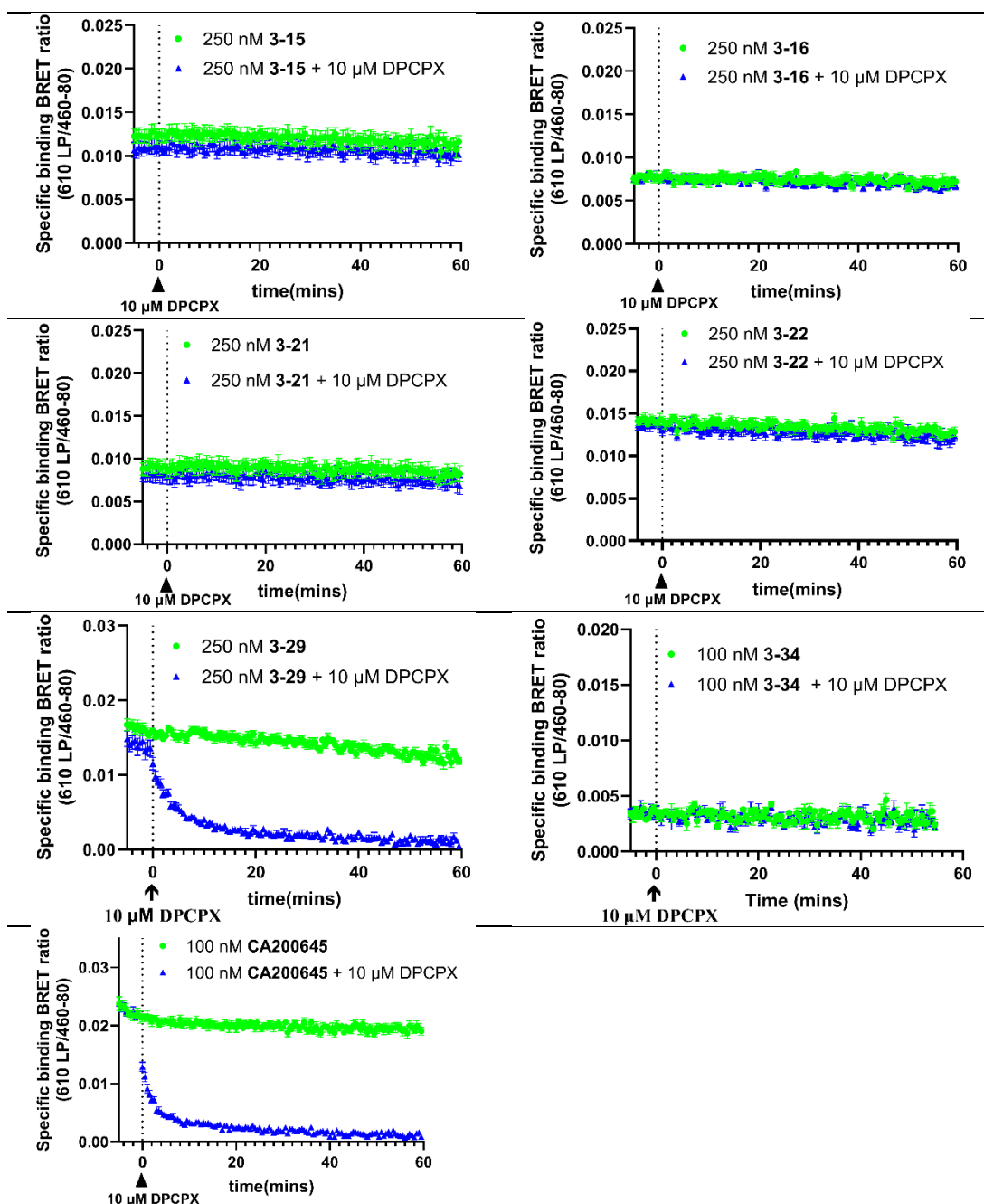
Figure 3-12. NLuc-A$_1$ AR Dissociation Assay.
The BRET signal from LD probes (**3-15**, **3-16**, **3-21**, **3-22**, and **3-34**) remained stable following antagonist treatment, whereas reversible ligands (**CA200645** and **3-29**) exhibited a gradual decline in BRET signal after antagonist addition. The stable BRET signal observed for LD probes suggests successful covalent fluorophore transfer onto NLuc-A$_1$ ARs. In contrast, the decreasing BRET signal for reversible ligands indicates displacement by the antagonist over time. The assay began with a two-hour incubation of test probes, followed by furimazine addition. After a five-minute baseline measurement, the antagonist was introduced, and a 60-minute kinetic recording (one measurement every 30 seconds) was performed. Data represent specific binding, calculated by subtracting non-specific binding (from wells pretreated with 10 μM DPCPX) from total binding. Values are presented as the mean ± SEM from five independent dissociation assays, each performed in triplicate.

A dissociation assay was conducted using HEK293T cells transiently transfected with NLuc-hA$_{2A}$ ARs to determine whether these novel LD probes covalently label

124

A$_{2A}$ ARs or act as reversible ligands in the absence of a suitably positioned nucleophilic amino acid side chain. This assay employed the same methodology as the NLuc-A$_1$ dissociation assay but utilised cells expressing NLuc-A$_{2A}$ ARs and ZM241385 as the antagonist (full experimental details are described in **Chapter 2**, **Section 2.1.3**). The experimental results (**Figure 3-13**) revealed a BRET signal change pattern analogous to that observed in the NLuc-A$_1$ assay, suggesting that the LD probes are capable of covalently labelling NLuc-A$_{2A}$ ARs at a ligand concentration of 250 nM. This finding is consistent with the hypothesis that LD probe-specific labelling is driven by the pharmacophore. Specifically, upon ligand binding to the target receptor, cargo transfer may occur if nucleophilic amino acids are positioned in close proximity to the reactive moiety. Four novel LD probes were shown to bind to the A$_{2A}$ AR, as evidenced by the saturation binding assay. In this study, the unchanged BRET signal in four LD probes suggested that nucleophilic amino acids on A$_{2A}$ ARs located sufficiently near the 2-fluorophenyl ester moiety and realised the cargo transfer. To achieve selective labelling of A$_1$ ARs in a co-expression system of A$_1$ and A$_{2A}$ ARs, strategies such as pre-incubation with an A$_{2A}$ antagonist, adjustment of the LD probe concentration, and optimisation of the incubation time should be considered.
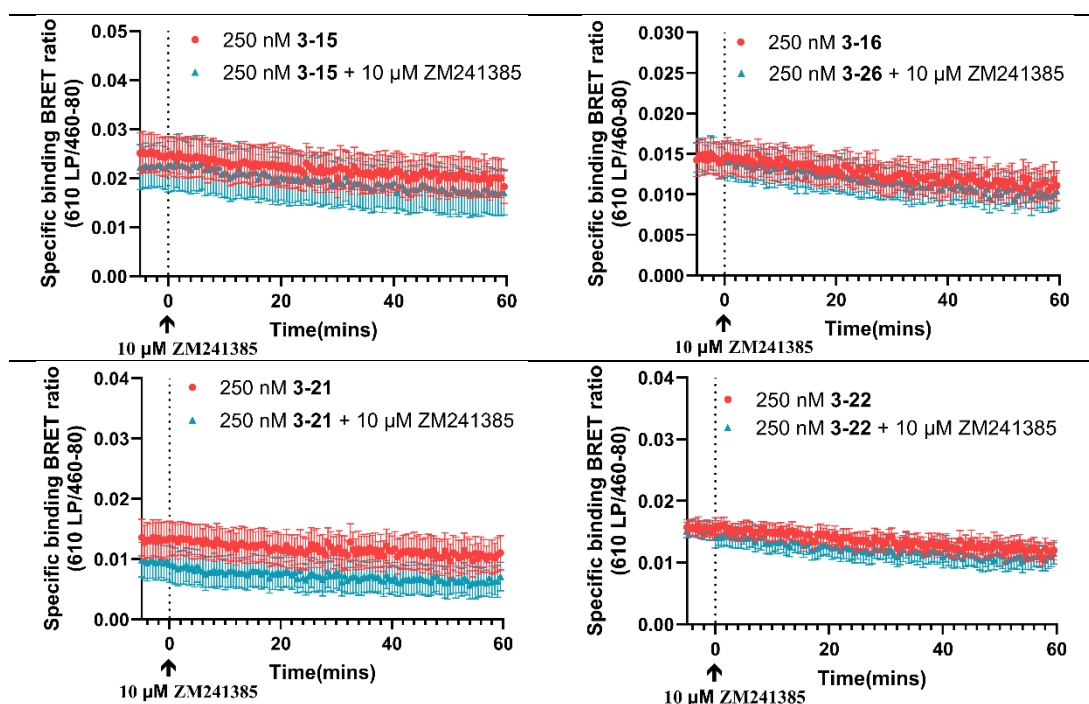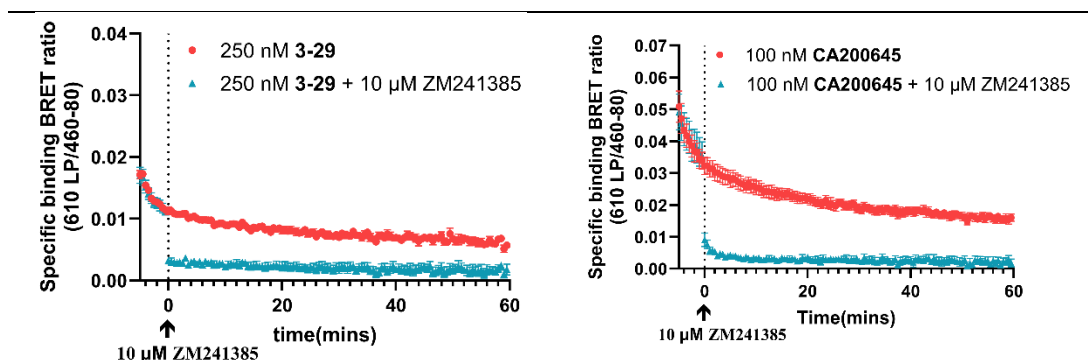
Figure 3-13. Dissociation assay conducted with NLuc-A$_{2A}$ ARs.
The BRET signal from LD probes (**3-15**, **3-16**, **3-21**, and **3-22**) remained stable with minor fluctuations following antagonist (ZM241385) treatment, whereas reversible ligands (**CA200645** and **3-29**) exhibited a gradual decline in BRET signal upon antagonist addition. The sustained BRET signal suggested that the four LD probes covalently transfer fluorophores onto NLuc-A$_{2A}$ ARs. In contrast, the decreasing BRET signal observed with reversible ligands indicated competitive displacement by the antagonist at the orthosteric binding site. The assay protocol involved a two-hour incubation of test probes, followed by the addition of furimazine. After a five-minute baseline measurement, the antagonist was introduced, and kinetic recording was performed for 60 minutes, with measurements taken every 30 seconds. Specific binding data were obtained by subtracting non-specific binding (determined from wells pretreated with 10 µM ZM241385) from total binding. Results are presented as the mean ± SEM from five independent dissociation assays, each conducted in triplicate.

The four novel LD probes exhibited sustained BRET signals in the NLuc-A$_1$ AR dissociation assay, supporting our hypothesis that LD probes covalently transfer fluorophores. However, this stable signal could also result from a slow dissociation rate, preventing antagonist-induced displacement within the one-hour monitoring period. To address this concern and confirm covalent labelling of A$_1$ ARs, an in-gel fluorescence scan was performed (full experimental details are described in **Chapter 2**, **Section 2.1.4**).

In this experiment, cells expressing A$_1$ ARs were incubated with the four LD probes for two hours. The A$_1$ ARs were then isolated, denatured using lithium dodecyl sulfate (LDS), and subjected to polyacrylamide gel electrophoresis (PAGE). LDS, an anionic detergent, disrupted the native protein structure, linearised A$_1$ AR, and coated it to neutralise charge differences, ensuring separation based solely on molecular weight[141]. Following electrophoresis, the gel was scanned under the Cyanine 5 channel to detect fluorescent bands. Since LDS disrupts tertiary protein structures and breaks ligand-receptor interactions, any slow-dissociating ligand would diffuse away. Thus, the presence of a fluorescent band at the expected molecular weight would confirm covalent labelling of A$_1$ ARs by the LD probes.

To perform this experiment, HEK293G cells stably expressing twin-strep (TS) SNAP-A$_1$ ARs were employed. The recombinant A$_1$ AR contained two tags: a TS tag and a SNAP tag. The TS tag consists of two Strep-tag II moieties

(SA<u>WSHPQFEK</u>GGGSGGGSGGSA<u>WSHPQFEK</u>) linked by a short peptide sequence[142]. Strep-tag II (WSHPQFEK) binds with high affinity to the biotin-binding pocket of Strep-Tactin (a streptavidin variant)[143,144], and this interaction is reversible upon biotin introduction, which competitively displaces Strep-tag II. While Strep-tag II/Strep-Tactin offers improved purification over Strep-tag I, its efficiency for low-concentration proteins remains suboptimal[142]. The TS tag (tandem Strep-tag II) enhances affinity for Strep-Tactin while preserving efficient protein elution with biotin[142]. In our experimental design, TS tag facilitated low concentration of A_1 ARs extraction from the solubilised cell supernatant containing multiple proteins. Meanwhile, the SNAP tag was conjugated with the SNAP-tag substrate AF647 (a red-emission fluorophore) as a positive control for covalent labelling of A_1 ARs.

To obtain protein samples for SDS-PAGE, cells were incubated with the LD probes for two hours. Following labelling, cell pellets were collected and solubilised in a buffer containing lauryl maltose neopentyl glycol (LMNG) and cholesteryl hemisuccinate tris salt (CHS), with mixing for two hours. LMNG served as a detergent to solubilise cell membranes, while CHS stabilised A_1 AR structure, as GPCRs are inherently fragile[145]. After solubilisation, cell debris was removed by centrifugation, and the supernatant was incubated overnight with Strep-Tactin magnetic beads for A_1 AR extraction. The next day, the supernatant was discarded, and the magnetic beads were washed twice before A_1 ARs were eluted by adding a biotin-containing buffer. After a four-hour elution, the supernatant was mixed with LDS and loaded onto a gel for electrophoresis (**Figure 3-14** illustrates the process). The resulting gel image, scanned under the Cyanine 5 channel (**Figure 3-15**), displayed fluorescent bands corresponding to TS-SNAP-A_1 AR (59 kDa) in lanes containing samples labelled with **3-15**, **3-34**, **3-35** and SNAP-tag substrate AF647. These bands confirmed that LD probes (**3-15**, **3-34**, and **3-35**) covalently labelled A_1 ARs, similar to the SNAP-tag substrate AF647, ruling out slow dissociation as the cause of sustained BRET signals in dissociation assays. Additionally, bands slightly above 40 kDa, observed in samples labelled with both the LD probes and the SNAP-tag substrate AF647, were suspected to represent A_1 AR fragments rather than nonspecific labelling, as a similar band was also detected in SNAP-tag labelling, which involves a specific bioorthogonal reaction.

In addition, no fluorescent bands were observed in the lane containing **3-29**-labelled samples, confirming that **3-29** is a reversible ligand, consistent with previous dissociation assay results. Furthermore, a comparison of **3-29** and **3-34** reaffirmed that the 2-fluorophenyl ester moiety is essential for fluorophore transfer, whereas the 2-fluorophenyl amide moiety does not facilitate this process.

Notably, the A_1 AR band from the **3-34**-labelled sample appeared dimmer than those observed in samples labelled with sulfoCy5-conjugated LD probes (**3-15** and **3-35**). This discrepancy may be attributed to differences in fluorophore properties. BODIPY-630/650, the fluorophore attached to **3-34**, has higher lipophilicity compared to sulfoCy5, leading to increased non-specific binding to cell membranes—a phenomenon previously reported for fluorescent ligands carrying BODIPY-630/650. Consequently, a substantial portion of **3-34** may have become sequestered within the cell membrane, reducing its availability for labelling A_1 ARs and thereby resulting in lower fluorescence intensity.
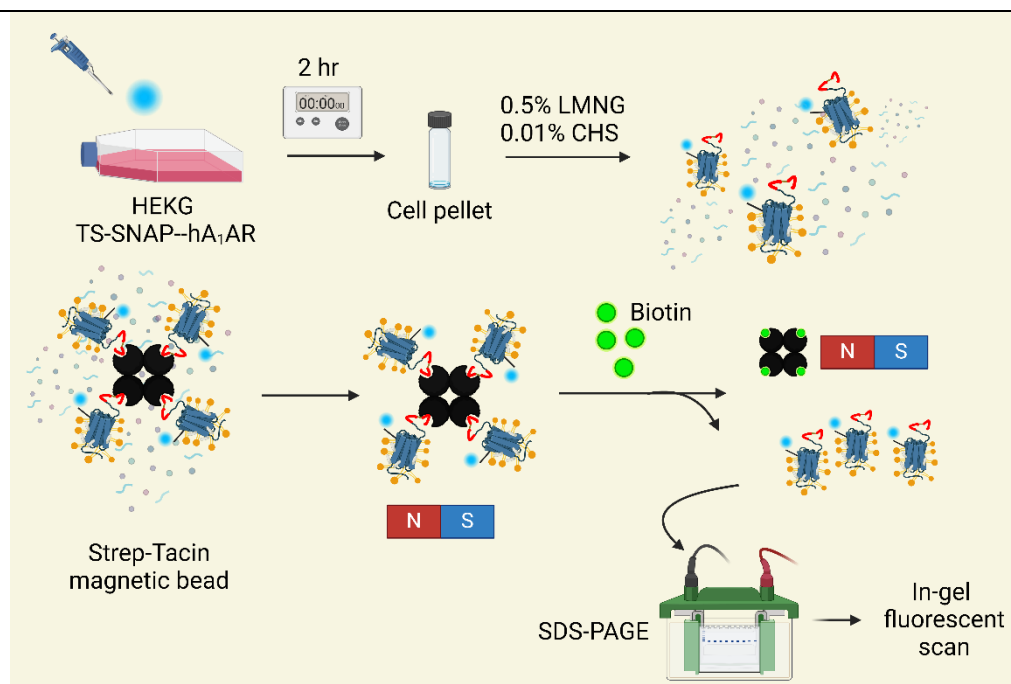
Figure 3-14. A Schematic Representation of SDS-PAGE Sample Preparation.
Cells were labelled, pelleted, and solubilised, followed by centrifugation to separate cell debris from the supernatant. A_1 ARs were then purified from the supernatant using a twin-strep tag and Strep-Tactin-coated magnetic beads. Bound A_1 ARs were eluted with biotin, and the purified protein samples were prepared for SDS-PAGE analysis and subsequent in-gel fluorescence scanning. The graph was created through BioRender (www.biorender.com).
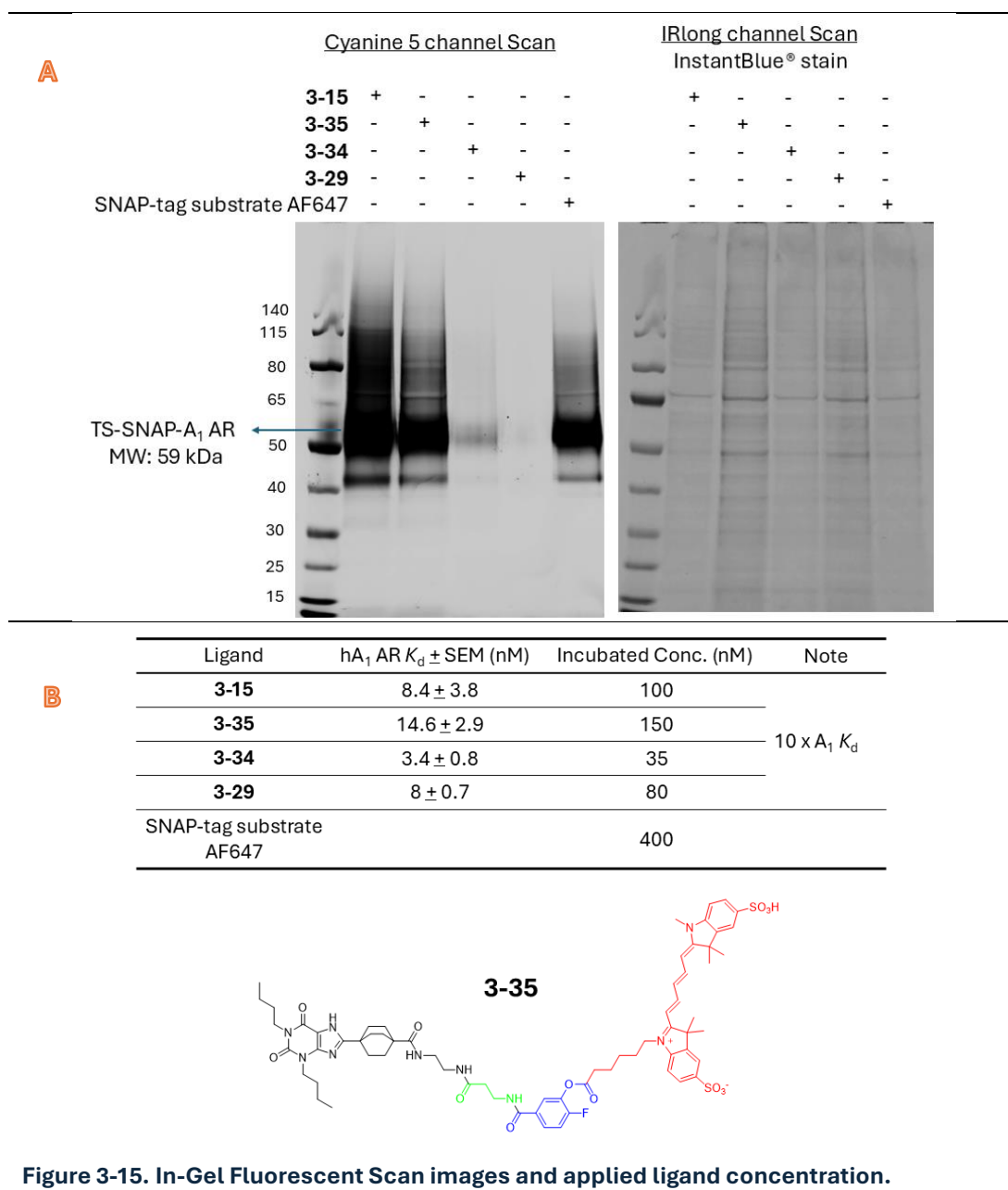
Figure 3-15. In-Gel Fluorescent Scan images and applied ligand concentration.
(A) In-Gel Fluorescence Scan results. The image displays two gel scans: the cyanine 5 channel (left) and the IRlong channel (right). In the cyanine 5 scan, LD probes (**3-15**, **3-35**, and **3-34**) exhibited TS-SNAP-A_1 AR labelling as SNAP-tag-substrate AF647, confirming covalent labelling. The observed bands, appearing between 50 and 65 kDa, correspond to the calculated molecular weight of TS-SNAP-A_1 AR. In contrast, no bands were detected in the lane containing the **3-29** labelled sample, indicating its reversible nature. The IRlong scan, obtained after overnight staining with InstantBlue®, confirms that the **3-29** labelled sample was successfully loaded. PageRuler™ Prestained Protein Ladder (10–180 kDa) was used as the molecular weight marker. This image represents one of three independent experiments. The sample labelled with SNAP-tag substrate AF647 was loaded at half the quantity compared to those labelled with other ligands. **(B) Ligand Concentrations used for Labelling HEK293G TS-SNAP-A_1 ARs.** The table lists the concentrations of each ligand used in the labelling process. Compound **3-35** is an analogue of **1-56**, incorporating a meta-2-fluorophenyl ester, and was synthesised by Comeo.

129

In the NLuc-A_{2A} AR dissociation assay, 250 nM **3-15** exhibited a sustained BRET signal following the addition of 10 µM ZM241385 over a 60-minute monitoring period, indicating its ability to covalently label A_{2A} AR. To assess whether **3-15** selectively labels A_1 ARs at a lower concentration, an in-gel fluorescence scan was performed with 8 nM **3-15** (equivalent to the K_d of A_1 AR and 0.05-fold the K_d of A_{2A} AR) labelled A_1 and A_{2A} ARs on the same gel. The methodology followed that of a previous in-gel fluorescence assay conducted with TS-SNAP-A_1 ARs.

For A_{2A} AR expression, an HEK Tetracycline-regulated expression (HEK T-Rex) cell line was employed. The T-Rex system comprises an inducible expression plasmid and a regulatory plasmid[146]. The inducible plasmid encodes the protein of interest (TS-SNAP-A_{2A} AR in this case) under the control of the cytomegalovirus (CMV) promoter and two tetracycline operator 2 ($TetO_2$) elements[146]. The regulatory plasmid constitutively expresses the tetracycline repressor (TetR)[146]. In the absence of tetracycline, TetR binds to $TetO_2$, preventing inducible gene expression. Upon tetracycline binding, TetR undergoes a conformational change, reducing its affinity for $TetO_2$ and allowing transcriptional activation[146] (**Figure 3-16**). Tetracycline concentration and incubation duration influence the protein expression level[146]; in this study, 1 µg/mL tetracycline with overnight incubation was used.

The in-gel fluorescence scan of A_1 and A_{2A} ARs is shown in **Figure 3-17**. Bands between 50 and 65 kDa correspond to the molecular weight of TS-SNAP-A_1 AR, while bands around 65 kDa match TS-SNAP-A_{2A} AR. As shown in **Figure 3-15 A**, the suspected A_1 AR fragments appeared slightly above 40 kDa, and an A_{2A} AR dimer was suspected in the band observed between 115 and 140 kDa. The gel images confirmed that both A_1 and A_{2A} ARs were covalently labelled by **3-15**. However, due to differences in expression models—where the HEK T-Rex system produced significantly higher levels of TS-SNAP-A_{2A} AR than the HEK293G stable cell line expressing TS-SNAP-A_1 AR— non-selective labelling could not be definitively concluded. This disparity was visually evident in SNAP-tag substrate AF647-labelled cell pellets, where HEK T-Rex produced a faint blue pellet, whereas HEK293G resulted in a white pellet under identical labelling conditions. Although the in-gel fluorescence image did not demonstrate subtype-selective labelling, the experiment confirmed that **3-15** covalently labels A_{2A} AR.
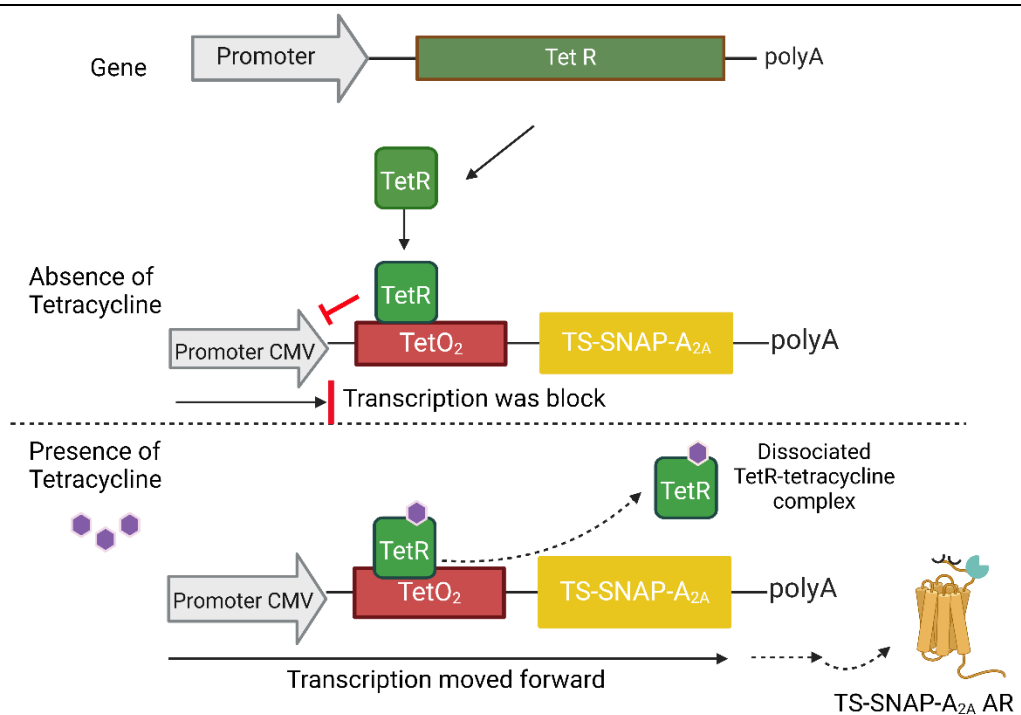
Figure 3-16. Expression of TS-SNAP-A$_{2A}$ ARs in the HEK T-Rex system.
In this system, a regulatory plasmid expresses tetracycline repressors (TetR), which bind to TetO$_2$ sequences on the inducible plasmid, thereby blocking transcription. Consequently, the TS-SNAP-A$_{2A}$ AR protein is not produced under these conditions. Upon the addition of tetracycline, the compound binds to TetR, inducing a conformational change that reduces its binding affinity for TetO$_2$. This dissociation of TetR from TetO$_2$ allows transcription to proceed, leading to the expression of the target gene. The image was adapted from Jones *et al*. (2005)[146] and created using BioRender (www.biorender.com).

	Cyanine 5 channel Scan		IRlong channel Scan Instant Blue stain	

HEK293G TS-SNAP-A_1 AR   HEK T-Rex TS-SNAP-A_{2A} AR   HEK293G TS-SNAP-A_1 AR   HEK T-Rex TS-SNAP-A_{2A} AR

3-15	+	-	-	+	-	-	+	-	-	+	-	-
Negative control	-	+	-	-	+	-	-	+	-	-	+	-
SNAP-tag substrate AF647	-	-	+	-	-	+	-	-	+	-	-	+

TS-SNAP-A_{2A} AR MW: 67.9 kDa

TS-SNAP-A_1 AR MW: 59 kDa

Ladder: 140, 115, 80, 65, 50, 40, 30, 25, 15

Ligand	$K_d \pm$ SEM (nM)	Incubated Conc. (nM)	Note
3-15	hA_1 AR : 8.4 $\pm$ 3.8 hA_{2A} AR: 158.6 $\pm$ 14.5	8	1 x A_1 K_d 0.05X A_{2A} K_d
SNAP-tag substrate AF647		200	½ sample amount compared to **3-15** and negative control was loaded into PAGE

Figure 3-17. In-Gel Fluorescence Scan Results of A_1 and A_{2A} ARs.
The figure presents two gel scans: the Cyanine 5 fluorescence channel (left) and the IRlong channel (right). In the Cyanine 5 scan, the LD probe **3-15** (8 nM) exhibited covalent labelling of both A_1 and A_{2A} ARs, comparable to the SNAP-tag substrate AF647. The observed band positions corresponded to the expected molecular weights of TS-SNAP-A_1 AR and TS-SNAP-A_{2A} AR, confirming specific labelling. The negative control, representing cells not incubated with any ligand, showed no detectable fluorescence signal. Based on prior observations of strong fluorescence signals from the SNAP-tag substrate AF647-labelled sample, half the sample amount (compared to the other two labelled conditions) was loaded onto the gel for electrophoresis. Relative protein amounts were visualised in the IRlong scan of the InstantBlue®-stained gel, where the SNAP-tag AF647-labelled sample lanes appeared dimmer than those of **3-15** and the negative control. The PageRuler™ Prestained Protein Ladder (10–180 kDa) was used as the molecular weight marker. The ligand concentrations used for labelling are listed in the table below the gel images. The image shown is representative of three independent experiments.

3.2.2.3 Assessing the Accessibility of the A_1 AR Orthosteric Binding Site After Tagging with **3-15**

An ideal ligand-directed (LD) probe should covalently label the target receptor while preserving the accessibility of the orthosteric binding pocket for other ligands[88]. The probe **3-15** demonstrated enhanced selectivity between A_1 and A_{2A} ARs, increasing from a 6-fold preference of **1-56** to an 18-fold preference. Its covalent labelling of A_1 AR was confirmed *via* in-gel fluorescence scanning (**Figure 3-15A** and **Figure 3-17**). The key question is whether the orthosteric binding pocket of A_1 AR remains accessible after tagging with **3-15** or if it becomes inaccessible due to incomplete dissociation of the congener or obstruction of the pocket entrance by the transferred fluorophore[147].

A functional assessment is an effective approach to determine the accessibility of the orthosteric binding pocket following LD probe labelling. If downstream signalling or specific A_1 AR behaviours are observed after agonist treatment, it suggests that the agonist can access the orthosteric site and that A_1 AR retains its function. Previous studies have shown that agonist treatment induces A_1 AR internalisation[18,148–151]. This internalisation has been visualised using electron microscopy[148] and confocal imaging[150]. Additionally, A_1-specific binding in membrane and intracellular vesicles decreased and increased, respectively, under agonist-treated conditions compared to controls, indicating receptor trafficking from the membrane into the cell[149,151]. These findings are consistent with microscopy observations[148,150]. Soave *et al*. built upon this evidence and investigated A_1 AR internalisation using NanoLuc Binary Technology (NanoBiT) complementation assays[118]. This approach provided a high-throughput method to monitor A_1 AR internalisation at varying agonist concentrations and validated NanoBiT as a robust tool for studying membrane protein behaviour[118].

Given the established relationship between A_1 AR internalisation and agonist treatment, two assays were employed to assess the accessibility of the orthosteric binding site following **3-15** labelling: the NanoBiT complementation assay and agonist-induced internalisation recorded *via* confocal microscopy. These assays were previously utilised in the investigation of **1-56** by Comeo[74].

The NanoBiT assay relies on NanoLuc luciferase (NLuc), a small (19 kDa) and highly luminescent enzyme[136], making it an optimal reporter for protein-fragment complementation assays (PCA)[119,152]. PCA is widely used to study protein-protein interactions (PPI) by splitting a reporter protein into two fragments, which are individually expressed on two interacting proteins[119,152,153]. When PPI occurs, the fragments reconstitute a functional reporter, generating a detectable signal proportional to the interaction strength[119,152,153]. Dixon *et al*. developed a PCA system using NLuc, splitting it into two subunits: LgBiT (18 kDa, 156 amino acids)

and SmBiT (1.3 kDa, 11 amino acids)[152]. SmBiT exhibited the lowest affinity (K_d = 190 µM) with LgBiT, making it ideal for minimising false-positive PPI detections[152]. Conversely, HiBiT, a variant with high affinity (K_d = 700 pM) for LgBiT, was demonstrated to be effective in monitoring hypoxia-induced cellular adaptations[154]. Both Soave[118] and Comeo[74] utilised the HiBiT-LgBiT system for A_1 AR internalisation studies.

In this study, the HiBiT-LgBiT NanoBiT system was applied to assess A_1 AR internalisation. HiBiT was fused to the *N*-terminus of A_1 AR stably expressed in HEK293G cells (full experimental details are described in **Chapter 2**, **Section 2.1.10**). To evaluate the effect of **3-15** labelling, cells were incubated with or without 500 nM **3-15** (60 times the A_1 AR K_d) for one hour, followed by two washes. Subsequently, cells were incubated with or without 10 nM DPCPX for 30 minutes to determine whether agonist-induced internalisation was affected by competitive binding. Finally, varying concentrations of NECA (10 nM to 100 µM), a non-selective AR agonist, were applied for two hours. Following incubation, purified LgBiT was added for 15 minutes to enable HiBiT-LgBiT reconstitution, and luminescence was recorded five minutes after furimazine introduction. Due to its large size, LgBiT cannot penetrate cell membranes, ensuring that luminescence signals reflect only A_1 ARs remaining on the membrane (**Figure 3-18**) [74,118].

Normalised luminescence from NECA-induced complementation is presented in **Figure 3-19**. In the control (untagged) condition, luminescence intensity decreased as NECA concentration increased, consistent with Soave's findings[118]. Additionally, DPCPX shifted the luminescence curve rightward, indicating competition with NECA. In **3-15**-labelled conditions, NECA-luminescence response curves, with or without DPCPX, closely overlapped with control curves, suggesting that the orthosteric binding site remained accessible in **3-15**-tagged HiBiT-A_1 ARs, similar to untagged controls. Furthermore, there were no significant differences in NECA EC_{50} between experimental and control conditions. The pK_b values of DPCPX, derived using the Schild equation, also showed no significant variation between labelled and unlabelled conditions.

These results indicate that the orthosteric binding site of **3-15**-tagged HiBiT-A_1 ARs remains accessible to NECA and DPCPX. Moreover, **3-15**-labelled HiBiT-A_1 ARs retained their ability to internalise, with no observable impairment relative to controls. Finally, NECA EC_{50} and DPCPX pK_b values were consistent with literature-reported values[74,76,118], as summarised in **Table 3-6**.
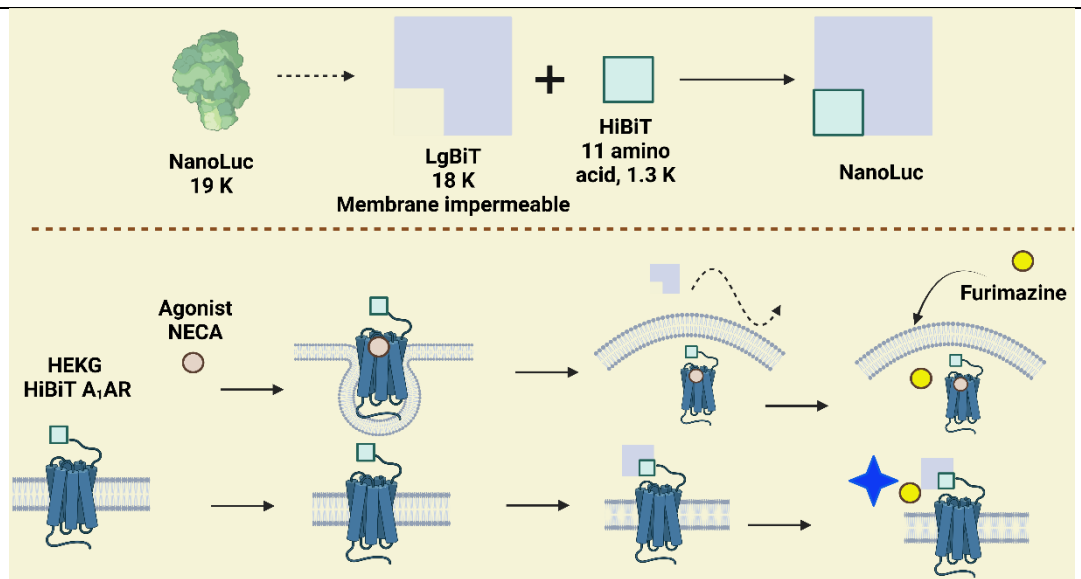
Figure 3-18. Schematic Representation of the HiBiT-LgBiT System and Its Application in A_1 AR Internalisation Assay.

NanoLuc (NLuc) is adapted for a protein complementation assay by splitting it into two subunits: a large subunit, LgBiT (18 kDa), and a complementary small subunit, HiBiT (1.3 kDa). LgBiT and HiBiT exhibit a strong binding affinity (K_d = 700 pM) and reconstitute into a functional NLuc when brought into proximity. The small size of HiBiT minimises interference with the protein of interest (A_1 AR in this case). Due to its large size, LgBiT cannot penetrate the cell membrane. During NECA-induced A_1 AR internalisation, LgBiT can only reconstitute with HiBiT-tagged A_1 ARs that remain on the membrane. By introducing furimazine, luminescence from fully reconstituted NLuc on membrane-bound A_1 ARs can be measured, providing an assessment of receptor internalisation. The illustration was created using BioRender (www.biorender.com).
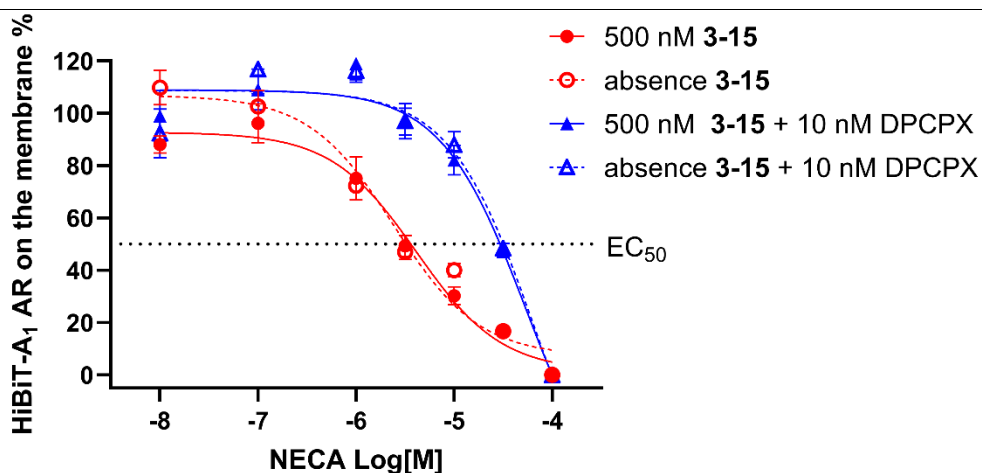
Figure 3-19. Normalised Luminescence and Corresponding NECA Concentration-Response Curves.

The red curves represent HiBiT-A_1 AR treated with varying concentrations of NECA in the presence (solid dots) or absence (hollow circles) of **3-15** pretreatment. Both conditions exhibited nearly identical responses, except at lower NECA concentrations, where slight divergence was observed. The blue curves depict HiBiT-A_1 AR with (solid triangles) or without (hollow triangles) **3-15** tagging, followed by 10 nM DPCPX pretreatment before exposure to different concentrations of NECA. The near-complete overlap of the blue curves suggests that DPCPX exhibits similar competitive behaviour with NECA, irrespective of **3-15** tagging. The closely aligned curves, identical EC_{50} values for NECA, and the consistent rightward shift upon DPCPX treatment indicate that the orthosteric binding pocket of **3-15**–tagged HiBiT-A_1 AR remains accessible to both NECA and DPCPX without significant alteration compared to control conditions. Furthermore, HiBiT-A_1 AR retains its ability to internalise in response to NECA. Data represent the mean ± SEM from five independent experiments, each conducted in triplicate.

Table 3-6. NECA pEC_{50} and DPCPX pK_b derived from HiBiT-A$_1$ AR Internalisation Assay.

HiBiT-A$_1$ AR	NECA pEC_{50} (Mean $\pm$ SEM)		DPCPX pK_b (Mean $\pm$ SEM)	
	experiment	literature	experiment	literature
Control	5.56 $\pm$ 0.05 (n=5)	5.67 $\pm$ 0.21 (n=10), Soave *et al.*[118] 5.79 $\pm$ 0.06 (n=4), Comeo *et al.*[74]	8.86 $\pm$ 0.03 (n=5)	8.28 $\pm$ 0.12 (n=6), Soave *et al.*[118] 8.97 $\pm$ 0.14 (n=4), Comeo *et al.*[74]
LD probe tagging	5.56 $\pm$ 0.11 (n=5) **3-15** tagged	5.53 $\pm$ 0.15 (n=4), **1-56** tagged Comeo *et al.*[74]	8.88 $\pm$ 0.12 (n=5) **3-15** tagged	8.58 $\pm$ 0.13 (n=4), **1-56** tagged Comeo *et al.*[74]
Independent *t*-test	No significant difference between control and **3-15** tagged set *t* (8) = 0.01767, P=0.9863		No significant difference between control and **3-15** tagged set *t* (8) = 0.09789, P=0.9244	

- DPCPX hA$_1$ AR pK_i : 7.4-9.2 (from IUPHAR website)

The NanoBiT assay used to assess the accessibility of the orthosteric binding pocket and the internalisation capability of HiBiT-A_1 AR following **3-15** tagging demonstrated a positive result. To further support these findings, confocal microscopy was employed to visualise A_1 AR internalisation upon agonist stimulation. Prior to the internalisation assay, specific labelling of A_1 AR was evaluated (full experimental details are described in **Chapter 2, Section 2.1.5.1**). HEK293T cells transiently transfected with *N*-terminally SNAP-tagged A_1 AR were used as the cell model. Cells were labelled with 250 nM SNAP-tag substrate AF488 for 30 minutes, serving as a control due to its well-characterised covalent labelling properties. After a single wash with serum-free medium (SFM), cells were incubated with either SFM or 1 µM DPCPX for 30 minutes, followed by the addition of 100 nM **3-15** for a 2-hour incubation. Following labelling, cells were washed twice with PBS, fixed with 4% paraformaldehyde for 20 minutes at room temperature, washed again, and prepared for confocal imaging. As shown in **Figure 3-20**, in the Cy5 channel, DPCPX blocked **3-15** labelling of A_1 AR, confirming the specificity of **3-15** binding. Additionally, significant differences in signal intensity (**Figure 3-21**) further supported this specificity. The strong colocalisation of AF488 and Cy5 signals in the merged channel indicated that **3-15** labelled the same protein population as the SNAP-tag substrate AF488.
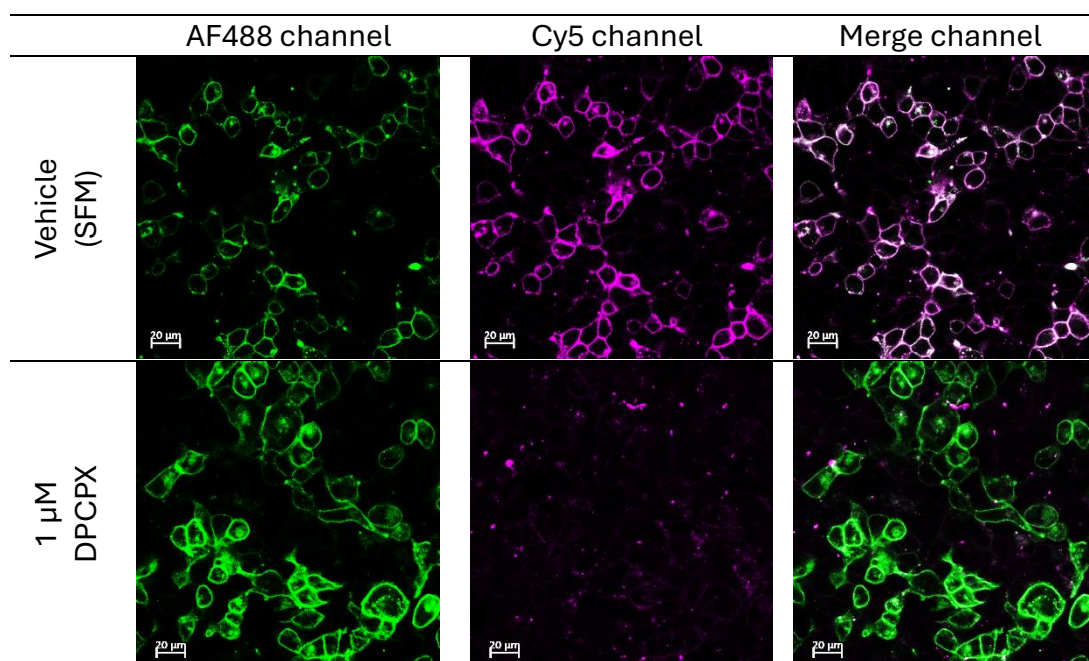
Figure 3-20. Confocal Imaging of SNAP-A_1 AR Labelled with 3-15 and SNAP-tag Substrate AF488.
HEK293T cells transiently expressing SNAP-tagged A_1 AR were labelled with **3-15** and AF488. The top row shows cells preincubated for 30 minutes in serum-free medium, while the bottom row shows cells preincubated with 1 µM DPCPX. Cy5 signal intensity was markedly lower in DPCPX-pretreated cells, confirming the specificity of **3-15** binding to A_1 AR. The merged image demonstrates colocalisation of AF488 and Cy5 signals, indicating that **3-15** labels A_1 AR. Scale bar = 20 µm. Images are representative of five independent experiments.
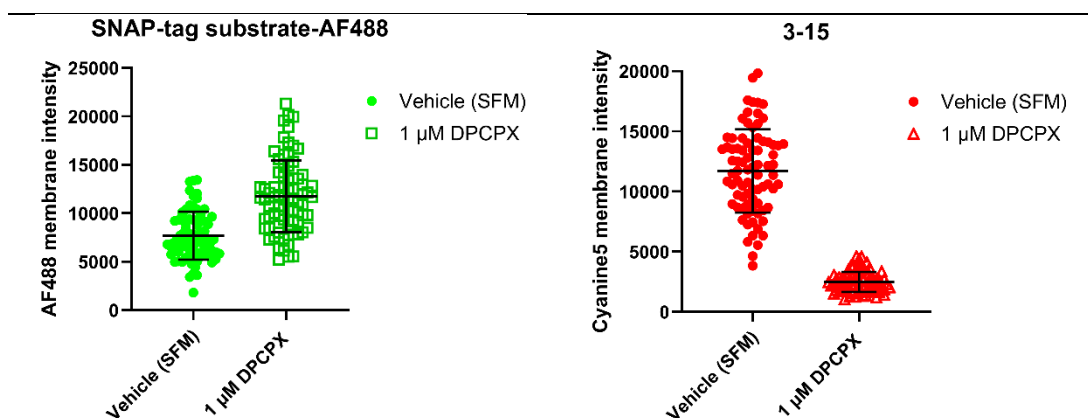
Figure 3-21. Quantification of Membrane Fluorescence Intensity from AF488 and Cyanine5 (Cy5) channels.
Graphs depict the membrane fluorescence intensity measured in the AF488 (green) and Cy5 (red) channels. In the AF488 channel, signal intensity remained comparable between vehicle-treated and DPCPX-preincubated conditions, with a slight increase in the DPCPX-treated group, potentially due to blocking endogenous adenosine-induced A_1 AR internalisation[151]. In the Cy5 channel, fluorescence intensity was approximately fourfold lower in the DPCPX-treated group, indicating significant differences in labelling efficiency. The broad intensity distribution observed in the serum-free medium condition may result from variability in receptor expression across wells or potential operator selection bias during imaging and intensity measurement. Fluorescence intensity was quantified using ImageJ (FIJI) by manually drawing regions of interest (ROIs) around the cell membrane in confocal images. Data were collected from five independent experiments, each with two replicates. Each replicate was imaged in two separate regions, and four cells per image were selected for ROI analysis. Data points represent membrane fluorescence intensities from individual ROIs, with error bars indicating the mean ± SD.

After confirming the specificity of A_1 AR labelling by **3-15**, confocal imaging was conducted to observe receptor internalisation. HEK293T cells transiently expressing *N*-terminally SNAP-tagged A_1 AR were used as the cell model. The same labelling procedure with SNAP-tag substrate AF488 and **3-15** was performed as described previously. Following **3-15** labelling, cells were washed twice with serum-free medium (SFM) and incubated for 2 hours in the presence or absence of 10 µM 2-Chloro-N^6-cyclopentyladenosine **(**CCPA), a selective A_1 AR agonist (**Figure 3-22**). At the end of the incubation, cells were washed twice with PBS, fixed with 4% paraformaldehyde for 20 minutes at room temperature, washed once with PBS, and prepared for confocal imaging. As shown in **Figure 3-22**, compared to vehicle-treated cells, CCPA treatment led to the formation of A_1 AR aggregates, evident in both the AF488 and Cy5 channels. These findings are consistent with previous studies by Escriche[148] and Comeo[74], demonstrating agonist-induced receptor aggregation and internalisation. Furthermore, colocalisation of AF488 and Cy5 signals in cells from the merged channel indicates that CCPA binds the orthosteric site of A_1 AR and triggers receptor internalisation. Quantified intracellular fluorescence intensity from **Figure 3-22** is displayed in **Figure 3-23**. Marked differences were noted between sets with and without CCPA treatment in the AF488 and Cy5 channels. The differences

were validated by statistical analysis applied to the AF488 channel (independent *t*-test, $t(154) = 16.57$, P < 0.0001) and the Cy5 channel (Mann-Whitney test, $U = 206$, P < 0.0001).
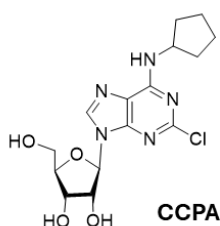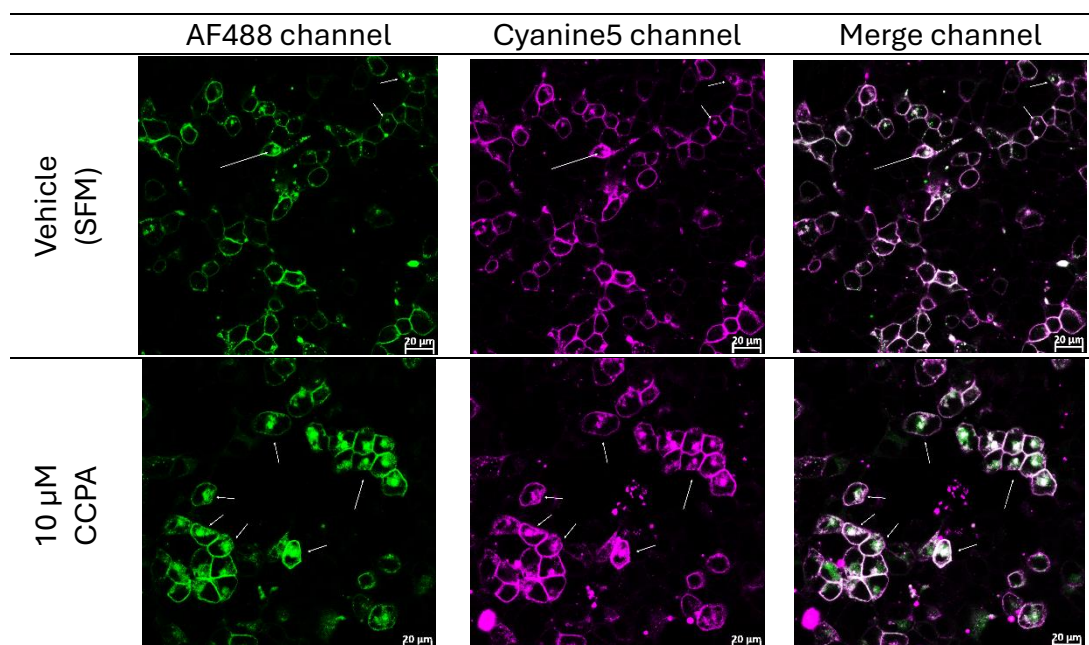
Figure 3-22. Agonist-Induced Internalisation of A$_1$ AR Visualised by Confocal Microscopy. The top panels show HEK293T cells (transiently expressing SNAP-A$_1$ ARs) incubated with vehicle (serum-free medium, SFM) for 2 hours, while the bottom panels depict cells treated with 10 µM CCPA. White arrows indicate internalised and aggregated A$_1$ ARs, primarily observed in the CCPA-treated group, consistent with the results of the NanoBiT internalisation assay. Scale bar = 20 µm. Images are representative of five independent experiments.
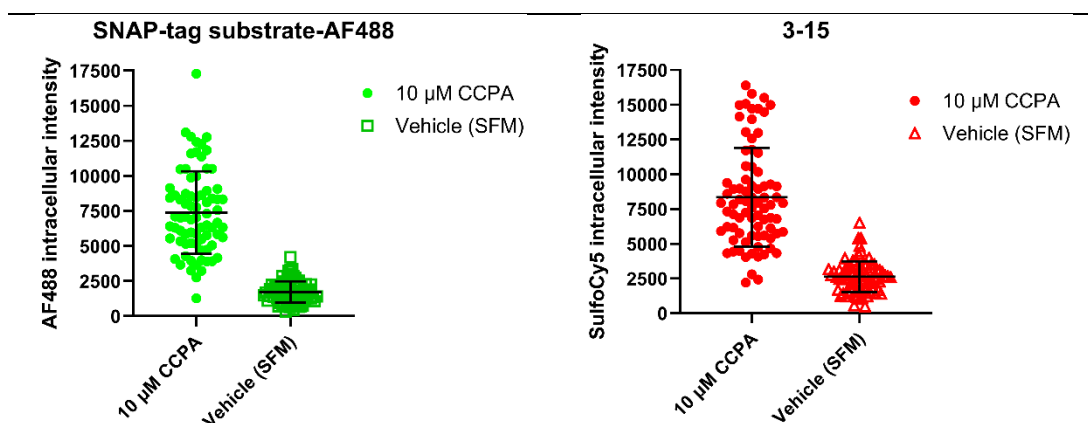
Figure 3-23. Quantification of Intracellular Fluorescence Intensity in the AF488 and Cy5 channels.

Graphs illustrate the fluorescence intensity measured within the intracellular area for the AF488 (green) and Cy5 (red) channels. In the AF488 channel, fluorescence intensity exhibited a significant difference between cells treated with 10 µM CCPA and untreated cells [$t(154)$ = 16.57, P < 0.0001]. Similarly, in the Cy5 channel, a significant difference was observed between the two conditions [U = 206, P < 0.0001]. These fluorescence intensity measurements are consistent with confocal imaging results, demonstrating that A_1 ARs form prominent intracellular clusters following agonist stimulation. This aggregation suggests that membrane-associated A_1 ARs undergo intracellular trafficking upon CCPA treatment, further indicating that the orthosteric binding pocket of A_1 AR remains accessible to CCPA following labelling with the SNAP-tag substrate AF488 and **3-15**. Fluorescence intensity was quantified using ImageJ (FIJI) by manually drawing regions of interest (ROIs) to define the intracellular area within confocal images. Data were obtained from five independent experiments, each including two replicates. Each replicate was imaged in two distinct regions, with four cells per image selected for ROI analysis. Data points represent fluorescence intensity measurements from individual ROIs, with error bars denoting the mean ± SD.

3.2.2.4 Identification of the Specific Amino Acid on A_1 AR Covalently Labelled by SulfoCyanine5 Fluorophores from LD Probes

Previous analyses confirmed that **3-15** exhibits key characteristics as an LD probe with specific binding to A_1 AR, covalent attachment, and accessibility to the orthosteric binding pocket following labelling. However, the precise amino acid residue on A_1 AR covalently labelled by **3-15** remains unidentified. Similar studies have employed site-specific mutagenesis of suspected residues followed by verification of covalent labelling, as demonstrated by Moss *et al*. for A_{2A} ARs[147] and Yang *et al*. for A_3 ARs[155]. Following this approach, point-mutated A_1 ARs were generated, and their specific binding was assessed *via* BRET signal detection after DPCPX competition to determine potential labelling sites on A_1 AR.

The probe **3-22** was selected for investigation due to its highest Bmax in NLuc-A_1 AR saturation binding assays, facilitating the detection of variations in specific binding. The reversible probe **3-29** was used as a control. Candidate residues for mutagenesis were selected based on Comeo's hypothesis[74] that lysine 168 (K168) on extracellular loop (ECL) 2, in close proximity (4.5 nm) to the 2-fluorophenyl

ester of probe **1-56**, may serve as the covalent labelling site. Additionally, molecular docking simulations of A_1 AR (PDB: 5UEN) with **3-20**, a congener of **3-22**, indicated that K173 was positioned 2.8 nm from the 2-fluorophenol group, whereas K168 and K265 were at distances of 14 nm and 22.5 nm, respectively (**Figure 3-24**). Given that molecular docking provides only a static snapshot of receptor structure, and considering the flexibility of both **3-22** and the ECL region in live cells, K168, K173, and K265 were selected for mutagenesis.
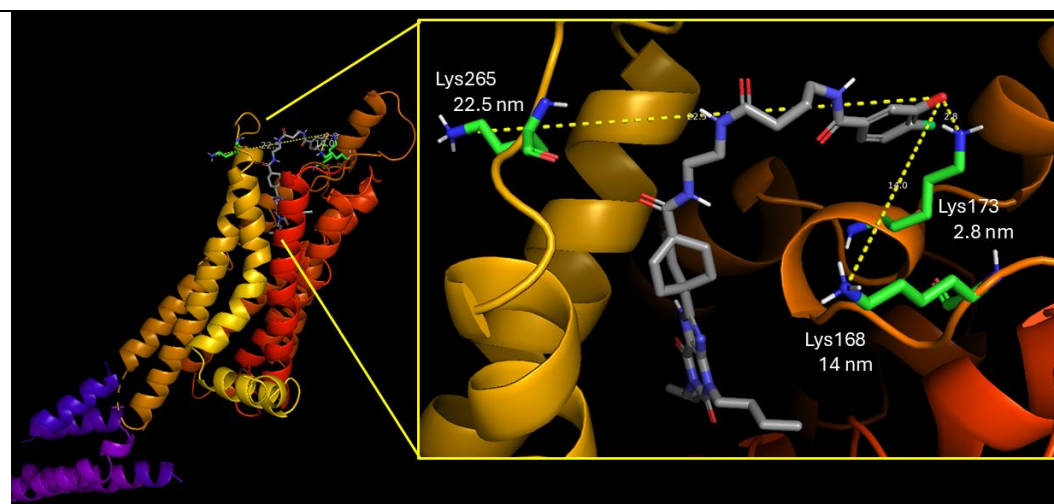
Figure 3-24. Results of Molecular Docking Simulation.
Molecular docking simulation of A_1 AR (PDB: 5EUN) with probe **3-20**, performed using Schrödinger's Glide. Distances from the 2-fluorophenyl group of probe **3-20** to three potential lysine residues were measured in PyMOL based on the docking results: 2.8 nm for Lys173 (K173), 14 nm for Lys168 (K168), and 22.5 nm for Lys265 (K265). The close proximity of K173, along with the flexibility of both the extracellular loop and the tested probe, may enhance nucleophilic substitution with LD probes.

To test these hypotheses, NLuc-A_1 AR plasmids carrying single (K168A, K173A, K265A), double (K168A/K173A), and triple (K168A/K173A/K265A) mutations, as well as the wild-type (WT) construct, were obtained from GenScript. The binding affinities of **3-22** and **3-29** toward each mutated receptor were assessed to confirm successful binding to transiently expressed NLuc-A_1 ARs in HEK293T cells (full experimental details are described in **Chapter 2, Section 2.1.2.1**). One-site specific binding curves for **3-22** and **3-29** are presented in **Figure 3-25**. While no significant differences in binding affinity were observed across the mutated receptors compared to WT (**Table 3-7**), variations in Bmax were noted. These differences may be influenced by receptor expression levels, probe orientation, or the distance between NLuc and the fluorescent probe.

3-22 One-site specific binding

3-29 One-site specific binding
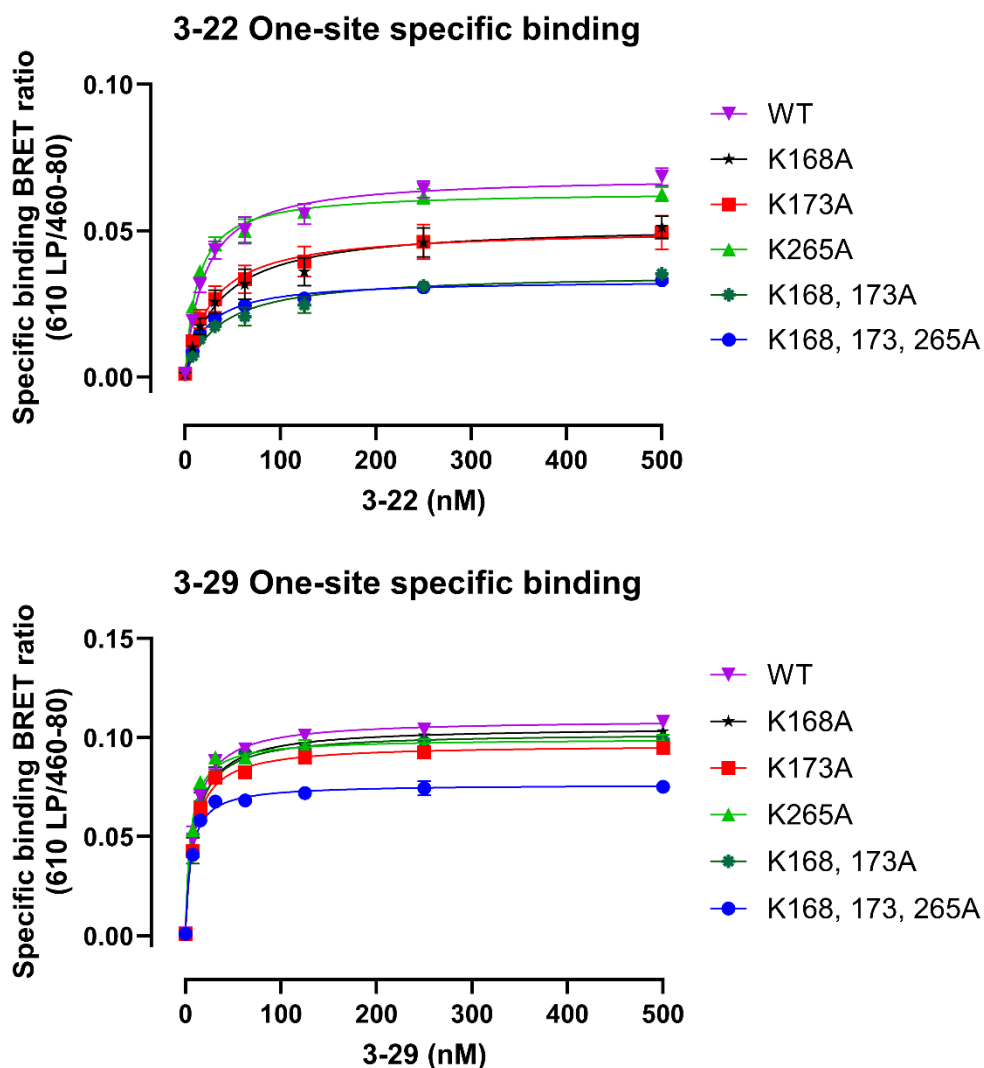
Figure 3-25. One-Site Specific Binding Curves of Probes 3-22 and 3-29 across Five Mutated and Wild-Type (WT) NLuc-A$_1$ ARs.
The top panel presents the results for **3-22**, while the bottom panel shows data for **3-29**. For **3-22**, a similar binding pattern with variations in Bmax was observed. The smallest change was detected in K265A, moderate changes in K168A and K173A single mutants, and more pronounced reductions in the double and triple mutants. In contrast, for **3-29**, only the triple mutant exhibited a lower Bmax compared to the other models. Data represent the mean ± SEM from five independent experiments for **3-22** and four for **3-29**, each conducted in triplicate for each concentration.

Table 3-7. Probe **3-22** and **3-29** pK_d values derived from NLuc-A_1 AR saturation binding assay with wild type and five mutated models.

probe\ NLuc-A_1AR	pK_d (mean $\pm$ SEM)					
	WT[c]	K168A[c]	K173A[c]	K265A[c]	K168A[c] K173A[c]	K168A[c] K173A[c] K265A[c]
3-22[a]	7.70 $\pm$ 0.07 (n=5)	7.37 $\pm$ 0.14 (n=5)	7.54 $\pm$ 0.07 (n=5)	7.89 $\pm$ 0.05 (n=5)	7.39 $\pm$ 0.16 (n=5)	7.76 $\pm$ 0.06 (n=5)
3-29[b]	8.04 $\pm$ 0.08 (n=4)	8.00 $\pm$ 0.08 (n=4)	8.06 $\pm$ 0.04 (n=4)	8.25 $\pm$ 0.07 (n=4)	8.03 $\pm$ 0.06 (n=4)	8.22 $\pm$ 0.04 (n=4)

a) One-way ANOVA indicates significant pK_d differences [$F_{(5,24)}$=3.934, P=0.0095, < 0.01]. *Post hoc* analysis (Dunnett's test) set WT as the control group; no significant difference presented compared to pK_d values derived from other five mutated NLuc-A_1 ARs.

b) One-way ANOVA indicates significant pK_d differences [$F_{(5,18)}$=2.8811, P=0.0441, < 0.05]. *Post hoc* analysis (Dunnett's test) set WT as the control group; no significant difference presented compared to pK_d values derived from other five mutated NLuc-A_1 ARs.

c) WT: wild type; K168A: lysine 168 mutated into alanine; K173A: lysine 173 mutated into alanine; K265A: lysine 265 mutated into alanine.

Given that **3-22** and **3-29** retained binding to NLuc-A$_1$ AR, a reversibility assay was performed using DPCPX. In this assay, 100 nM of **3-22** was incubated with WT and mutated NLuc-A$_1$ ARs for one hour, followed by a wash to remove unbound probe. The samples were then treated with or without 10 µM DPCPX and incubated for an additional hour. After five minutes of furimazine incubation, BRET signals were measured. While a reduction in **3-22**-specific binding was observed across different mutants, complete reversibility was not achieved with 10 µM DPCPX (**Figure 3-26**). In contrast, the control probe **3-29** demonstrated full reversibility upon DPCPX treatment across all tested models (**Figure 3-26**).
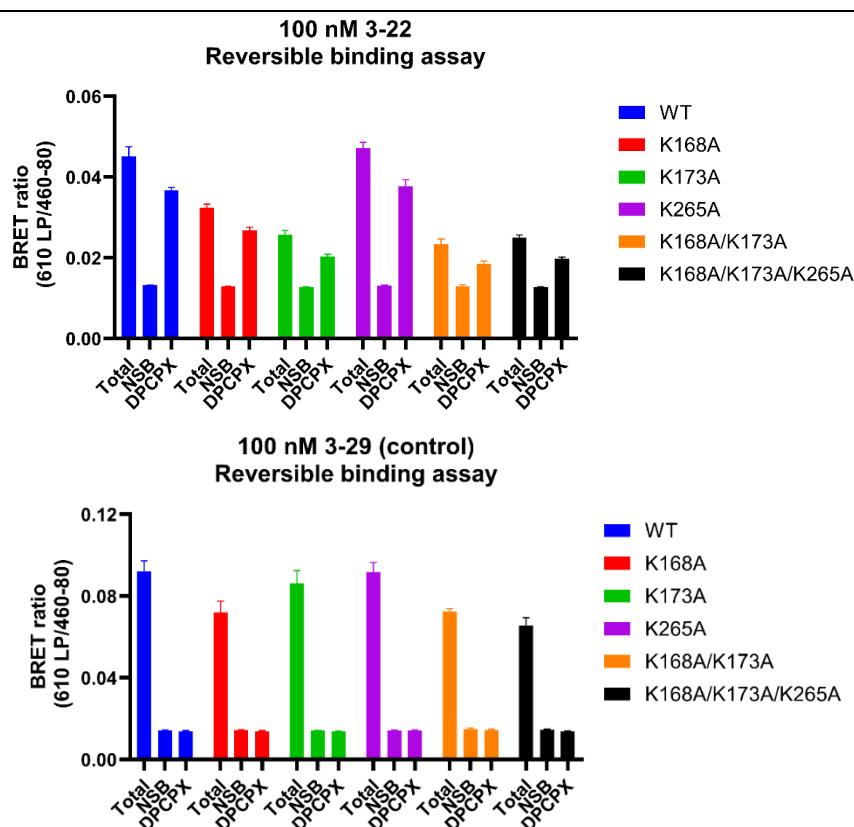
Figure 3-26. Reversible binding assay of five NLuc-A$_1$ AR mutated models, with wild-type NLuc-A$_1$ AR serving as the control.
The top graph presents the experimental results from **3-22**, while the bottom graph illustrates those from **3-29**. "Total" represents the total binding following a single wash to remove unbound ligands. "NSB" (non-specific binding) refers to wells preincubated with 10 µM DPCPX for 30 minutes before the addition of the test probe. "DPCPX" indicates wells treated with 10 µM DPCPX to displace the test ligand from the orthosteric binding pocket. The results demonstrated that DPCPX treatment partially displaced **3-22** from the binding pocket, indicating the persistence of covalent labelling. In contrast, **3-29** exhibited fully reversible binding in the presence of a high concentration of DPCPX, consistent with its reversible binding properties. Data are presented as the mean ± SEM from four independent experiments, each conducted in triplicate.

Since **3-22** demonstrated a covalent labelling pattern for A_{2A} ARs in dissociation assays (**Figure 3-13**), the potential influence of endogenous A_{2A} AR expression in HEK293T cells was investigated. HEK293G cells endogenously express A_{2A} ARs, as verified by Goulding *et al*[156]. To exclude potential interference, the reversibility assays were repeated using A_{2A} AR knockout HEK293T cells transiently expressing the mutated NLuc-A_1 ARs. The reversibility patterns in **Figure 3-27** are consistent with those obtained in ordinary HEK293T cells, confirming that the observed specific binding originated from A_1 AR rather than endogenous A_{2A} AR.
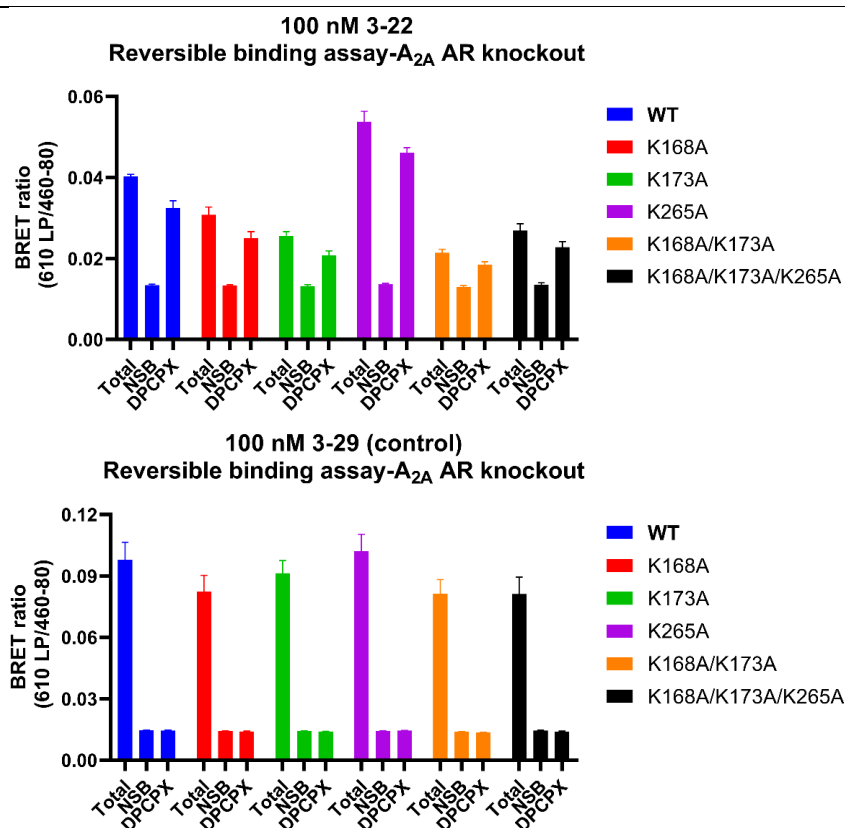
Figure 3-27. Reversible binding assay of five NLuc-A_1 AR mutated models and wild-type NLuc-A_1 AR, all transiently expressed in HEK293T A_{2A} AR-knockout cells.
The top graph represents the experimental results from **3-22**, while the bottom graph illustrates those from **3-29**. "Total" denotes the total binding following a single wash to remove unbound ligands. "NSB" refers to non-specific binding, defined as wells preincubated with 10 µM DPCPX for 30 minutes before the addition of the test probe. "DPCPX" represents wells treated with 10 µM DPCPX to displace the test ligand from the orthosteric binding pocket. The results were consistent with those in **Figure 3-26**, confirming that the specific binding observed in **Figure 3-26** originated from A_1 ARs rather than A_{2A} ARs. Data are presented as the mean ± SEM from three independent experiments, each performed with six replicates per condition.

Table 3-8. Percentage decrease in specific binding of probe **3-22** following DPCPX addition in five mutated NLuc-A_1 ARs and wild-type NLuc-A_1 AR, transiently expressed in either HEK293T or HEK293T A_{2A} AR-knockout cells.

	Specific binding descending percentage [a] (mean ± SEM)					
	WT [d]	K168A [d]	K173A [d]	K265A [d]	K168A [d] K173A [d]	K168A [d] K173A [d] K265A [d]
HEK293T [b]	25.42 ± 3.62 %	28.45 ± 4.25 %	41.11 ± 0.31 % [*]	27.42 ± 4.72 %	45.87 ± 2.91 % [**]	43.24 ± 4.48 % [*]
HEK293T [c] A_{2A} AR knockout	28.71 ± 5.61 %	32.31 ± 4.21 %	38.13 ± 3.92 %	18.31 ± 3.09 %	34.18 ± 6.26 %	30.37 ± 1.76 %

a) Specific binding from the total binding wells (SB-T) was calculated by subtracting the non-specific binding (NSB) value. Similarly, specific binding from DPCPX-treated wells (SB-D) was determined by subtracting the NSB value. The percentage decrease in specific binding was calculated as [(SB−T) − (SB−D)]/ (SB−T). The observed reduction in WT may result from some probes binding to A_1 AR without successfully transferring the fluorophore. The introduction of DPCPX could displace these intact probes, leading to a decrease in specific binding.

b) Data are presented as the mean ± SEM from four independent experiments, each performed in triplicate. A one-way ANOVA revealed significant differences in the percentage decrease in specific binding **$F_{(5,18)} = 6.085$, P = 0.0018, P < 0.05**. *Post hoc* analysis (Dunnett's test), with WT as the control group, indicated significant differences for K173A (P = 0.0305), K168A/K173A (P = 0.0044), and K168A/K173A/K265A (P = 0.013).

c) Data are presented as the mean ± SEM from three independent experiments, each conducted with six replicates. No significant differences were observed in the percentage decrease in specific binding **$F_{(5,12)} = 2.338$, P = 0.1059, P > 0.05**. The absence of significant differences in the A_{2A} AR-knockout model may be attributed to higher variability in the data, potentially resulting from lower replication and variability in receptor expression due to transfection.

d) WT: wild-type; K168A: lysine 168 mutated to alanine; K173A: lysine 173 mutated to alanine; K265A: lysine 265 mutated to alanine.

The findings suggest that multiple amino acid residues in A_1 AR may serve as covalent labelling sites for **3-22**. As shown in **Table 3-8**, the K173 single mutation resulted in a substantial decrease in specific binding compared to the WT, whereas K168 and K265 mutations did not exhibit significant differences. This observation aligns with their spatial arrangement, as K173 is positioned closest to the phenyl ester moiety relative to K168 and K265 in **3-20** simulation. However, despite the K173A mutation, specific binding persisted, suggesting that additional residues may be involved in labelling. Furthermore, molecular docking simulations indicated that serine 150 (S150), serine 176 (S176), and cysteine 169 (C169) are located near the phenol group of **3-20** at distances of 7.8 nm, 9.0 nm, and 13.1 nm, respectively (**Figure 3-28**). These findings imply that **3-22** may covalently label multiple residues with differing likelihoods, and individual mutations may shift labelling to alternative sites. However, introducing mutations at all potential labelling sites is impractical and may lead to artificial outcomes by significantly altering receptor properties. To precisely determine the covalent labelling site, future studies utilising liquid chromatography-mass spectrometry (LC-MS) may provide a more definitive approach.
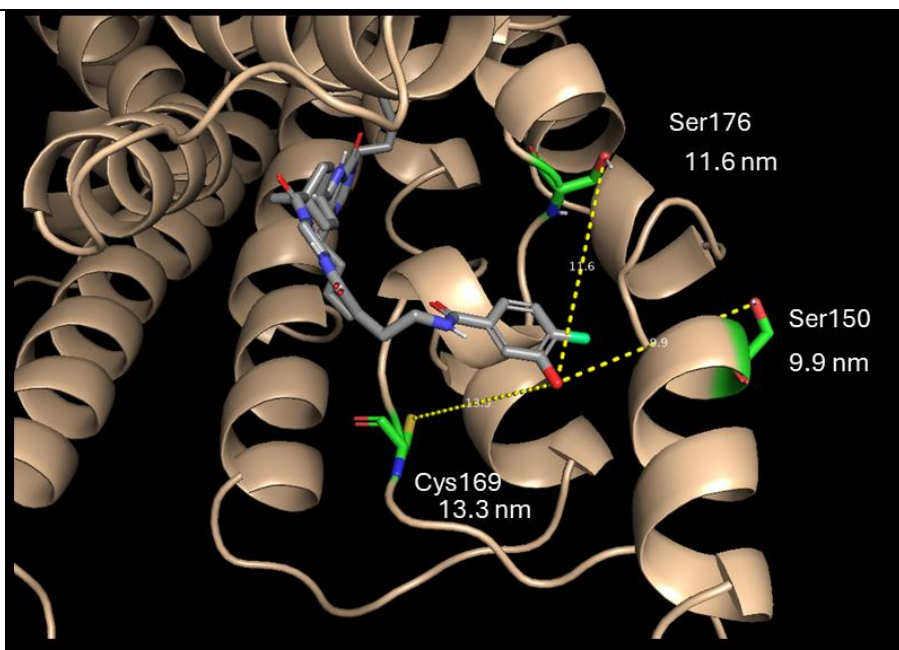
Figure 3-28. Molecular docking simulation of A_1 AR (PDB: 5EUN) with probe 3-20, conducted using Schrödinger's Glide.
The distances between the 2-fluorophenyl group of probe **3-20** and three residues—Ser150 (S150), Ser176 (S176), and Cys169 (C169)—were measured in PyMOL based on the docking results. The measured distances were 9.9 nm for S150, 11.6 nm for S176, and 13.3 nm for C169. Due to their close proximity, these residues may also serve as labelling sites for probe **3-22**.

3.2.2.5 Profile of **3-29** Kinetic Parameters

The compound **3-29**, which incorporates a phenyl amide moiety, was designed as a reversible analogue of the LD probe **3-34**, which contained a phenyl ester. The reversible binding of **3-29** was confirmed through the NLuc-A$_1$ and A$_{2A}$ AR dissociation assays (**Figure 3-12** and **Figure 3-13**), TS-SNAP-A$_1$ AR in-gel fluorescence scanning (**Figure 3-15**), and specific binding reversibility tests (**Figure 3-26** and **Figure 3-27**). To characterise its association and dissociation kinetics, a BRET-based kinetic association analysis was performed, a methodology previously utilised by Stoddart for investigating CA200645[77] with NLuc-A$_1$ ARs and by Bouzo-Lorenzo for studying four fluorescent ligands with NLuc-A$_3$ ARs[157].

Association assays with two or more concentrations were conducted to assess the kinetic parameters of the reversible probes[158]. Tested reversible fluorescent probes served as the fluorescent ligands, and three different concentrations were prepared. To monitor receptor-ligand binding over time, HEK293T cells stably expressing NLuc-A$_1$ ARs were employed to measure the BRET signal as the ligand binding indicator. Measurements commenced immediately after introducing the fluorescent ligand into the test system and continued over a defined period. By fitting the specific binding data from each concentration to a one-phase association curve, the time required for the signal to reach half of Bmax ($t_{1/2}$) was determined[159]. The observed association rate constant ($K_{on(obs)}$) was calculated as ln(2) / $t_{1/2}$[159]. A plot of fluorescent ligand concentration versus $K_{on(obs)}$ was generated, and linear regression was applied to derive K_{on} as the slope and K_{off} as the y-intercept, following the equation $K_{on(obs)}$ = K_{on}[fluorescent ligand] + K_{off}[159–161].

The association assay was performed by treating HEK293T cells stably expressing NLuc-A$_1$ ARs with furimazine, followed by a 5-minute incubation. Three different concentrations of **3-29** were introduced in the presence (for NSB measurement) or absence of 10 µM DPCPX. The BRET signal was recorded at 30-second intervals over a 60-minute period (full experimental details are described in **Chapter 2**, **Section 2.1.7**). The resulting association graph is presented in **Figure 3-29**. The observed association rate constant ($K_{on(obs)}$), as well as the association (K_{on}) and dissociation (K_{off}) rate constants, were determined using the previously described method, with the values shown in **Table 3-9** and regression graph displayed in **Figure 3-30**.
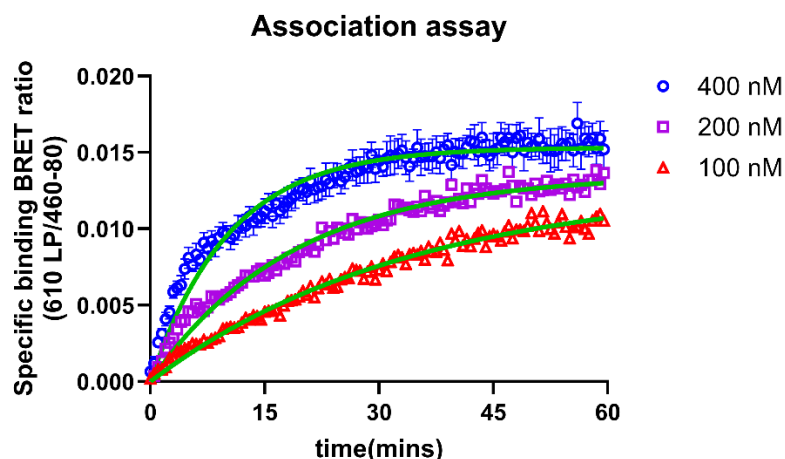
Association assay

Figure 3-29. Association Kinetics of 3-29 at Three Different Concentrations.
HEK293T cells expressing NLuc-A_1 AR were pre-incubated with 10 μM DPCPX (for NSB determination) or HBSS for 30 minutes. Furimazine was then added, followed by a 5-minute incubation. Subsequently, three concentrations of **3-29** were introduced, and the BRET signal was recorded every 30 seconds over 60 minutes. Specific binding values were plotted against time and fitted to an exponential association curve (green curves), as shown in the figure. Data are presented as the mean ± SEM from five independent experiments, each conducted in triplicate.

Table 3-9. Kinetic Assessment of **3-29** – Association Assay

3-29 Kinetic data shown as mean $\pm$ SEM (n)		
100 nM	200 nM	400 nM
$t_{1/2}$ [a] (min)		
23.93 $\pm$ 4.60 (5)	11.66 $\pm$ 1.58 (5)	6.92 $\pm$ 1.01 (5)
$K_{on(obs)}$ [b] (min^{-1})		
333 $\pm$ 60 (5)	641 $\pm$ 88 (5)	1094 $\pm$ 160 (5)
K_{off} [c] (min^{-1})		
0.0106 $\pm$ 0.0048 (5)		
K_{on} [c] (M^{-1}*min^{-1})		
249,920 $\pm$ 40,666.13 (5)		

a. The time required for specific binding to reach half-maximal binding (Bmax) from time 0.
b. $K_{on(obs)}$ was calculated as ln(2) devided by $t_{1/2}$.
c. K_{off} and K_{on} were derived by fitting three ligand concentrations (100, 200, and 400 nM) into a linear regression model. K_{on} was the slope and K_{off} was the Y-intercept according to the equation: $K_{on(obs)} = K_{on}$ [ligand concentration] $+ K_{off}$.
d. Data are presented as the mean ± SEM from five independent experiments, each conducted in triplicate.

Linear regression

$R^2=0.66$
$Y=0.00025*X + 0.011$
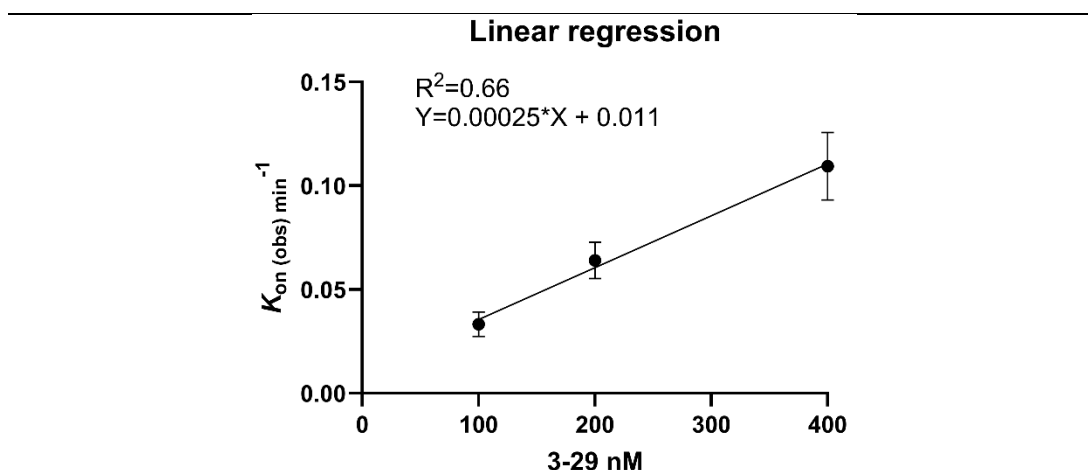
Figure 3-30. Linear Regression Graph.
The observed association rate constants ($K_{on(obs)}$) were derived from the association assay by dividing ln(2) by the half-life ($t_{(1/2)}$). By plotting the $K_{on(obs)}$ values against the corresponding concentrations of compound **3-29**, a line was generated by fitting the data into a linear regression model, as shown in the graph. The line yielded a Y-intercept of 0.011 and a slope of 0.00025×10^9. Data are presented as the mean ± SEM from five independent experiments.

A comparison of dissociation constants (K_d) obtained from saturation binding (equilibrium) and association assays (kinetic) is provided in **Table 3-10**. No significant differences were observed between these methods, indicating that **3-29** adhered to the law of mass action. However, greater variability was noted in K_d values obtained from kinetic assays compared to equilibrium assays. This variation may result from differences in experimental design, as kinetic assays involved measuring a single well once per time point, whereas equilibrium assays involved triplicate measurements per well.

Table 3-10. Comparison of K_d Values for **3-29** Derived from Equilibrium and Kinetic Approaches

3-29 K_d	Mean ± SEM (nM)
Equilibrium saturation	7.99 ± 0.72
Kinetics (K_{off}/K_{on})	46.72 ± 19.91

Statistical analysis (independent *t*-test): $t(8) = 1.944$, P = 0.0878. No significant difference was observed between K_d values obtained from equilibrium saturation and association kinetic assays, indicating that **3-29** binding to A_1 AR follows the law of mass action. Additionally, the one-hour incubation in saturation binding assays appears sufficient to reach equilibrium. Data are presented as the mean ± SEM from five independent experiments.

3.2.3 Conclusion and Summary

In this chapter, four **1-56** LD probe analogues (**3-15**, **3-16**, **3-21**, and **3-22**) and a reversible hydrolysis stable anilide analogue (**3-29**) were synthesised. Binding affinity screening of the four LD probe analogues across the four AR subtypes revealed varying degrees of improved selectivity between A_1 and A_{2A} ARs, ranging from an 8.2- to 18.9-fold increase compared to the 5.9-fold selectivity of **1-56**, while maintaining selectivity against A_{2B} and A_3 ARs. However, the observed selectivity did not fully align with computational predictions, potentially due to the molecular docking simulations being performed with the congener rather than the intact LD probe, which exceeded the size constraints of standard docking algorithms.

Subsequent dissociation assays and in-gel fluorescence scans for A_1 ARs provided evidence that the four novel LD probes covalently labelled A_1 ARs, whereas the reversible analogue **3-29**, which contains a 2-fluorophenyl amide group, lacked covalent labelling capability. To confirm that the newly synthesised LD probes did not obstruct the orthosteric binding pocket of A_1 ARs, internalisation-based experiments were conducted. The NanoBiT internalisation assay and agonist-induced internalisation observed *via* confocal microscopy demonstrated a dose-dependent internalisation of LD probe-tagged A_1 ARs upon NECA treatment, and well-colocalised fluorescence clusters inside cells in confocal images. These findings suggest that the orthosteric binding pocket of A_1 ARs labelled by the LD probes remained accessible to NECA, CCPA, and DPCPX. However, since complete (100%) labelling of A_1 ARs could not be confirmed, the observed internalisation was mediated by unlabelled A_1 ARs cannot be entirely ruled out.

To determine the specific labelling site on A_1 ARs, point-mutation studies were conducted. The incomplete reversibility observed in mutated A_1 ARs, along with the presence of other potential nucleophilic residues, suggested that **3-22** may label multiple residues rather than a single site. Given these findings, a more precise approach, such as LC-MS, would be preferable for identifying the exact labelling position rather than relying on binding reversibility analysis using multiple-mutated A_1 ARs.

In addition to evaluating the new LD probes, **3-29** was also characterised. Dissociation assays and in-gel fluorescence scans confirmed its reversible binding properties, with covalent transfer occurring *via* a 2-fluorophenyl ester moiety rather than a 2-fluorophenyl amide, as demonstrated by direct comparison with LD probe **3-34**. Furthermore, its kinetic profile was assessed through the association assay.

In conclusion, **3-15** was identified as an LD probe capable of transferring a sulfoCy5 moiety onto A_1 ARs, exhibiting the highest A_1/A_{2A} selectivity at this stage. Although its selectivity was improved compared to the lead compound **1-56**, further optimisation remained necessary.

Chapter 4: Optimisation, Synthesis, and Pharmacological Evaluation of a Two-Phase Labelling Probe for A_1 AR

4.1 Introduction

4.1.1 General Introduction

Ligand-directed (LD) covalent labelling probes offer an alternative method for labelling proteins of interest (POIs) with covalently attached reporters[88,162]. Unlike fluorescent protein tags (e.g., GFP[79]) and self-labelling protein tags (e.g., SNAP-tag[82,122] and CLIP-tag[122]), which require genetic engineering, LD probes utilise chemical labelling[88,162]. The reporters (e.g., biotin, fluorophores) transferred by LD probes are significantly smaller than fluorescent protein tags and self-labelling protein tags, thereby minimising their impact on the POI[88]. The choice of reporter depends on the specific POI and the experimental design. For instance, an LD probe transferring a biotin tag can facilitate protein extraction from live cells or cell lysates using streptavidin-coated beads or resins. Conversely, an LD probe transferring a fluorescent tag can be employed to investigate POI localisation and trafficking[74,113]. However, synthesising selective LD probes that deliver various reporters for a specific POI is challenging. The preparation of a well-characterised LD probe involves extensive chemical synthesis and comprehensive pharmacological investigations. Conjugating a new reporter may alter ligand binding affinity and/or subtype selectivity from the original template probe[60,68], necessitating structural tuning and repeated pharmacological evaluations, which can be inefficient and exhaustive.

The combination of LD probes and click reactions presents a promising solution. LD probes transfer a click reaction handle onto the POI, followed by the corresponding click reaction partner to achieve reporter attachment. This approach allows the same LD probe to be used with various reporters tethered to the click reaction partner, satisfying the need for different reporters in pharmacological investigations. In Chapter 1, four click reactions applied in biomolecular studies were discussed: Staudinger ligation[101,104,163], Cu(I)-Catalysed Azide-Alkyne Click Reaction (CuAAC)[105,112,163], Strain-Promoted Azide-Alkyne Cycloaddition (SPAAC)[108,163,164], and Inverse Electron Demand Diels-Alder Reaction (IEDDA)[110,163,165]. Each reaction has its strengths and weaknesses. Considering the reaction rate (IEDDA and CuAAC are much faster than Staudinger ligation and SPAAC)[166] and cytotoxicity concerns (Cu(I) ion in CuAAC)[106,166], IEDDA is deemed a suitable choice for combination with LD probes.

4.1.2 Inverse Electron Demand Diels-Alder Reaction (IEDDA) Introduction

Bioorthogonal labelling through IEDDA was first introduced in 2008 by two groups: Devaraj[167] and Blackman[165]. Devaraj demonstrated live cell imaging with SKBR3 cancer cells expressing Her2/neu receptors (another term for Her2, a transmembrane protein in epidermal growth factor receptor family)[167,168]. Trastuzumab (a Her2 selective antibody) coupled with norbornene (a dienophile) and rhodamine (reporter) was applied to SKBR3 cells[167]. A tetrazine attached to Vivo Tag 680 (VT680)[169,170] reacted with norbornene, producing a Near-IR signal that colocalised with the rhodamine signal, demonstrating successful labelling in live cells[167] (**Figure 4-1**). Blackman reported protein-thioredoxin labelling through *trans*-cyclooctene (TCO) and a tetrazine partner, verified by mass spectrometry[165]. These cases highlighted IEDDA as a fast and metal-free click reaction[165,167]. The Diels-Alder reaction is a [4 + 2] cycloaddition involving a diene and a dienophile, forming two new σ bonds and collapsing two π bonds[171]. The energy gap is illustrated in the frontier orbitals (**Figure 4-2**)[172]. Typically, the Diels-Alder reaction involves an electron-rich diene and an electron-deficient dienophile to minimise the energy gap between the highest occupied molecular orbital (HOMO) of the diene and the lowest unoccupied molecular orbital (LUMO) of the dienophile[171,172]. In IEDDA, an electron-deficient diene and an electron-rich dienophile are used, with the LUMO of the diene and the HOMO of the dienophile involved[171,172]. The energy gap can be minimised by introducing electron-withdrawing groups (EWGs) on the diene and electron-donating groups (EDGs) on the dienophile[171,172]. This reverse electron demand pattern gives the reaction its name: inverse electron demand Diels-Alder reaction[171].

Various dienes and dienophiles have been investigated to enhance the IEDDA reaction rate. Among dienophiles, EDGs can elevate the reaction rate, and the strain effect from cycloalkenes also promotes the reaction rate[172–174]. TCO significantly improves the reaction rate by releasing ring strain and its unique "crown" conformation, which closely resembles the transition state, requiring less energy[171,172,175]. Several ring-fused TCO derivatives have been studied[174–176]. Cyclopropane-fused TCO further increases the reaction speed but has inferior stability, isomerising to the *cis* form faster than the original TCO[174,175]. *Cis*-dioxolane-fused TCO improves stability but decreases the reaction rate due to reduced electron density in the dienophile[174,176].

Dienes have also been extensively studied[172,174]. 1,2,4,5-Tetrazine creates an electron-deficient diene by incorporating heteroatoms and prevents the reverse reaction by releasing nitrogen gas after the IEDDA reaction[171,172,177]. Further modifications of 1,2,4,5-tetrazine at positions 3 and 6 have been explored. The

reaction rate can theoretically be enhanced by introducing EWGs[171] or limiting tetrazine distortion[178], but these modifications may introduce steric hindrance or result in less stable tetrazine derivatives[172,174]. Chen *et al.* (2016)[166] reviewed the reaction rates of various dienes and dienophiles, summarising their findings in a table.
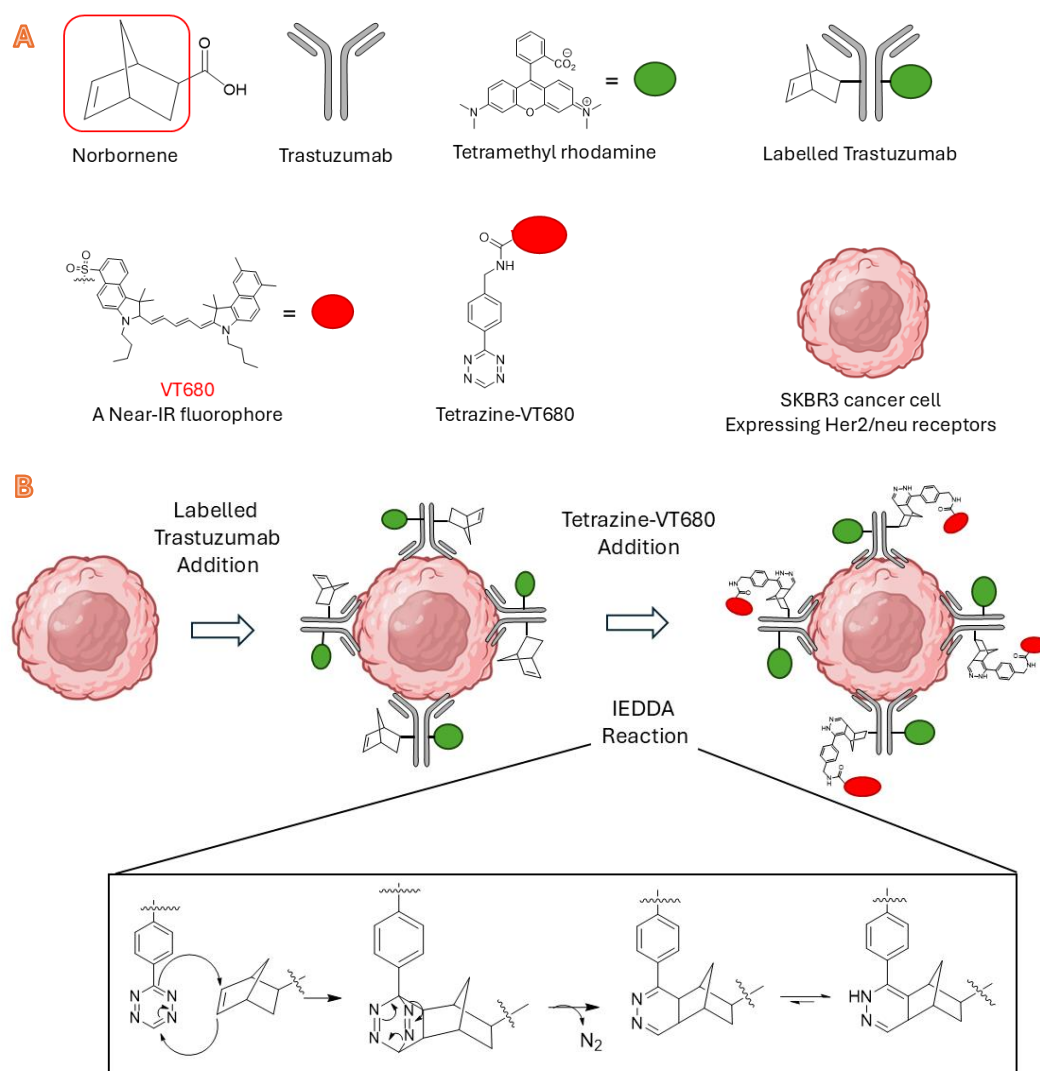
Figure 4-1. Schematic Representation of Her2/neu Receptor Labelling in SKBR3 cells using Modified Trastuzumab and Tetrazine-Conjugated VT680.
(**A**) Key annotations corresponding to the schematic illustration in panel (**B**). The Her2/neu-specific monoclonal antibody, Trastuzumab, is functionalised with norbornene (a dienophile) and rhodamine (a fluorophore) to generate the labelled antibody. (**B**) SKBR3 breast cancer cells, which overexpress Her2/neu receptors, are first incubated with the labelled Trastuzumab for primary targeting. Subsequently, tetrazine-conjugated VivoTag680 (VT680) is introduced, enabling a covalent cycloaddition with the norbornene moiety *via* an inverse electron-demand Diels–Alder (IEDDA) reaction. This schematic is adapted from Devaraj *et al.* (2008)[167] and created using BioRender (www.biorender.com).
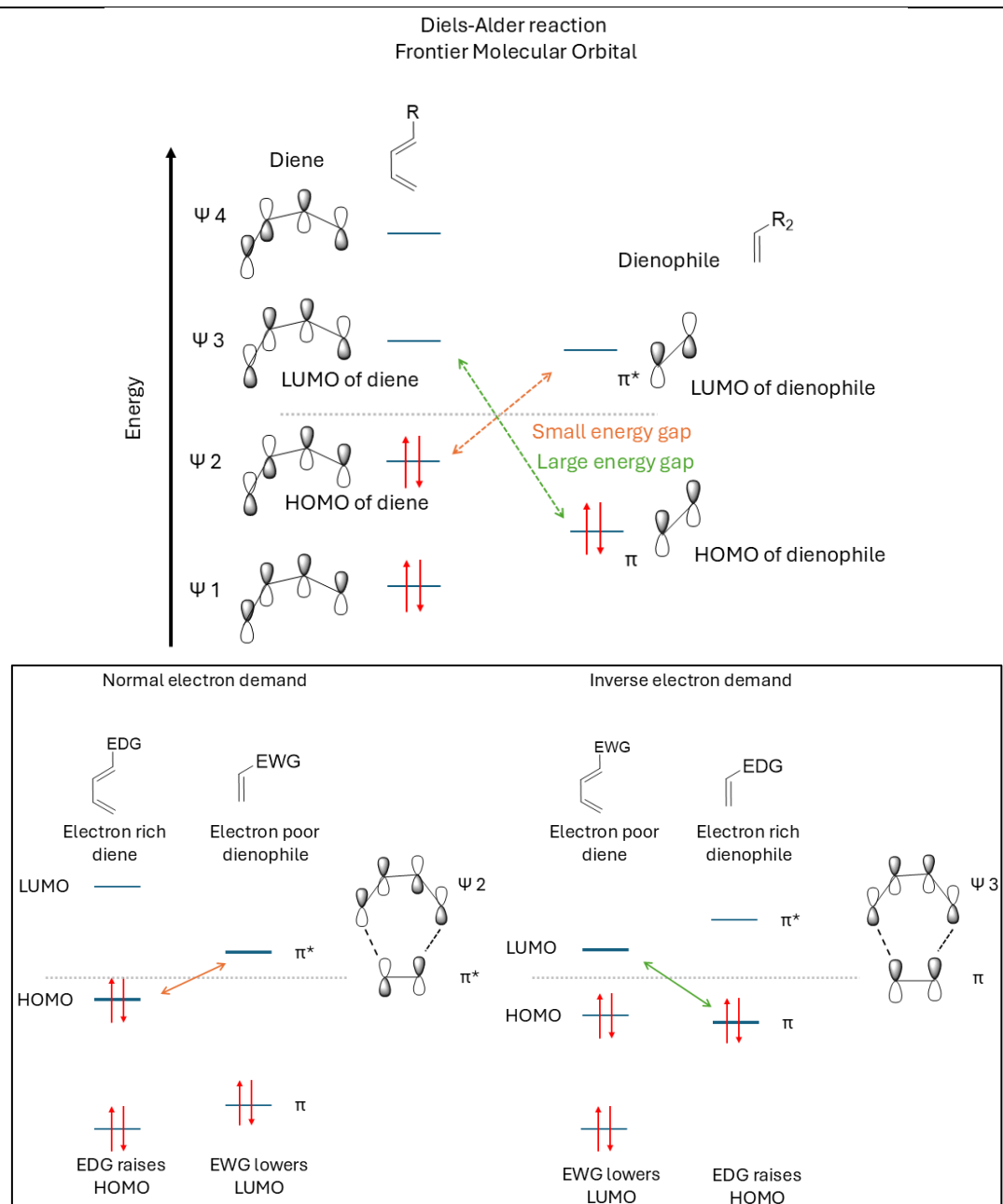
Figure 4-2. Illustration of Frontier Molecular Orbitals in the Diels-Alder and Inverse Electron Demand Diels-Alder Reactions.
The top panel depicts two possible paired orbitals between the diene and dienophile. The bottom panel illustrates the energy gap minimisation strategies in both reactions: the left part shows the normal electron demand Diels-Alder reaction, where the energy gap between the reactants is minimised by incorporating electron-donating groups (EDGs) on the diene and electron-withdrawing groups (EWGs) on the dienophile. The right part depicts the inverse electron demand Diels-Alder reaction, where the EDGs and EWGs are positioned on the dienophile and diene, respectively, opposite to the normal Diels-Alder reaction. Figures modify from Oliveira *et al*., 2017[172].

4.1.3 Aim of This Study

Comeo *et al*. (2024)[74] demonstrated the combination of LD probes and click reactions by covalently labelling A_1 ARs with a TCO handle *via* LD probe (**1-57, Figure 4-3**) in phase 1 labelling, followed by methyl tetrazine sulfoCy5 (MTCy5) in phase 2 labelling. This approach offered a broader selection of reporters by switching phase 2 labelling reagents. However, the labelling efficiency was not as high as its analogue (**1-56, Figure 4-3**), which directly labelled A_1 AR with SulfoCy5. This result was expected, as **1-57** requires an additional IEDDA labelling step. Similar to organic synthesis, the overall yield decreases with more steps in the synthesis scheme. Additionally, GPCRs have low expression levels, so two sequential reactions with extremely low concentration reactants (A_1 ARs) resulted in inferior labelling efficiency.

To improve the labelling efficiency of **1-57**, three aspects were investigated. First, structural modifications were made to enhance the efficiency of TCO cargo transfer to A_1 AR. Second, the cell incubation environment was optimised to minimise LD probe degradation before TCO cargo transfer. Third, methyl-tetrazine sulfoCy5 (MTCy5) was replaced with tetrazine-sulfoCy5 (HTCy5) to enhance the IEDDA reaction rate by removing the EDG on the diene[166]. Finally, the flexibility of the biosensor transferred to A_1 AR through this system provided an alternative method to assess orthosteric binding pocket accessibility after LD probe labelsing using a reversible ligand (**3-29, Figure 4-3**) in a distance-sensitive BRET approach.
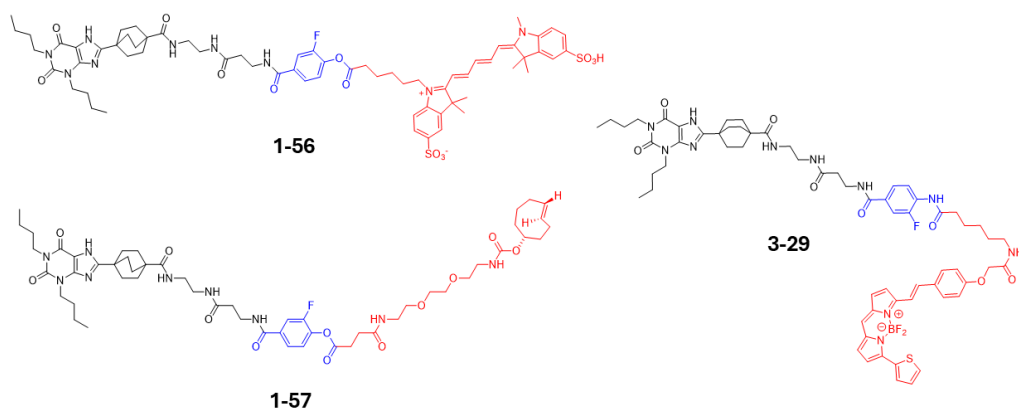
Figure 4-3. Chemical Structures of Probes 1-56, 1-57, and 3-29.
Probe **1-56** functions as a LD probe that directly transfers a SulfoCy5 fluorophore onto A_1 ARs. Probe **1-57**, in contrast, transfers a *trans*-cyclooctene (TCO) handle for subsequent bioorthogonal labelling. Probe **3-29** is a reversible ligand targeting A_1, A_{2A}, and A_{2B} AR subtypes, incorporating a phenyl amide moiety and a BODIPY630/650 fluorophore for fluorescence-based detection.

4.2 Design of the Two-Phase Labelling Probe **1-57** Analogue

Structural modifications focused on the linker region and the position of the 2-fluorophenyl ester, following the same strategy employed for **1-56** analogues in Chapter 3. Among four tested linker and ester configurations, the γ-aminobutyric acid (GABA) linker with a *meta*-2-fluorophenyl ester was selected for **1-57** modification. This composition yielded the highest A_1 AR-specific binding signal among the four **1-56** analogues, demonstrating nearly a twofold intensity (**Chapter 3**, **Section 3.2.2.1**, **Figure 3-9**). The enhanced binding signal likely resulted from improved spatial orientation and proximity between the transferred cargo and NLuc, as well as increased cargo transfer efficiency. Additionally, the corresponding **1-56** analogue (probe **3-22**) incorporating this modification exhibited a 2-fold increase in A_1/A_{2A} selectivity compared to **1-56** (**Chapter 3 Section 3.2.2.1, Table 3-5**), further supporting the rationale for the **1-57** analogue design.

4.3 Results and Discussion

4.3.1 Chemistry

4.3.1.1 Synthesis

The synthesis of the **1-57** analogue is outlined in **Scheme 4-1**. This analogue was synthesised by conjugating compound **3-20** with a click-reactive cargo containing TCO. All synthetic procedures were adapted from Comeo's previously reported method, with minor modifications.

Cargo synthesis commenced with the coupling of commercially available precursor **4-1** with succinic anhydride, yielding intermediate **4-2**. In this step, **4-1** was dissolved in chloroform ($CHCl_3$) and cooled to 0°C in an ice bath before the addition of succinic anhydride. The reaction mixture was then subjected to solvent evaporation, followed by purification *via* automated flash column chromatography. The next step involved TCO conjugation. First, *t*-Boc deprotection of **4-2** was carried out using HCl, yielding intermediate **4-3** as hydrochloride salt. The resulting alkyl amine in DIPEA neutralised **4-3** was subsequently coupled with TCO-NHS ester (a commercially available preactivated TCO) in DMF at room temperature overnight. To maximise yield and maintain TCO stability—given its sensitivity to light and propensity to isomerise into *cis*-cyclooctene—the reaction was conducted under nitrogen with minimal light exposure. The crude product was purified *via* flash column chromatography, affording intermediate **4-4**. The final step involved coupling the congener **3-20** with the TCO-functionalised cargo (**4-4**). First**, 4-4** was activated using BEP and DIPEA in DMF, followed by the addition of **3-20**. The reaction was carried out at room temperature in the dark overnight. The crude product was purified *via* RP-HPLC using a C8 semipreparative column, and the collected fraction was lyophilised to yield the final compound **4-5**, a **1-57** analogue.

Scheme 4-1. Schematic illustration of **4-5** synthesis
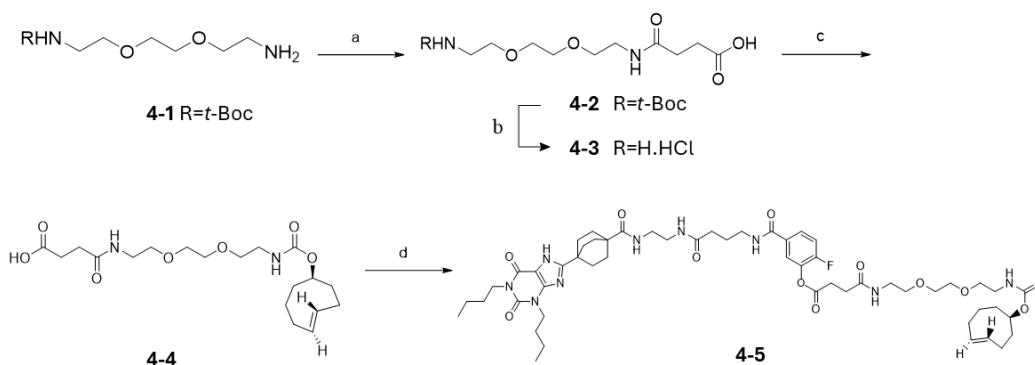
ª Reagents and conditions: a) 1: 0°C, $CHCl_3$, 20 min; 2: succinic anhydride, rt, overnight, 36%; b) 4 N HCl in dioxane, rt, 1 hr; c)TCO-NHS ester, DIPEA, DMF, rt, N_2, avoid light, overnight, 63%; d) BEP, DIPEA, DMF, compound **3-20**, rt, avoid light, overnight, 49%.

4.3.2 Pharmacology

Prior to pharmacological assessment, compound **4-5** was verified using NMR and high-resolution mass spectrometry (HRMS), with an error margin of less than 10 ppm between calculated and observed values. The purity exceeded 95%, as determined by analytical reverse-phase high-performance liquid chromatography (RP-HPLC). The NMR, HRMS, and RP-HPLC spectra are presented in **Chapter 2, Section 2.2.8**.

4.3.2.1 AR Subtype Affinity Screening

Initially, the affinity of compound **4-5** for the A_1 AR was screened to ensure retention of binding ability following structural modification. Unlike fluorescent probes assessed with BRET-based saturation binding assays, a BRET-based competition binding assay was employed to evaluate the binding affinity of compound **4-5**. This competition assay measures the binding of a fixed concentration of a fluorescent ligand in the presence of varying concentrations of test probes, rather than directly measuring the binding of the test probe[70]. From this assessment, the concentration of test ligand required to displace 50% of fluorescent ligand from A_1 ARs can be calculated (IC_{50}) and converted into the inhibitory constant (K_i) using the Cheng-Prusoff equation[159,179]. HEK293T cells stably expressing NLuc-A_1 ARs were used as the cell model for the BRET signal measurement from NLuc-tag on the *N*-terminus of A_1 AR and the CA200645. In this assay, cells were incubated with 15 nM of CA200645 and varying concentrations of probe **4-5** or DPCPX (as a control) ranging from 0.1 nM to 10 μM for one hour, followed by furimazine treatment. After a 5-minute incubation, the plate was read using a plate reader, and the competition binding curves are displayed in **Figure 4-4(A)**. Detailed experimental procedures are described in **Chapter 2, Section 2.1.2.2**.

Compound **4-5** demonstrated displacement ability, as evidenced by a decreased CA200645 BRET ratio with increasing concentrations of **4-5**, similar to the DPCPX set. These results indicate that the phenyl ester position modification preserved A_1 AR binding.

To obtain binding affinity information for the other three AR subtypes, competition binding assays were conducted with cells expressing NLuc-hA_{2A}, NLuc-hA_{2B}, and NLuc-hA_3 ARs, using subtype-selective antagonists as controls (ZM241385 for A_{2A}, PSB603 for A_{2B}, and MRS1220 for A_3). 15 nM of CA200645 was used as the fluorescent ligand. Detailed experimental procedures are described in **Chapter 2, Section 2.1.2.2**.

The normalised specific binding curves for compound **4-5** across the four AR subtypes and the pK_i values are presented in **Figure 4-4(B)** and **Table 4-1**

respectively. Compared to probe **1-57** reported by Comeo, compound **4-5** exhibited enhanced selectivity for A_1/A_{2B} receptors while maintaining selectivity for A_1/A_{2A} and A_1/A_3 receptors.
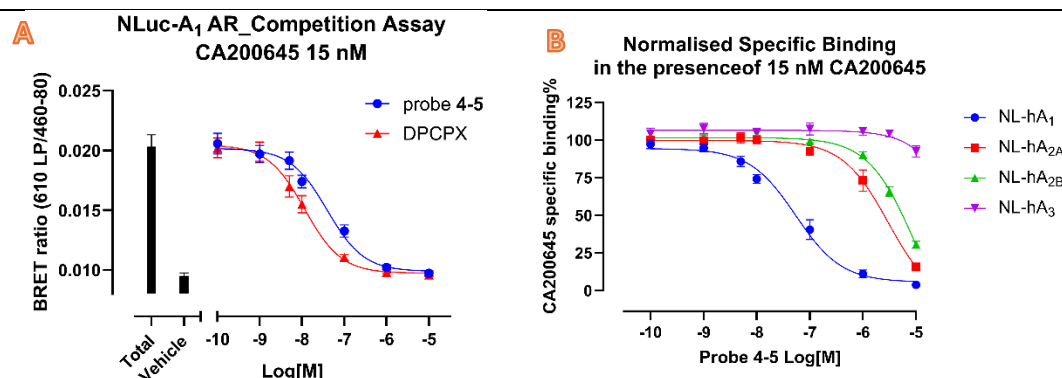
Figure 4-4. Competition Binding Graphs for Probe 4-5.
(A) Competition binding assay with HEK293T cells stably expressing NLuc-hA$_1$ARs. CA200645 (15 nM) was used as the fluorescent ligand, and DPCPX served as the control. The BRET signal decreased with increasing concentrations of **4-5** and DPCPX, indicating that both ligands can bind to A_1 ARs and displace CA200645. The total signal was defined by cells treated only with 15 nM CA200645, while the vehicle control represented cells incubated with HBSS. Data are presented as the mean ± SEM from five independent experiments conducted in triplicate. **(B) Normalised specific binding curves for probes 4–5 across all AR subtypes.** Competition binding assays were performed using 15 nM CA200645 as the fluorescent ligand across four AR subtypes. To enable comparison across subtypes within a single figure, specific binding values were normalised for each receptor. Total binding was defined as the BRET ratio from cells incubated with CA200645 alone. Non-specific binding (NSB) was determined by co-incubation with 10 μM of a subtype-selective antagonist: DPCPX for A_1, ZM241385 for A_{2A} and A_3, and PSB603 for A_{2B}. Specific binding was calculated by subtracting NSB from total binding, and normalised to define 100% specific binding. The resulting curves represent normalised specific binding of CA200645 in the presence of increasing concentrations of probes **4–5**, fitted using a one-site competition binding model. Data are presented as mean ± SEM from five independent experiments (four for A_{2A}), each conducted in triplicate.

162

Table 4-1. Probe **4-5** and its template probe (**1-57**) pK_i values

Probe	Human adenosine receptor affinity (pK_i ± SEM)				A$_1$/A$_{2A}$ selectivity (folds)[e]
	NLuc-hA$_1$	NLuc-hA$_{2A}$	NLuc-hA$_{2B}$	NLuc-hA$_3$	
1-57[a]	7.87 ± 0.16 (4)	5.86 ± 0.03 (4)	6.09 ± 0.06 (4)	< 5 (3)[d]	102.3
4-5[b]	7.78 ± 0.13 (5)	5.73 ± 0.05 (4)	5.39 ± 0.01 (5)	< 5 (5)[d]	112.2
DPCPX[c]	8.25 ± 0.06 (5)				
ZM241385[c]		8.52 ± 0.03 (6)			
PSB603[c]			8.48 ± 0.08 (5)		
MRS1220[c]				8.82 ± 0.15 (5)	

[a] pK_i for probe **1-57** was reported by Comeo[74] *et al.*. [b] pK_i values were calculated as the negative logarithm of the equilibrium inhibitory constant (K_i in M) through competition binding assay with 15 nM of CA200645 as the fluorescent ligand. [c] Selective adenosine subtype antagonist served as the control in respective competition binding assay. The measured pK_i values were consistent with previous studies (DPCPX[74], ZM241385[117], PSB603[121], and MRS1220[70]). [d] K_i cannot be determined below 10 μM of ligand concentration. [e] Selectivity ratios were calculated as the antilogarithm of the difference between pK_i values for A$_1$ and A$_{2A}$ receptors (i.e., 10^(pK_i-A$_1$ − pK_i-A$_{2A}$)). Data are presented as the mean ± SEM from *n* independent experiments (indicated in parentheses) conducted in triplicate. NLuc-hA$_1$ ARs were stably expressed in HEK293T cells. NLuc-hA$_{2B}$ and hA$_3$ ARs were stably expressed in HEK293G cells, while NLuc-hA$_{2A}$ ARs were transiently expressed in HEK293T cells.

4.3.2.2 Click Reaction Condition Investigation

4.3.2.2.1 Incubation Duration for Click Reaction

The binding of probe **4-5** to A$_1$ ARs was previously validated *via* competition binding assays, yielding a K_i value of 19.86 ± 4.31 nM (**Table 4-1**). However, it remained unclear whether the click-reactive moiety (*trans*-cyclooctene, TCO) on probe **4-5** was successfully transferred to A$_1$ ARs. To investigate this, cells were treated with the complementary click partner, methyl-tetrazine-sulfoCy5 (MTCy5), and the resulting fluorescence signal was measured.

For this experiment, a suitable cellular model expressing A$_1$ ARs was required. HEK293G cells stably expressing Twin-Strep-SNAP-tagged A$_1$ ARs (TS-SNAP-A$_1$ ARs), previously established in our laboratory for receptor pull-down assays, were employed. The presence of the TS and SNAP tags was previously shown not to interfere the covalent labelling of A$_1$ ARs with probes **3-15**, **3-34**, and **3-35** (**Chapter 3, Figure 3-14**). Thus, these cells were deemed appropriate for evaluating the transfer of the TCO moiety from probe **4-5** to A$_1$ ARs.

Probe **1-56**, a sulfoCy5-conjugated transfer probe previously demonstrated by Comeo[74] *et al.* to covalently label A$_1$ ARs, was used as a positive control. A time-

course experiment was conducted to determine the duration required for the two-step labelling system (probe **4-5** followed by MTCy5) to achieve fluorescence intensity comparable to that of the direct labelling by probe **1-56**.

HEK293G cells stably expressing TS-SNAP-A$_1$ ARs were seeded in black 96-well plates at a density of 30,000–35,000 cells per well one day prior to the experiment. On the day of the assay, the culture medium was aspirated, and cells were washed once with warm phosphate-buffered saline (PBS). Cells were then incubated with 250 nM of either probe **4-5** or probe **1-56** for 3 hours. Following this initial labelling step, cells were washed and the medium was replaced with DMEM-D6546. 1 μM MTCy5 was added to wells pre-labelled with probe **4-5** at various time points ranging from 15 minutes to 3 hours. At the end of the second labelling phase, the medium was removed, and cells were washed twice with PBS. HEPES-buffered saline solution (HBSS) was added to each well in preparation for fluorescence measurement. Detailed experimental procedures are provided in **Chapter 2, Section 2.1.8.1**.

The measured fluorescence intensity is presented in **Figure 4-5**. The fluorescence intensity from the two-phase labelling (sequential incubation with probe **4-5** and MTCy5) increased with longer incubation times. Only the 3-hour MTCy5 incubation yielded a fluorescence intensity comparable to direct labelling with probe **1-56**. No significant differences were observed between the sets incubated with MTCy5 for 15 minutes and 30 minutes, or between the sets incubated for 1 hour and 2 hours. These results suggest that a minimum of 3 hours of incubation with MTCy5 is required to achieve a similar A$_1$ AR labelling effect as probe **1-56**, likely due to the low concentration of A$_1$ ARs in the system. In chemical synthesis, effective molecular collisions with sufficient energy are essential for a reaction to proceed. In the case of probe **1-56**, labelling occurred efficiently even at low concentrations of TS-SNAP-A$_1$ ARs (nanomolar or even lower). For probe **4-5**, however, the labelling process involved a two-step mechanism: initial transfer of the TCO group to TS-SNAP-A$_1$ ARs, followed by a click reaction with the complementary partner, MTCy5. This second step relies on the successful reaction between low concentrations of TCO-tagged receptors and MTCy5.

Unlike reactions conducted in a controlled chemical environment, cellular systems present a more complex milieu, particularly due to the diverse components present on the cell membrane. This complexity, combined with the inherently lower probability of effective molecular collisions in the two-step labelling system of probe **4-5**, likely necessitates a longer incubation period to achieve fluorescence intensities comparable to those observed with probe **1-56**.
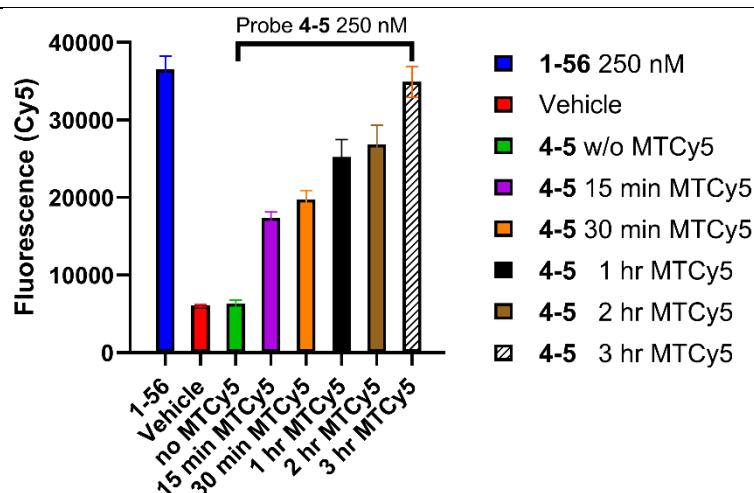
Figure 4-5. Incubation Duration for Click Reaction.
The graph displays fluorescence intensity from cells pre-labelled with 250 nM of probe **4-5**, subjected to various incubation times with methyl-Tetrazine-sulfoCy5 (MTCy5). Fluorescence intensity from probe **1-56** served as the control. Only the fluorescence intensity after 3 hours of MTCy5 incubation was comparable to that of probe **1-56**. Statistical analysis using one-way ANOVA between revealed a significant difference [$F_{(7, 24)} = 51.23$, $P < 0.0001$]. Post hoc analysis (Tukey's multiple comparisons) indicated no significant difference between probe **1-56** and 3-hour MTCy5 incubation ($P = 0.9963$). All other MTCy5 incubation sets showed significant differences compared to the control (probe **1-56**). Data are presented as the mean ± SEM from four independent experiments conducted in quadruplet.

However, the fluorescence signal observed in the probe labelling system cannot be directly interpreted as evidence of successful **4-5** receptor labelling. Prolonged incubation with 1 µM MTCy5 may lead to increased non-specific binding, thereby confounding the interpretation of fluorescence intensity. Further investigation is required to determine whether the observed increase in fluorescence with extended MTCy5 incubation is attributable to specific labelling or to non-specific interactions.

4.3.2.2.2 Evaluation of Non-Specific Binding of Methyl-tetrazine-SulfoCy5

The time-dependent increase in fluorescence observed in previous assays cannot be conclusively attributed to effective IEDDA labelling on A_1 ARs, as it may also result from non-specific binding (NSB) of MTCy5. To visually assess the NSB of MTCy5, confocal microscopy was employed. For clarity in subsequent interpretations, HEK293T cells transiently expressing SNAP-hA_1ARs were incubated with 1 µM of MTCy5 for varying durations, as depicted in **Figure 4-6**. Detailed experimental procedures are described in **Chapter 2, Section 2.8.1.2**.

The NSB observed *via* the Cy5 channel increased with prolonged MTCy5 incubation. Based on this assessment, it is recommended that incubation with 1 µM of MTCy5 should not exceed 15 minutes, as NSB becomes significantly pronounced.
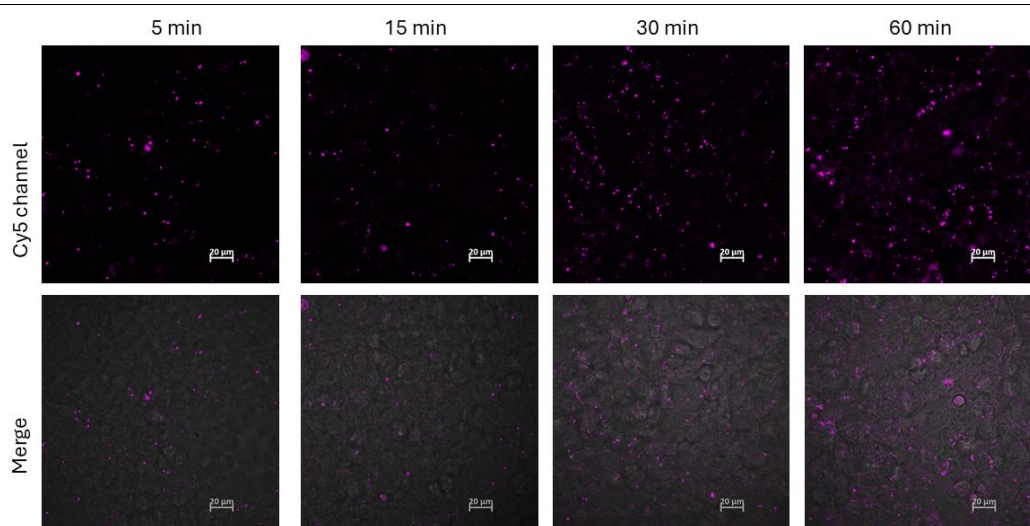
Figure 4-6. Observation of Non-Specific Binding (NSB) of MTCy5 *via* Confocal Microscopy. HEK293T cells transiently expressing SNAP-hA_1 ARs were incubated with 1 µM of MTCy5 for four different durations. Post-incubation, cells were washed twice with PBS, fixed with 4% paraformaldehyde, washed twice again with PBS, and refilled with PBS for imaging. The top frames display images observed in the Cy5 channel at four time points, with brightness and contrast enhanced by 40%. The bottom frames show merged images of the Cy5 and transparent light channels at the same time points, with brightness decreased by 40% and contrast increased by 40%. The NSB of MTCy5 exhibited a time-dependent increase in the Cy5 channel. The scale bar = 20 µm. These images are from a single pilot study.

4.3.2.2.3 Optimal Incubation Period for Probe **4-5** (Phase 1 Labelling)

Prolonged incubation with 1 µM MTCy5 beyond 15 minutes is not recommended for confocal imaging studies due to a marked increase in non-specific binding (NSB) signals. Consequently, the next objective was to determine the optimal incubation duration for probe **4-5** (Phase 1 labelling) to maximise labelling efficiency. This investigation was conducted using confocal microscopy to enable direct visual assessment of labelling outcomes. To evaluate A_1 AR labelling *via* probe **4-5** in combination with MTCy5, a reference fluorescent tag

with a distinct emission wavelength was required. HEK293T cells transiently expressing SNAP-hA$_1$ ARs were utilised for this purpose. The SNAP-tag allowed for fluorescent labelling with SNAP-Surface AF488, serving as a control for receptor localisation and expression.

Cells were prepared in an 8-well chamber slide according to the protocol described in **Chapter 2, Section 2.1.1.4**. For control labelling, cells were incubated with 250 nM SNAP-Surface AF488 for 30 minutes. Following a wash with warm DMEM-D6546, cells were incubated with 100 nM probe **4-5** for either 30 or 60 minutes, with or without pretreatment using 1 µM DPCPX. Upon completion of Phase 1 labelling, cells were washed twice with DMEM-D6546 and subsequently incubated with 1 µM MTCy5 for 5 minutes. Prior to imaging, cells were washed twice with PBS, fixed with 4% paraformaldehyde, washed again twice with PBS, and soaked in PBS in the end. Detailed experimental procedures are provided in **Chapter 2, Section 2.1.8.3**.

As shown in **Figure 4-7A**, A$_1$ ARs were clearly visualised in the AF488 channel, confirming successful labelling *via* the SNAP-tag and the existence of A$_1$ ARs. In contrast, the Cy5 channel revealed minimal A$_1$ AR signal, accompanied by prominent NSB in the DPCPX-pretreated samples following both 30- and 60-minute incubations with 100 nM probe **4-5**. These observations indicated that the initial labelling conditions required optimisation.

The pronounced NSB observed with 1 µM DPCPX pretreatment likely reflects insufficient receptor blockade, allowing residual probe **4-5** binding to A$_1$ ARs. Increasing the DPCPX concentration could therefore improve the definition of NSB signals. Additionally, the weak Cy5 signal suggests a low proportion of A$_1$ ARs successfully labelled with TCO handles *via* probe **4-5**, potentially due to suboptimal Phase 1 labelling efficiency. Extending the incubation period with probe **4-5** was thus considered as a strategy to enhance receptor labelling.

A subsequent experiment was conducted with the following adjustments: the DPCPX concentration was increased from 1 µM to 10 µM to more effectively suppress probe **4-5** specific binding and define NSB, the probe **4-5** incubation time was extended from 1 hour to 2 hours to improve labelling efficiency, and the MTCy5 incubation period was increased to 10 minutes. The results of this condition-optimisation experiment are presented in **Figure 4-7B**.

These preliminary findings suggest that optimal conditions for confocal imaging include a 2-hour incubation with 100 nM probe **4-5** for Phase 1 labelling, 10 µM DPCPX for accurate assessment of NSB, and a 10-minute incubation with 1 µM MTCy5 for Phase 2 labelling.
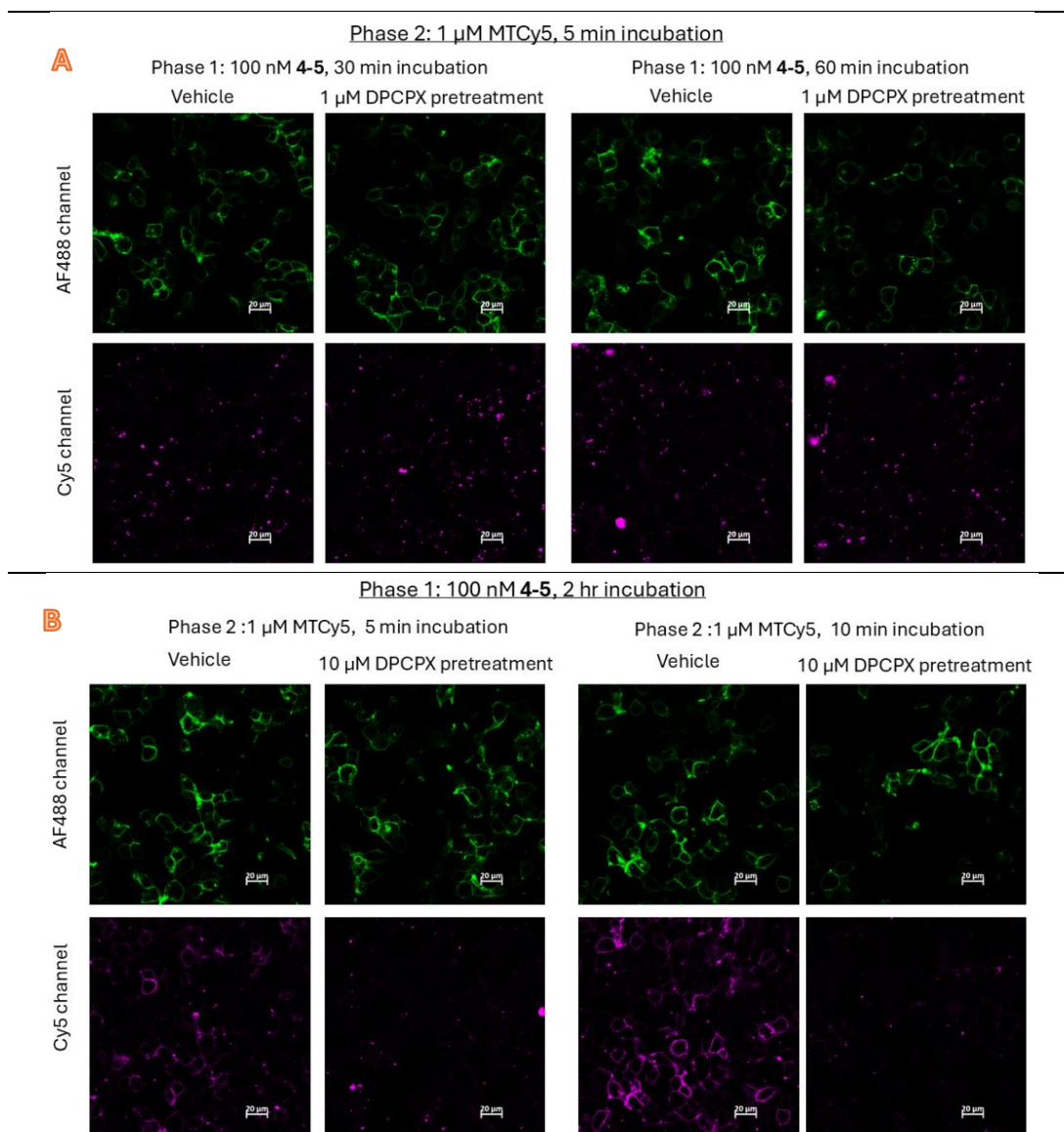
Figure 4-7. Condition Tuning for A_1 AR Labelling Using Probe 4-5 and MTCy5 Observed *via* Confocal Microscopy.

(**A**) HEK293T cells transiently expressing SNAP-hA_1 ARs were first labelled with SNAP-surface AF488 as a control. Subsequently, cells were labelled with 100 nM of probe **4-5** for either 30 or 60 minutes, with or without 1 µM DPCPX pretreatment. A_1 ARs are clearly observed in the AF488 channel, while A_1 AR labelling in Cy5 chanel are indistinguishable between the presence or absence of 1 µM of DPCPX pretreatment. **(B)** Confocal images following condition tuning based on the results in **(A)**. With an extended incubation period for probe **4-5** and increased DPCPX concentration, A_1 ARs are clearly observed in the Cy5 channel and easily distinguish between sets in the presence or absence of DPCPX preincubation. Additionally, a 10-minute incubation with 1 µM MTCy5 provids better A_1 AR labelling in the Cy5 channel with minimal NSB increase. All images were captured with the same signal settings, with a 40% enhancement in brightness and contrast. Scale bar = 20 µm. The images are from a single pilot experiment.

4.3.2.2.4 Phase 2 labelling reagent selection

According to frontier molecular orbital theory(**Figure 4-2**) , attaching an electron-withdrawing group to the diene and an electron-donating group to the dienophile

can minimise the energy gap between the diene's LUMO and the dienophile's HOMO, thereby facilitating the inverse electron-demand Diels-Alder (IEDDA) reaction[171,172]. In probe **4-5**, the dienophile component is fixed as *trans*-cyclooctene (TCO). Therefore, a potential method to enhance the IEDDA reaction is to replace methyl-Tetrazine-sulfoCy5 (MTCy5) with a more reactive click reaction partner. By searching for commercially available TCO-compatible reagents, two types of reporters were identified: those attached to methyl tetrazine and those attached to tetrazine. Given that the methyl group is an electron-donating group, a slower IEDDA reaction in the TCO-methyl tetrazine pair compared to the pair of TCO-tetrazine is anticipated based on frontier molecular orbital theory. Additionally, several studies have reported a faster reaction rate for the TCO-tetrazine pair[166,174].

To evaluate whether Tetrazine-SulfoCy5 (HTCy5) enhances labelling efficiency compared to MTCy5, a confocal microscopy study was conducted. HEK293T cells transiently expressing SNAP-hA$_1$ ARs were used as the cellular model, as the SNAP tag allows for fluorescent labelling with SNAP-Surface AF488, serving as a control for A$_1$ AR expression.

Cells were seeded in an 8-well chamber slide and labelled with 250 nM SNAP-Surface AF488 to visualise A$_1$ ARs as a reference. Phase 1 labelling involved incubation with 100 nM probe **4-5** for 2 hours, with or without pretreatment using 10 µM DPCPX to assess non-specific binding. Phase 2 labelling was performed under four conditions, combining two concentrations (1 µM and 10 µM) of either MTCy5 or HTCy5, each applied for 15 minutes. Following each labelling step, cells were thoroughly washed. At the end of incubation, cells were fixed with 4% paraformaldehyde. Detailed experimental procedures are provided in **Chapter 2, Section 2.1.8.4**.

Figure 4-8A presents the experimental sets in which MTCy5 was used as the Phase 2 labelling reagent, while **Figure 4-8B** displays the corresponding sets labelled with HTCy5. In the Cy5 fluorescence channel, both reagents produced clear labelling of A$_1$ ARs at a concentration of 10 µM, although this was accompanied by increased NSB. At the lower concentration of 1 µM, HTCy5 continued to yield distinct labelling of A$_1$ ARs, whereas MTCy5 produced only faint receptor outlines.

These findings were consistent with theoretical expectations (**Figure 4-2**) and previously reported data[166,174], which indicated that HTCy5 exhibits a faster reaction rate with TCO moieties compared to MTCy5. This enhanced reactivity likely contributed to the improved labelling efficiency observed with HTCy5, particularly at lower concentrations.
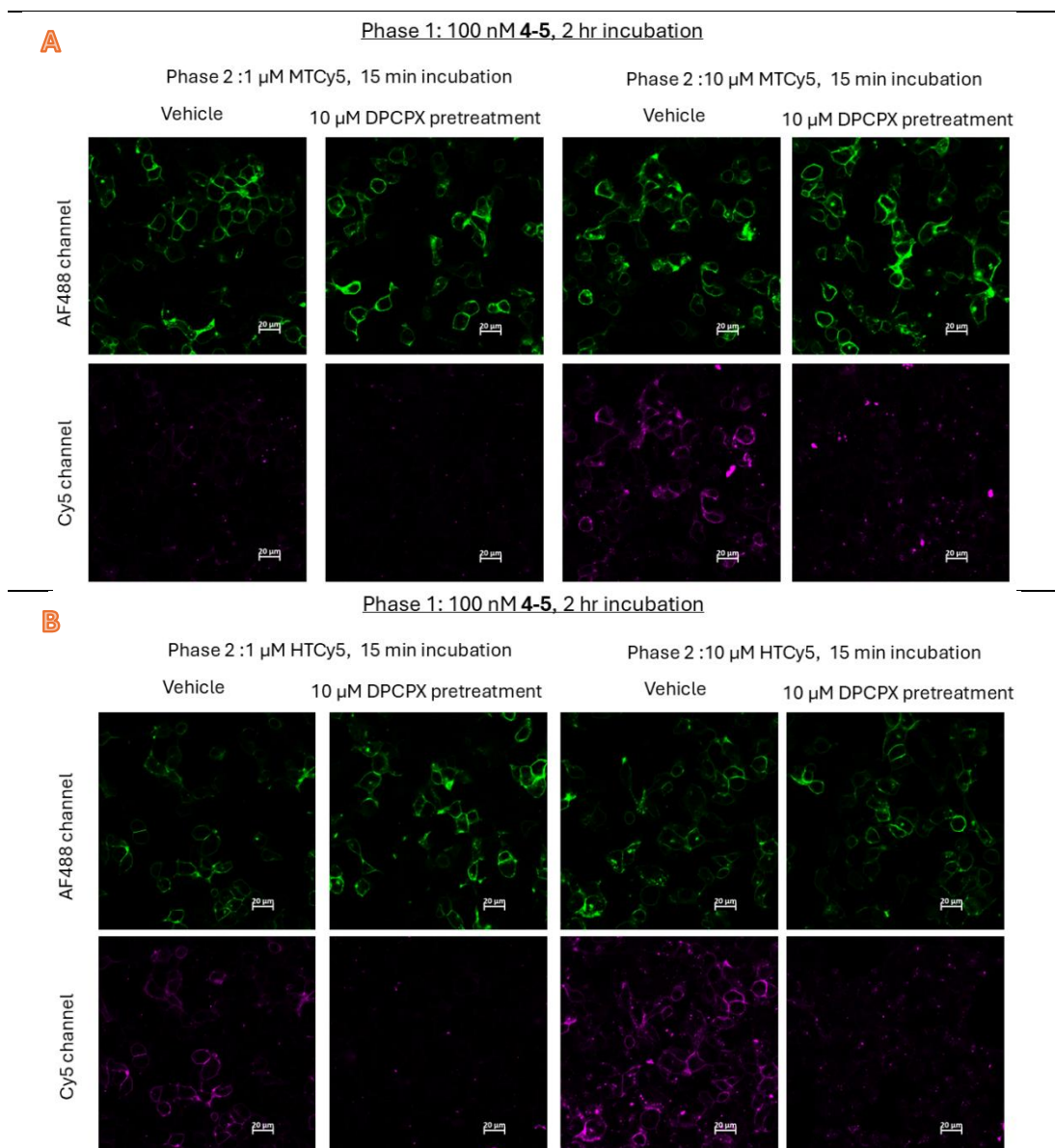
Figure 4-8. Comparison of Phase 2 Labelling Reagents *via* Confocal Imaging.
(**A**) MTCy5 was used at concentrations of 1 µM and 10 µM for phase 2 labelling. In the Cy5 channel, 10 µM provided clear A_1 AR labelling but was accompanied by higher non-specific binding. **(B)** HTCy5 was used at concentrations of 1 µM and 10 µM for phase 2 labelling. A_1 ARs were clearly observed at both concentrations, with lower non-specific binding noted in the 1 µM set. All images were captured with identical signal settings, with a 20% enhancement in brightness and a 40% enhancement in contrast. Scale bar = 20 µm. Images are representative of (A) five and (B) four independent experiments, with each condition performed in duplicate within each experiment.

Membrane intensity quantification was performed using FiJi (ImageJ) by manually drawing the region of interest (ROI), and the results are presented in **Figure 4-9**. The signal intensity from the AF488 channel was similar across all conditions, suggesting comparable A_1 AR expression in these sets. In the Cy5 channel, a significant signal drop in the DPCPX pretreatment arm compared to the paired vehicle arm was observed, indicating that probe **4-5** specific bound to A_1 ARs.
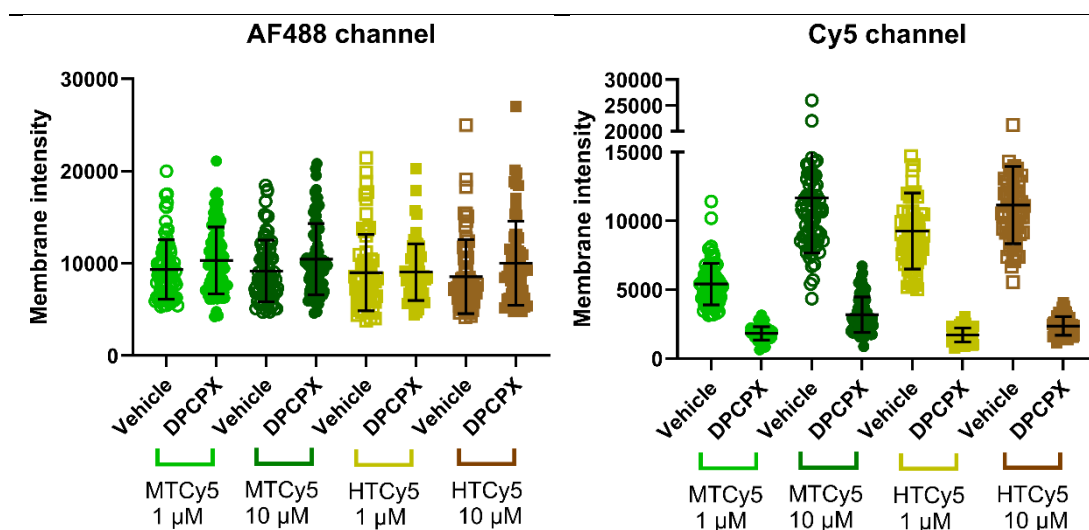
Figure 4-9. Membrane Intensity Quantification *via* Fiji (ImageJ).
The left panel shows the intensity measured from the AF488 channel. Consistent intensity indicated that A_1 AR expression was comparable across these sets. The right panel displays the intensity measured from the Cy5 channel. In each vehicle and DPCPX pretreatment pair, an apparent signal drop was observed, indicating that probe **4-5** labelling was blocked by 10 μM DPCPX. The vehicle in the 1 μM HTCy5 pair showed enhanced signal compared to 1 μM MTCy5, while slightly lower intensity compared to 10 μM MTCy5 or HTCy5. Overall, 1 μM HTCy5 effectively enhanced A_1 AR labelling while maintaining low non-specific binding. Intensity was measured by manually drawing the cell membrane region of interest (ROI) using Fiji (ImageJ) in the AF488 and Cy5 channels. Quantitative data for MTCy5 are presented as the mean ± SD from five independent experiments, with a total of 80 cells analysed. HTCy5 data are presented as the mean ± SD from four independent experiments, comprising a total of 64 cells.

The membrane fluorescence intensity of vehicle-treated samples, measured *via* the Cy5 channel, is presented in **Figure 4-10**. As four of the experimental conditions did not follow a normal distribution (as determined by the Shapiro-Wilk test), the Kruskal-Wallis test was employed for statistical analysis. This test revealed significant differences among the four conditions. Subsequently, Dunn's *post hoc* test was conducted to perform pairwise comparisons. With the exception of the MTCy5 and HTCy5 conditions at 10 μM (P > 0.9999), all other pairwise comparisons showed statistically significant differences. Notably, in the 1 μM comparison between MTCy5 and HTCy5, the P-value was less than 0.0001. The 1 μM HTCy5 condition demonstrated a higher labelling effect compared to 1 μM MTCy5, although it remained lower than the 10 μM MTCy5 condition. This difference was also statistically significant (P = 0.0049). Based on these findings, 1 μM HTCy5 was identified as the optimal condition for Phase 2

labelling in confocal imaging studies. It significantly improved A_1 AR labelling efficiency relative to 1 µM MTCy5 while maintaining low levels of NSB. In contrast, both MTCy5 and HTCy5 at 10 µM exhibited elevated NSB signals, highlighting the advantage of using HTCy5 at lower concentrations.
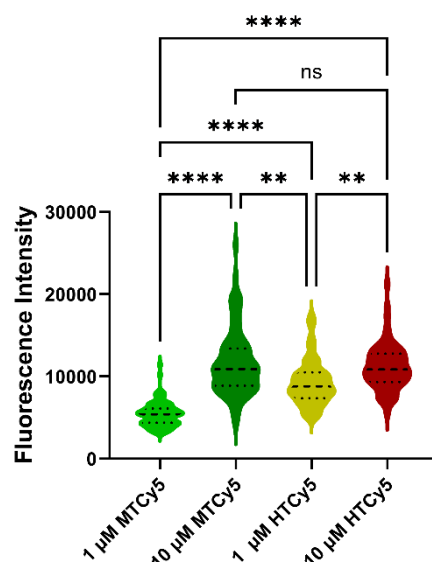
Figure 4-10. Comparison of membrane fluorescence intensity across sets incorporating different Phase 2 reagents and concentrations.
The raw intensity data did not follow a normal distribution; therefore, a Kruskal-Wallis test was performed, revealing significant differences among the groups [$H(3) = 154.5$, $P < 0.0001$]. *Post hoc* analysis using Dunn's multiple comparisons test indicated significant differences between all pairwise comparisons, except between MTCy5 and HTCy5 at 10 µM ($P > 0.9999$). Due to the non-normal distribution, data are presented as violin plots, with dotted lines indicating the median and interquartile range.

4.3.2.2.5 Incubation Media with or without Phenol Red

The final incubation condition assessed was the media. Two different types of Dulbecco's Modified Eagle Medium (DMEM) were available in our lab: one with phenol red as a pH indicator and one without. Previous assessments and the imaging work by Comeo *et al*. (2024)[74] were conducted using DMEM with phenol red. In this experiment, the labelling procedure was repeated as follows: HEK293T cells transiently expressing SNAP-hA$_1$ ARs were labelled with SNAP-surface AF488 for 30 minutes, followed by 100 nM of probe **4-5** for 2 hours in the presence or absence of 10 µM DPCPX pretreatment, and then 15 minutes of 1 µM MTCy5 for phase 2 labelling, with wash steps after each labelling step. The difference in this experiment was that cells were incubated in reagents prepared with DMEM either with or without phenol red in parallel. Samples were fixed and prepared for imaging collection.

The confocal images (**Figure 4-11A**) showed apparent intensity differences in Cy5 channel between sets incubated with DMEM in the presence or absence of

phenol red. The quantified intensity is displayed in **Figure 4-11B**. The signal from the AF488 channel showed similar intensity, indicating consistent A_1 AR expression across the four sets. In the Cy5 channel, the expected signal drop in the DPCPX pretreatment set compared to the vehicle was observed in both media. Additionally, an increased signal intensity from the vehicle in DMEM without phenol red was noted (Mann-Whitney test U=806, P<0.0001).
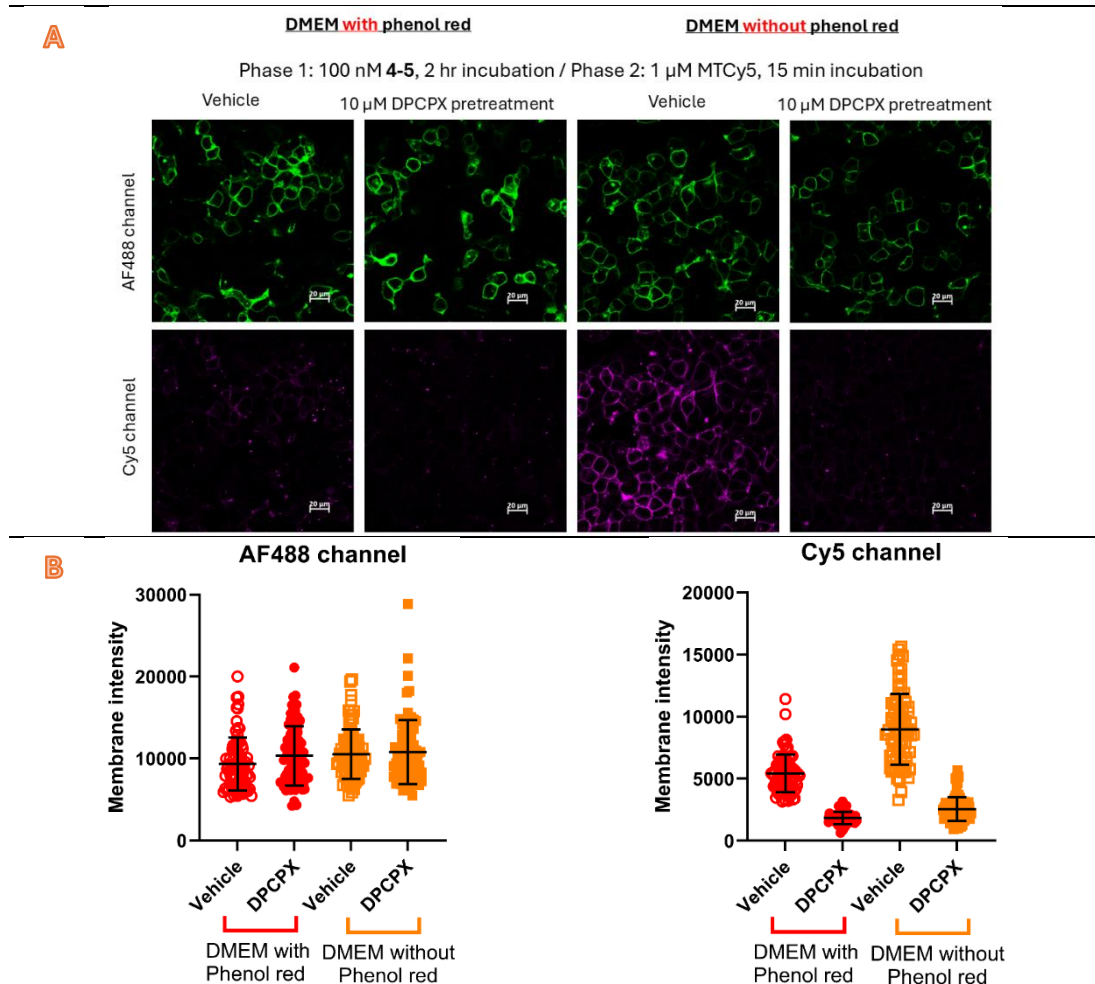
Figure 4-11. Evaluation of Labelling Effects Following Incubation in DMEM With or Without Phenol Red.

(**A**) Representative confocal images from parallel experiments conducted using DMEM either containing or lacking phenol red. SNAP-surface AF488 was used as a control for A_1 AR labelling. In the Cy5 channel, a marked difference in signal intensity is visually apparent between vehicle-treated samples incubated in DMEM with versus without phenol red. Scale bar = 20 μm. Images are representative of five independent experiments, each performed in duplicate. (**B**) Membrane fluorescence intensity was quantified using Fiji (ImageJ) by manually drawing the membrane region of interest (ROI). In the AF488 channel, membrane intensity remained consistent across all four experimental conditions. In contrast, the Cy5 channel revealed a higher intensity in the vehicle group incubated in DMEM without phenol red, in addition to the expected reduction in intensity in the DPCPX-pretreated group relative to its vehicle control. As the raw data did not follow a normal distribution, the Mann–Whitney U test was applied in place of an independent t-test (U = 806, P < 0.0001). Data are presented as the mean ± SD from five independent experiments conducted in duplicate, with a total of 80 cells analysed.

Given that the final labelling effects from DMEM without phenol red were superior to those with phenol red, a subsequent investigation was conducted to determine which labelling step was affected by the media. In this study, HEK293T cells transiently expressing SNAP-hA$_1$ ARs were labelled with SNAP-surface AF488 for 30 minutes, followed by 100 nM of probe **4-5** for 2 hours, and then 1 µM of MTCy5 for phase 2 labelling for 15 minutes, with wash steps after each labelling step. The reagents for probe **4-5** and MTCy5 were prepared using DMEM with or without phenol red. Consequently, phase 1 and phase 2 labelling were performed in two different media, resulting in four condition pairs. Detail experiment procedures were slightly modified from **Chapter 2, Section 2.1.8.5** description. Confocal images and quantified membrane intensity are presented in **Figure 4-12A and B**.

The imaging results indicated that Phase 1 labelling performed in DMEM containing phenol red produced dimmer fluorescence compared to labelling conducted in DMEM without phenol red. Quantitative analysis of the AF488 signal revealed comparable intensities across all four experimental conditions, suggesting consistent A$_1$ AR expression levels. In contrast, the Cy5 channel showed significantly higher signal intensity in samples labelled during Phase 1 with DMEM lacking phenol red.

Membrane-associated Cy5 fluorescence was analysed using the Kruskal–Wallis test due to the non-normal distribution of the data. A statistically significant difference was observed among the groups [$H(3) = 37.78$, $P < 0.0001$]. *Post hoc* analysis using Dunn's multiple comparisons test identified significant differences between groups labelled in DMEM with versus without phenol red during Phase 1, while no significant differences were found between groups differing only in Phase 2 media composition. These findings suggest that the absence of phenol red during Phase 1 enhances A$_1$ AR labelling efficiency.

Phenol red exists in different ionic forms depending on the pH of the environment (as illustrated in **Figure 4-13**). At physiological pH (~7.4), phenol red predominantly exists in its anionic form, with a concentration of approximately 40 µM in DMEM (based on the Sigma-Aldrich DMEM-D6546 formulation, which contains 0.0159 g/L phenol red sodium salt). The phenolic group in phenol red may act as a nucleophile[180], potentially reacting with the 2-fluorophenyl ester moiety in probe **4-5**. Given that probe **4-5** was incubated in DMEM at 37 °C for 2 hours during Phase 1, degradation of the probe may have occurred under these conditions. Therefore, the enhanced labelling observed in **Figure 4-12** is likely attributable to phenol red–mediated degradation of probe **4-5** and/or isomerisation of the *trans*-cyclooctene (TCO) moiety.
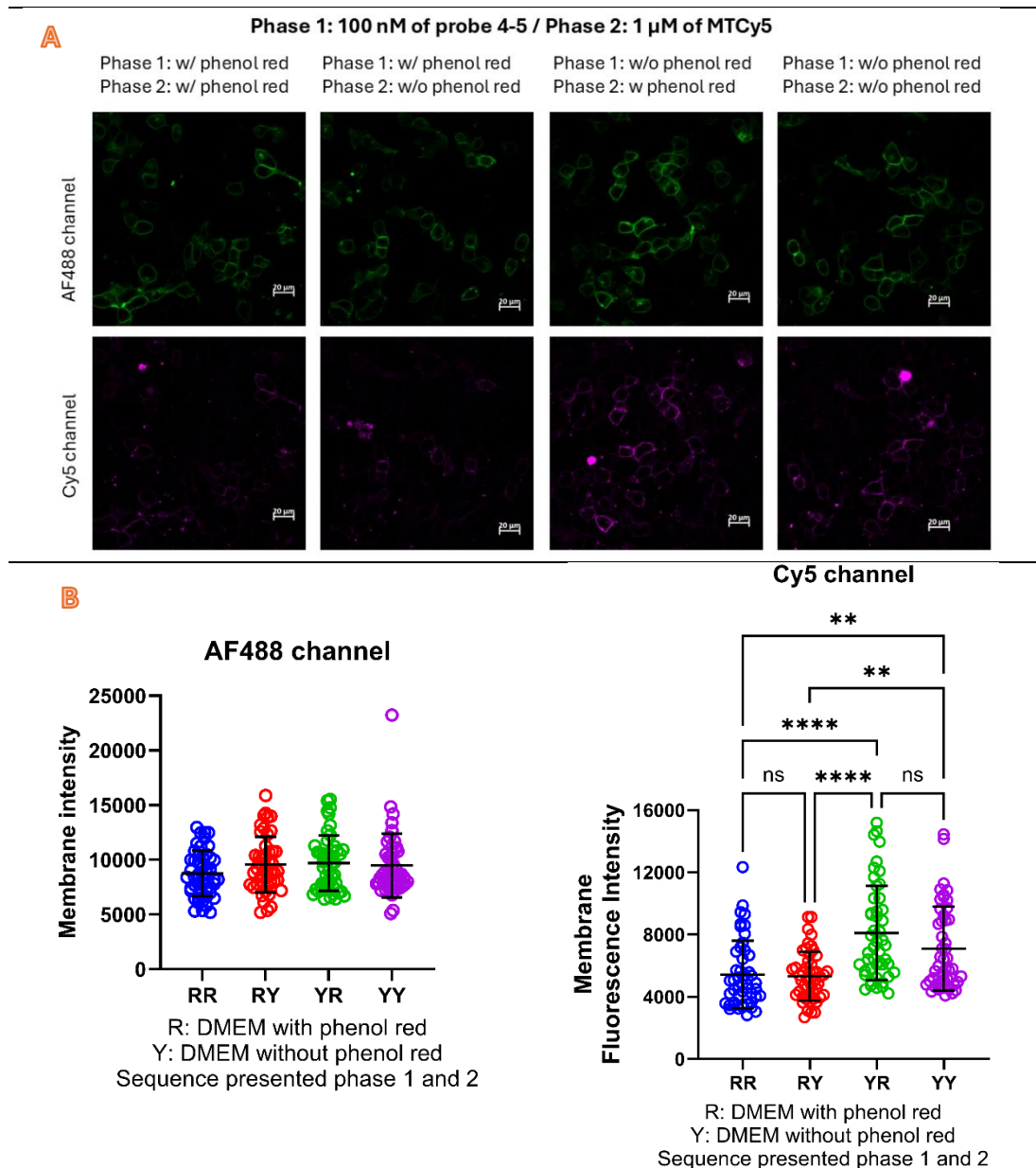
Figure 4-12. Evaluation of Media Effects at Different Labelling Stages.
(**A**) Representative confocal images showing four combinations of Phase 1 and Phase 2 media compositions. In the Cy5 channel, samples labelled during Phase 1 with DMEM containing phenol red exhibited reduced fluorescence intensity compared to those labelled with DMEM lacking phenol red. Scale bar = 20 µm. Images are representative of three independent experiments, each conducted in duplicate. (**B**) Quantification of membrane fluorescence intensity was performed using Fiji (ImageJ) by manually drawing the membrane region of interest (ROI). In the AF488 channel, signal intensity remained consistent across all four conditions, indicating comparable A_1 AR expression. In the Cy5 channel, lower signal intensity was observed in groups where Phase 1 labelling was performed in DMEM containing phenol red. Notably, samples sharing the same Phase 1 medium exhibited similar Cy5 intensities regardless of the Phase 2 medium used. Statistical analysis of Cy5 membrane fluorescence was conducted using the Kruskal–Wallis test due to non-normal data distribution, revealing a significant difference among groups [$H(3) = 37.78$, $P < 0.0001$]. *Post hoc* analysis using Dunn's multiple comparisons test identified significant differences between the following pairs: RR vs. YY ($P = 0.003$), RR vs. YR ($P < 0.0001$), RY vs. YY ($P = 0.0072$), and RY vs. YR ($P < 0.0001$). No significant differences were observed between RR and RY ($P > 0.999$) or between YY and YR ($P = 0.599$). Data are presented as mean ± SD from three independent experiments, with a total of 48 cells analysed in each condition.
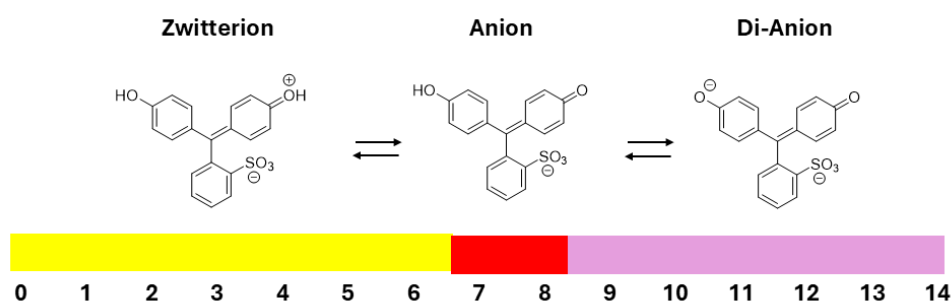
Figure 4-13. Ionisation States of Phenol Red Across Different pH Ranges.
Phenol red exists in distinct ionic forms depending on the pH of the solution. It predominantly exists as a zwitterion under acidic conditions (yellow bar), as a monoanionic species near neutral pH (red bar), and as a dianion under basic conditions (pink bar). This figure is adapted from Weiskirchen *et al*. (2023)[181].

The impact of DMEM, with or without phenol red, on phase 1 labelling has been demonstrated through confocal imaging. This study investigates whether HEPES-buffered saline solution (HBSS) and complete media (DMEM without phenol red supplemented with 10% FCS) influence the labelling effect. Phase 1 labelling was proceeded in HBSS or complete media following the same procedures as previous examinations with two types of DMEM. In this experiment, DMEM was replaced with HBSS and complete media (DMEM without phenol red supplemented with 10% FCS). Phase 2 labelling was performed using 1 μM HTCy5 prepared in DMEM with phenol red. Detailed experimental procedures are described in **Chapter 2, Section 2.1.8.5**. Confocal images are presented in **Figure 4-14**. The AF488 channel showed similar A_1 AR repression *via* SNAP surface AF488 labelling. In the Cy5 channel, HBSS exhibited comparable or superior signal to DMEM with phenol red, whereas complete media (DMEM without phenol red supplemented with 10% FCS) showed reduced A_1 AR labelling. TCO isomerises to a stable *cis*-form, and this transition is accelerated in the presence of serum or thiol derivatives[182–184]. This may explain the poor phase 1 labelling in complete media (DMEM without phenol red supplemented with 10% FCS) compared to DMEM with phenol red. Conversely, HBSS showed slightly better labelling, possibly due to slower degradation of probe **4-5**, as DMEM contains high concentrations of amino acids (e.g., 1 mM lysine hydrochloride salt, 0.2 mM cystine hydrochloride salt according to the supplier's recipe), which can react with the reactive moiety (2-fluorophenyl ester).
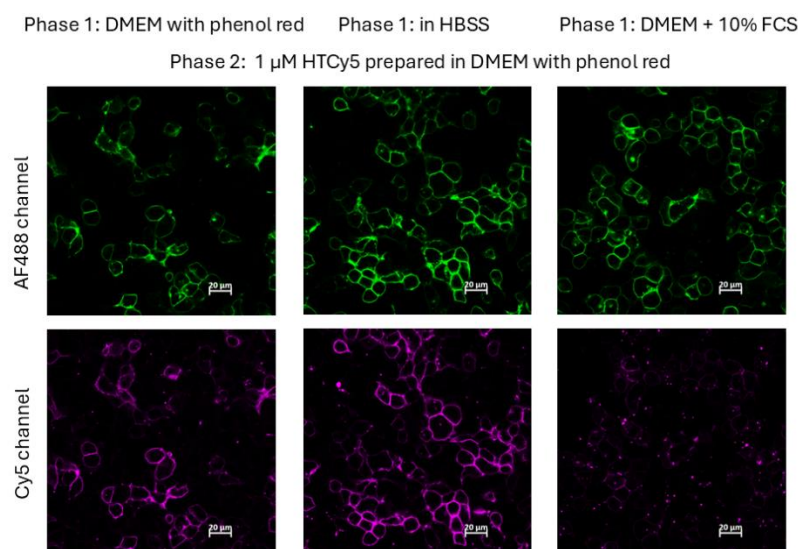
Figure 4-14. Influence of Incubation Environment on Final Labelling Efficiency.
The left panel shows Phase 1 labelling performed in DMEM with phenol red (used as the reference condition, consistent with previous assays). The middle panel represents labelling in HBSS, while the right panel corresponds to labelling in complete medium (DMEM without phenol red supplemented with 10% FCS). All samples were subsequently treated with 1 μM HTCy5 as the Phase 2 reagent, prepared in DMEM with phenol red. In the AF488 channel, A_1 ARs were clearly visualised across all three conditions, indicating consistent receptor expression. However, the Cy5 channel revealed notable differences in labelling efficiency. The HBSS condition (middle panel) exhibited comparable or slightly enhanced labelling relative to the reference (left panel), while the complete medium condition (right panel) showed markedly reduced labelling. Scale bar = 20 μm. Images are from a single pilot experiment conducted with two replicates.

To summarise the conditions for A_1 AR labelling using probe **4-5** with a click reaction partner:

1. **Incubation**: A two-hour incubation with 100 nM of probe **4-5** was required.

2. **Labelling Agent**: HTCy5 was preferred over MTCy5.

3. **Effectiveness**: The order of labelling effectiveness was: HBSS ≥ DMEM with phenol red >>>> complete media (DMEM without phenol red supplemented with 10% FCS). DMEM without phenol red is more effective than DMEM with phenol red.

4. **Concentration and Duration**: Higher concentrations of phase 1 and phase 2 reagents and prolonged labelling times improve labelling but increase the risk of non-specific labelling.

The optimal conditions depend on the experimental design and investigation objectives.

4.2.2.3 Covalent Labelling of A_1 ARs

A_1 ARs were specifically labelled using probe **4-5**, followed by an inverse electron-demand Diels–Alder (IEDDA) reaction with reporter-tagged tetrazine derivatives, as demonstrated in previous confocal imaging experiments (e.g., **Figure 4-11**). To determine whether the labelling achieved *via* probe **4-5** and the corresponding click chemistry reagent was covalent, an in-gel fluorescence scan was performed.

To isolate A_1 ARs from the complex solubilised cellular mixture and to include a known covalent labelling as a positive control, HEK293G cells stably expressing TwinStrep-SNAP-tagged human A_1 ARs (TS-SNAP-hA_1 ARs) were utilised. The Twin-Strep (TS) tag enables affinity purification *via* binding to MagStrep "Type3" XT magnetic beads coated with Strep-Tactin[142]. The bound protein can subsequently be eluted using biotin, which has a higher binding affinity for Strep-Tactin than the TS tag[142]. As a positive control for covalent labelling, the SNAP-tag was labelled with SNAP-surface AF647, which forms a stable covalent bond with the SNAP-tag[81]. Detailed experimental procedures are provided in **Chapter 2, Section 2.1.4**.

HEK293G cells stably expressing TS-SNAP-hA_1 ARs in T175 flasks, reaching approximately 80-95% confluence, were used for sample preparation. Four labelling conditions were designed and carried out using DMEM without phenol red as the medium in an incubator with a humidified atmosphere of air/CO_2 in a 19:1 ratio. For the positive control, cells were incubated for one hour with 50 nM SNAP-surface AF647 in 10 mL of media. For the negative control, cells were incubated with 10 mL of media. For the experimental sets, cells were gently washed with PBS once, followed by incubation with 200 nM probe **4-5** prepared in DMEM without phenol red in the presence or absence of 10 µM DPCPX pretreatment for one hour. At the end of phase 1 labelling, cells were washed twice with PBS and then incubated with 500 nM HTCy5 in DMEM without phenol red for one hour. After labelling, the media was aspirated, and cells were gently washed twice with PBS. Enzyme-free cell dissociation solution was added to each flask, and cells were collected, centrifuged, and the supernatant discarded. The cell pellets were then ready for subsequent extractions.

Cell pellets were solubilised in a buffer containing 0.5% (w/v) lauryl maltose neopentyl glycol (LMNG), 0.01% (w/v) cholesteryl hemisuccinate tris salt, 20 mM HEPES, 10% (v/v) glycerol, 150 mM NaCl, and a complete protease inhibitor cocktail, adjusted to pH 7.5. The buffer was added at a 1:10 (w/v) ratio relative to the cell pellet mass. Solubilisation was carried out in a cold room maintained at 4 °C for 2 hours. Following centrifugation for 20 minutes, the supernatant was

transferred to a new microcentrifuge tube containing MagStrep "Type3" XT magnetic beads coated with Strep-Tactin for affinity purification.

Protein extraction using the magnetic beads was performed overnight at 4 °C. The following day, the beads were separated from the solution using a magnetic separator and washed twice with solubilisation buffer to remove non-specifically bound proteins. To elute the bound TS-SNAP-hA$_1$ ARs, the beads were incubated with a biotin solution at 4 °C for 4 hours, allowing biotin to displace the Twin-Strep tag due to its higher binding affinity for Strep-Tactin.

The eluted protein solution was then separated from the beads using a magnetic separator and mixed with NuPAGE™ LDS sample buffer in preparation for SDS-PAGE analysis. The LDS buffer, which contains lithium dodecyl sulfate, facilitates protein denaturation. Electrophoresis was performed at 200 V for 50 minutes. The resulting gel was scanned using a Typhoon gel imager under the Cy5 channel to detect fluorescently labelled proteins. Subsequently, the gel was stained with InstantBlue® overnight and rescanned using the Typhoon imager under the infrared long-wavelength channel. Gel images are presented in **Figure 4-15**, and detailed sample preparation procedures are described in **Chapter 2, Section 2.1.4**.

In the Cy5 channel, bands were observed in the positive control (SNAP-surface AF647) and in cells labelled with probe **4-5** and HTCy5. The band height matched the calculated molecular weight of TS-SNAP-hA$_1$ AR (59 kDa), indicating covalent labelling of A$_1$ ARs through probe **4-5** with HTCy5. Additionally, the set pretreated with 10 µM DPCPX did not show any bands in the Cy5 channel, demonstrating the specificity of probe **4-5** for A$_1$ AR labelling.
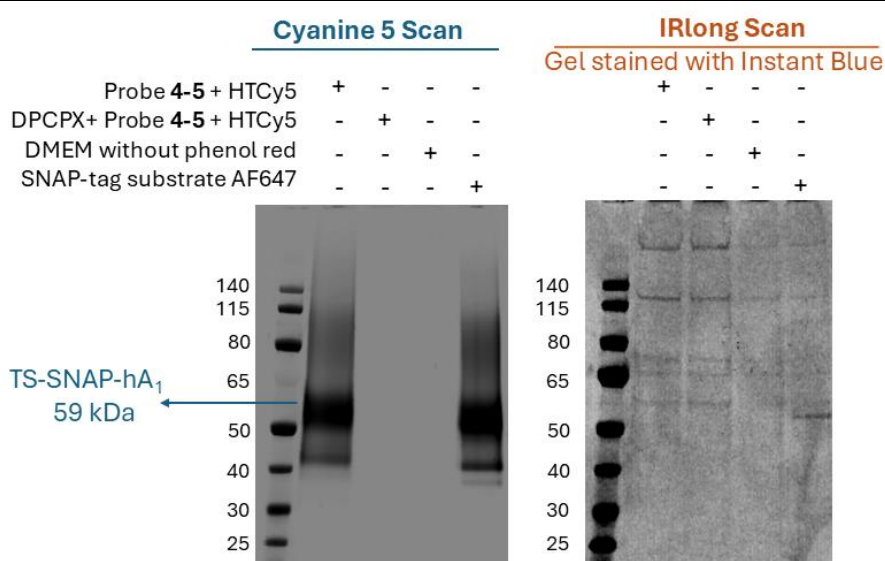
Figure 4-15. Covalent labelling of TS-SNAP-hA$_1$ ARs demonstrated *via* in-gel fluorescent scans.

TS-SNAP-A$_1$AR was labelled with 200 nM of probe **4-5** in the presence or absence of 10 μM DPCPX preincubation, followed by incubation with 500 nM HTCy5 for one hour. DMEM without phenol red and SNAP-surface AF647 served as negative and positive controls, respectively. In the Cy5 scan (left panel), a fluorescent band was present in cells without DPCPX pretreatment and absent in cells pretreated with DPCPX. The band position was consistent with the positive control and matched the calculated protein weight (59 kDa), indicating that probe **4-5** with HTCy5 can covalently tag A$_1$ ARs. The InstantBlue® image confirmed that protein samples were loaded into the gel. PageRuler™ Prestained Protein Ladder (10–180 kDa) was used as the molecular weight marker. Images are representative of three independent experiments.

4.2.2.4 Investigating A$_1$ AR Orthosteric Binding Pocket Accessibility After Probe 4-5 and HTCy5 Labelling

4.2.2.4.1 Confocal Image Observation

Agonist-induced aggregation and internalisation of A$_1$ ARs have been previously reported[18,148–151]. To assess whether these processes remain observable following fluorophore labelling *via* probe **4-5** and a tetrazine-reporter partner, a confocal imaging study was conducted. If receptor internalisation and aggregation are still evident after agonist treatment, it would suggest that the orthosteric binding site of A$_1$ ARs remains accessible post-labelling. This would provide evidence that probe **4-5** and the subsequent click reaction do not interfere with agonist binding.

HEK293T cells transiently expressing SNAP-tagged hA$_1$ ARs were used in this experiment. The SNAP tag enabled covalent labelling with SNAP-surface AF488, serving as a control to monitor receptor localisation. The selective A$_1$ AR agonist 2-chloro-N^6-cyclopentyladenosine (CCPA) was chosen based on its previously demonstrated ability to induce A$_1$ AR internalisation (Soave *et al.*, 2020)[118]. Detailed experimental procedures are described in **Chapter 2, Section 2.1.5.2**.

On the day of the experiment, HEK293T cells seeded in 8-well plates were labelled with 250 nM SNAP-surface AF488 for 30 minutes. Following this, cells were incubated with 100 nM probe **4-5** for 2 hours. Phase 2 labelling was then performed using 1 µM HT-Cy5 for 15 minutes. After each labelling step, cells were washed twice with warm DMEM (without phenol red). Upon completion of labelling, cells were incubated 2 hours in the presence or absence of 10 µM CCPA. Cells were subsequently fixed, washed with PBS, and prepared for confocal imaging.

Representative confocal images are shown in **Figure 4-16A**. In both the AF488 and Cy5 channels, CCPA-treated cells exhibited clustered intracellular fluorescence, indicating receptor internalisation. The merged images revealed strong colocalisation between the two fluorophores, confirming that probe **4-5** and HTCy5 successfully labelled A_1 ARs. These results suggest that the orthosteric binding site remains accessible to CCPA following labelling, and that receptor trafficking from the membrane to intracellular compartments is preserved.

In addition to visual assessment, intracellular fluorescence intensity was quantified using Fiji (ImageJ) by manually defining intracellular regions of interest. A clear increase in intracellular signal was observed in both the AF488 and Cy5 channels following CCPA treatment (**Figure 4-16B**), further supporting the conclusion that A_1 AR internalisation remains functional after labelling with probe **4-5** and HT-Cy5.
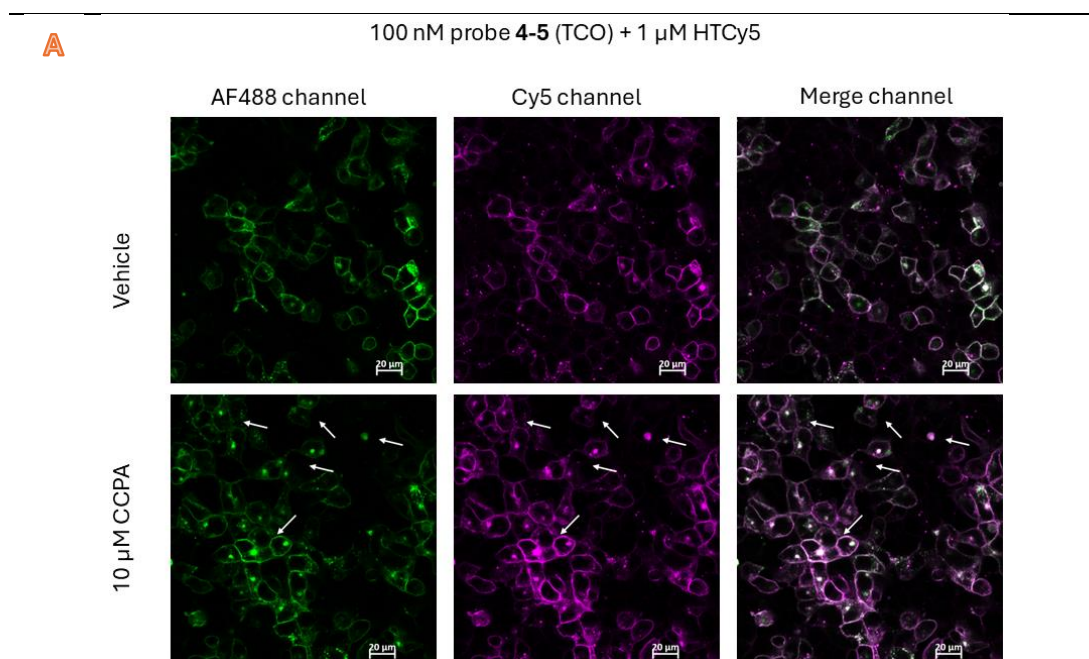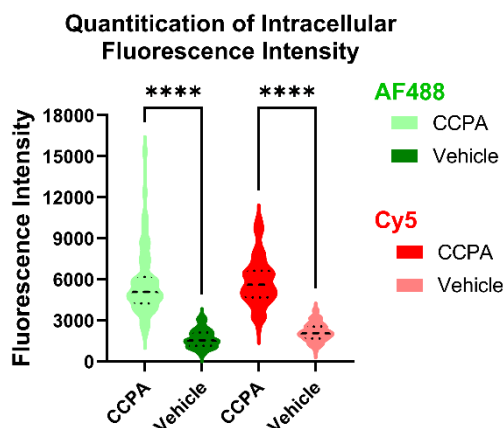
Figure 4-16. Agonist-Induced Internalisation of A$_1$ ARs.
(**A**) HEK293T cells transiently expressing SNAP-tagged hA$_1$ ARs were labelled with 250 nM SNAP-surface AF488 for 30 minutes, followed by incubation with 100 nM probe **4-5** for 2 hours at 37 °C. Phase 2 labelling was performed using 1 µM HTCy5 for 15 minutes. Each labelling step was followed by two washes with warm DMEM lacking phenol red. After labelling, cells were incubated for 2 hours in the absence (vehicle, top panels) or presence (bottom panels) of 10 µM CCPA. Cells were then washed, fixed, and prepared for confocal imaging. In the CCPA-treated group, many intracellular A$_1$ AR clusters (indicated by white arrows) were observed in both the AF488 and Cy5 channels. The merged images showed strong colocalisation, confirming A$_1$ AR-specific labelling. In contrast, minimal clustering and internalisation were observed in the vehicle-treated group. These results suggest that the orthosteric binding site of A$_1$ ARs remains accessible following labelling with probe **4-5** and HTCy5, and that receptor trafficking is not disrupted. Images are representative of six independent experiments conducted in duplicate. Scale bars = 20 µm. Image brightness and contrast were uniformly enhanced by 20%. (**B**) Intracellular fluorescence intensity was quantified using Fiji (ImageJ) by manually defining intracellular regions of interest (ROIs). As the data were not normally distributed, statistical analysis was performed using the Mann–Whitney U test. Significant differences in intracellular signal intensity were observed between vehicle- and CCPA-treated cells in both the AF488 channel (U = 79, P < 0.0001) and the Cy5 channel (U = 82, P < 0.0001), indicating receptor internalisation. Data are presented as median values with interquartile ranges, based on six independent experiments, each analysing 96 cells per condition.

4.2.2.4.2 BRET Assessment

The confocal images shown in **Figure 4-16A** implied that CCPA could access the A$_1$ AR's orthosteric binding pocket after probe **4-5** and HTCy5 labelling. The clustered and internalised A$_1$ ARs in the CCPA treatment set suggested that A$_1$ AR preserved its function after probe **4-5** and HTCy5 tagging, and the tag posed minimal impact on trafficking. However, as no evidence proved that all A$_1$ ARs were labelled by the probe **4-5** and HTCy5 system, the signal clump observed in confocal images might have originated from untagged or SNAP surface AF488 tagged A$_1$ ARs stimulated by CCPA. A$_1$ ARs tagged by probe **4-5** and HTCy5 were co-aggregated and co-internalised due to their proximity to untagged A$_1$ ARs. To rule out this possibility, a distance-sensitive BRET assay was arranged.

The experimental concept is illustrated in **Figure 4-17**. If the orthosteric binding pocket of the A$_1$ AR remained accessible following labelling with probe **4-5** and

Tetrazine-AF488, both red and green BRET signals were expected. In contrast, in the condition with DPCPX pretreatment, only green BRET was anticipated due to competitive inhibition at the orthosteric site. To ensure the robustness of the assessment, several control conditions were included. To verify that both Phase 1 and Phase 2 labelling steps were essential for successful AF488 tagging of A_1 AR, control groups were prepared in which receptors were labelled with either Phase 1 or Phase 2 alone. Furthermore, to confirm that the orthosteric binding site remained unoccupied in the employed cell model, red BRET resulting from the incubation of probe **3-29** with NLuc-hA$_1$ AR in the absence of two-phase labelling was measured. To evaluate whether probe **3-29** and DPCPX influenced green BRET, a reference experiment was conducted in which AF488-tagged NLuc-hA$_1$ ARs were incubated with HBSS, with or without DPCPX pretreatment.
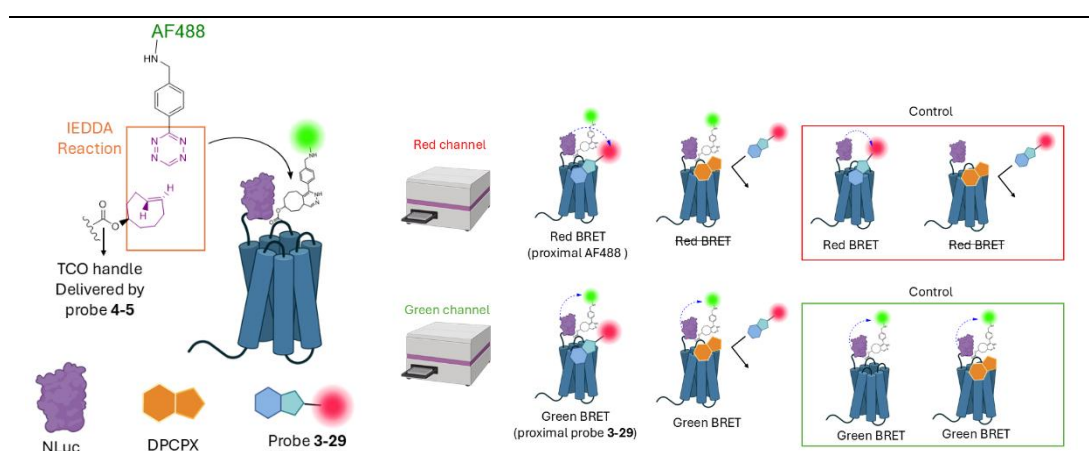
Figure 4-17. Experimental Design for Assessing Orthosteric Binding Site Accessibility *via* BRET.

HEK293T cells transiently expressing NLuc-hA$_1$ ARs were labelled with an AF488 fluorophore through click chemistry between the TCO moiety delivered by probe **4-5** and Tetrazine-AF488. Excess ligands were removed by two washes with warm HBSS following each labelling step. Subsequently, cells were incubated with probe **3-29** in the presence or absence of 1 µM DPCPX pretreatment. After a 1-hour incubation, furimazine was added, followed by a 5-minute equilibration period. BRET signals were then measured sequentially: first using the red channel (long-pass 610 nm), followed by the green channel (535 ± 15 nm). Figure created with BioRender.com.

To assess orthosteric binding pocket accessibility *via* NanoBRET, A_1 ARs tagged at the *N*-terminus were required. Therefore, HEK293T cells transiently expressing NLuc-hA$_1$ ARs were employed. Detailed experimental procedures are provided in **Chapter 2, Section 2.1.9.1**. In this assay, HEK293T cells expressing NLuc-hA$_1$ ARs were first labelled with AF488 using probe **4-5** and Tetrazine-AF488. Subsequently, the cells were incubated with 100 nM probe **3-29** in the presence or absence of 1 µM DPCPX pretreatment for 1 hour. Following the addition of furimazine and a 5-minute equilibration period, BRET signals were measured using a PHERAstar plate reader (BMG, Germany), with readings taken once for

each channel (red and green). The experimental results are presented in **Figure 4-18**.
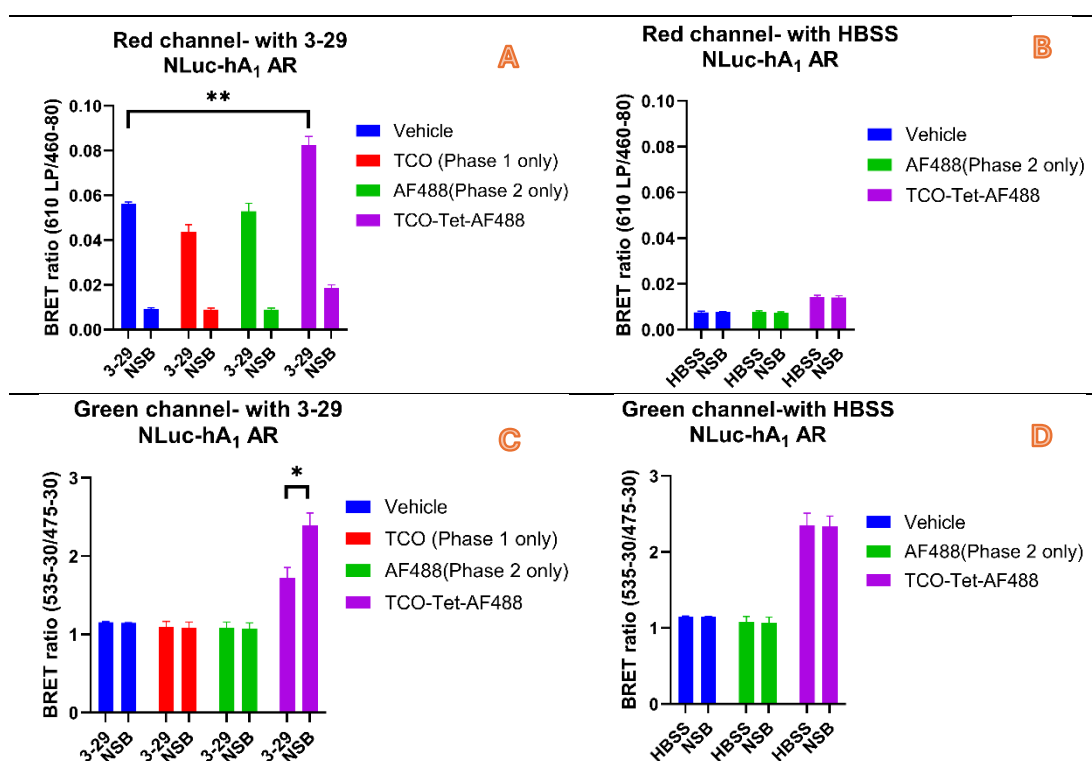
Figure 4-18. Investigating Orthosteric Binding Pocket Accessibility Following LD Probe Labelling Using BRET.
(**A**) BRET signals were measured in the red channel. The vehicle condition represents hA_1 AR with an N-terminal NLuc tag only. AF488 tagging was achieved through a two-step process: first, conjugation of the TCO group to NLuc-hA_1 AR, followed by a click reaction with Tet-AF488. Experimental conditions included combinations of the full two-step labelling, probe **4-5** alone, or Tet-AF488 alone. The bar chart shows reduced total binding in A_1 ARs tagged with the TCO group and enhanced signal in receptors labelled with TCO-Tet-AF488. Conditions with Tet-AF488 alone exhibited BRET signals comparable to the vehicle. A Mann–Whitney U test was performed between the vehicle and TCO-Tet-AF488-tagged groups treated with probe **3-29** due to non-normally distributed data, revealing a significant difference ($U = 0, P = 0.0043$). (B) Control experiments for red BRET measurements were conducted using HBSS in place of probe **3-29**. A slightly elevated background signal was observed in TCO-Tet-AF488-labeled A_1 ARs, potentially due to light bleed-through from the green fluorescence of AF488. (**C**) BRET signals were measured in the green channel. The vehicle and partially labelled conditions (phase 1 or phase 2 only) lacked AF488 on A_1 ARs and therefore showed no specific binding. In contrast, A_1 ARs labelled with TCO-Tet-AF488 exhibited increased BRET signals upon DPCPX preincubation compared to those without DPCPX treatment. The absence of signal reduction in wells pretreated with 1 µM DPCPX suggests that the observed signal drop was due to probe **3-29** binding to A_1 AR. A Mann–Whitney U test comparing TCO-Tet-AF488-labelled groups with and without DPCPX preincubation indicated a significant difference ($U = 4, P = 0.026$). (**D**) Control experiments for green BRET measurements were conducted using HBSS instead of probe **3-29**. HBSS addition did not result in signal reduction compared to the non-specific binding control. All data are presented as the mean ± SEM from five independent experiments, each performed in triplicate.

In the red BRET graph (**Figure 4-18**A), a prominent specific binding signal was observed in experimental conditions incubated with the reversible red probe **3-29**, which contains the BODIPY630/650 fluorophore. In contrast, no specific binding was detected in the control conditions treated with HBSS (**Figure 4-18**B), indicating that probe **3-29** binds to the orthosteric binding pocket of A_1 AR. The proximity between BODIPY630/650 (acceptor) and NLuc (donor) facilitated energy transfer, resulting in a measurable BRET signal.

Among the **3-29**-treated conditions (**Figure 4-18**A), NLuc-hA_1 AR labelled with phase 1 reagent alone exhibited a slightly reduced total binding signal compared to the vehicle. This suggests that the presence of the TCO group may alter the spatial orientation between NLuc and probe **3-29**, thereby diminishing the efficiency of energy transfer. Alternatively, residual probe **4-5** or its congener (**3-20**) might have competed with probe **3-29** for binding to A_1 AR, although this is unlikely given the extensive washing steps performed.

The condition treated with phase 2 reagent alone produced a BRET signal comparable to the vehicle, reaffirming that phase 2 labelling does not occur in the absence of prior phase 1 modification. Finally, the condition involving complete two-phase labelling yielded a significantly stronger BRET signal than the vehicle.

In the green BRET graph (**Figure 4-18**C and D), the vehicle control and the conditions labelled with either phase 1 or phase 2 alone did not produce a specific binding signal, as no green fluorescent acceptor was present under these conditions. This result directly confirmed that AF488 could not be conjugated to A_1 AR using only the phase 2 reagent. In contrast, A_1 AR labelled with both phase 1 and phase 2 reagents exhibited increased BRET signals in the samples preincubated with 1 µM DPCPX or with HBSS alone, compared to the sample treated solely with probe **3-29**.

Unexpected BRET signals in both the red and green channels were observed in Nluc-A_1 ARs tagged with AF488, relative to the vehicle control lacking additional covalent fluorescent tags. This phenomenon is likely attributable to FRET between the AF488 tag and BODIPY630/650 (probe **3-29**), as illustrated in **Figure 4-19**. When nanoluciferase oxidises furimazine, it emits luminescence that can be absorbed by both AF488 and BODIPY630/650. Due to the close proximity between these fluorophores, part of the emission from AF488 may be absorbed by BODIPY630/650, resulting in an elevated BRET signal in the red channel compared to the AF488-free control. Consequently, energy transfer to BODIPY630/650 leads to a reduction in the green channel BRET signal, which returns to control levels when DPCPX prevents probe **3-29** from binding to A_1 ARs.
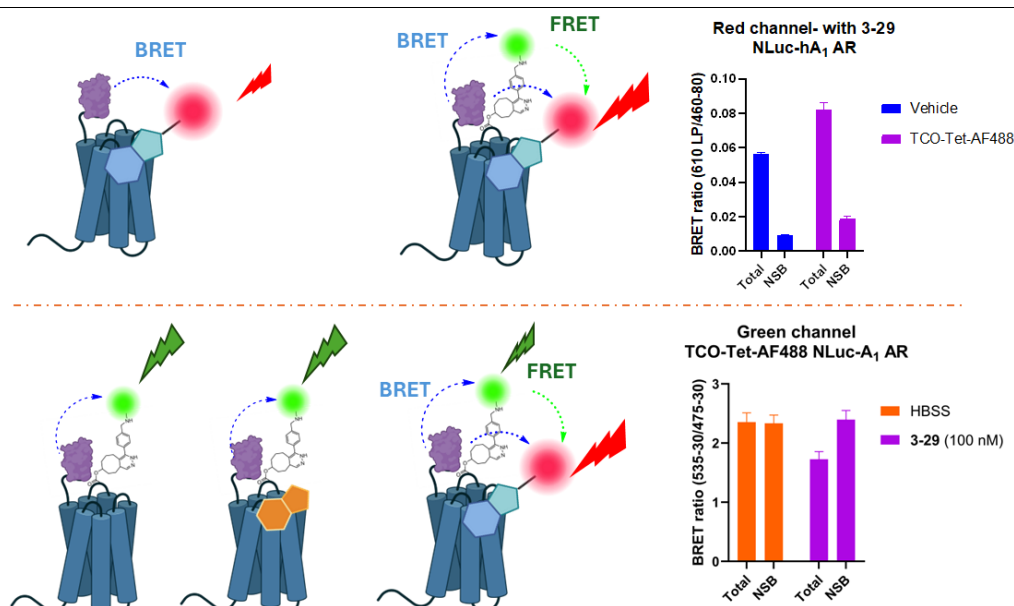
Figure 4-19. Illustration of FRET as a potential cause of the unexpected BRET signal. The top panel illustrates the scenario observed during BRET measurements in the red channel. Due to FRET, the red fluorophore absorbs more energy compared to the vehicle control (lacking the green tag), resulting in an enhanced signal in the total binding of probe **3-29**. The bottom panel depicts the BRET measurement in the green channel. Here, the green tag transfers a portion of its energy to the red fluorophore *via* FRET, leading to a decreased BRET signal relative to the condition without red reversible ligand binding. Figure created using BioRender (www.biorender.com).

To investigate the changes in BRET ratio signals, both raw fluorescence and luminescence data were analysed. Although similar signal trends were observed across individual experiments, pooled data could not reliably reflect these trends due to variability in cell numbers and transfection efficiency between experiments. Therefore, experiments exhibiting comparable levels of raw signal were selected and summarised in **Figure 4-20**.
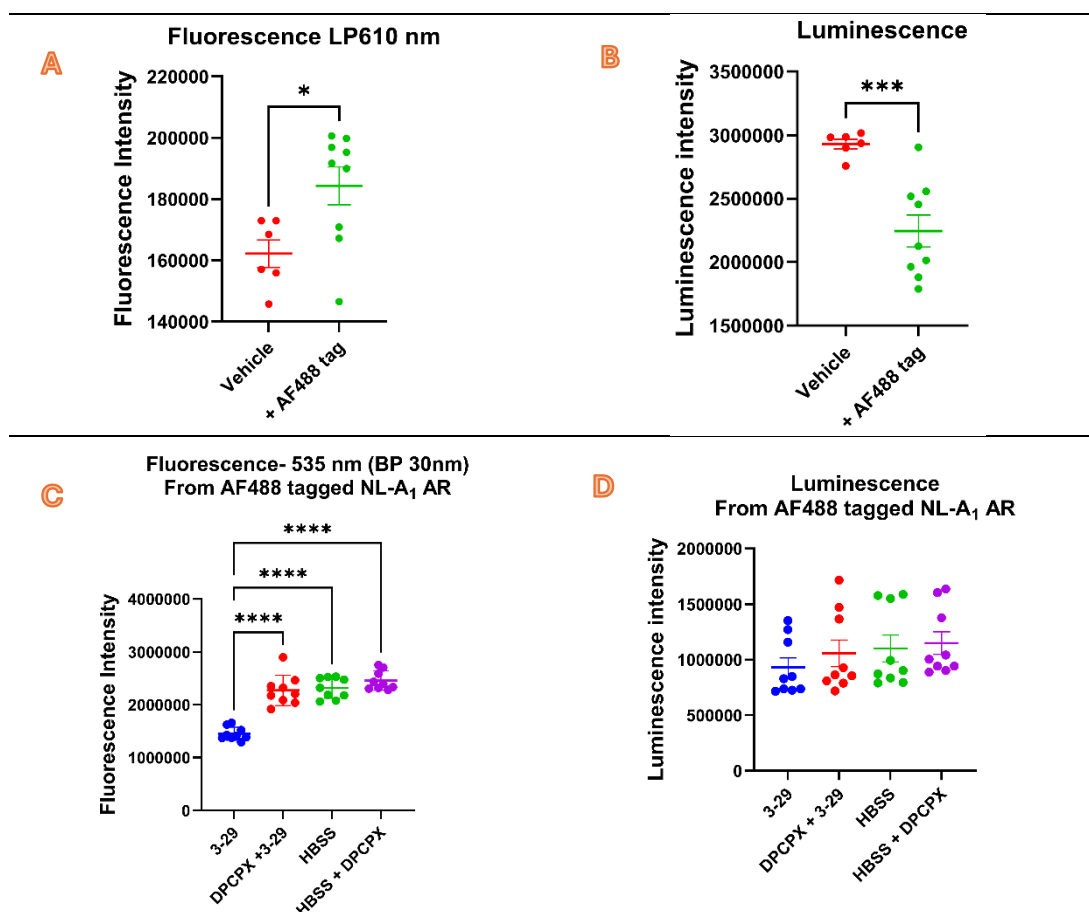
Figure 4-20. Examination of raw luminescence and fluorescence data in experimental sets exhibiting unexpected BRET signals.

(**A**) Top left panel: Fluorescence measured using a long-pass 610 nm filter. The "Vehicle" group represents NLuc-A_1AR incubated with probe **3-29** (a red, reversible fluorescent ligand). Fluorescence intensity was higher in NLuc-A_1AR tagged with AF488, consistent with FRET, where AF488 transfers a portion of its energy to **3-29**. Statistical analysis revealed a significant difference between the two groups [$t(13)$ = 2.604, P = 0.0218]. Data are presented as the mean ± SEM from two independent experiments (6 wells for the vehicle group) and three independent experiments (9 wells for the AF488-tagged group). (**B**) Top right panel: Luminescence signal measured during BRET detection. NLuc-A_1AR tagged with AF488 exhibited lower luminescence, likely due to partial absorption of luminescence by AF488. This difference was statistically significant [$t(13)$ = 4.307, P = 0.0009]. Data are shown as the mean ± SEM from two independent assays (6 wells for the vehicle group) and three independent experiments (9 wells for the AF488-tagged group). (**C**) Bottom left panel: Fluorescence measured at 535 nm with a 30 nm bandpass filter. Among the four experimental conditions, only the group incubated with probe **3-29** without DPCPX pre-treatment showed reduced fluorescence intensity. This suggests that AF488 transfers energy to probe **3-29** upon binding to AF488-tagged NLuc-A_1AR. One-way ANOVA indicated a significant difference among the four groups [$F(3,32)$ = 44.09, P < 0.0001]. *Post hoc* Tukey's test showed that the **3-29**-only group (blue) differed significantly from the other three groups (P < 0.0001). Data are presented as the mean ± SEM from three independent experiments (9 wells per group). (**D**) Bottom right panel: Luminescence measured in the green BRET channel. Only the group incubated with **3-29** showed a slight decrease in intensity; however, no statistically significant difference was detected using the Kruskal–Wallis test due to non-normal data distribution [$H(3)$ = 5.825, P = 0.1205]. Data are presented as the mean ± SEM from three independent experiments (9 wells per group).

187

In the red channel measurements, fluorescence intensity was higher in A_1ARs tagged with AF488 compared to those without the AF488 tag, supporting the occurrence of FRET (**Figure 4-20A**). Conversely, luminescence intensity was lower in the AF488-tagged group, which is consistent with the expectation that luminescence is absorbed by both AF488 and the red fluorophore, unlike in the control group where only the red fluorophore acts as the acceptor (**Figure 4-20B**).

In the green channel measurements, binding of the reversible red fluorescent ligand (**3-29**) to AF488-tagged A_1ARs resulted in reduced fluorescence intensity, which can be attributed to energy transfer to the red fluorophore *via* FRET (**Figure 4-20C**). Luminescence in the presence of **3-29** was slightly lower, although no statistically significant differences were observed among the four experimental conditions (**Figure 4-20D**). This minor decrease may be explained by luminescence absorption by **3-29**. The limited luminescence signal is likely due to the minimal spectral overlap between NanoLuc emission and BODIPY630/650 absorption.

The occurrence of FRET further indicates that the orthosteric binding pocket remains accessible following labelling with probe **4-5** and its click chemistry partner. The effective BRET signal suggests that both the AF488 tag and **3-29** are in close proximity to NLuc tag on A_1ARs. The observed FRET implies that AF488 and **3-29** are within a distance of less than 10 nm. A plausible explanation for the simultaneous occurrence of BRET and FRET is that probe **3-29** binds to AF488-tagged NLuc-A_1ARs, indicating that the orthosteric binding site remains available.

4.2.2.4.3 Fluorescence Lifetime Imaging Microscopy (FLIM) - FRET Assessment

The excitation and emission of fluorescence are illustrated in **Figure 4-21**. When the fluorophore absorbed specific wavelength energy, its energy state is elevated from the ground state to an excited state (S1, S2…). As the excited state falls back to the ground state, the energy release can be categorised into three main routes: fluorescence emission, internal conversion into heat, and transfer to the surrounding environment[185]. Three primary pathways contribute to the overall energy release rate, which collectively determines the fluorescence decay rate[185]. This decay rate can be converted into the fluorescence lifetime[185]. Fluorescence emission and internal heat conversion are characteristics of specific fluorophores[185]. Conversely, different surrounding environments could cause unequal decay rates and change the fluorescence lifetime of the fluorophore[185,186]. Hence, fluorescence lifetime change can be used as an indicator for differentiating fluorophore states (free in solution or bound to protein) or surrounding environments (high concentration of ions or proximity to another fluorescent-labelled protein)[185,186].
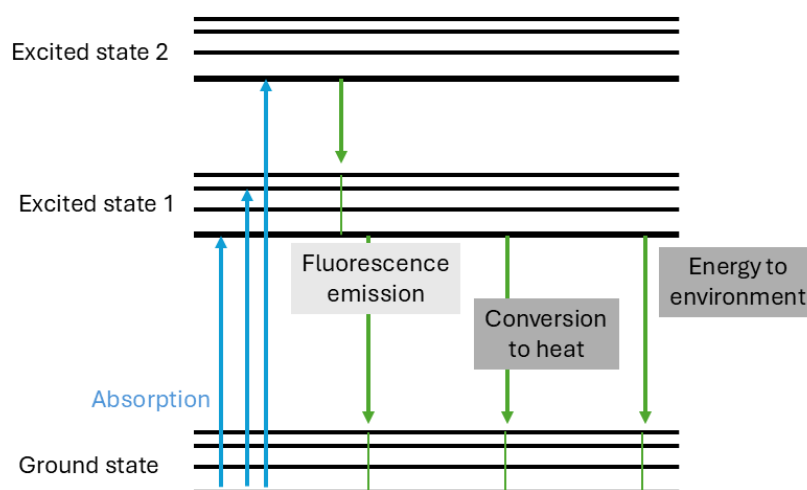
Figure 4-21. Illustration of Fluorophore's Three Main Energy Releasing Routes.
After energy absorption (blue), the state of the fluorophore is elevated from the ground state to an excited state. The energy can be released by three main routes: emission as fluorescence, internal conversion to heat, and transfer to the surrounding environment. The picture was adapted from Shcheslavskiy *et al*. (2025)[185].

FLIM-FRET had been used to investigate protein-protein interactions, protein conformation change, and ligand-protein binding assessments[186–188]. When the paired acceptor fluorophore is in close proximity to the observed fluorophore (donor), energy can be transferred to the acceptor by FRET, which will change the fluorophore's fluorescence lifetime[120,186]. The distance relationship between donor and acceptor (surrounding environment) can be monitored by fluorescence lifetime change, making FLIM-FRET a powerful technique in life sciences.

In the assessment of the orthosteric binding pocket using the BRET approach, it was hypothesised that FRET occurs between TCO-Tet-AF488 conjugated to the A_1AR and BODIPY630/650 attached to probe **3-29**. The presence of FRET would provide strong evidence that AF488 and BODIPY630/650 are in close spatial proximity. To confirm this interaction, a FLIM-FRET experiment was conducted to directly assess FRET between AF488 and probe **3-29**.

The same cellular model was employed to investigate whether the FRET observed in the previous BRET assay could be validated. HEK293T cells transiently expressing NLuc-hA_1ARs were seeded into 8-well plates. The cells were sequentially labelled with 200 nM of probe **4-5** and 500 nM of Tetrazine-AF488, with each incubation step lasting one hour and followed by two washing steps.

AF488-tagged NLuc-A_1ARs were examined under four experimental conditions: (1) treatment with HBSS, serving as a control to establish the baseline AF488 fluorescence lifetime; (2) addition of probe **3-29**, to assess FRET occurrence; (3) pre-incubation with 10 µM DPCPX for 30 minutes followed by the addition of probe **3-29**, to evaluate the inhibition of FRET by blocking probe **3-29** access to NLuc-A_1AR *via* DPCPX; and (4) incubation with 10 µM DPCPX alone, serving as a control to determine whether DPCPX interferes with the AF488 fluorescence lifetime. These experimental conditions are illustrated in **Figure 4-22**. FLIM-FRET data acquisition and analysis were performed by Dr. Joelle Goulding. Detailed experimental procedures are depicted in **Chapter 2, Section 2.1.9.2**.
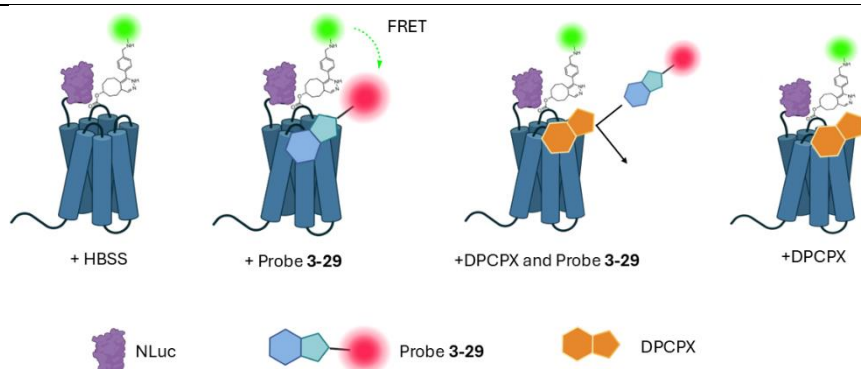
Figure 4-22. Schematic Representation of the Experimental Conditions used in the FLIM-FRET Evaluation.
The baseline fluorescence lifetime is established using AF488-tagged A_1ARs treated with HBSS. A reduction in fluorescence lifetime is expected upon incubation with probe **3-29**, indicating FRET due to energy transfer from AF488 to the nearby BODIPY630/650 fluorophore. To assess the specificity of this interaction, a third condition involves pre-incubation with 10 µM DPCPX to block probe **3-29** binding, with fluorescence lifetime anticipated to remain comparable to the baseline. The final condition, involving incubation with DPCPX alone, confirms that DPCPX does not independently alter the AF488 fluorescence lifetime. Figure created with BioRender (www.biorender.com).

The FLIM-FRET images and corresponding AF488 fluorescence lifetimes are presented in **Figure 4-23**. Fluorescence lifetime data were analysed using the Kruskal–Wallis test, as the baseline dataset did not meet the assumption of normality. A statistically significant difference was observed among the four experimental groups, **$H(3) = 26.62$, p < 0.0001**. *Post hoc* comparisons using Dunn's test revealed a significant reduction in fluorescence lifetime in the group incubated with probe **3-29** (**2.706 ± 0.038 ns**) compared to the AF488 baseline group (**2.914 ± 0.051 ns, p = 0.0072**). In contrast, no significant differences were observed between the baseline and the groups treated with DPCPX alone (**3.040 ± 0.020 ns**) or pre-incubated with DPCPX followed by probe **3-29** addition (**3.006 ± 0.042 ns**).
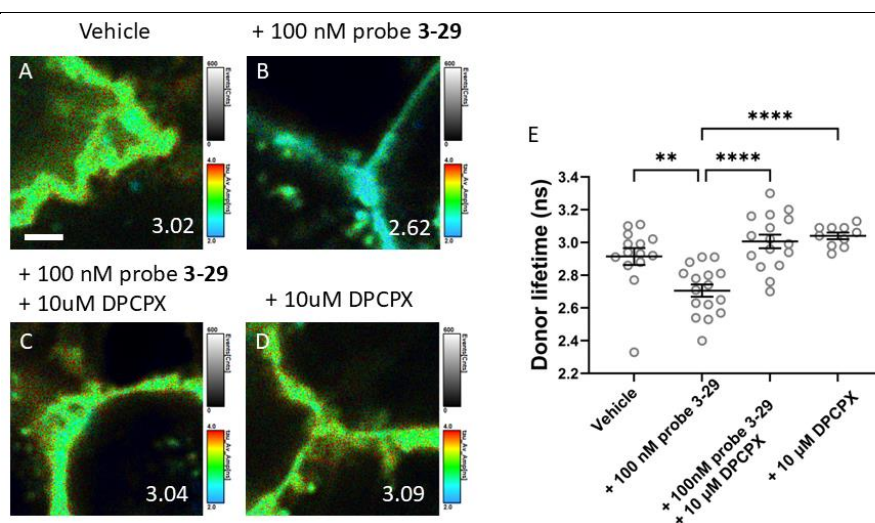
Figure 4-23. FLIM-FRET Images and Measured AF488 (Donor) Lifetime.
Representative pseudo-colored images show amplitude-weighted average donor lifetimes under the following conditions: (A) vehicle treatment (HBSS), (B) 100 nM probe **3-29**, (C) 100 nM probe **3-29** following pre-incubation with 10 µM DPCPX, and (D) 10 µM DPCPX alone. Scale bar = 2 µm. (E) Quantification of single-cell donor lifetimes under each condition. Sample sizes were as follows: vehicle (n = 14), probe **3-29** (n = 16), probe **3-29** + DPCPX (n = 16), and DPCPX alone (n = 10). Data are presented as the mean ± SEM. Statistical analysis was performed using the Kruskal–Wallis test, revealing a significant difference among groups ($H(3) = 26.62$, p < 0.0001). *Post hoc* analysis using Dunn's test identified a significant reduction in donor lifetime in the probe **3-29** group compared to vehicle (p = 0.0072); no other comparisons reached statistical significance.

These findings are consistent with the hypothesis that FRET occurs specifically in the presence of probe **3-29**, indicating close proximity between AF488 and the BODIPY630/650 fluorophore. The confirmation of FRET supports the interpretation of the previous BRET analysis, which showed an enhanced red BRET signal when both the AF488 tag and the red fluorophore were bound to NLuc-A$_1$AR, along with a reduced green BRET signal compared to conditions involving only the red fluorescent ligand or AF488 tag presence. Together, the sequential BRET and FLIM-FRET experiments, along with confocal imaging of agonist-induced internalisation, provide strong evidence that the orthosteric

binding pocket of A_1AR remains accessible following the two-phase labelling strategy.

4.2.2.5 Assessment of Reversible Ligand Binding Affinity After A_1 AR Labelling with Probe **4-5** and Tetrazine-AF488

The accessibility of the orthosteric binding pocket of A_1 AR following labelling with probe **4-5** and Tetrazine-AF488 was previously validated through agonist-induced internalisation studies, BRET-based assessments, and FLIM-FRET experiments. The subsequent question addressed whether the presence of the AF488 tag, introduced *via* the two-phase labelling strategy, alters the ligand binding affinity of A_1 AR compared to untagged receptors. To investigate this, a BRET-based saturation binding assay using probe **3-29** was performed on A_1 ARs with and without the AF488 tag. The binding affinity of probe **3-29** served as a quantitative indicator for evaluating ligand-receptor interactions in both receptor models—tagged and untagged. Detailed experimental procedures are provided in **Chapter 2, Section 2.1.2.1**.

HEK293T cells transiently expressing NLuc-hA$_1$ ARs were seeded in 96-well plates. On the day of the experiment, the media were aspirated, and the cells were washed twice with warm HBSS. The cells were either incubated with HBSS (control set) or subsequently incubated with probe **4-5** and Tetrazine-AF488, each step followed by an hour of incubation in a humidified atmosphere without additional CO_2. The cells were washed twice with warm HBSS after each labelling step. The cells were then incubated with varying concentrations (0 to 250 nM) of probe **3-29** in the presence or absence of 1 µM DPCPX pretreatment for one hour. At the end of the incubation, furimazine was added to each well, followed by a 5-minute equilibrium, and the plate was read on the PHERAstar FSX (BMG) twice (once for red BRET and once for green BRET measurement).

The saturation binding curves are displayed in **Figure 4-24**. In the red channel, A_1 AR with or without the AF488 tag exhibited a similar pattern, with a higher signal in the AF488-attached set, which aligned with previous findings that FRET occurred between AF488 and **3-29**. In the green channel, no specific binding was observed in A_1 AR without the AF488 tag, as there was no green acceptor in the system. Conversely, a concentration-dependent signal drop was noticed in A_1 AR with the AF488 tag compared to its non-specific binding set. This signal drop was consistent with the FRET observed previously when **3-29** was introduced into the AF488-tagged A_1 AR. The measured K_d values from A_1 AR with or without the AF488 tag in the red channel and the K_d measured from the green channel with decreased BRET signal as a ligand binding response did not show significant differences through one-way ANOVA analysis (**Table 4-2**). This experiment

indicated that ligand binding affinity to A_1 AR was not altered after tagging with AF488 through two-phase labelling.
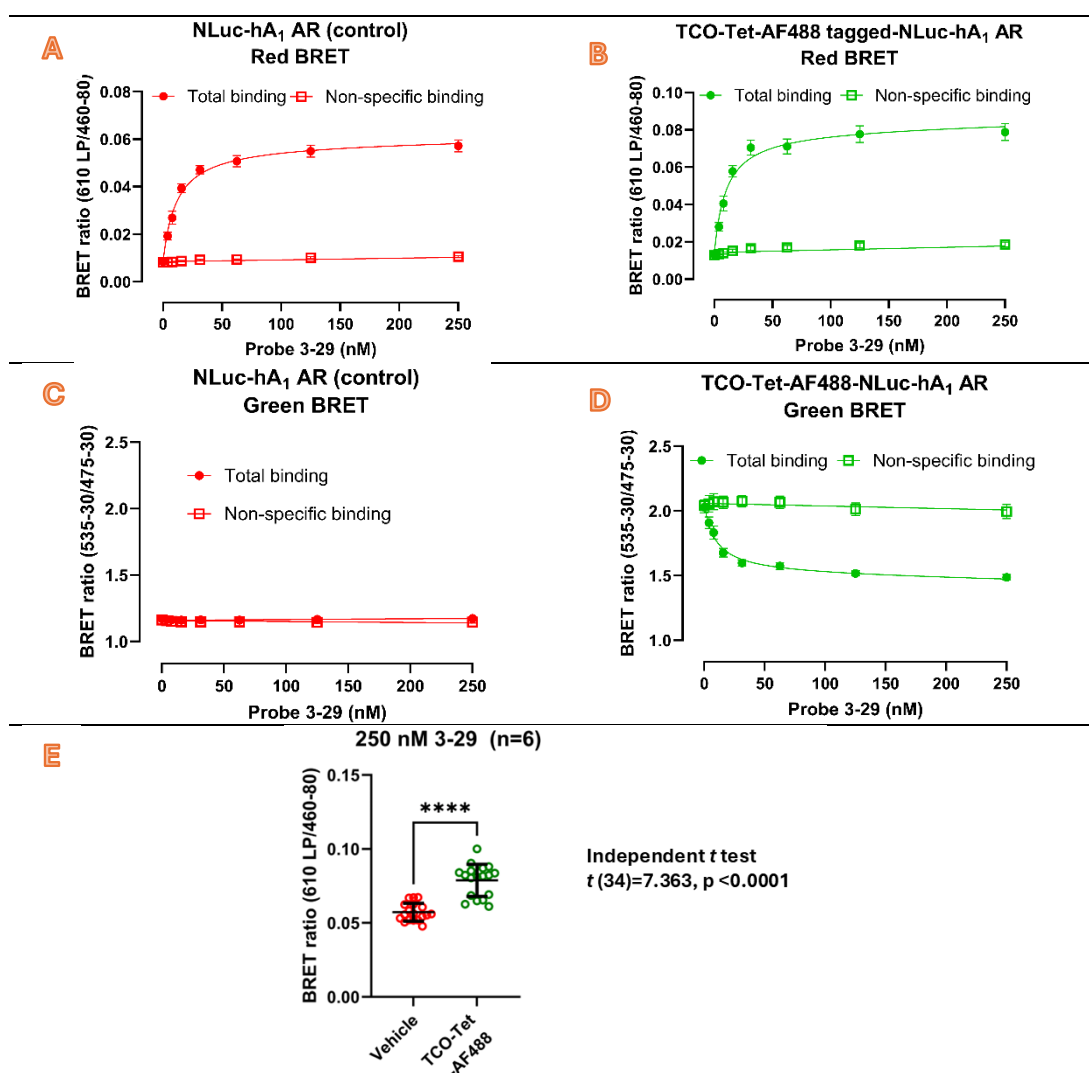
Figure 4-24. Effect of LD Probe Labelling on Ligand Binding Affinity Assessed *via* Saturation Binding Assays using probe 3-29 in Two forms of NLuc-hA$_1$ AR (with and without LD Probe labelling).
Panels (A) and (B) show saturation binding curves measured in the red channel for untagged NLuc-hA$_1$AR (control) and NLuc-hA$_1$AR labelled with TCO-Tet-AF488, respectively. In both cases, specific binding increased with rising concentrations of probe **3-29**. To assess differences in signal intensity, BRET signals at the highest probe concentration (250 nM) were compared using an unpaired *t*-test, as shown in panel (E). A significant difference was observed [t(34) = 7.363, p < 0.0001], consistent with previously reported FRET between AF488 and BODIPY630/650. Panels (C) and (D) display saturation binding curves measured in the green channel for control and LD probe-labelled NLuc-hA$_1$AR, respectively. In panel (C), both total and non-specific binding signals appear as flat lines, indicating the absence of a green fluorophore acceptor on the untagged receptor. The detected signal is attributed to luminescence bleed-through. In contrast, panel (D) shows a green BRET signal in the LD probe-labelled condition, with a concentration-dependent decrease in total binding signal, consistent with energy transfer from AF488 to BODIPY630/650 *via* FRET. Panel (E) summarises the enhanced red BRET signal observed in AF488-tagged A$_1$ARs. For the *t*-test analysis, data from 18 wells per condition were included. Non-specific binding was defined using cells pre-incubated with 1 μM DPCPX for 30 minutes. All data represent the mean ± SEM from six independent experiments, each performed in triplicate.

Table 4-2. Measured probe **3-29** K_d values

Model- NLuc-hA$_1$ AR	mean $\pm$ SEM [nM (n)]	One-way ANOVA
control / Red channel	12.27 $\pm$ 2.03 (6)	
+ TCO-Tet-AF488 / Red channel	10.92 $\pm$ 1.88 (6)	F (2,15) =0.4650, P=0.6369
+ TCO-Tet-AF488 / Green channel	9.73 $\pm$ 1.66 (6) [a]	

[a] The observed decrease in the BRET signal was interpreted as a response to the increasing ligand concentration in Prism, similar to a competition assay. However, while the signal decrease in a competition assay is typically due to the displacement of a labelled ligand by an unlabelled one, in this case, the signal decrease was attributed to the energy transfer from the BRET acceptor (AF488) to probe **3-29** *via* FRET.

4.3.3 Conclusion and Summary

The aim of the series of experiments in this chapter was to refine the A_1 AR labelling effect through probe **1-57** in conjunction with methyl-tetrazine-SulfoCyanine 5 (MTCy5). A structural modification was carried out in an attempt to either elevate AR subtype selectivity or enhance A_1 AR binding. Probe **4-5**, an analogue of probe **1-57**, demonstrated similar A_1/A_{2A} and A_1/A_3 AR subtype selectivity and A_1 AR binding affinity but improved A_1/A_{2B} selectivity (from 60[74] to 245-fold). A series of labelling condition investigations were conducted, including phase 1 incubation length, phase 2 incubation period, incubation environment (media or buffer selection), and paired click reaction reagent [Tetrazine-SulfoCyanine 5 (HTCy5) was superior to MTCy5]. A suggested incubation condition for preparing confocal imaging samples was incubation with 100 nM of probe **4-5** for 2 hours, followed by phase 2 labelling with HTCy5 for 15 minutes. HBSS was recommended as the buffer for at least phase 1 labelling. Hence, the preliminary goal was achieved: optimised probe **1-57** AR subtype selectivity and improved two-phase labelling efficiency on A_1 AR.

In addition to optimising the labelling conditions, the flexibility of the two-phase labelling system was harnessed to set up an AF488 tag on A_1 AR for orthosteric binding pocket assessment using Tetrazine-AF488 as the phase 2 reagent. Unlike the typical assessment of orthosteric binding pocket availability *via* agonist stimulation after LD covalent labelling, a BRET-based assessment in the red and green channels was demonstrated using the two-phase labelling system. With well-designed controls and distance-restricted BRET, the accessibility of the orthosteric binding site was confirmed. Subsequent FLIM-FRET assays further solidified the BRET-based orthosteric binding site investigation results. Lastly, a saturation binding assay was used to evaluate the interference of the tag set by two-phase labelling on A_1 AR ligand binding. The results showed no significant difference between A_1 AR with or without the tag set *via* two-phase labelling.

The series of evaluations presented a promising potential for the two-phase labelling system. As it covalently labelled A_1 AR purely *via* chemical reactions without gene engineering work, it offered flexibility for reporter type by using different phase 2 reagents, and the orthosteric binding pocket remained free for another ligand access. It could serve as an alternative to self-labelling protein tags commonly used in biomolecular study, which required genetic engineering and large tag sizes, raising concerns about their impact on the target protein.

Chapter 5. Development and Optimisation of Ligand-Directed Probes Targeting A$_1$ Adenosine Receptors: Insights from Two-Phase Labelling Probes

5.1 General

5.1.1 Brief Introduction

The beauty of ligand-directed (LD) covalent labelling probes lies in their ability to covalently tag proteins of interest (POI) in multi-component live cell systems through chemical reactions[96], without prior genetic engineering[88], while maintaining ligand accessibility post-labelling[89]. Compared to fluorescent proteins and self-labelling protein tags, which require genetic engineering[88], LD probes represent a relatively natural approach. Additionally, the minimal impact arising from the small tag size (fluorophores, below 1 kDa) compared to protein tags (GFP, 27 kDa[79]; SNAP-tag, 19 kDa[122]) is valuable for biomolecule studies. To serve as reliable tools, LD probes must exhibit several key characteristics: high selectivity for the target POI, rapid labelling kinetics, sufficient chemical stability, minimal interference with ligand access to the orthosteric binding pocket following tagging, and negligible impact on the native function of the POI[189] (**Figure 5-1**). High selectivity is essential to minimise off-target labelling and enhance the signal-to-noise ratio, thereby facilitating accurate interpretation of downstream data, such as the subcellular localisation of the POI when fluorescent tags are employed. Rapid labelling kinetics reduce the required incubation time, making the approach more practical for experimental workflows[95,96]. Adequate stability is also critical, as the LD probe must remain intact until it reaches and labels the POI[88,189]. Degradation in stock solutions or aqueous environments can reduce the effective concentration of the probe and increase the presence of competing ligands (e.g., congeners), thereby diminishing labelling efficiency.

Importantly, the labelling tag must not obstruct access to the orthosteric binding pocket. If access is blocked, the probe functions as an irreversible ligand rather than a true LD probe, precluding subsequent functional assays. In contrast, successful LD labelling should preserve orthosteric accessibility, enabling continued receptor activity and downstream pharmacological evaluation[96,190]. Finally, the labelling process should exert minimal influence on the POI's

function to ensure that experimental observations reflect physiological conditions rather than artifacts introduced by the labelling strategy[74,189].

Several of the key characteristics of LD probes are interrelated. For instance, high reactivity is often accompanied by reduced stability, as the reactive moiety is prone to undesired interactions with nucleophiles such as amino acids in the medium (e.g., lysine and cysteine), water molecules in solution, or even the phenol group within the LD probe itself[88,180]. As a result, a balance must be struck between reactivity and stability to achieve optimal performance. For example, 2,3,5,6-tetrafluorophenyl ester is too reactive to be incorporated into LD probes due to its low stability, which poses challenges during synthesis[92]. In contrast, 2,6-dibromophenyl ester[92], 2,6-dichlorophenyl ester[92], and 2-fluorophenyl ester[74,113] are less reactive due to the presence of fewer electron-withdrawing halogens on the phenyl ring. However, these moieties offer improved stability and can be successfully incorporated into LD probes[74,92,113].

Another interdependent relationship exists between selectivity and labelling duration. Extremely high selectivity allows for the use of higher LD probe concentrations during the labelling step without inducing off-target effects. Increased probe concentration enhances the rate of binding to the target POI, as the observed association rate constant ($K_{on(obs)}$) is directly proportional to ligand concentration. Since LD probe labelling involves an initial binding event followed by a covalent cargo transfer reaction, accelerating the binding step can reduce the overall labelling time[189].

Designing an LD probe that simultaneously fulfils all desired criteria remains a significant challenge. Iterative structural modifications informed by pharmacological data, along with strategic compromises, are often necessary to optimise probe performance.
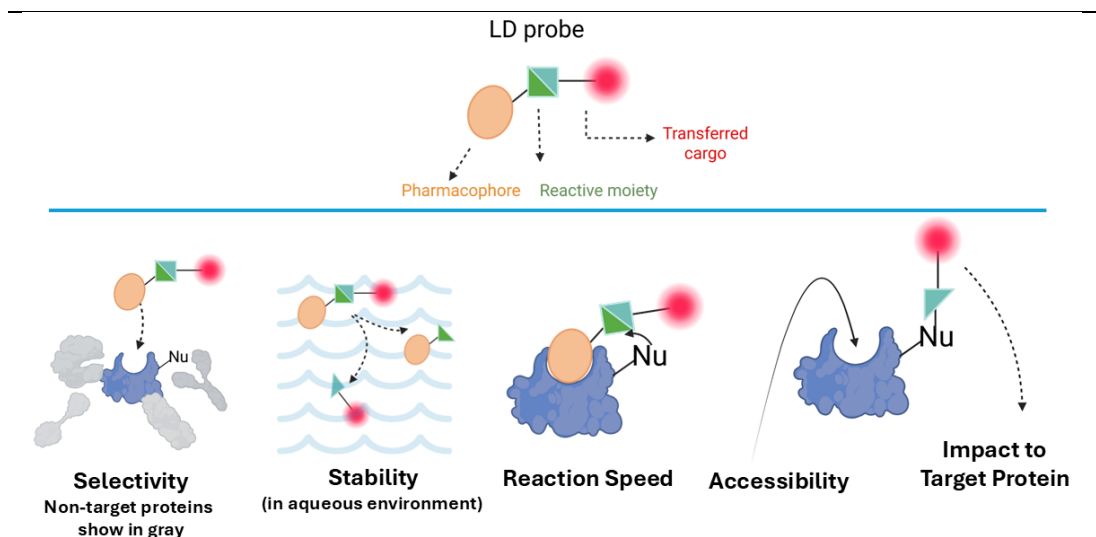
Figure 5-1. Five Aspects for Characterising LD Probes.
Selective Binding: The ability of LD probes to selectively bind to target proteins in a multi-component environment. Stability: Fast degradation in aqueous environments limits the pragmatic application of LD probes. Reaction Speed: The reaction speed between LD probes and nucleophilic amino residues on the target protein, influenced by the type of reactive moiety and nucleophile, the distance between the reactants, and the microenvironment where the reaction occurs. Ligand Accessibility: The ability of ligands to freely bind to tagged target proteins post-labelling, enabling further investigation. Impact on Target Protein: The effects of labelling on the target protein, including changes in function and trafficking. Figure created *via* BioRender (www.biorender .com)

5.1.2 The Aim of This Chapter

Comeo's LD probe **1-56**, which transfers a sulfo-Cy5 group onto A_1 AR, demonstrated nanomolar binding affinity for A_1 AR. No binding was observed for A_{2B} or A_3 ARs at concentrations up to 500 nM in saturation binding assays, effectively eliminating concerns about off-target labelling for these subtypes. However, probe **1-56** also exhibited measurable binding to A_{2A} ARs, with an A_1/A_{2A} selectivity ratio of only 5.9-fold (affinity data present in **Chapter 3, Table 3-5**).

To address the limited A_1/A_{2A} selectivity, structural modifications were made to probe **1-56**, focusing on the linker and phenyl ester position. These modifications yielded four new LD probes with improved A_1/A_{2A} selectivity, ranging from 8.2- to 18.9-fold, while maintaining selectivity against A_{2B} and A_3 ARs (**Chapter 3, Table 3-5**). Although these changes enhanced selectivity modestly, further improvement was still necessary.

In Chapter 4, a related LD probe, **1-57** (which transfers a TCO group), was structurally optimised through similar modifications to produce probe **4-5**. Both probe **1-57** and probe **4-5** demonstrated approximately 100-fold selectivity for A_1 over A_{2A} ARs (**Chapter 4, Table 4-1**). Notably, probes **3-22** (sulfo-Cy5) and **4-5** (TCO) share the same pharmacophore, γ-aminobutyric acid linker, and *meta*-phenyl ester. In contrast, probes **1-56** (sulfo-Cy5) and **1-57** (TCO) incorporate the

same pharmacophore, a *β*-alanine linker and a *para*-substituted phenyl ester. Despite these similarities, the TCO-tethered probes consistently exhibited higher A_1/A_{2A} selectivity (**Figure 5-2**A).

These structure–activity relationships between the two probe sets highlight the influence of cargo constitution on receptor subtype selectivity. This insight guided further structural modifications aimed at enhancing the selectivity of single-phase LD probes, such as sulfoCy5 derivatives.

5.2 Structure Design

Probe sets **1-56** (SulfoCy5) and **1-57** (TCO), along with sets **3-22** (SulfoCy5) and **4-5** (TCO), are presented in **Figure 5-2**A. Within each pair, the only structural difference lies in the transferred cargo—either SulfoCy5 or a linear chain conjugated to TCO. Ligands bearing the TCO group exhibited a higher A_1/A_{2A} selectivity ratio compared to their SulfoCy5-containing analogues, suggesting that the linear chain may play a critical role in modulating selectivity. Furthermore, LD probes incorporating a *γ*-aminobutyric acid (GABA) linker and a *meta*-2-fluorophenyl ester demonstrated slightly enhanced selectivity relative to those containing a *β*-alanine linker and a *para*-2-fluorophenyl ester. Based on these observations, a new probe, **5-3**, was designed by substituting the TCO group in probe **4-5** with SulfoCy5. Given that the linear chain in probe **5-3** was longer than that in probe **4-5**, a polyethylene glycol (PEG) truncated version (probe **5-8**) was also developed to preserve the original chain length (**Figure 5-2**B).

Figure 5-2. Ligand Design Strategy Informed by Structure–Selectivity Relationship Data.
(A) Two sets of LD probes are shown, each comprising one probe conjugated to sulfoCy5 and another tethered to a TCO group. The upper set features a *β*-alanine linker (green) and a *para*-2-fluorophenyl ester (blue), while the lower set incorporates a *γ*-aminobutyric acid (GABA) linker (green) and a *meta*-2-fluorophenyl ester (blue). Probes **4-5** and **1-57**, both containing the TCO cargo, exhibited approximately 100-fold selectivity for A_1 over A_{2A} ARs, suggesting that the additional linear structure in the cargo might have been key for selectivity. (B) Given that probe **4-5** demonstrated the highest A_1/A_{2A} selectivity, it was used as a structural template for further optimisation. Probe **5-3** was designed by replacing the TCO group in probe **4-5** with sulfoCy5, while probe **5-8** was generated by truncating the polyethylene glycol (PEG) moiety to preserve the linear chain length of probe **4-5**.

5.3 Result and Discussion

5.3.1 Chemistry

5.3.1.1 Synthesis

The synthesis route of probes **5-3** and **5-8** is outlined in **Scheme 5-1** and **Scheme 5-2**. The synthesis commenced with the preparation of the cargo's linear chain. Compound **4-1** was extended through a coupling reaction with succinic anhydride in the presence of DIPEA in CHCl₃, yielding compound **4-2**. Subsequently, esterification with compound **3-20** produced compound **5-1**. In this reaction, compound **4-2** was first activated with BEP in the presence of DIPEA in DMF. Compound **3-20**, dissolved in DMF, was then added to the preactivated **4-2** solution, and the reaction proceeded at room temperature overnight. Further purification was performed *via* RP-HPLC using a C18 semipreparative column. To couple the SulfoCy5 fluorophore, acid *t*-Boc deprotection was applied to compound **5-1**, yielding compound **5-2**, which possessed an alkyl amine moiety in hydrochloride salt form. Compound **5-2** and SulfoCy5 NHS ester were coupled in the presence of DIPEA in DMF for two hours at room temperature. Final purification was conducted *via* RP-HPLC using a C18 semipreparative column, affording probe **5-3**.

Scheme 5-1. Synthesis of Probe 5-3
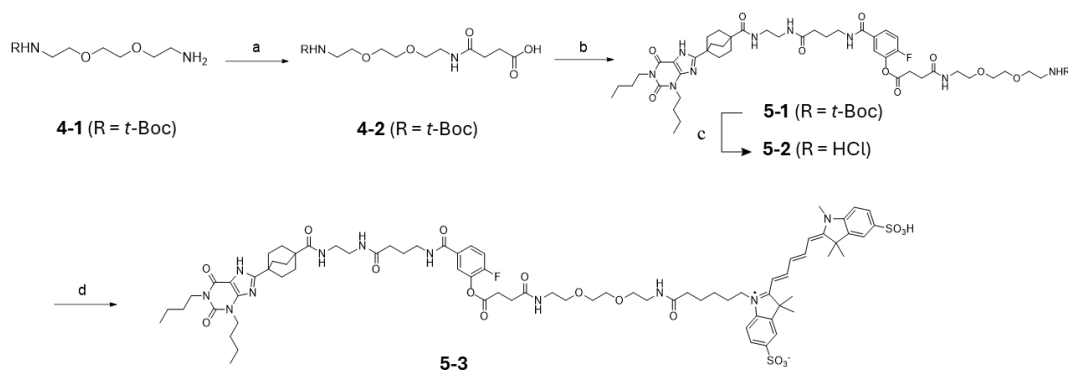
ᵃ Reagents and conditions: (a) succinic anhydride, DIPEA, CHCl₃, rt, overnight, (**4-2**) 36%; (b) BEP, DIPEA, compound **3-20**, DMF, rt, overnight, (**5-1**) 37%; (c) 4 N HCl in dioxane, rt, 1 hr; (d) SulfoCy5 NHS ester, DIPEA, DMF, rt, 2 hr, (**5-3**) 43%.

The synthesis of probe **5-8** replicated the procedures mentioned above but started with compound **5-4**. Through chain extension with succinic anhydride, esterification with compound **3-20**, followed by *t*-Boc deprotection, and coupling with SulfoCy5 NHS ester, probe **5-8** was obtained as the final product.

Scheme 5-2. Synthesis of Probe 5-8

5-4 (R = *t*-Boc)   5-5 (R = *t*-Boc)   5-6 (R = *t*-Boc)
                                                      5-7 (R = HCl)

5-8
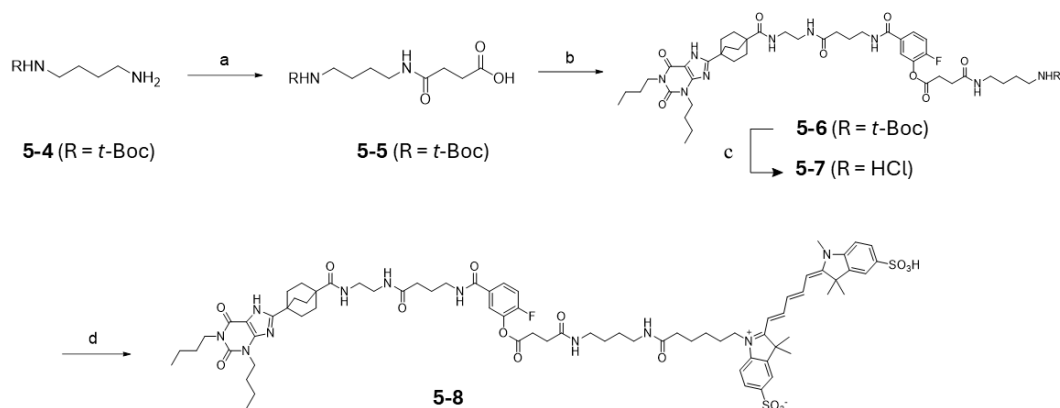
ᵃ Reagents and conditions: (a) succinic anhydride, DIPEA, CHCl₃, rt, overnight, (**5-5**) 73%; (b) BEP, DIPEA, compound **3-20**, DMF, rt, overnight, (**5-6**) 56%; (c) 4 N HCl in dioxane, rt, 1 hr; (d) SulfoCy5 NHS ester, DIPEA, DMF, rt, 2 hr, (**5-8**) 70%.

5.3.1.2 Synthesis Sequence

The synthetic route for probes **5-3** and **5-8** differed from that employed for probe **4-5**. In the synthesis of probe **4-5**, the complete cargo transfer moiety was assembled prior to forming an ester linkage with compound **3-20** in the final step. In contrast, the synthesis of probes **5-3** and **5-8** was divided into two stages: initial attachment of the linear chain to compound **3-20**, followed by final coupling with NHS-SulfoCy5 (**Figure 5-3**). Although this stepwise approach was counterintuitive—given that linear synthesis typically results in lower overall yields—it was adopted as a practical compromise to overcome synthetic challenges.

Initially, the strategy involved preparing the entire cargo moiety for subsequent esterification. However, this approach failed to yield the desired products, even when various coupling reagents such as DMTMM, BEP, and T3P were employed (**Figure 5-4**). The failure was likely due to the hydrophilic nature of the SulfoCy5 moiety, which may have impeded the reaction, whereas reactions involving more lipophilic termini (e.g., *t*-Boc or TCO) proceeded successfully. Consequently, two novel probes were synthesised by first attaching the linear chain, followed by coupling with NHS-SulfoCy5 as the final step (**Figure 5-3**).
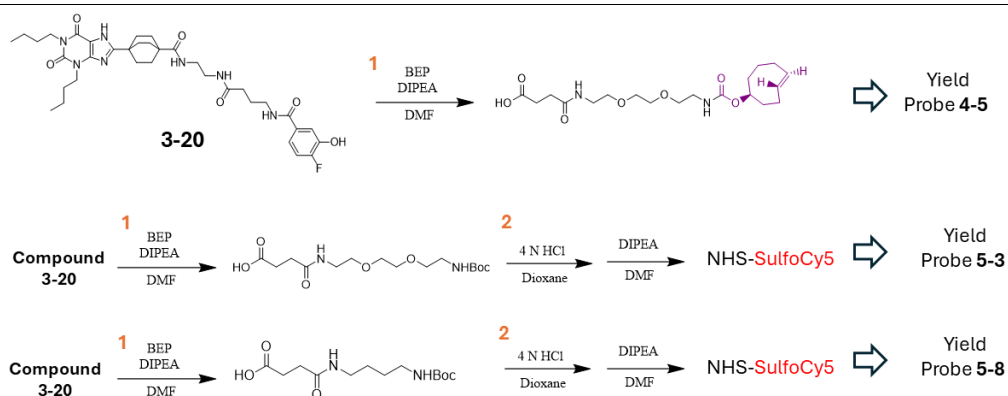
Figure 5-3. Synthetic Strategies for Incorporating the Cargo Transfer Moiety to Yield the Final Probes.

The top route illustrates the synthesis of probe **4-5**, in which compound **3-20** is coupled in a single step with the fully assembled cargo moiety. The middle and bottom routes depict the synthetic strategies for probes **5-3** and **5-8**, respectively. In these cases, compound **3-20** is first coupled with a linear chain moiety, followed by acid-mediated *t*-Boc deprotection and subsequent coupling with NHS-SulfoCy5. This stepwise approach, while necessary to overcome synthetic challenges, resulted in a lower overall yield for probes **5-3** and **5-8**.
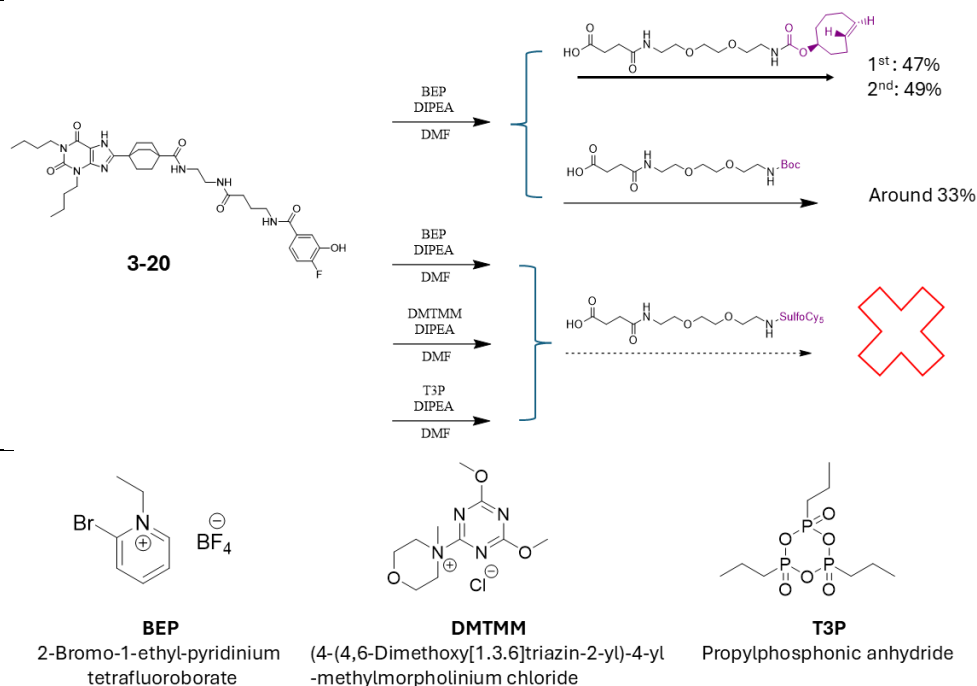
Figure 5-4. Esterification Reaction.

The upper part displays the **3-20** esterification with different reactants. Carboxylic acid tethering TCO or *t*-Boc at the other end of the linear chain give the desired compound in the presence of BEP and DIPEA in DMF. However, carboxylic acid tethering SulfoCy5 does not afford the desired compound under three coupling conditions. The structures of the coupling reagents are displayed at the bottom.

5.3.1.3 Stability Assessment

5.3.1.3.1 Stability 24-Hour Assessment

The LD probe was designed to react with nucleophilic amino acid residues on the target protein in live cells, facilitating the covalent transfer of cargo. However, water and other ingredients in the labelling environment reacted with LD probes, accelerating the degradation rate. To validate whether the newly synthesised LD probe possessed acceptable stability for live cell application, RP-HPLC-based analysis was conducted as a preliminary assessment. The experiment details are described in **Chapter 2**, **Section 2.2.6.1**. In Chapter 4, different incubating solutions in the LD probe labelling step affected the final labelling efficiency. Therefore, in addition to HBSS (used for stability assessment in Chapter 3, session 3.2.1.3), three other solutions were tested: Dulbecco's Modified Eagle Medium (DMEM) with phenol supplemented with 10% foetal calf serum (FCS), DMEM without phenol red, and DMEM with phenol. Probe **5-8** was prepared at 1.2 mM in each of the four solutions. Caffeine at 2 mM was used as the internal standard. The prepared solutions were placed on a heat block preheated to 37°C. Samples were analysed through RP-HPLC with a C18 analytic column at various time points. The results are displayed in **Figure 5-5** to **Figure 5-8**.

Retention Time (min)				
Time point	Caffeine	SulfoCy5	**5-8**	Congener
Start	5.101	6.44	9.142	10.249
1 hr	5.04	6.66	9.102	10.12
3 hr	5.092	6.703	9.154	10.167
5 hr	5.06	6.696	9.275	10.234
24 hr	5.085	6.661	9.403	10.2

AUC percentage (%)			
Time point	SulfoCy5	**5-8**	Congener
Start	0.24	98.84	0.92
1 hr	5.16	84.18	10.66
3 hr	13.95	65.08	20.97
5 hr	19.95	52.55	27.50
24 hr	44.28	10.72	45
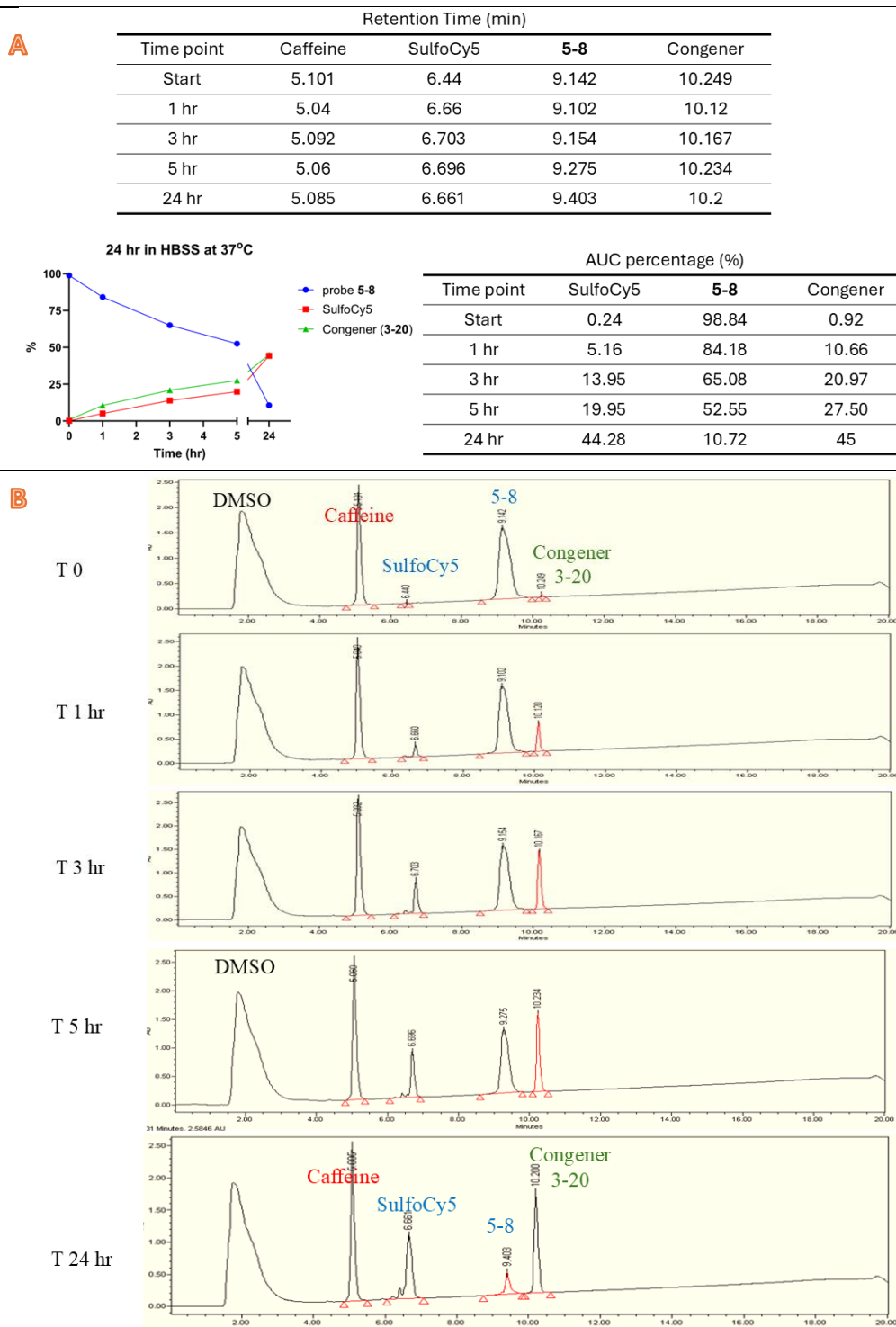
Figure 5-5. Stability Assessment of Probe 5-8 in HBSS at 37 °C.

Probe **5-8** was prepared at a concentration of 1.2 mM in HBSS and incubated at 37 °C. The percentage of intact probe **5-8** decreased over time, with approximately 50% remaining after five hours of incubation. Panel (A) presents the retention times of caffeine (internal standard), probe **5-8**, compound **3-20** (a congener), and sulfoCy5. The area under the curve (AUC) for probe **5-8**, compound **3-20**, and sulfoCy5 was normalised to that of caffeine, converted into percentages, and displayed as both a table and a line graph. Panel (B) shows the RP-HPLC spectra of probe **5-8** samples collected at various time points, with annotated peaks corresponding to the identified compounds.

Retention Time (min)				
Time point	Caffeine	SulfoCy5	**5-8**	Congener
Start	5.108	6.494	9.333	10.193
1 hr	5.056	6.674	9.535	10.215
3 hr	5.088	6.735	-	10.2

24 hr in DMEM + FCS at 37°C

Probe **5-8**
SulfoCy5
Congener (**3-20**)

AUC percentage (%)			
Time point	SulfoCy5	**5-8**	Congener
Start	0.12	98.26	1.62
1 hr	42.03	3.13	54.84
3 hr	40.32	0	59.68

B

DMSO · Caffeine · SulfoCy5 · 5-8 · Congener 3-20

T 0

T 1 hr

T 3 hr
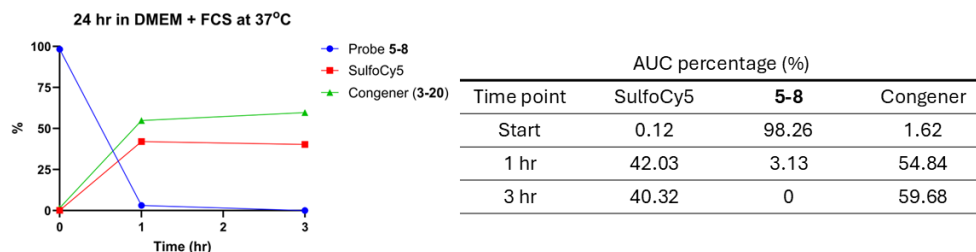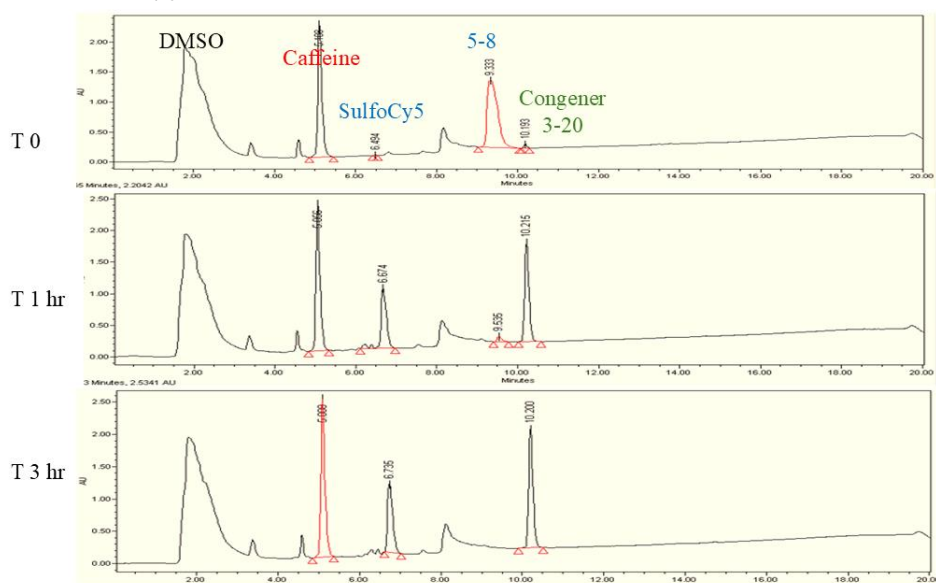
Figure 5-6. Stability Assessment of Probe 5-8 in DMEM Supplemented with 10% FCS at 37 °C.

Probe **5-8** was prepared at a concentration of 1.2 mM in DMEM containing phenol red and supplemented with 10% FCS, and incubated at 37 °C. The percentage of intact probe **5-8** decreased over time and was no longer detectable after three hours of incubation. Panel (A) presents the retention times of caffeine (internal standard), probe **5-8**, compound **3-20** (a congener), and sulfoCy5. The area under the curve (AUC) for probe **5-8**, compound **3-20**, and sulfoCy5 was normalised to that of caffeine, converted into percentages, and displayed as both a table and a line graph. Panel (B) shows the RP-HPLC spectra of probe **5-8** samples collected at various time points, with annotated peaks corresponding to the identified compounds.

A

	Retention Time (min)			
Time point	Caffeine	SulfoCy5	**5-8**	Congener
Start	5.131	-	9.288	10.277
1 hr	5.088	6.724	9.6	10.299
3 hr	5.114	6.777	-	10.285

24 hr in DMEM with phenol red at 37°C

	AUC percentage (%)		
Time point	SulfoCy5	**5-8**	Congener
Start	0	98.38	1.62
1 hr	49.99	3.20	46.81
3 hr	52.51	0	47.49

B
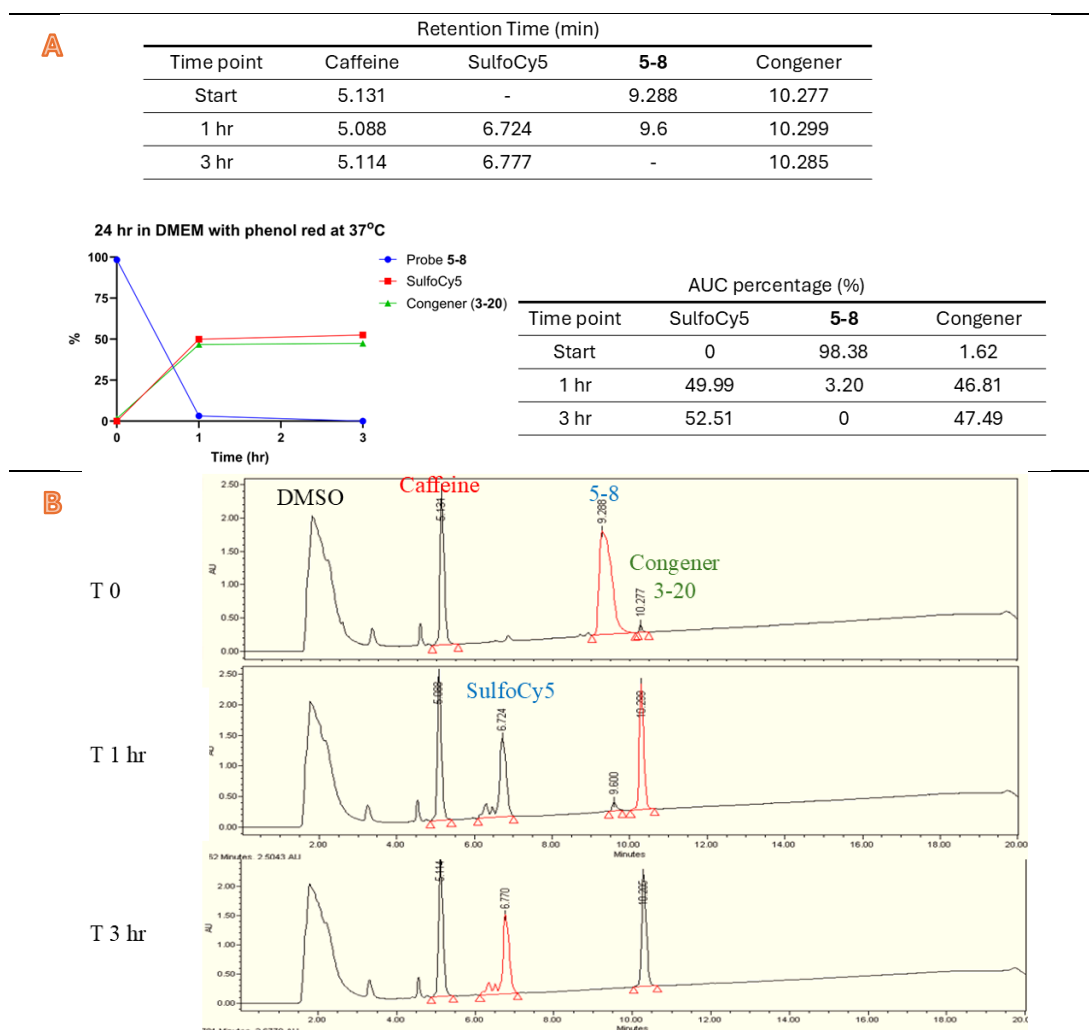
Figure 5-7. Stability Assessment of Probe 5-8 in DMEM at 37 °C.
Probe **5-8** was prepared at a concentration of 1.2 mM in DMEM containing phenol red and incubated at 37 °C. The percentage of intact probe **5-8** decreased over time and was no longer detectable after three hours of incubation. Panel (A) presents the retention times of caffeine (internal standard), probe **5-8**, compound **3-20** (a congener), and sulfoCy5. The area under the curve (AUC) for probe **5-8**, compound **3-20**, and sulfoCy5 was normalised to that of caffeine, converted into percentages, and displayed as both a table and a line graph. Panel (B) shows the RP-HPLC spectra of probe **5-8** samples collected at various time points, with annotated peaks corresponding to the identified compounds.

Panel A — Retention Time (min)

Time point	Caffeine	SulfoCy5	5-8	Congener
Start	5.115	6.851	9.272	10.333
1 hr	5.081	6.616	9.414	10.186
3 hr	5.074	6.611	-	10.176

24 hr in DMEM without phenol red at 37°C

AUC percentage (%)

Time point	SulfoCy5	5-8	Congener
Start	0.76	96.32	2.92
1 hr	49.97	7.03	43
3 hr	52.25	0	47.75

Figure 5-8. Stability Assessment of Probe 5-8 in DMEM Without Phenol Red at 37 °C.

Probe **5-8** was prepared at a concentration of 1.2 mM in DMEM without phenol red and incubated at 37 °C. The percentage of intact probe **5-8** decreased over time and became undetectable after three hours of incubation. Panel (A) displays the retention times of caffeine (internal standard), probe **5-8**, compound **3-20** (a congener), and sulfoCy5. The area under the curve (AUC) for probe **5-8**, compound **3-20**, and sulfoCy5 was normalised to that of caffeine, converted into percentages, and presented as both a table and a line graph. Panel (B) shows the RP-HPLC spectra of probe **5-8** samples collected at various time points, with annotated peaks corresponding to the identified compounds.

HBSS provided the most stable environment for probe **5-8** among the four tested solutions, with over 80% of the probe remaining intact after one hour of incubation, whereas the other three conditions resulted in less than 10% remaining (**Table 5-1**).

Table 5-1. Area Under the Curve (AUC) values for Probe 5-8 Incubated at 37 °C in Four Different Solutions.

Solution	HBSS	DMEM with Phenol red and 10% FCS	DMEM with phenol red	DMEM without phenol red
Incubation (Hr)	Raw AUC of probe **5-8**/ Raw AUC of caffeine (internal standard)/ Intact probe **5-8** percentage *			
0	30,902,469/ 16,890,709/ 98.84%	20,290,837/ 15,187,737/ 98.26%	33,658,483/ 16,800,126/ 98.38%	38,462,836/ 15,750,372/ 96.32%
1	25,326,858/ 17,519,724/ 84.18%	671,717/ 15,709,690/ 3.13%	1,139,863/ 17,405,603/ 3.20%	2,976,578/ 17,550,795/ 7.03%
3	25,493,497/ 18,337,030/ 65.08%	0	0	0

* The percentage of intact probe **5-8** was calculated by normalising the AUC values of probe **5-8**, congener **3-20**, and sulfoCy5 to that of the internal standard, caffeine. The final percentage was determined using the formula: probe **5-8** / (probe **5-8** + congener **3-20** + sulfoCy5).

The accelerated degradation of probe **5-8** in DMEM may be attributed to its high concentrations of amino acids, such as 1 mM lysine and 0.2 mM cysteine. The nucleophilic side chains of these amino acids are capable of reacting with the electrophilic moiety of probe **5-8**, thereby promoting its decomposition. In contrast, HBSS—composed of inorganic salts, HEPES, glucose, and water— lacks amino acids, resulting in greater stability of probe **5-8** under the same conditions.

Surprisingly, similar degradation profiles were observed in DMEM with and without FCS. This was unexpected, as the addition of FCS—containing a complex mixture of hormones, growth factors, proteins, and lipids—was anticipated to enhance the degradation rate of probe **5-8**.

A notable difference was observed between DMEM formulations with and without phenol red. Although phenol red is commonly used as a pH indicator in cell culture media, its presence appeared to affect the stability of probe **5-8**. After one hour of incubation, the amount of intact probe was approximately two-fold lower in the presence of phenol red (**Table 5-1**). This effect may be explained by the nucleophilic nature of the phenol group in phenol red, which can react with the reactive moiety of probe **5-8** (see **Chapter 4, Figure 4-13**). According to the supplier's formulation (Sigma-Aldrich, catalogue number D6545), the

concentration of phenol red in DMEM is approximately 40 µM, which may be sufficient to contribute to the observed degradation.

These findings also relate to observations discussed in **Chapter 4, Section 4.3.2.2.5**, which examines the influence of incubation media on the final labelling outcomes of the two-phase labelling probe **4-5**. The comparable extent of ester bond cleavage observed for probe **5-8** in DMEM with and without FCS helps explain the suboptimal labelling performance of probe **4-5** in DMEM with FCS. This may be attributed to the isomerisation of *trans*-cyclooctene (TCO) into its less reactive *cis* form. In contrast, improved confocal imaging results were obtained in DMEM without FCS (see **Chapter 4**, **Figure 4-14**), supporting this hypothesis.

Furthermore, the slightly slower degradation of probe **5-8** in DMEM without phenol red, compared to DMEM with phenol red, provides a plausible explanation for the enhanced two-phase labelling observed in confocal images (**Chapter 4**, **Figure 4-12**). This suggests that phenol red may contribute to probe instability, likely through nucleophilic attack on the ester moiety.

These results also connect to the discussion in **Chapter 3**, **Section 3.2.1.2**, which addresses ligand stability in HBSS at 37 °C over a 25-hour period. In that study, over 85% of probes **3-16** and **3-22** remained intact after 25 hours of incubation. In contrast to probe **5-8**, probes **3-16** and **3-22** lack long linear linkers between the sulfoCy5 fluorophore and the 2-fluorophenyl ester group, and exhibited significantly slower degradation. This difference may be attributed to the steric hindrance provided by the proximity of sulfoCy5 to the ester moiety in probes **3-16** and **3-22**—a feature absent in probe **5-8**, where sulfoCy5 is spatially distant from the reactive site. These findings underscore that even when probes share the same reactive moiety, their overall molecular architecture can significantly influence their stability.

5.3.1.3.2 Stability of DMSO-Aliquoted Probe **5-8** Stored in a -20°C Freezer

Synthesised LD probes were prepared as a 1 mM stock solution in DMSO and stored in a -20°C freezer for subsequent pharmacological assessment. To ensure that probe **5-8** remained above 95% purity, a weekly analysis of the DMSO-aliquoted **5-8** stock solution was conducted. The experimental details are described in **Chapter 2**, **Section 2.2.6.3**. Probe **5-8** was prepared as a 1.2 mM solution in DMSO and dispensed in 20 µL aliquots into amber microcentrifuge tubes, which were stored in a -20°C freezer. Each week, a microcentrifuge tube was taken from the freezer, thawed at room temperature for 30 minutes, and subjected to RP-HPLC analysis. The analysis data are displayed in **Figure 5-9**. The results showed that the purity of probe **5-8** fell below 95% after seven weeks of storage in the -20°C freezer. Based on these findings, it is recommended that

probe **5-8** be stored in dry powder form for long-term storage. The powder can be pre-weighed into individual glass vials in quantities ranging from 0.1 to 0.2 mg. It is recommended that the DMSO-aliquoted **5-8** stock solution be re-prepared every six weeks to ensure that the purity used in pharmacological assessments remains above 95%.

A

		Retention Time (min)		
Week	Caffeine	SulfoCy5	**5-8**	Congener
0	5.126	6.486	9.369	10.229
1	4.915	6.374	9.203	10.137
2	-	-	-	-
3	5.167	6.616	9.696	10.642
4	5.042	6.526	9.436	10.378
5	4.901	6.421	9.280	10.208
6	5.005	6.468	9.334	10.256
7	5.148	6.461	9.142	10.063
8	5.081	6.417	9.193	10.158

	AUC percentage (%)		
Week	SulfoCy5	**5-8**	Congener
0	0.34	98.5	1.16
1	0.96	95.67	3.36
2	-	-	-
3	0.77	96.87	2.36
4	1.3	95.26	3.44
5	1.19	95.01	3.8
6	1.23	95.08	3.69
7	1.28	94.96	3.77
8	2.06	93.26	4.68

Weekly Assessment

B
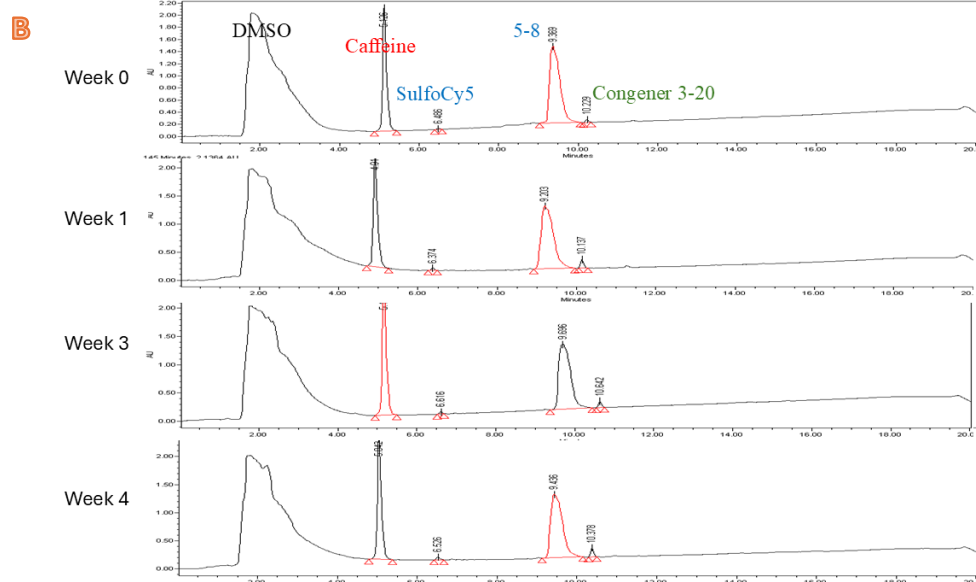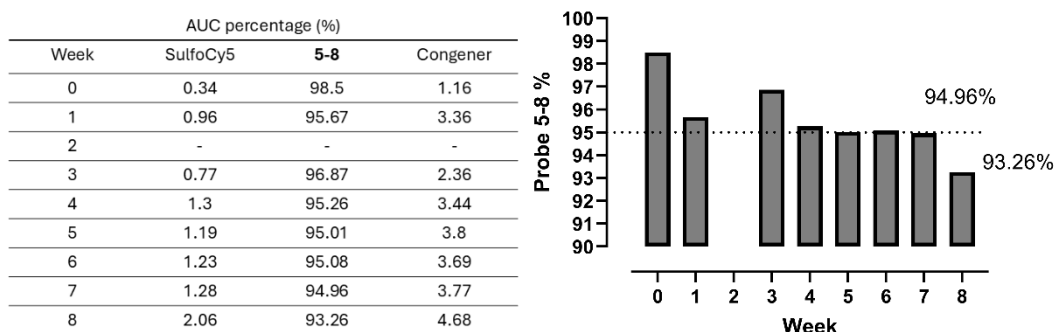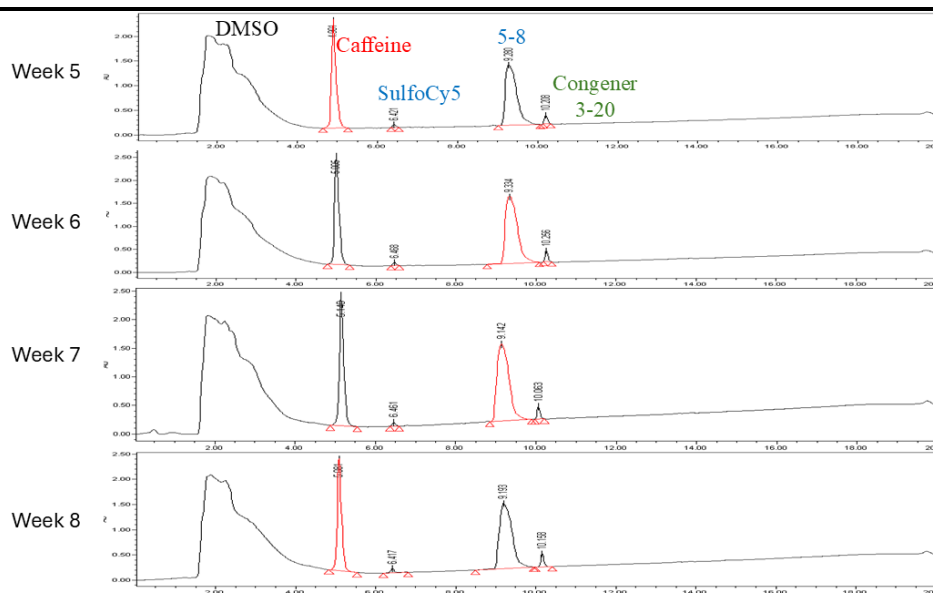
Figure 5-9. Purity Examination of DMSO-Aliquoted Probe 5-8 *via* RP-HPLC.
(A) 20 μL of the **5-8** stock solution in DMSO was submitted to RP-HPLC with 2 mM caffeine as the internal standard. The retention times and percentages of the compounds were tabulated. After seven weeks of storage, the percentage of intact probe **5-8** fell below 95%, as shown in the bar chart. The experiment for Week 2 was not conducted due to attendance at a medicinal chemistry summer school. (B) HPLC spectra from the weekly assessments are displayed, with annotations of compounds corresponding to their peaks.

5.3.2 Pharmacology

5.3.2.1 AR Subtype Binding Affinity Screen

The investigation of AR affinity for newly synthesised ligands began with the A_1 subtype to determine whether binding affinity was retained following structural modifications. The NanoBRET saturation binding assay, a widely used method for evaluating the binding affinity of fluorescent ligands[72,74,77,117,121], was employed for this purpose. HEK293T cells stably expressing NLuc tag on the *N*-terminus of human A_1 ARs (NLuc-hA₁ARs), which are readily available in our laboratory, were used in the assay.

Accordingly, the binding affinities of probes **5-3** and **5-8** toward A_1 AR were assessed using the NanoBRET-based saturation binding assay. The experimental design and procedures are detailed in **Chapter 2**, **Section 2.1.2.1**. On the day of the experiment, HEK293T cells expressing NLuc-hA₁ARs were incubated with either HBSS or HBSS containing 1 μM DPCPX (a selective A_1 AR antagonist) for 30 minutes. Subsequently, varying concentrations of probes **5-3** or **5-8** were added to the respective wells and incubated for one hour. At the end of the incubation period, furimazine was added to each well, followed by a 5-minute equilibration, and BRET measurements were performed using a PHERAstar FS plate reader (BMG Labtech).

The resulting saturation binding curves are shown in **Figure 5-10**. Both probes demonstrated specific binding to A_1 ARs, with low nanomolar dissociation constants (K_d): 5.04 ± 1.18 nM (n = 5) for probe **5-3** and 4.11 ± 0.53 nM (n = 5) for probe **5-8**. These preliminary results are promising, indicating that the structural modifications not only preserved but may have enhanced the binding affinity of the probes toward A_1 AR.
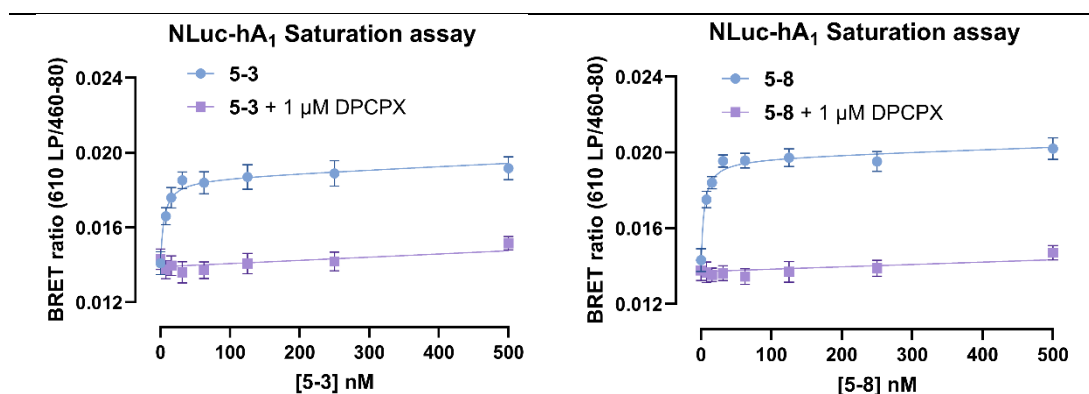
Figure 5-10. NLuc-hA₁ AR Saturation Binding Assay.
The left panel shows the experimental results for probe **5-3**, while the right panel displays the results for probe **5-8**. Both probes **5-3** and **5-8** exhibited a concentration-dependent increase in total binding. Non-specific binding was defined by cells preincubated with 1 μM DPCPX. The data are presented as the mean ± SEM from five independent experiments conducted in triplicate.

The binding affinity of probes **5-3** and **5-8** toward the other three subtypes of ARs was investigated to obtain selectivity information. Experimental details are described in Chapter 2, Section 2.1.2.1. The procedures were similar to the A_1 AR binding affinity assessment but utilised different cell models and antagonists. For the A_{2B} and A_3 AR assessments, HEK293G cells stably expressing NLuc-hA_{2B} and NLuc-hA_3 ARs were employed, respectively. For the A_{2A} AR assessment, HEK293T cells transiently expressing NLuc-hA_{2A} ARs were used. The selective antagonists used at 1 µM to define non-specific binding in each subtype saturation binding assay were as follows: ZM241385 for A_{2A}, PSB603 for A_{2B}, and MRS1220 for A_3 ARs. The pK_d values measured from the saturation binding assays for the four AR subtypes are summarised in **Table 5-2**.

Table 5-2. **Binding Affinity of LD Probes to AR Subtypes**

Probe [a]	Cargo additional chain structure	Reporter	pK_d (pK_i) mean $\pm$ SEM (n)				A_1/A_{2A} selectivity (Folds) [e]
			NLuc-hA$_1$	NLuc-hA$_{2A}$	NLuc-hA$_{2B}$	NLuc-hA$_3$	
3-22	--[b]	SulfoCy5	7.55 $\pm$ 0.17 (5)	6.45 $\pm$ 0.09 (5)	< 6.60 (5) [c]	< 6.60 (5) [c]	12.6
4-5	Succinic acid-PEG-	TCO	7.78 $\pm$ 0.13 (5)	5.73 $\pm$ 0.05 (4)	5.39 $\pm$ 0.01 (5)	< 5 (5)[d]	112
5-3	Succinic acid-PEG-	SulfoCy5	8.35 $\pm$ 0.12 (5)	7.00 $\pm$ 0.06 (5)	< 6.60 (5) [c]	< 6.60 (5) [c]	22.4
5-8	Succinic acid-butyl-	SulfoCy5	8.41 $\pm$ 0.07 (5)	6.80 $\pm$ 0.10 (5)	< 6.60 (5) [c]	< 6.60 (5) [c]	40.7

Data represented the mean ± SEM from independent saturation experiments (competition assays for probe **4-5,** proceeded with CA200645 as the fluorescent ligand at 15 nM across four AR subtypes) performed in triplicate (the repetition is indicated in the parentheses). Nonspecific binding was defined by preincubating cells with 1 µM of a specific antagonist (DPCPX for A$_1$, ZM241385 for A$_{2A}$, PSB603 for A$_{2B}$, and MRS1220 for A$_3$ ARs) for 30 minutes. NLuc-hA$_1$ ARs were expressed by HEK293T stable cell line while NLuc-hA$_{2B}$, and hA$_3$ ARs were expressed by HEK293G stable cell lines. NLuc-hA$_{2A}$ ARs were expressed by transiently transfected HEK293T cells with the NLuc-hA$_{2A}$ AR plasmid.

a. These probes shared the same orthostere, linker, and reactive moiety (*meta*-2-fluorophenyl ester).
b. Probe **3-22** was synthesised by direct esterification of the congener and SulfoCy5 free acid, without an additional chain between the ester bond and SulfoCy5.
c. Saturation was not reached at 500 nM. Additionally, the total binding presented as a flat line parallel to the non-specific binding line. Therefore, its K_d must be greater than 250 nM, which converted to a pK_d of 6.60.
d. 50% displacement was not reached at a concentration of 10 µM in a competition assay with 15 nM CA200645 as the fluorescent ligand.
e. A$_1$/A$_{2A}$ selectivity was calculated as the antilogarithm of the difference between pK_d values: 10^(pK_d A$_1$ − pK_d A$_{2A}$).

Cargo moiety modification inspired by probe **4-5** elevated A_1/A_{2A} selectivity. Probe **5-3**, which duplicated the linear chain in the cargo moiety, increased the selective ratio to 22-fold compared to probe **3-22**'s 13-fold, which lacked an additional linear chain. By adjusting the chain length, probe **5-8** further improved A_1/A_{2A} selectivity to 40-fold. These findings highlight that fine-tuning the length of the linear linker between the reactive moiety and the sulfoCy5 fluorophore can significantly influence receptor subtype selectivity.

5.3.2.2 Covalently Labelling A_1 ARs

5.3.2.2.1 Pilot Study to Determine the DPCPX Concentration Required to Inhibit Probe **5-8** Labelling

Probe **5-8** demonstrated the highest A_1/A_{2A} selectivity among a series of LD probes that directly transferred SulfoCy5 onto A_1 ARs. Consequently, probe **5-8** was selected for investigating the covalent labelling of A_1 ARs. An in-gel fluorescence scan was employed to validate the covalent labelling capability of the LD probes. To subject the labelled A_1 ARs to SDS-PAGE and subsequent fluorescence imaging, the receptors first had to be extracted from cell membrane.

Twin-Strep (TS) tags and Strep-Tactin®-coated magnetic beads are widely used for protein purification[74,113,142]. By engineering a recombinant protein with TS tags, the tagged protein can bind to Strep-Tactin® on magnetic beads, enabling its separation from complex protein mixtures[142]. This interaction is reversible, as biotin can displace the TS tag due to its higher affinity for Strep-Tactin®[142].

HEK293G cells stably expressing TS-SNAP-A_1ARs, prepared by Dr. Simon Platt, were used as the cellular model for SDS-PAGE sample preparation. The TS tag facilitated A_1 AR purification, while the SNAP tag allowed covalent labelling with SNAP-surface AF647[74], serving as a positive control. Thus, HEK293G cells expressing TS-SNAP-hA_1 AR were employed for this study.

To confirm the specificity of probe **5-8** labelling and its dependence on A_1 AR binding, cells were preincubated with DPCPX, a selective A_1 AR antagonist, prior to probe **5-8** treatment. Instead of using a high concentration of DPCPX (e.g., 10 µM), lower concentrations were explored to assess the sensitivity of probe **5-8** labelling in the presence of the antagonist.

To identify a DPCPX concentration near the threshold required to inhibit A_1 AR labelling by probe **5-8**, a BRET-based competition assay was conducted using 8 nM of probe **5-8** as the fluorescent ligand. The competition assay procedure is detailed in **Chapter 2**, **Section 2.1.2.2**. HEK293T cells stably expressing NLuc-hA_1 ARs were seeded in a 96-well plate. On the day of the experiment, the medium was aspirated, and 8 nM of probe **5-8** was added to each well, followed by varying concentrations of DPCPX. After one hour of incubation, furimazine

was added, and the plate was equilibrated for five minutes. BRET measurements were then performed using a PHERAstar FS plate reader. The resulting competition curve is shown in **Figure 5-11**.
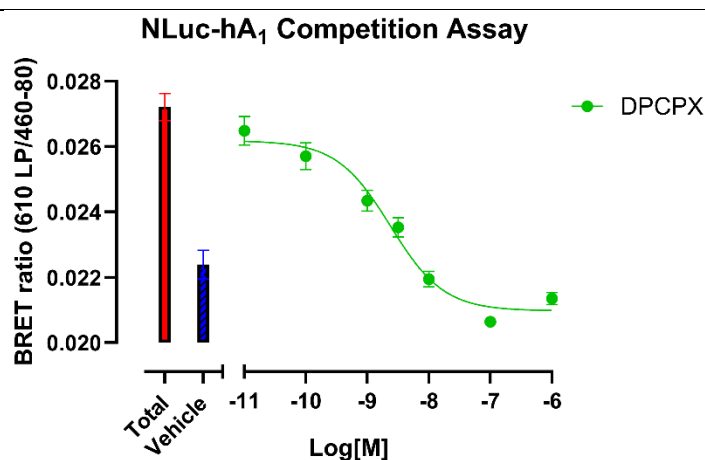
Figure 5-11. NLuc-hA1 AR Competition Assay.
The assay was conducted with HEK293T cells stably expressing NLuc-hA$_1$ ARs. In this assay, 8 nM of probe **5-8** was used as the fluorescent ligand against DPCPX, the non-fluorescent ligand, ranging from 0.01 nM to 1 µM. After an hour of incubation, furimazine was added to each well. The BRET measurement was carried out after a 5-minute furimazine equilibrium. The specific binding signal of probe **5-8** was nearly eradicated between 10 to 100 nM of DPCPX. "Total" indicated the wells treated with 8 nM of probe **5-8** only, while "vehicle" represented wells treated with HBSS only. Data are presented as the mean ± SEM from five independent experiments conducted in triplicate.

The specific binding of probe **5-8** was nearly completely inhibited by DPCPX concentrations ranging from 10 to 100 nM. Therefore, a DPCPX concentration corresponding to a pIC_{50} of 7.5 (approximately 30 nM) was selected for preparing samples for in-gel fluorescence scanning to block A$_1$ AR labelling by 4 nM of probe **5-8**.

5.3.2.2.2 A$_1$ AR Labelling Validated *via* In-Gel Fluorescent Scan

The concentration of DPCPX determined by competition was 30 nM (equal to 7.5 (-log)), allowing the sample preparation for the in-gel fluorescent scan to proceed. The experimental details are described in **Chapter 2**, **Section 2.1.4**. In the receptor labelling steps, four conditions were arranged. Cells in a T175 flask (80-95% confluence) incubated with 50 nM of SNAP surface AF647 or DMEM without phenol red for one hour served as positive and negative controls, respectively. For the experimental sets, cells in a T175 flask were incubated with 4 nM of probe **5-8** in the presence or absence of 30 nM DPCPX pretreatment for one hour. At the end of incubation, the media were removed, and the cells were gently washed twice with warm phosphate buffered saline (PBS). Cells were detached using enzyme-free cell detachment solution, pelleted by centrifugation, and the supernatant was discarded. The cell pellet was then ready for receptor extraction or temporarily stored in a -80°C freezer. The procedures for subsequent receptor solubilisation, extraction *via* MagStrep "type3" XT beads, receptor elution *via* biotin, SDS-PAGE separation and gel scanning are detailed in **Chapter 2**, **Section 2.1.4**. The gel images are displayed in **Figure 5-12**. A fluorescent band was observed in the probe **5-8** labelling set and was absent in the DPCPX pretreatment set. The fluorescent band not only positioned at the same height as the band in the positive control lane (SNAP-surface AF647) but also matched the calculated TS-SNAP-A$_1$ AR molecular weight (59 kDa). This gel image indicated that probe **5-8** specifically and covalently labelled A$_1$ ARs.
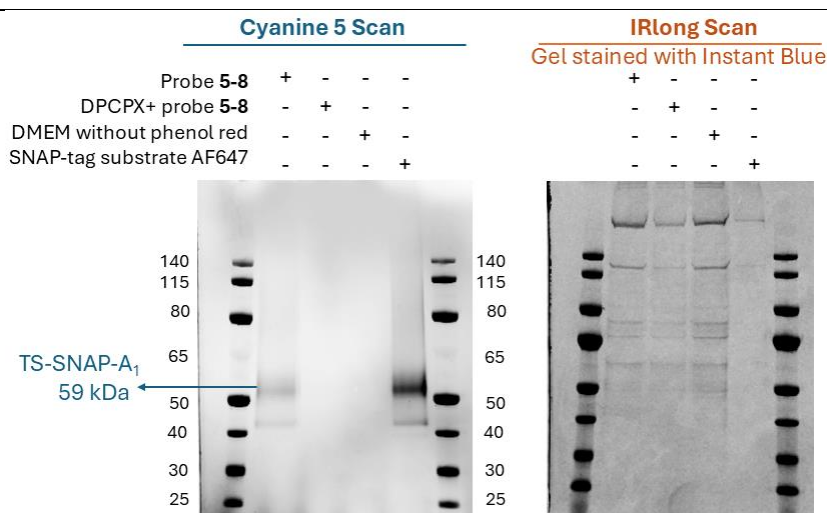
Figure 5-12. Covalent Labelling of hA$_1$ ARs Demonstrated *via* In-Gel Fluorescence Scanning.
HEK293G cells stably expressing human A$_1$ adenosine receptors (hA$_1$ ARs) with N-terminal Twin-Strep and SNAP tags were used as the cellular model. For the negative control, cells were incubated with DMEM without phenol red. As a positive control, cells were treated with 50 nM SNAP-surface AF647, which covalently binds to the SNAP tag on A$_1$ ARs. Experimental conditions included incubation with 4 nM probe **5-8**, either alone or following preincubation with 30 nM DPCPX, a selective A$_1$ AR antagonist. In the Cy5 fluorescence scan (left panel), a distinct fluorescent band was observed in cells treated with probe **5-8**, which was absent in the DPCPX-pretreated group. The band position matched that of the positive control and corresponded to the expected molecular weight of 59 kDa. These findings confirm that probe **5-8** specifically and covalently labelled A$_1$ ARs. The IRlong scan (right panel) shows the same gel stained overnight with InstantBlue®, verifying protein loading across all lanes. Samples of A$_1$ ARs extracted using MagStrep Type 3 XT beads were loaded into the gel as follows: 20 μL for the SNAP-Surface AF647-labelled sample and 40 μL for all other conditions. This difference in loading volume was evident in the IRlong scan, where the SNAP-Surface AF647 lane appeared dimmer. PageRuler™ Prestained Protein Ladder (10–180 kDa) was used as the molecular weight marker. Images shown are representative of three independent experiments.

5.3.2.2.3 Improved Labelling Selectivity with A$_{2A}$ AR Antagonist

In Chapter 3, section 3.2.2, the covalent labelling assessment demonstrated that both A$_1$ and A$_{2A}$ ARs could be covalently labelled by probe **3-15** through in-gel fluorescent scans. Two approaches were mentioned to achieve selective AR subtype labelling: optimising the AR subtype selectivity profile of probe **3-15** and preincubating cells with an A$_{2A}$ antagonist to block A$_{2A}$ ARs. In this study, selective labelling of A$_1$ AR while leaving A$_{2A}$ AR untagged was investigated using probe **5-8**, following the approaches mentioned in Chapter 3. Probe **5-8** optimised A$_1$/A$_{2A}$ selectivity (40-fold compared to probe **3-15**'s 18-fold). The adequate concentration of the A$_{2A}$ antagonist, ZM241385, remained to be defined. As the K_i of ZM241385 toward hA$_1$ AR was 255 nM[191], a high concentration (10 μM, 39-fold K_i) would block both A$_1$ and A$_{2A}$ ARs simultaneously. To determine the proper concentration of ZM241385 that would block A$_{2A}$ AR but allow A$_1$ AR labelling, a BRET-based competition assay was conducted. Competition binding assay procedures are described in **Chapter 2**, **Section 2.1.2.2**. HEK293T cells

transiently expressing NLuc-hA$_1$ or NLuc-hA$_{2A}$ ARs, seeded in separate halves of the plate, were examined. 40 nM of probe **5-8** acted as the fluorescent ligand, and varied concentrations of ZM241385 served as the non-fluorescent ligand. Cells were incubated with the fluorescent ligand and the competing non-fluorescent ligand for an hour. At the end of the incubation, furimazine was added to each well, followed by a 5-minute equilibrium. The plate was read using a plate reader (BMG, PHERAstar FS). The competition curves are shown in **Figure 5-13**.
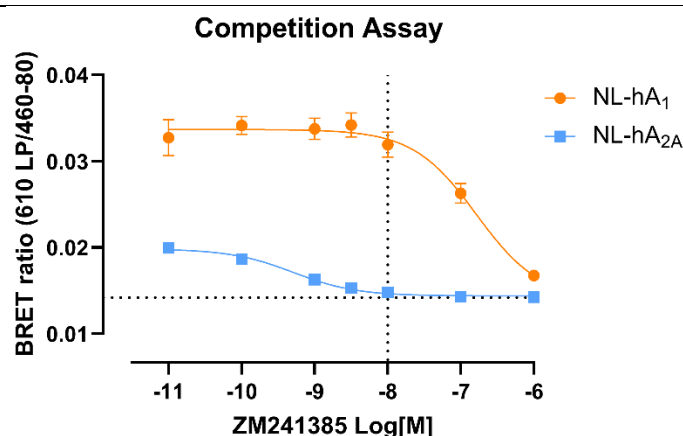
Figure 5-13. Determination of ZM241385 Concentration for Selective A$_{2A}$ AR Blockade While Preserving A$_1$ AR Accessibility to Probe 5-8 *via* Competition Assay.
HEK293T cells transiently expressing NLuc-hA$_1$ or NLuc-hA$_{2A}$ were used to assess the optimal concentration of ZM241385 for selective A$_{2A}$ AR blockade while minimising interference with A$_1$ ARs. Probe **5-8** (40 nM) was employed as the fluorescent ligand, while varying concentrations of ZM241385 served as the non-fluorescent competing ligand. Following a 1-hour incubation with both ligands, furimazine was added to each well, and BRET signals were measured after a 5-minute equilibration using a PHERAstar FS plate reader (BMG Labtech). Probe **5-8** exhibited differing affinities for A$_1$ and A$_{2A}$ ARs, with dissociation constants (K_d) of approximately 4 nM and 160 nM, respectively (**Table 5-2**). At 40 nM, the probe concentration corresponded to roughly 10× K_d for A$_1$ ARs and 0.25× K_d for A$_{2A}$ ARs, resulting in differential receptor occupancy and a lower BRET signal in NLuc-hA$_{2A}$ compared to NLuc-hA$_1$. As shown in the graph, 10 nM ZM241385 effectively inhibited the probe 5-8 BRET signal in A$_{2A}$ ARs (blue curve), while minimally affecting the signal in A$_1$ ARs (orange curve). These results indicate that 10 nM ZM241385 is an appropriate concentration to selectively block A$_{2A}$ ARs while maintaining A$_1$ AR labelling with 40 nM probe **5-8**. Data are presented as mean ± SEM from five independent experiments performed in triplicate.

In **Figure 5-13**, the BRET ratio was lower in A$_{2A}$ ARs compared to A$_1$ ARs. This difference is attributed to the distinct binding affinities of probe **5-8** for the two receptor subtypes. As shown in **Table 5-2**, the dissociation constants (K_d) for A$_1$ and A$_{2A}$ ARs are approximately 4 nM and 160 nM, respectively. When 40 nM of probe **5-8** was applied as the fluorescent ligand in the competition assay, this concentration represented approximately 10-fold the K_d for A$_1$ ARs and only 0.25-fold the K_d for A$_{2A}$ ARs. Consequently, the differential receptor occupancy led to a higher BRET signal in NLuc-hA1-expressing cells and a lower signal in NLuc-hA$_{2A}$-expressing cells.

In this context, 10 nM ZM241385 was identified as the optimal concentration to effectively block probe **5-8** binding to A_{2A} ARs while exerting minimal interference with A_1 AR binding. To ensure complete blockade of A_{2A} ARs in a high-expression system (HEK T-Rex cells with tetracycline induced A_{2A} AR expression; see **Chapter 3**, **Section 3.2.2.2**), 10 nM ZM241385 was used in combination with a reduced probe **5-8** concentration of 4 nM.

To validate the selective labelling of A_1 ARs, an in-gel fluorescence scan was performed. HEK293G cells stably expressing TS-SNAP-hA_1 ARs were used as the A_1 AR model, while HEK TRex cells stably expressing TS-SNAP-hA_{2A} ARs (induced with tetracycline 24 hours prior to labelling) served as the A_{2A} AR model. Both receptor constructs were *N*-terminally tagged with twin-strep and SNAP tags. The twin-strep tag enabled protein extraction using MagStrep Type 3 XT magnetic beads (Strep-Tactin® coated)[142], while the SNAP tag allowed covalent labelling with SNAP-surface AF647[74], which served as a positive control. Detailed experimental procedures are described **in Chapter 2**, **Sections 2.1.4.1** and **2.1.4.2**.

During receptor labelling, cells expressing TS-SNAP-hA_1 or TS-SNAP-hA_{2A} ARs were subjected to four conditions. Cells grown in T175 flasks (80–95% confluence) were incubated for one hour with either 50 nM SNAP-Surface AF647 (positive control) or phenol red-free DMEM (negative control). Experimental groups were incubated with 4 nM probe **5-8**, with or without 10 nM ZM241385 pretreatment. After labelling, cells were washed twice with warm PBS, detached using enzyme-free dissociation buffer, and collected by centrifugation. Cell pellets were either processed immediately or stored at –80 °C.

Subsequent steps—including receptor solubilisation, extraction using MagStrep Type 3 XT beads, elution with biotin, SDS-PAGE separation, and in-gel fluorescence scanning—were performed as described in **Chapter 2**, **Sections 2.1.4.3** to **2.1.4.5**. The resulting gel images are shown in **Figure 5-14**.
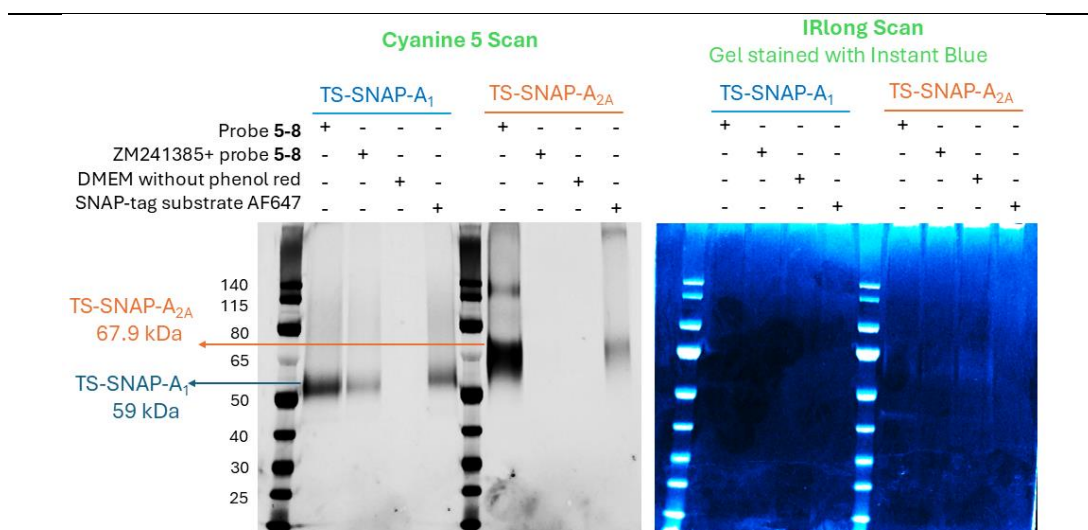
Figure 5-14. A$_1$ AR Selective Labelling with ZM241385 Preincubation Validated *via* In-Gel Fluorescent Scan.
The left panel displays the Cy5 fluorescence scan, while the right panel shows the corresponding InstantBlue®-stained gel imaged under IRlong settings (visualised using Cyan Hot adjustment to enhance band visibility). In the Cy5 scan, fluorescent bands were observed for A$_1$ ARs labelled with probe **5-8**, both in the presence and absence of ZM241385. These bands aligned with the positive control and corresponded to the expected molecular weight of TS-SNAP-hA$_1$ AR (59 kDa). In contrast, for A$_{2A}$ ARs, a fluorescent band was detected only in the positive control and in the probe **5-8**-labelled sample without ZM241385 preincubation, indicating effective blockade of A$_{2A}$ AR labelling by the antagonist. These results confirm that selective labelling of A$_1$ ARs was achieved using the optimised probe **5-8** in combination with ZM241385 preincubation. The IRlong image verifies proper sample loading across lanes. Notably, the loading amounts for the positive controls differed: half a portion was loaded for A$_1$ AR and one-fiftieth for A$_{2A}$ AR, while all other samples were loaded at full volume (40 µL). PageRuler™ Prestained Protein Ladder (10–180 kDa) was used as the molecular weight marker. The images shown are representative of three independent experiments.

In the Cy5 fluorescence scan, bands corresponding to A$_1$ ARs labelled with probe **5-8** were observed in both the presence and absence of ZM241385, although the band intensity was slightly reduced with ZM241385. This reduction is likely due to the lower probe concentration (4 nM) compared to the initial competition assay (40 nM, **Figure 5-13**). Both bands aligned with the positive control (SNAP-surface AF647-labelled A$_1$ AR) and matched the expected molecular weight of TS-SNAP-hA$_1$ AR (59 kDa). In contrast, for A$_{2A}$ ARs, a fluorescent band was only detected in the absence of ZM241385, confirming that 10 nM ZM241385 effectively blocked probe **5-8** binding to A$_{2A}$ ARs. These results validate the applicability of the methods described in Chapter 3 and demonstrate successful selective labelling of A$_1$ ARs in an antibiotic-inducible A$_{2A}$ AR overexpression system.

5.3.2.2.4 Validation of A_1 AR Covalent Labelling *via* Mass Spectroscopy

In **Chapter 3**, **Section 3.2.2.4**, point-mutated A_1 ARs were utilised to investigate the amino acid residue labelled by probe **3-22**. However, probe **3-22** presented more than one possible labelling position on A_1 ARs, as the specific binding signal was not completely absent with the addition of DPCPX in five mutated A_1 ARs. An alternative method to elucidate the precise labelling position was through liquid chromatography-mass spectroscopy (LC-MS), as mentioned in Chapter 3 as well. LC-MS and LC-tandem-MS have been employed in proteomics to detect and assign protein posttranslational modifications (PTMs) such as phosphorylation, glycosylation, and methylation[192–194]. LC-MS samples could be pure protein samples or peptides from enzyme-digested protein fragments, depending on the research aim[193]. Digesting the target protein with different enzymes (e.g., trypsin[195], LysC[196], and GluC[196]) and mapping the MS-acquired data had been applied to determine the precise PTM site[193,197,198]. Therefore, the precise modified site of A_1 AR by probe **5-8** might be elucidated through digesting A_1 ARs into multiple peptides with different enzymes, fractionating *via* the LC system, detecting by mass, and fragments mapping analysis.

5.3.2.2.4.1 Elevating A_1 AR quantity

Sample quality (purity and sufficient quantity) is an essential aspect of LC-MS proteomic analysis[199]. Pure protein samples minimise background noise, and the sufficient amount of protein enables effective MS detection. TS-SNAP-A_1 ARs stably expressed by HEK293G cells served as the labelling model, as the TS tag allowed protein purification through MagStrep "type3" XT beads. However, Dr. Clare Harwood (previous postdoc) found that the quantity of A_1 ARs extracted from the original HEK293G TS-SNAP-hA_1 AR cell line was too low to be stained by SYPRO Orange dye (sensitive protein gel dye, 4-10 ng protein/band[200]). The protein quantity issue was addressed through two approaches. The first was elevating A_1 AR expression, and the second was extending the protein elution period to minimise protein trapped on extraction beads.

The method to improve target protein expression involved selecting cells with higher A_1 AR expression from the original cell line through fluorescence-activated cell sorting (FACS)[201]. FACS applies flow cytometry to sort cells based on fluorescence[201]. In this study, TS-SNAP A_1 ARs were labelled with a SNAP tag substrate, and cells were separated by FACS, allowing the removal of cells with low or no TS-SNAP-A_1 AR expression. Sample preparation details for FACS are described in **Chapter 2**, **Section 2.1.11**. Original HEK293G TS-SNAP-A_1 AR cells in T75 were labelled with or without (control) 50 nM of SNAP-surface 647 for 30 minutes. Cells were then washed with warm PBS to remove excess dye and detached using enzyme-free cell detachment solution. After centrifugation, cells were resuspended at a concentration of $10*10^6$/mL and sorted through FACS.

The sorting step was performed by Nicola Croxall (School of Life Sciences, technician). Cells were separated into two groups: those labelled with AF647 and those with the top 25% of AF647 signal intensity. Cell sorting signal graphs are displayed in **Figure 5-15**. The separated cell subpopulations were immediately seeded into T25 flasks. To examine whether A_1 AR expression was improved *via* FACS, a confocal imaging study was employed. The original cell line (HEK293G TS-SNAP-hA$_1$AR) and two subpopulations (AF647 positive and top 25% AF647 intensity) were seeded in an 8-well plate. After 30 minutes of labelling with 250 nM SNAP-surface AF488, cells were fixed with 4% paraformaldehyde at room temperature for 20 minutes, followed by nuclear staining with Hoechst 33258 at room temperature for 20 minutes. The plate was stored in a 4°C fridge and prepared for confocal imaging the next day. The images are presented in **Figure 5-16**. The selected top 25% subpopulation exhibited the brightest AF488 labelling signal, while the other sets presented dimmer signals. The images indicated that A_1 AR expression improvement through FACS selection of high A_1 AR expression subpopulations was successful.

Negative control
Without labelling

Picking cells
With AF647 signal

Picking cells
With Top 25% AF647 signal
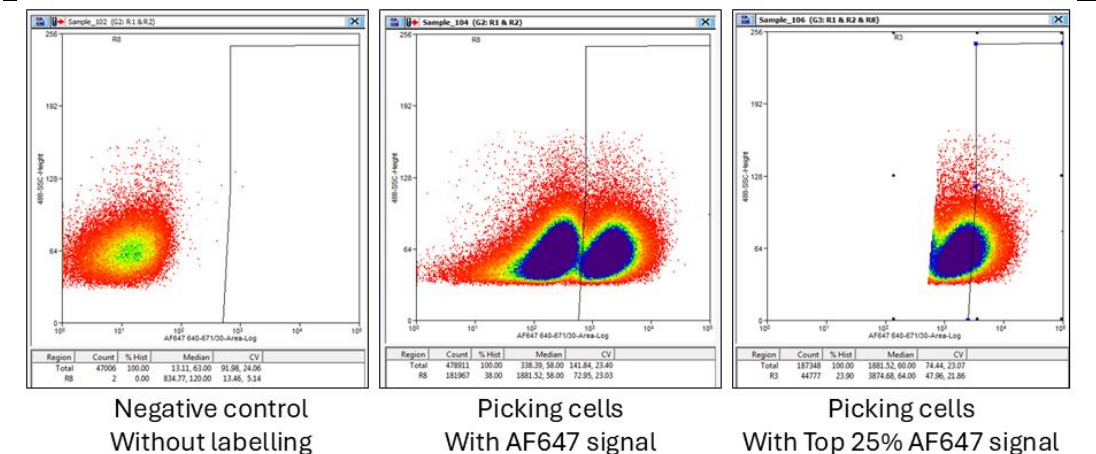
Figure 5-15. FACS Graphs.
HEK293G cells stably expressing TS-SNAP-hA$_1$ARs were incubated with or without SNAP-surface AF647 and subjected to FACS analysis. The left panel shows the negative control, representing cells without fluorescent labelling. The middle panel displays the sorting result, where the right oval within the black rectangle indicates cells exhibiting signal from the AF647. The right panel illustrates the selection of cells with the top 25% AF647 intensity, highlighted within the black rectangle. The graphs were obtained from a single FACS experiment conducted by Nicola Croxall.
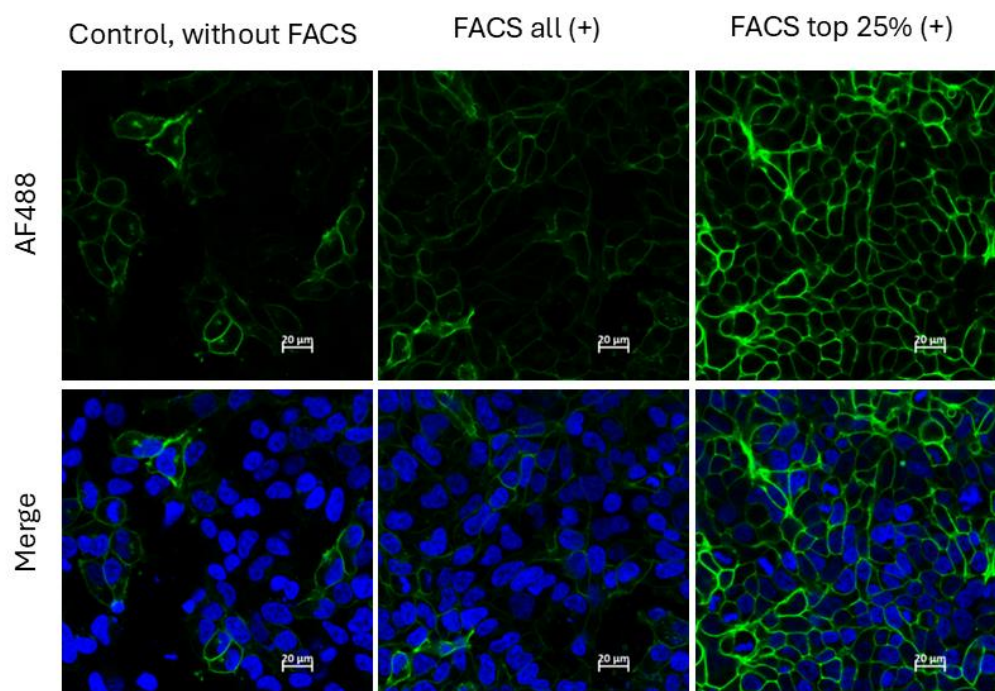
Figure 5-16. Investigating TS-SNAP-A$_1$ AR Expression through Confocal Microscopy.
The left frames depict original HEK293G TS-SNAP-hA$_1$AR cells. The middle frames show images of the FACS-separated subpopulation—cells labelled with AF647. The right frames exhibit images of cells with the top 25% AF647 labelling signal. The top frames display cells under the AF488 channel, while the bottom frames show the merged channel of AF488 (membrane A$_1$ AR) and Hoechst 33258[202] (nuclei stain). It was apparent that the top 25% FACS selection resulted in the brightest A$_1$ AR labelling, indicating successful sorting of high A$_1$ AR expression cells through FACS. The scale bar represents 20 µm. Brightness and contrast were enhanced by 20% for all images. The images were obtained from a single experiment conducted in triplicate for FACS-sorted cells and duplicate for the control.

The second approach to elevate A$_1$ AR quantity involved minimising A$_1$ AR trapped on extraction beads. To verify whether a considerable amount of A$_1$ AR remained on the beads after a 4-hour biotin elution, an in-gel fluorescent scan was arranged with FACS-sorted top 25% cells labelled with 50 nM of SNAP-surface AF647. The experimental procedures were essentially the same as those for assessing probe **5-8** covalent labelling *via* in-gel fluorescent scanning, with details described in **Chapter 2**, **Section 2.1.4**. The difference lay in the elution step. The first elution was carried out as usual for 4 hours. A second elution was conducted for 16 hours with the beads used in the first elution. Both eluates were run through SDS-PAGE, and the gel images were obtained using a gel scanner (**Figure 5-17**). A dim fluorescent band was observed in the second eluate lane compared to the first eluate under the Cy5 channel. In the IRlong channel, no protein band was detected in the second eluate lane, indicating that only a trace amount of A$_1$ AR remained trapped on the beads after the first elution. Hence, extending the elution period may be beneficial for increasing eluted A$_1$ AR, but not excessively.
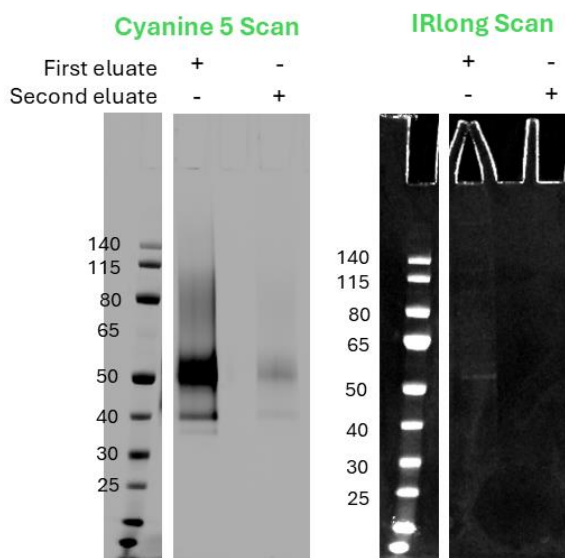
Figure 5-17. Evaluation of A$_1$ AR Remaining on Beads After First Elution.
FACS-separated top 25% HEK293G TS-SNAP-hA$_1$ AR cells were labelled with 50 nM of SNAP-surface AF647. The labelled A$_1$ ARs were then solubilised and extracted using MagStrep "type3" XT beads. The beads were sequentially eluted for 4 hours and 16 hours. Both eluates were subjected to SDS-PAGE and in-gel scanning. The left image shows the gel scan under the Cy5 channel, where a faint fluorescent band was observed in the second eluate compared to the first eluate. The right image displays the InstantBlue® overnight-stained gel scanned under the IRlong channel, where no band was observed in the second eluate. The experiment suggested that some A$_1$ AR remained trapped on the beads after first elution, but not a significant amount. PageRuler™ Prestained Protein Ladder (10–180 kDa) was used as the molecular weight marker. The images shown are from a single pilot experiment.

5.3.2.2.4.2 Improved Sample Purity

A pure protein sample was essential for LC-MS analysis, as impurities would complicate data interpretation and potentially mask signals from the target protein[199]. Except for the band corresponding to A$_1$ AR, other bands were observed after overnight InstantBlue® staining from previous IRlong in-gel scan images. These additional bands were assumed to be endogenous biotin-tagged proteins from the membrane and/or cytosol, as the MagStrep "type3" XT beads could not differentiate between twin-strep tags and biotin tags. Rather than proceeding with solubilisation of membrane proteins using whole cells, membrane preparation was considered before solubilisation to minimise the extraction of biotin-tagged proteins from soluble proteins, nuclear material, and the inner membrane[203]. Membrane preparation procedures are described in **Chapter 2**, **Section 2.1.12**. After membrane preparation, subsequent SDS-PAGE sample preparation and gel scans were conducted as previously described in the in-gel fluorescent scan. The images are presented in **Figure 5-18**. Fewer additional bands were observed under the IRlong channel, indicating that membrane collection prior to receptor solubilisation was effective. However, some dim fluorescent bands were observed under the Cy5 channel in samples processed with membrane preparation. These bands could represent fragments

of A_1 AR after mechanical cell membrane disruption or non-specific labelling due to the higher concentration used (100 nM of probe **5-8**, 25 times the A_1 K_d).

Figure 5-18. Evaluation of Impurity Content Following an Additional Membrane Preparation Step.
(A) An in-gel fluorescence scan was performed without a membrane preparation step, as previously shown in Figure 5-12 and used here for comparison. The original HEK293G TS-SNAP-hA$_1$ AR cell line was used, and labelling was conducted with 4 nM probe **5-8**. In the IRlong scan image, multiple bands were observed, indicating the presence of impurities. (B) An in-gel fluorescence scan was performed with the inclusion of a membrane preparation step during SDS-PAGE sample processing. FACS-selected top 25% expressing cells were used, and labelling was conducted with 100 nM probe **5-8**. In the IRlong scan image, fewer bands were observed, suggesting improved sample purity. However, additional faint fluorescent bands appeared around 40, 30, and 25 kDa. It remains inconclusive whether these bands represent A_1 AR fragments or result from non-specific labelling. The images shown in (B) are from a single pilot experiment.

5.3.2.2.4.3 LC-MS analysis

Samples for LC-MS analysis were prepared from HEK293G cells stably expressing TS-SNAP-A_1 ARs, selected *via* FACS. Cells were cultured in T175 flasks to 80–95% confluence and subsequently incubated with 100 nM of probes **5–8** or maintained in HBSS for one hour. Following incubation, cells were washed with PBS, detached using enzyme-free dissociation buffer, and centrifuged to obtain cell pellets. Membrane preparations were performed as described in Chapter 2, Section 2.1.4. The isolated membranes were solubilised and subjected to affinity purification using MagStrep-type X beads, followed by elution with biotin buffer lacking enzyme inhibitors. The resulting A_1 AR eluates were frozen at –80 °C and shipped to Leiden University for LC-MS/MS analysis. At the time of writing, the analysis is pending; the corresponding data will be incorporated into this section upon completion.

5.3.2.3 Confocal Imaging Study

Probe **5-8** exhibited a superior AR selectivity profile compared to probe **5-3**. The A_1 AR covalent labelling through probe **5-8** was validated using in-gel fluorescent scans. The subsequent investigation involved the application of confocal microscopy to determine whether probe **5-8** exhibited good signal-to-noise contrast. To evaluate the labelling specificity of probe **5-8** for A_1 ARs, a reference labelling approach was employed. HEK293T cells transiently expressing SNAP-hA_1 ARs were used, as they not only provided a model for probe **5-8** labelling but also enabled covalent labelling with SNAP-surface AF488 *via* the SNAP tag, serving as a reference signal. Experimental procedures are detailed in **Chapter 2**, **Section 2.1.5.1**.

Cells were seeded in an 8-well plate and, on the day of the experiment, the medium was aspirated. Cells were first incubated with 250 nM SNAP-surface AF488 for 30 minutes to label A_1 ARs as a positive control. Subsequently, a second labelling step was performed using 40 nM probe **5-8** (equivalent to 10× the K_d for A_1 ARs), in the presence or absence (vehicle control) of 10 μM DPCPX for two hours. After each labelling step, cells were washed twice with warm phenol red-free DMEM. At the end of the labelling procedure, cells were washed with PBS, fixed with 4% paraformaldehyde, washed again with PBS, and finally soaked in 300 μL PBS per well in preparation for confocal imaging.

The resulting images and signal quantification are presented in **Figure 5-19**A. In the vehicle-treated group, membrane-localised labelling was observed in both the AF488 and Cy5 channels, with strong colocalisation in the merged image. In contrast, in the DPCPX-pretreated group, fluorescence was only detected in the AF488 channel, indicating that probe **5-8** labelling was specific to A_1 AR and effectively blocked by DPCPX.

Quantitative analysis (**Figure 5-19**B) showed no significant difference in AF488 signal intensity between the vehicle and DPCPX-treated groups, suggesting comparable A_1 AR expression levels (Mann–Whitney U test, U = 3099, P = 0.7323). In contrast, a significant reduction in Cy5 signal intensity was observed in the DPCPX group (Mann–Whitney U test, U = 0, P < 0.0001), confirming that probe **5-8** labelling was specifically inhibited by the A_1 AR antagonist. These findings are consistent with previous results and support the specificity of probe **5-8** for A_1 AR labelling.
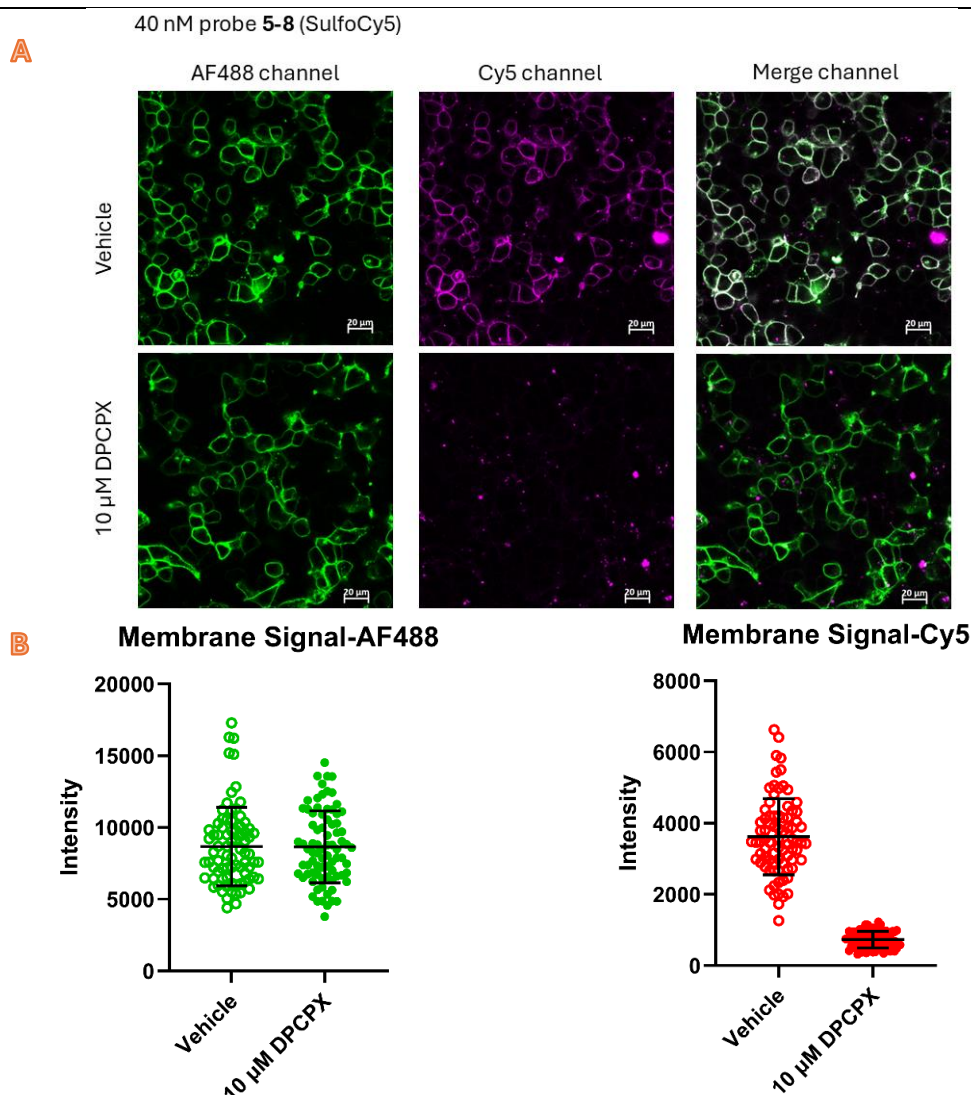
Figure 5-19. Confocal images and signal quantification results of A_1 AR labelling by probe **5-8**.

(A) The left frames show the images observed under the AF488 channel, the middle frames exhibit the images observed under the Cy5 channel, and the right frames display the merged AF488 and Cy5 images. The top frames present the set without DPCPX preincubation (vehicle), while the bottom frames show the results from the DPCPX pretreatment set. Cell membranes were clearly visualised under the AF488 channel in both sets, while labelling was clearly seen under the Cy5 channel only in the vehicle set. Additionally, the well colocalisation observed in the vehicle set. These indicated probe **5-8** specific labelling of A_1 ARs. Scale bar = 20 μm. Contrast and brightness were enhanced by 20% for all images. Images are representative of five independent experiments conducted in duplicate. (B) Signal quantification was performed by manually drawing the cell membrane (region of interest, ROI) using Fiji (ImageJ) and measuring the ROI intensity in the same software. No significant difference in AF488 intensity was observed between the two sets (Mann-Whitney U test, U = 3099, P = 0.7323). However, a significant difference in Cy5 intensity was noted between the sets with and without DPCPX pretreatment (Mann-Whitney U test, U = 0, P < 0.0001). Data are presented as measurements from 80 cells in five independent experiments for each condition, and the error bars show the mean ± SD.

The A_1 AR-specific labelling *via* probe **5-8** was validated with confocal microscopy (**Figure 5-19**A). Probe **5-8** was subsequently applied for an agonist-induced internalisation study. The aim was to investigate whether the orthosteric binding pocket of A_1 AR remained accessible post **5-8** tagging. The experimental details are described in **Chapter 2**, **Section 2.1.5.2**. HEK293T cells transiently expressing SNAP-hA$_1$ARs were seeded in an 8-well plate. On the day of the experiment, the cells were sequentially labelled with 250 nM of SNAP surface AF488 for 30 minutes and 40 nM of probe **5-8** for two hours. The cells were washed with warmed DMEM (without phenol red) twice after each labelling step. The cells were then incubated for 2 hours in the presence or absence (vehicle) of 10 µM 2-Chloro-N^6-cyclopentyladenosine (CCPA). At the end of the incubation, the cells were washed with PBS twice, fixed with 4% paraformaldehyde, washed twice with PBS, refilled with 300 µL of PBS, and prepared for confocal imaging. The images and signal quantification results are displayed in **Figure 5-20**. In the agonist treatment set, both the AF488 and Cy5 channels showed clustered signals inside the cells, and the signals were colocalised in the merged channel. In contrast, only a few clustered signals inside the cells were observed in the vehicle set. The image results were consistent with the internalisation studies in Chapters 3 and 4 and the literature findings[118,148] that A_1 ARs aggregated and internalised after agonist treatment. The quantification results showed a significant signal difference between the sets incubated with or without the agonist under the AF488 and Cy5 channels. The agonist-induced internalisation study visualised through confocal imaging suggested that the orthosteric binding pocket remained accessible after **5-8** labelling, and the receptor function (internalisation) and trafficking were minimally impacted.

A   40 nM probe **5-8** (SulfoCy5)
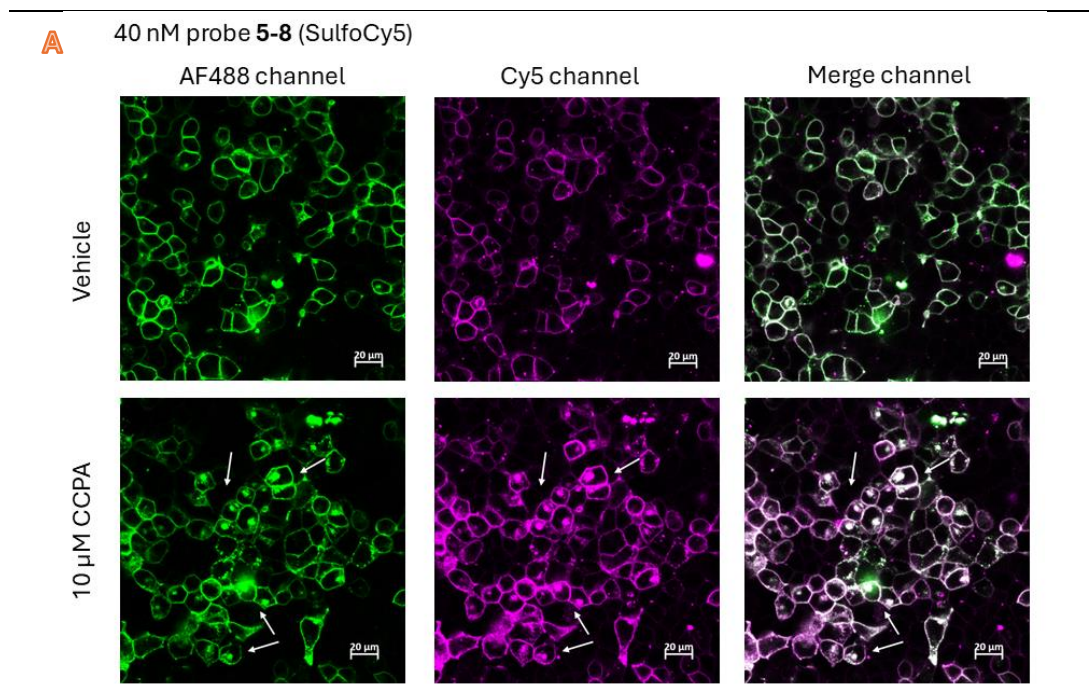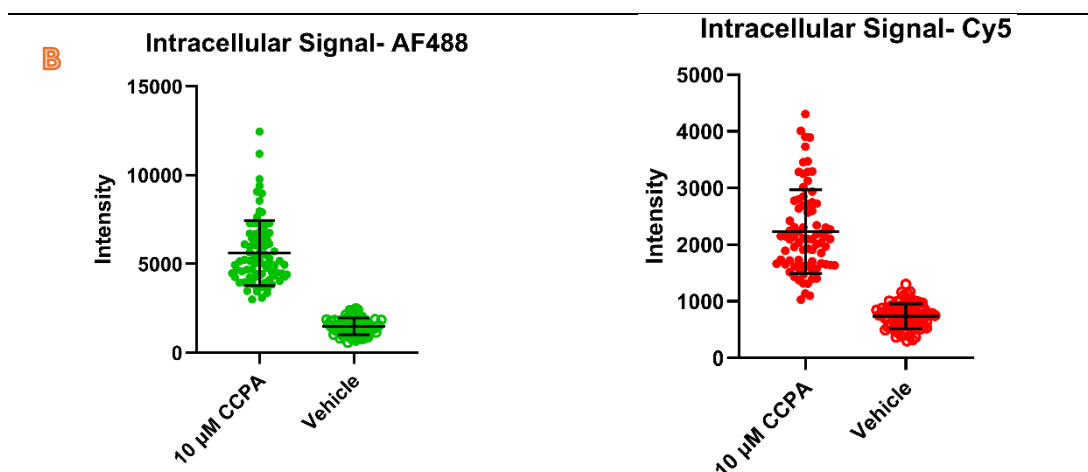
Figure 5-20. Orthosteric Binding Pocket Accessibility Investigation.
(**A**) HEK293T cells transiently expressing SNAP-hA$_1$ ARs were labelled with SNAP surface AF488 and probe **5-8** sequentially. The cells were incubated with or without (vehicle) the A$_1$ selective agonist CCPA for 2 hours. The left images show cells observed in the AF488 channel (green), the middle frames show cells observed in the Cy5 channel (magenta), and the right frames display the merged images of both channels. The vehicle set is presented in the top frames, while the agonist-treated set is presented in the bottom frames. Clustered A$_1$ ARs were observed in the bottom frames and were well colocalised. This suggested that the orthosteric binding pocket of A$_1$ ARs remained accessible to CCPA after probe **5-8** labelling, and the internalisation was minimally impacted. Scale bar = 20 μm. The brightness and contrast were enhanced by 20% for all images. The images are representative of five independent experiments conducted in duplicate. (**B**) Signal quantification was performed by manually drawing the intracellular region (region of interest, ROI) using Fiji (ImageJ) and measuring the ROI intensity in the same software. Significant differences between the two sets were noticed in both channels (AF488: Mann-Whitney U test, $U = 0$, $P < 0.0001$; Cy5: Mann-Whitney U test, $U = 14$, $P < 0.0001$). Data are presented as measurements from 80 cells in five independent experiments for each condition, and the error bars show the mean ± SD.

5.3.3 Summary and Conclusions

In this chapter, the A$_1$ AR-targeted LD probe directly transferring SulfoCy5 cargo was optimised based on structural and pharmacological data analysis. Probe **5-8** elevated the A$_1$/A$_{2A}$ selectivity ratio by 40-fold by modifying the linear chain length in the cargo moiety (**Table 5-2**). Although the new probe **5-8** provided a better AR affinity profile, it was less stable than the analogue probe **3-22**, which lacked the additional linear chain in the cargo moiety. This instability may have resulted from the improved accessibility of nucleophiles to the phenyl ester by moving the bulky SulfoCy5 group an additional 10 atoms away. Despite the fast degradation rate, 84% of probe **5-8** remained intact after one hour of incubation in HBSS at 37°C (**Figure 5-5**), which was sufficient for A$_1$ AR labelling in cell-based pharmacology studies.

Probe **5-8** specifically and covalently labelled A$_1$ ARs, as validated through in-gel fluorescent scans (**Figure 5-12**). Additionally, selective labelling was achieved by the selectivity-optimised probe **5-8** and preincubation with the A$_{2A}$ antagonist (ZM241385), as shown in **Figure 5-14**. The confocal image study demonstrated A$_1$-specific labelling by probe **5-8**, along with good signal-to-noise contrast

(**Figure 5-19**). Furthermore, the subsequent agonist-induced internalisation implied that the orthosteric binding pocket remained accessible after probe **5-8** labelling and that the function of tagged A_1 ARs was preserved (**Figure 5-20**).

These assessments verified probe **5-8** as an acceptable LD probe for A_1 ARs, with specificity, covalent labelling, fast cargo transfer (completed within 1-2 hours; shorter incubation periods were not tested), free A_1 AR orthosteric binding site after tagging, and preserved internalised function of tagged A_1 ARs without discernible impairment. The characteristics and low non-specific binding observed in confocal images made probe **5-8** a promising tool for labelling A_1 ARs without prior genetic engineering, and it could be coupled with other techniques (e.g., FRET, confocal microscopy, and FLIM) for further A_1 AR studies.

Chapter 6. General Conclusion and Outlook

As a member of the GPCR superfamily, the A_1 AR modulates downstream signalling pathways *via* $G_{i\alpha}$, $G_{\beta\gamma}$, and *β*-arrestin[20]. A_1 ARs are broadly expressed throughout the human body, including the central nervous system, cardiovascular system, kidneys, and respiratory system[20,31]. Upon stimulation by adenosine, A_1 ARs participate in a range of physiological processes across various organs and tissues. In cardiac tissue, A_1 AR activation has been shown to exert negative chronotropic, inotropic, and dromotropic effects[22,31,34]. In the spinal cord and peripheral neurons, activation of A_1 ARs contributes to analgesic effects[19,31]. In the kidneys, A_1 AR activation induces constriction of afferent arterioles, thereby reducing the glomerular filtration rate and producing an antidiuretic effect[19,32].

The considerable clinical potential of A_1 AR modulation has garnered substantial scientific interest. To enhance therapeutic efficacy while minimising off-target effects associated with other adenosine receptor subtypes, several potent and selective A_1 AR agonists and antagonists have been developed and evaluated in clinical trials—such as FK352 for its antidiuretic properties[32] and tecadenoson for the treatment of atrial fibrillation[34,204]. However, most of these candidates failed to progress through clinical trials due to on-target adverse effects (e.g., unintended activation or inhibition of A_1 ARs in non-target tissues) and receptor desensitisation following prolonged exposure to full agonists[19,34,47]. Although partial agonists were subsequently introduced to mitigate desensitisation, they also proved ineffective—neladenoson, for instance, failed to demonstrate a dose-dependent improvement in left ventricular ejection fraction compared to placebo[48]. Consequently, attention has shifted towards allosteric modulators and biased agonists of A_1 ARs as promising future therapeutic strategies[11,17,47,49].

Beyond their clinical relevance, recent findings have highlighted a novel role for A_1 ARs in presynaptic neuronal modulation. Lefton *et al.* (2025) reported that norepinephrine (NE) released from locus coeruleus neurons activates α1-adrenergic receptors on astrocytes, leading to elevated intracellular Ca^{2+} levels and subsequent ATP release[205]. Extracellular ATP is rapidly hydrolysed to adenosine *via* the ectonucleotidases CD39 and CD73[205,206]. The resulting adenosine then activates presynaptic A_1 ARs, producing an inhibitory effect on neuronal activity[205]. Complementary evidence was provided by Chen *et al.* (2025), who investigated the futility response in larval zebrafish[206]. Their study demonstrated that NE-induced ATP release from astrocytes is swiftly converted to adenosine, which in turn activates A_{2B} ARs, contributing to neuronal inhibition[206]. These findings underscore the complex and indirect mechanisms

by which astrocytes modulate neuronal activity in response to NE stimulation, and further highlight the multifaceted roles of ARs in neurophysiological regulation.

Over the past two decades, numerous radioligands and fluorescent ligand tools targeting A_1 ARs have been developed to support the growing demand for A_1 AR research[73,207]. Due to safety concerns associated with radioactive materials, as well as the advantages of simplified protocols (e.g., elimination of separation steps) and advanced techniques such as resonance energy transfer and confocal microscopy, research has increasingly shifted towards the use of fluorescent ligands[55]. Both agonist- and antagonist-based fluorescent ligands targeting A_1 ARs are summarised in Chapter 1[73,207]. These tools have proven instrumental in various applications, including the screening of potential drug candidates[55,70], the assessment of kinetic binding parameters[77]—such as the characterisation of probe **3-29** (Chapter 3, Section 2.2.5)—visualisation of receptor localisation (Chapter 3, Figure 3-19), and the monitoring of receptor trafficking following agonist stimulation (Chapter 3, Figure 3-21).

In addition to reversible fluorescent probes, fluorescent protein tags[79] (e.g., GFP) and self-labelling protein tags (e.g., SNAP-tag[81], HaloTag[83]) have emerged as valuable tools. These tags covalently bind to target biomolecules, thereby eliminating concerns regarding dissociation during washing steps. However, both fluorescent protein and self-labelling tags require expression in genetically engineered cells[88]. To address this limitation, ligand-directed (LD) labelling probes—pioneered by Hamachi's group—offer a chemical approach to label biomolecules in live cells without the need for genetic modification[89–92,94]. LD probes enable covalent labelling of target proteins while preserving access to the orthosteric binding site, in contrast to irreversible fluorescent ligands that block this site upon binding. The combination of covalent labelling, orthosteric site accessibility, minimal tag size, and independence from cell engineering renders LD probes highly valuable for the investigation of biomolecular functions in live-cell contexts.

Comeo *et al*. (2024) applied the LD probe strategy to A_1 ARs, demonstrating the covalent labelling capabilities of probe **1-56** (SulfoCy5) and probe **1-57** (TCO)[74]. However, probe **1-56** exhibited cross-reactivity with A_{2A} ARs, displaying an A_1/A_{2A} selectivity ratio of only 5.9-fold, thereby raising concerns about off-target labelling in systems co-expressing both receptor subtypes. In contrast, probe **1-57** showed improved AR subtype selectivity but yielded weaker labelling efficiency compared to probe **1-56**. The primary objective of this thesis was to develop novel LD probes targeting A_1 ARs with enhanced subtype selectivity and improved labelling performance.

In Chapter 3, four analogues of probe **1-56** were synthesised by modifying the linker and phenyl ester positions. These structural adjustments modestly improved A_1/A_{2A} selectivity, increasing it from 8.2-fold to 18.9-fold. Building on the success of these modifications, the same design principles were applied to probe **1-57** (TCO), resulting in the development of a novel probe, **4-5** (TCO), as described in Chapter 4. Probe **4-5** demonstrated superior A_1/A_{2B} selectivity while maintaining favourable selectivity profiles against A_{2A} and A_3 ARs. Labelling efficiency was further enhanced by optimising experimental conditions, including serum removal prior to labelling, incubation in HBSS, and the use of Tetrazine-SulfoCy5 as the secondary labelling reagent.

Additionally, probe **4-5** was employed to investigate orthosteric binding site accessibility. In this experiment, NLuc-tagged A_1 ARs were labelled with TCO handle *via* probe **4-5** first, followed by an IEDDA reaction with tetrazine-AF488. BRET signals were then monitored in the presence of the reversible ligand **3-29** (BODIPY-630/650). A significant BRET signal in the red channel indicated that **3-29** was able to bind to AF488-labelled NLuc-A_1 ARs. Pre-incubation with 1 μM DPCPX prior to the addition of **3-29** abolished this signal, suggesting that DPCPX competitively bound to the AF488-labelled receptor, thereby preventing **3-29** access.

In the green channel, the presence of **3-29** reduced the BRET signal relative to vehicle-treated controls (HBSS), while pre-incubation with DPCPX had no effect. The observed decrease in green BRET signal, alongside the increase in red BRET signal, supports the occurrence of FRET between AF488 and BODIPY-630/650, indicating that both fluorophores were simultaneously bound to the A_1 AR. These findings confirm that AF488-labelled A_1 ARs retain orthosteric binding site accessibility and that probe **3-29** can bind concurrently, thereby validating the utility of probe **4-5** for functional receptor studies.

The FRET interaction between AF488 and BODIPY-630/650 (probe **3-29**) on NLuc-tagged A_1 ARs was further validated using fluorescence lifetime imaging microscopy (FLIM-FRET) analysis (Chapter 4, Figure 4-32). A reduction in the AF488 fluorescence lifetime was observed upon the introduction of probe **3-29**, compared to vehicle-treated controls. Notably, the fluorescence lifetime remained unchanged in the presence of 10 μM DPCPX, either alone or following pre-incubation prior to the addition of probe **3-29**. These results support the occurrence of FRET and confirm the accessibility of the orthosteric binding site on AF488-labelled NLuc-A_1 ARs.

To assess whether the covalent AF488 tag affected ligand binding, binding affinity studies were conducted using probe **3-29**, a reversible fluorescent ligand. Comparative analyses between unlabelled NLuc-A_1 ARs and those labelled with

AF488 *via* the two-phase labelling system (probe **4-5** followed by tetrazine-AF488) revealed no significant differences in the K_d values. These findings indicate that the covalent tagging strategy does not substantially interfere with ligand access to the orthosteric site. Collectively, these results highlight the utility of ligand-directed probes as a viable alternative for covalent protein labelling, offering minimal disruption to receptor function.

In Chapter 5, the optimised A_1 AR LD probe **5-8**, incorporating a SulfoCy5 fluorophore, was synthesised based on structure–affinity relationship insights derived from earlier probes. Probe **5-8** exhibited enhanced A_1/A_{2A} selectivity, achieving a 40-fold preference, while maintaining favourable selectivity against A_{2B} and A_3 AR subtypes. To minimise off-target labelling in systems with high A_{2A} AR expression, pre-incubation with the selective A_{2A} antagonist ZM241385 was employed. This approach effectively blocked A_{2A} AR labelling while preserving specific labelling of A_1 ARs.

This thesis presents two optimised LD probes targeting A_1 ARs: probe **5-8** (SulfoCy5) and probe **4-5** (TCO). Probe **5-8** enables high-resolution visualisation of A_1 ARs using fluorescence microscopy, facilitating real-time tracking of receptor dynamics under stimulation and localisation studies across different tissues and cell types[79]. The covalent SulfoCy5 tag also supports FRET-based competition assays for evaluating ligand binding affinities in non-engineered cell models[208]. Furthermore, the stable fluorescent labelling enables the investigation of protein–protein interactions involving A_1 ARs. For instance, in HEK293T cells co-transfected with A_1 AR and SNAP-tagged A_{2A} ARs, A_{2A} ARs can be labelled with a SNAP-substrate conjugated to AF488, while A_1 ARs are labelled with probe **5-8**. If the two receptors form heterodimers and the fluorophores are in close proximity, FRET can be detected by exciting the AF488 donor and monitoring SulfoCy5 emission. Confocal microscopy can then be used to visualise the spatial distribution of heterodimers and monomers by merging Cy5 and AF488 fluorescence channels.

Probe **4-5** demonstrated even broader applicability due to its TCO handle, which enables versatile labelling through bioorthogonal conjugation with tetrazine-functionalised reporters. This modularity allows for flexible labelling strategies using various tetrazine-conjugated fluorophores, such as Tetrazine-AF488 and Tetrazine-SulfoCy5 (Chapter 4, Figure 4-14 & 4-23). Applications previously demonstrated with probe **5-8**—including real-time visualisation of A_1 ARs, fluorescent and non-fluorescent ligand binding studies, and protein–protein interaction analyses—can be replicated using probe **4-5** in combination with appropriate tetrazine-linked fluorophores. In particular, probe **4-5** offers enhanced flexibility for FRET-based protein–protein interaction studies by

enabling the selection of optimal FRET pairs through interchangeable tetrazine fluorophores.

Beyond fluorescence imaging, the TCO handle also offers potential for positron emission tomography (PET) imaging when paired with ^{18}F-labelled tetrazine derivatives. Adhikari *et al.* (2023) demonstrated this approach in vivo by administering a tetrazine-conjugated monoclonal antibody (CC49-Tz) to LS174T xenograft-bearing mice[209]. 72 hours later, ^{18}F-labelled *cis*-dioxolane-fused TCO (d-TCO) was injected, and PET/CT imaging performed one hour post-injection successfully visualised tumour localisation[209]. This study confirmed the viability of *in vivo* IEDDA chemistry for non-invasive imaging applications. Such a strategy presents a promising avenue for investigating A_1 AR distribution in the mouse brain using probe **4-5** in combination with an ^{18}F-labelled tetrazine partner. However, the potential isomerisation of the TCO moiety must be carefully considered in the design and application of this approach[174].

Additionally, the TCO handle enables biochemical applications such as protein purification. Previous studies have demonstrated the use of tetrazine-functionalised beads to extract proteins labelled with TCO tags[210,211]. This approach could be adapted for A_1 AR purification by reversing the tag configuration—labelling A_1 ARs with probe **4-5** and capturing them using tetrazine-functionalised beads or resins. Alternatively, A_1 ARs could be labelled with biotin *via* tetrazine–biotin conjugates, allowing for affinity purification using Strep-Tactin-coated magnetic beads.

Furthermore, probe **4-5** enables fluorination of A_1 ARs through conjugation with trifluoromethyl-substituted tetrazines, facilitating conformational studies *via* [19]F nuclear magnetic resonance (NMR)[212,213]. This technique could be used to monitor conformational changes in response to ligand binding or protein–protein interactions. However, the inherently low expression levels of GPCRs may pose challenges due to limited signal-to-noise ratios in ^{19}F NMR experiments.

In summary, probes **5-8** and **4-5** represent powerful and complementary tools for advancing A_1 AR research. Probe **5-8** offers optimised subtype selectivity and enables direct visualisation and FRET-based studies in non-engineered systems. In parallel, probe **4-5** provides exceptional versatility through its TCO handle, supporting a wide range of applications—from fluorescence imaging and PET to protein purification and ^{19}F NMR. Together, these probes establish a robust platform for exploring A_1 AR function across molecular, cellular, and in vivo contexts, paving the way for deeper mechanistic insights and future therapeutic innovations.

Suggestions for future work

1. Structural Optimisation of LDCL Probes

Previous studies have shown that GABA-*meta*-phenyl ester-based ligand-directed covalent labelling (LDCL) probes exhibit slightly improved selectivity for the A_1 A) over the A_{2A} subtype, when compared to β-alanine-derived analogues. Docking simulations of the GABA-*meta*-phenol congener with both A_1 and A_{2A} ARs (**Figure 6-1**) suggest potential for structural optimisation through side chain modification.

3-20

GABA-*meta*-Phenol Congener
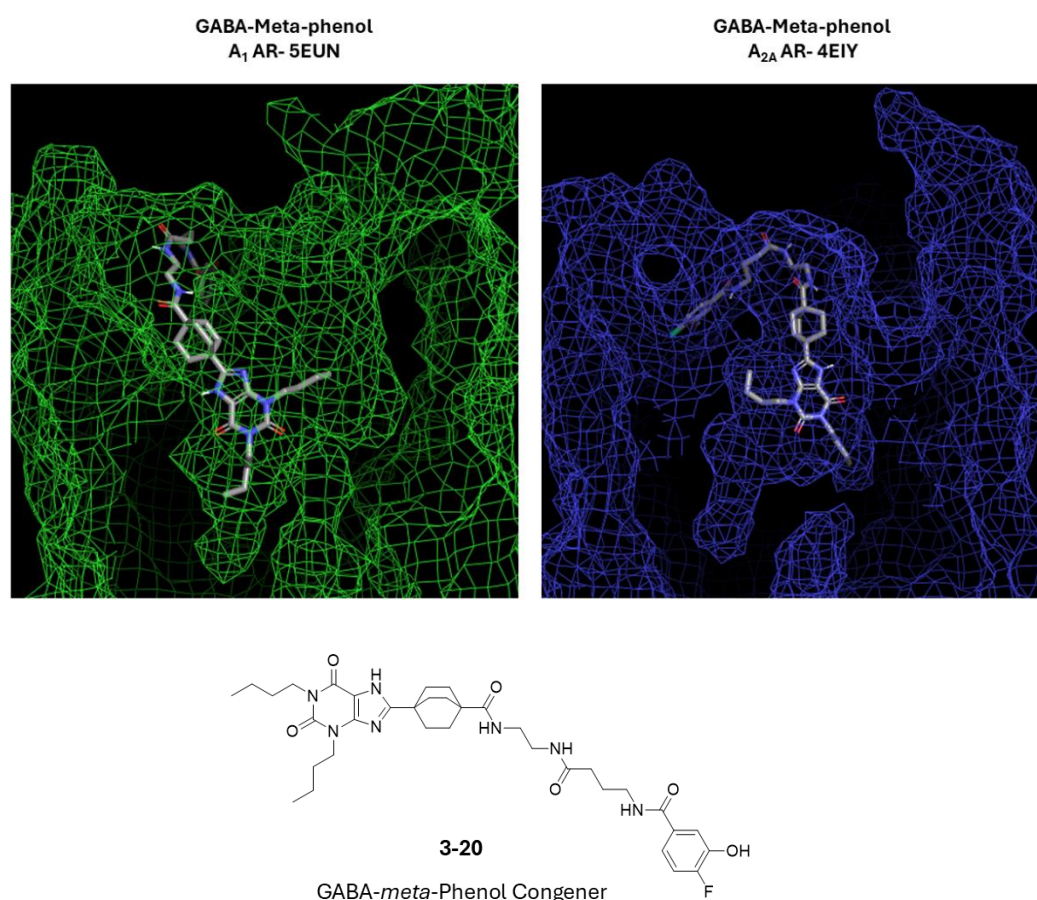
Figure 6-1. Docking poses of the GABA-*meta*-phenol congener in A_1 and A_{2A} ARs. This figure illustrates the docking configurations of the GABA-*meta*-phenol congener within the orthosteric binding sites of the A_1 AR (green) and the A_{2A} AR (blue). In the A_1 AR model, there appears to be sufficient space to accommodate both *n*-butyl side chains, with one extending towards the base of the binding pocket. In contrast, the A_{2A} AR model shows limited spatial accommodation for these side chains, suggesting that further elongation or substitution with bulkier alkyl groups—such as 3-methylbutyl or 4-methylpentyl—may enhance selectivity for A_1 over A_{2A} ARs. Docking simulations were performed using Schrödinger Glide. The A_1 AR structure was derived from PDB ID: 5EUN, and the A_{2A} AR structure from PDB ID: 4EIY. Receptor proteins are displayed in mesh format, while the congener is shown in stick representation.

In the A_1 AR binding model, one of the butyl side chains projects towards the base of the binding pocket, indicating that elongation by one or more methylene units may enhance receptor engagement. The second butyl chain, oriented laterally, could be modified either by elongation or substitution with bulkier alkyl groups such as 3-methylbutyl or 4-methylpentyl chains. In contrast, docking with the A_{2A} AR revealed that these side chains do not occupy deep cavities, which may reduce binding affinity for modified analogues. Additionally, the A_{2A} AR binding pocket entrance appears narrower than that of the A_1 AR (**Figure 6-2**), suggesting that bulkier side chains may favour A_1 AR selectivity.

GABA-Meta-phenol
A_1 AR- 5EUN

GABA-Meta-phenol
A_{2A} AR- 4EIY
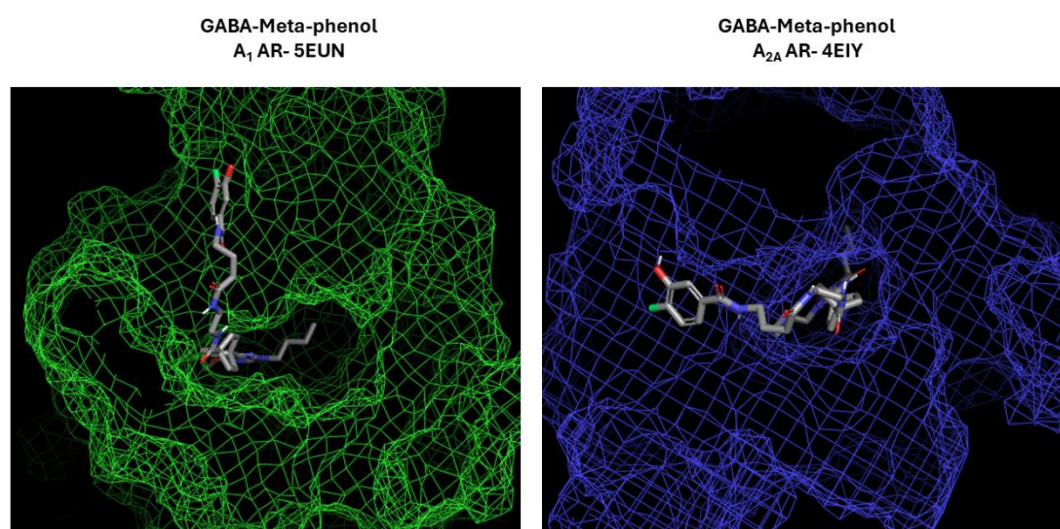
Figure 6-2. Top-down view of Congener 3-20 docked into A_1 and A_{2A} ARs. This figure presents the top-down docking poses of Congener **3-20** within the orthosteric binding sites of the A_1 AR (green) and the A_{2A} AR (blue). From this perspective, it is evident that the A_1 AR possesses a wider entrance to the binding pocket compared to the A_{2A} AR. This structural difference suggests that bulkier side chains may encounter steric hindrance at the A_{2A} AR entrance, potentially enhancing selectivity for A_1 AR. Docking simulations were performed using Schrödinger Glide. The A_1 AR structure was derived from PDB ID: 5EUN, and the A_{2A} AR structure from PDB ID: 4EIY. Receptor proteins are displayed in mesh format, while the congener is shown in stick representation.

Furthermore, docking results indicate that linker composition influences the overall binding pose. Introducing alkyl side chains into the linker region may help position the terminal groups more favourably within the A_1 AR pocket. For instance, replacing glycine with branched amino acids such as valine, leucine, or isoleucine could fine-tune the spatial orientation of the butyl or modified alkyl chains.

Although these congeners differ significantly from the final LDCL probes, docking simulations of modified congeners remain a valuable tool for predicting binding behaviour prior to synthesis.

2. Additional Pharmacological Assays

This thesis does not include data on endogenous A_1 AR labelling due to the temporary closure of the animal facility. Should the facility resume operations, labelling experiments using rat dorsal root ganglion (DRG) cells could be pursued. This model, previously validated by Comeo *et al*.[74], offers a practical starting point for evaluating probe performance in native systems.

In parallel, human cell models may also be considered. Preliminary tests using ACHN (human renal adenocarcinoma) cells yielded inconclusive results, likely due to low endogenous A_1 AR expression or limitations in imaging sensitivity. Alternative models such as glioblastoma cell lines, which reportedly express higher levels of A_1 AR mRNA, may be more suitable, although their availability from reliable sources (e.g., ATCC, ECACC) remains limited. Induced pluripotent stem cell (iPSC)-derived neurons or cardiomyocytes could serve as alternative platforms for endogenous labelling studies.

Upon successful labelling in an A_1-dominant model, more complex systems could be explored to demonstrate probe selectivity. For example, a co-expression model of A_1 and A_{2A} ARs could be used to sequentially label each subtype with distinct fluorophores. As demonstrated in Chapter 5, preincubation with a low concentration of A_{2A} antagonist followed by application of an A_1-selective LDCL probe enabled selective A_1 labelling. After thorough washing, a second LDCL probe targeting A_{2A} ARs could be applied. Confocal imaging would then allow visualisation of subtype-specific labelling and potential receptor heterodimerisation. This approach would further validate the selectivity and versatility of LDCL probes in live-cell systems.

3. Covalent Warhead Modulation for LDCL Probes

Covalent warheads are widely employed in the development of irreversible inhibitors; however, their direct application in ligand-directed labelling is limited. In conventional covalent inhibitors, the warhead often occupies the orthosteric site after forming a covalent bond with a nucleophilic residue, thereby blocking receptor function.

To address this, Reddi *et al*. introduced sulfamate acetamides as electrophilic moieties for covalent ligand-directed release (CoLDR) and labelling strategies (**Figure 6-3**)[214]. These warheads offer tunable reactivity and self-immolative cargo release, making them promising candidates for LDCL probe development. Replacing the 2-fluorophenyl ester moiety in current LDCL probes with a sulfamate acetamide could retain covalent labelling capability while improving aqueous solubility by reducing aromatic content and introducing polar functional groups.
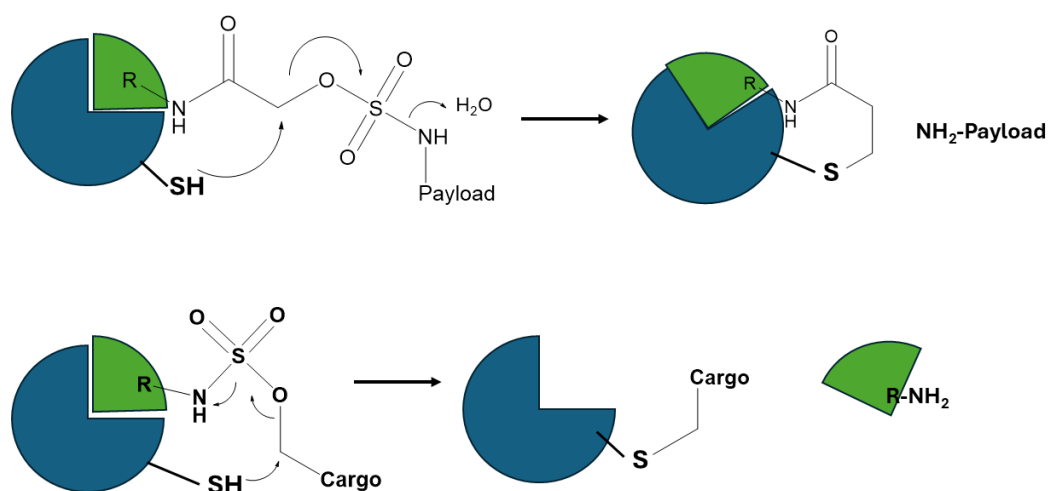
Figure 6-3. Sulfamate acetamide-based covalent ligand-directed release (CoLDR) and ligand-directed covalent labelling (LDCL) mechanisms. The top panel illustrates the mechanism of covalent ligand-directed release (CoLDR). A nucleophilic amino acid side chain, such as the thiol group of cysteine, forms a covalent bond with the α-carbon of the probe, triggering self-immolative cleavage and subsequent release of the attached payload. The bottom panel depicts the ligand-directed covalent labelling (LDCL) process, in which the cysteine thiol reacts with the electrophilic sulfamate acetamide moiety, resulting in covalent transfer of the cargo from the ligand to the target protein. In both panels, the target protein is shown in blue, and the ligand's orthostere is represented in green. The schematic mechanisms are adapted from Reddi *et al*. (2023)[214].

However, several factors require further investigation, including the cargo transfer rate, ligand stability in biological environments, and optimal positioning of the sulfamate acetamide within the probe architecture. Future work will focus on evaluating these parameters through synthetic modification and biological testing.

References

(1)   Schiöth, H. B.; Fredriksson, R. The GRAFS Classification System of G-Protein Coupled Receptors in Comparative Perspective. *Gen Comp Endocrinol* **2005**, *142* (1-2 SPEC. ISS.), 94–101. https://doi.org/10.1016/j.ygcen.2004.12.018.

(2)   Hilger, D.; Masureel, M.; Kobilka, B. K. Structure and Dynamics of GPCR Signaling Complexes. *Nat Struct Mol Biol* **2018**, *25* (1), 4–12. https://doi.org/10.1038/s41594-017-0011-7.

(3)   Milligan, G.; Kostenis, E. Heterotrimeric G-Proteins: A Short History. *Br J Pharmacol* **2006**, *147* (SUPPL. 1). https://doi.org/10.1038/sj.bjp.0706405.

(4)   Gurevich, V. V.; Gurevich, E. V. GPCR Signaling Regulation: The Role of GRKs and Arrestins. *Front Pharmacol* **2019**, *10* (FEB). https://doi.org/10.3389/fphar.2019.00125.

(5)   Sheth, S.; Brito, R.; Mukherjea, D.; Rybak, L. P.; Ramkumar, V. Adenosine Receptors: Expression, Function and Regulation. *Int J Mol Sci* **2014**, *15* (2), 2024–2052. https://doi.org/10.3390/ijms15022024.

(6)   Zhang, M.; Chen, T.; Lu, X.; Lan, X.; Chen, Z.; Lu, S. G Protein-Coupled Receptors (GPCRs): Advances in Structures, Mechanisms, and Drug Discovery. *Signal Transduct Target Ther* **2024**, *9* (1). https://doi.org/10.1038/s41392-024-01803-6.

(7)   Jean-Charles, P.-Y.; Kaur, S.; Shenoy, S. K. G Protein-Coupled Receptor Signaling Through b-Arrestin-Dependent Mechanisms. *J Cardiovasc Pharmacol* **2017**, *70*, 1–1.

(8)   Grundmann, M.; Merten, N.; Malfacini, D.; Inoue, A.; Preis, P.; Simon, K.; Rüttiger, N.; Ziegler, N.; Benkel, T.; Schmitt, N. K.; Ishida, S.; Müller, I.; Reher, R.; Kawakami, K.; Inoue, A.; Rick, U.; Kühl, T.; Imhof, D.; Aoki, J.; König, G. M.; Hoffmann, C.; Gomeza, J.; Wess, J.; Kostenis, E. Lack of Beta-Arrestin Signaling in the Absence of Active G Proteins. *Nat Commun* **2018**, *9* (1). https://doi.org/10.1038/s41467-017-02661-3.

(9)   Xu, Z.; Shao, Z. Dynamic Mechanism of GPCR-Mediated β-Arrestin: A Potential Therapeutic Agent Discovery of Biased Drug. *Signal Transduct Target Ther* **2022**, *7* (1). https://doi.org/10.1038/s41392-022-01140-6.

(10)   García-Nafría, J.; Tate, C. G. Structure Determination of GPCRs: Cryo-EM Compared with X-Ray Crystallography. *Biochem Soc Trans* **2021**, *49* (5), 2345–2355. https://doi.org/10.1042/BST20210431.

(11) Caroli, J.; Mamyrbekov, A.; Harpsøe, K.; Gardizi, S.; Dörries, L.; Ghosh, E.; Hauser, A. S.; Kooistra, A. J.; Gloriam, D. E. A Community Biased Signaling Atlas. *Nat Chem Biol* **2023**, *19* (5), 531–535. https://doi.org/10.1038/s41589-023-01292-8.

(12) Kolb, P.; Kenakin, T.; Alexander, S. P. H.; Bermudez, M.; Bohn, L. M.; Breinholt, C. S.; Bouvier, M.; Hill, S. J.; Kostenis, E.; Martemyanov, K. A.; Neubig, R. R.; Onaran, H. O.; Rajagopal, S.; Roth, B. L.; Selent, J.; Shukla, A. K.; Sommer, M. E.; Gloriam, D. E. Community Guidelines for GPCR Ligand Bias: IUPHAR Review 32. *Br J Pharmacol* **2022**, *179* (14), 3651–3674. https://doi.org/10.1111/bph.15811.

(13) Kaye, A. D.; Edinoff, A. N.; Babin, K. C.; Hebert, C. M.; Hardin, J. L.; Cornett, E. M.; Kaye, A. J.; Kaye, A. M.; Urman, R. D. Pharmacological Advances in Opioid Therapy: A Review of the Role of Oliceridine in Pain Management. *Pain Ther* **2021**, *10* (2), 1003–1012. https://doi.org/10.1007/s40122-021-00313-5.

(14) Ok, H. G.; Kim, S. Y.; Lee, S. J.; Kim, T. K.; Huh, B. K.; Kim, K. H. Can Oliceridine (TRV130), an Ideal Novel μ Receptor G Protein Pathway Selective (μ-GPS) Modulator, Provide Analgesia without Opioid-Related Adverse Reactions? *Korean Journal of Pain* **2018**, *31* (2), 73–79. https://doi.org/10.3344/kjp.2018.31.2.73.

(15) Lee, A. Avacopan: First Approval. *Drugs* **2022**, *82* (1), 79–85. https://doi.org/10.1007/s40265-021-01643-6.

(16) Conflitti, P.; Lyman, E.; Sansom, M. S. P.; Hildebrand, P. W.; Gutiérrez-de-Terán, H.; Carloni, P.; Ansell, T. B.; Yuan, S.; Barth, P.; Robinson, A. S.; Tate, C. G.; Gloriam, D.; Grzesiek, S.; Eddy, M. T.; Prosser, S.; Limongelli, V. Functional Dynamics of G Protein-Coupled Receptors Reveal New Routes for Drug Discovery. *Nat Rev Drug Discov* **2025**. https://doi.org/10.1038/s41573-024-01083-3.

(17) Hauser, A. S.; Attwood, M. M.; Rask-Andersen, M.; Schiöth, H. B.; Gloriam, D. E. Trends in GPCR Drug Discovery: New Agents, Targets and Indications. *Nat Rev Drug Discov* **2017**, *16* (12), 829–842. https://doi.org/10.1038/nrd.2017.178.

(18) Klaasse, E. C.; IJzerman, A. P.; de Grip, W. J.; Beukers, M. W. Internalization and Desensitization of Adenosine Receptors. *Purinergic Signal* **2008**, *4* (1), 21–37. https://doi.org/10.1007/s11302-007-9086-7.

(19) Deb, P. K.; Deka, S.; Borah, P.; Abed, S. N.; Klotz, K.-N. Medicinal Chemistry and Therapeutic Potential of Agonists, Antagonists and

Allosteric Modulators of A1 Adenosine Receptor: Current Status and Perspectives. *Curr Pharm Des* **2019**, *25* (25), 2697–2715. https://doi.org/10.2174/1381612825666190716100509.

(20)   Borea, P. A.; Gessi, S.; Merighi, S.; Vincenzi, F.; Varani, K. Pharmacology of Adenosine Receptors: The State of the Art. *Physiol Rev* **2018**, *98*, 1591–1625. https://doi.org/10.1152/physrev.00049.2017.-Adenosine.

(21)   Ciruela, F.; Casadó, V.; Rodrigues, R. J.; Luján, R.; Burgueño, J.; Canals, M.; Borycz, J.; Rebola, N.; Goldberg, S. R.; Mallol, J.; Cortés, A.; Canela, E. I.; López-Giménez, J. F.; Milligan, G.; Lluis, C.; Cunha, R. A.; Ferré, S.; Franco, R. Presynaptic Control of Striatal Glutamatergic Neurotransmission by Adenosine A1-A2A Receptor Heteromers. *Journal of Neuroscience* **2006**, *26* (7), 2080–2087. https://doi.org/10.1523/JNEUROSCI.3574-05.2006.

(22)   Jamwal, S.; Mittal, A.; Kumar, P.; Alhayani, D. M.; Al-Aboudi, A. Therapeutic Potential of Agonists and Antagonists of A1, A2a, A2b and A3 Adenosine Receptors. *Curr Pharm Des* **2019**, *25* (26), 2892–2905. https://doi.org/10.2174/1381612825666190716112319.

(23)   Ferré, S.; Ciruela, F. Functional and Neuroprotective Role of Striatal Adenosine A 2A Receptor Heterotetramers . *J Caffeine Adenosine Res* **2019**, *9* (3), 89–97. https://doi.org/10.1089/caff.2019.0008.

(24)   Ferré, S.; Sarasola, L. I.; Quiroz, C.; Ciruela, F. Presynaptic Adenosine Receptor Heteromers as Key Modulators of Glutamatergic and Dopaminergic Neurotransmission in the Striatum. *Neuropharmacology* **2023**, *223*. https://doi.org/10.1016/j.neuropharm.2022.109329.

(25)   Fredholm, B. B.; IJzerman, A. P.; Jacobson, K. A.; Linden, J.; Müller, C. E. International Union of Basic and Clinical Pharmacology. LXXXI. Nomenclature and Classification of Adenosine Receptors - An Update. *Pharmacol Rev* **2011**, *63* (1), 1–34. https://doi.org/10.1124/pr.110.003285.

(26)   Bonaventura, J.; Navarro, G.; Casadó-Anguera, V.; Azdad, K.; Rea, W.; Moreno, E.; Brugarolas, M.; Mallol, J.; Canela, E. I.; Lluís, C.; Cortés, A.; Volkowd, N. D.; Schiffmann, S. N.; Ferré, S.; Casadó, V. Allosteric Interactions between Agonists and Antagonists within the Adenosine A2A Receptordopamine D2 Receptor Heterotetramer. *Proc Natl Acad Sci U S A* **2015**, *112* (27), E3609–E3618. https://doi.org/10.1073/pnas.1507704112.

(27)   Maille, B.; Lalevée, N.; Marlinge, M.; Vahdat, J.; Mottola, G.; Degioanni, C.; De Maria, L.; Klein, V.; Thuny, F.; Franceschi, F.; Deharo, J. C.; Guieu, R.;

Fromonot, J. Adenosine and Adenosine Receptors: Advances in Atrial Fibrillation. *Biomedicines* **2022**, *10* (11). https://doi.org/10.3390/biomedicines10112963.

(28)   Coppi, E.; Dettori, I.; Cherchi, F.; Bulli, I.; Venturini, M.; Lana, D.; Giovannini, M. G.; Pedata, F.; Pugliese, A. M. A2b Adenosine Receptors: When Outsiders May Become an Attractive Target to Treat Brain Ischemia or Demyelination. *Int J Mol Sci* **2020**, *21* (24), 1–14. https://doi.org/10.3390/ijms21249697.

(29)   Little, J. W.; Ford, A.; Symons-Liguori, A. M.; Chen, Z.; Janes, K.; Doyle, T.; Xie, J.; Luongo, L.; Tosh, D. K.; Maione, S.; Bannister, K.; Dickenson, A. H.; Vanderah, T. W.; Porreca, F.; Jacobson, K. A.; Salvemini, D. Endogenous Adenosine A3 Receptor Activation Selectively Alleviates Persistent Pain States. *Brain* **2015**, *138* (1), 28–35. https://doi.org/10.1093/brain/awu330.

(30)   Salvatore, C. A.; Jacobson, M. A.; Taylort, H. E.; Lindeno, J.; Johnson, R. G. Molecular Cloning and Characterization of the Human A3 Adenosine Receptor. *Proc. Natl. Acad Sci.* **1993**, *90*, 10365–10369.

(31)   Effendi, W. I.; Nagano, T.; Kobayashi, K.; Nishimura, Y. Focusing on Adenosine Receptors as a Potential Targeted Therapy in Human Diseases. *Cells* **2020**, *9* (3). https://doi.org/10.3390/cells9030785.

(32)   Hocher, B. Adenosine A1 Receptor Antagonists in Clinical Research and Development. *Kidney Int* **2010**, *78* (5), 438–445. https://doi.org/10.1038/ki.2010.204.

(33)   Saini, A.; Patel, R.; Gaba, S.; Singh, G.; Gupta, G. D.; Monga, V. Adenosine Receptor Antagonists: Recent Advances and Therapeutic Perspective. *Eur J Med Chem* **2022**, *227*. https://doi.org/10.1016/j.ejmech.2021.113907.

(34)   Jacobson, K. A.; Tosh, D. K.; Jain, S.; Gao, Z. G. Historical and Current Adenosine Receptor Agonists in Preclinical and Clinical Development. *Front Cell Neurosci* **2019**, *13*. https://doi.org/10.3389/fncel.2019.00124.

(35)   Mason, P. K.; DiMarco, J. P. New Pharmacological Agents for Arrhythmias. *Circ Arrhythm Electrophysiol* **2009**, *2* (5), 588–597. https://doi.org/10.1161/CIRCEP.109.884429.

(36)   Spinozzi, E.; Baldassarri, C.; Acquaticci, L.; Del Bello, F.; Grifantini, M.; Cappellacci, L.; Riccardo, P. Adenosine Receptors as Promising Targets for the Management of Ocular Diseases. *Medicinal Chemistry Research* **2021**, *30* (2), 353–370. https://doi.org/10.1007/s00044-021-02704-x.

(37)   Boerrigter, G.; Burnett, J. C. Cardiorenal Syndrome in Decompensated Heart Failure: Prognostic and Therapeutic Implications. *Curr Heart Fail Rep* **2004**, *1*, 113–120.

(38)   Dennissen, F. J. A.; Anglada-Huguet, M.; Sydow, A.; Mandelkow, E.; Mandelkow, E. M. Adenosine A1 Receptor Antagonist Rolofylline Alleviates Axonopathy Caused by Human Tau ΔK280. *Proc Natl Acad Sci U S A* **2016**, *113* (41), 11597–11602. https://doi.org/10.1073/pnas.1603119113.

(39)   Peleli, M.; Carlstrom, M. Adenosine Signaling in Diabetes Mellitus and Associated Cardiovascular and Renal Complications. *Molecular Aspects of Medicine*. Elsevier Ltd June 1, 2017, pp 62–74. https://doi.org/10.1016/j.mam.2016.12.001.

(40)   Gardner, C. J.; Twissell, D. J.; Coates, J.; Strong, P. The Effects of GR79236 on Plasma Fatty Acid Concentrations, Heart Rate and Blood Pressure in the Conscious Rat. *Eur J Pharmacol* **1994**, *257*, 117–121.

(41)   Gao, Z. G.; Jacobson, K. A. Emerging Adenosine Receptor Agonists an Update. *Expert Opin Emerg Drugs* **2011**, *16* (4), 597–602. https://doi.org/10.1517/14728214.2011.644786.

(42)   Doi, T.; Kuzuna, S.; Maki, Y. Spinal Antinociceptive Effects of Adenosine Compounds in Mice. *Eur J Pharmacol* **1987**, *137*, 227–231.

(43)   Jung, S. M.; Peyton, L.; Essa, H.; Choi, D. S. Adenosine Receptors: Emerging Non-Opioids Targets for Pain Medications. *Neurobiology of Pain* **2022**, *11*. https://doi.org/10.1016/j.ynpai.2022.100087.

(44)   rn Johansson, B.; Halldner, L.; Dunwiddie, T. V; Masino, S. A.; Poelchen, W.; Gimé nez-Llort, L.; Escorihuela, R. M.; Ferná ndez-Teruel, A.; Wiesenfeld-Hallin, Z.; Xu, X.-J.; Hårdemark, A.; Betsholtz, C.; Herlenius, E.; Fredholm, B. B. Hyperalgesia, Anxiety, and Decreased Hypoxic Neuroprotection in Mice Lacking the Adenosine A 1 Receptor. *Proceedings of the National Academy of Sciences* **2001**, *98* (16), 9407–9412.

(45)   Jacobson, K. A.; Gao, Z. G. Adenosine Receptors as Therapeutic Targets. *Nat Rev Drug Discov* **2006**, *5* (3), 247–264. https://doi.org/10.1038/nrd1983.

(46)   Elzein, E.; Zablocki, J. A1 Adenosine Receptor Agonists and Their Potential Therapeutic Applications. *Expert Opin Investig Drugs* **2008**, *17* (12), 1901–1910. https://doi.org/10.1517/13543780802497284.

(47) Vincenzi, F.; Pasquini, S.; Battistello, E.; Merighi, S.; Gessi, S.; Borea, P. A.; Varani, K. A1 Adenosine Receptor Partial Agonists and Allosteric Modulators: Advancing Toward the Clinic? *Front Pharmacol* **2020**, *11*. https://doi.org/10.3389/fphar.2020.625134.

(48) Voors, A. A.; Bax, J. J.; Hernandez, A. F.; Wirtz, A. B.; Pap, A. F.; Ferreira, A. C.; Senni, M.; van der Laan, M.; Butler, J. Safety and Efficacy of the Partial Adenosine A1 Receptor Agonist Neladenoson Bialanate in Patients with Chronic Heart Failure with Reduced Ejection Fraction: A Phase IIb, Randomized, Double-Blind, Placebo-Controlled Trial. *Eur J Heart Fail* **2019**, *21* (11), 1426–1433. https://doi.org/10.1002/ejhf.1591.

(49) Nguyen, A. T. N.; Tran, Q. L.; Baltos, J. A.; McNeill, S. M.; Nguyen, D. T. N.; May, L. T. Small Molecule Allosteric Modulation of the Adenosine A1 Receptor. *Front Endocrinol (Lausanne)* **2023**, *14*. https://doi.org/10.3389/fendo.2023.1184360.

(50) Draper-Joyce, C. J.; Bhola, R.; Wang, J.; Bhattarai, A.; Nguyen, A. T. N.; Cowie-Kent, I.; O'Sullivan, K.; Chia, L. Y.; Venugopal, H.; Valant, C.; Thal, D. M.; Wootten, D.; Panel, N.; Carlsson, J.; Christie, M. J.; White, P. J.; Scammells, P.; May, L. T.; Sexton, P. M.; Danev, R.; Miao, Y.; Glukhova, A.; Imlach, W. L.; Christopoulos, A. Positive Allosteric Mechanisms of Adenosine A1 Receptor-Mediated Analgesia. *Nature* **2021**, *597* (7877), 571–576. https://doi.org/10.1038/s41586-021-03897-2.

(51) Weizmann, T.; Pearce, A.; Griffin, P.; Schild, A.; Flaßhoff, M.; Grossenbacher, P.; Lochner, M.; Reynolds, C. A.; Ladds, G.; Deganutti, G. Mechanistic Insights into the Adenosine A1 Receptor's Positive Allosteric Modulation for Non-Opioid Analgesics. *Cells* **2024**, *13* (24). https://doi.org/10.3390/cells13242121.

(52) Wall, M. J.; Hill, E.; Huckstepp, R.; Barkan, K.; Deganutti, G.; Leuenberger, M.; Preti, B.; Winfield, I.; Carvalho, S.; Suchankova, A.; Wei, H.; Safitri, D.; Huang, X.; Imlach, W.; La Mache, C.; Dean, E.; Hume, C.; Hayward, S.; Oliver, J.; Zhao, F. Y.; Spanswick, D.; Reynolds, C. A.; Lochner, M.; Ladds, G.; Frenguelli, B. G. Selective Activation of Gαob by an Adenosine A1 Receptor Agonist Elicits Analgesia without Cardiorespiratory Depression. *Nat Commun* **2022**, *13* (1). https://doi.org/10.1038/s41467-022-31652-2.

(53) Pasquini, S.; Contri, C.; Cappello, M.; Borea, P. A.; Varani, K.; Vincenzi, F. Update on the Recent Development of Allosteric Modulators for Adenosine Receptors and Their Therapeutic Applications. *Front Pharmacol* **2022**, *13*. https://doi.org/10.3389/fphar.2022.1030895.

(54) Pernomian, L.; Gomes, M. S.; Moreira, J. D.; Silva, C. H. T. de P. da; Rosa, J. M. C.; Cardoso, C. R. de B. New Horizons on Molecular Pharmacology Applied to Drug Discovery: When Resonance Overcomes Radioligand Binding. *Curr Radiopharm* **2017**, *10* (1), 16–20. https://doi.org/10.2174/1874471010666170208152420.

(55) Soave, M.; Briddon, S. J.; Hill, S. J.; Stoddart, L. A. Fluorescent Ligands: Bringing Light to Emerging GPCR Paradigms. *Br J Pharmacol* **2020**, *177* (5), 978–991. https://doi.org/10.1111/bph.14953.

(56) Harder, D.; Fotiadis, D. Measuring Substrate Binding and Affinity of Purified Membrane Transport Proteins Using the Scintillation Proximity Assay. *Nat Protoc* **2012**, *7* (9), 1569–1578. https://doi.org/10.1038/nprot.2012.090.

(57) Rossi, A. M.; Taylor, C. W. Analysis of Protein-Ligand Interactions by Fluorescence Polarization. *Nat Protoc* **2011**, *6* (3), 365–387. https://doi.org/10.1038/nprot.2011.305.

(58) Stoddart, L. A.; White, C. W.; Nguyen, K.; Hill, S. J.; G Pfleger, K. D. Fluorescence- and bioluminescence-Based to Study GPCR Binding. *Br J Pharmacol* **2016**, *173*, 3028–3037. https://doi.org/10.1111/bph.v173.20/issuetoc.

(59) Jun, J. V.; Chenoweth, D. M.; Petersson, E. J. Rational Design of Small Molecule Fluorescent Probes for Biological Applications. *Org Biomol Chem* **2020**, *18* (30), 5747–5763. https://doi.org/10.1039/d0ob01131b.

(60) Baker, J. G.; Middleton, R.; Adams, L.; May, L. T.; Briddon, S. J.; Kellam, B.; Hill, S. J. Influence of Fluorophore and Linker Composition on the Pharmacology of Fluorescent Adenosine A 1 Receptor Ligands: Themed Section: Imaging in Pharmacology Research Paper. *Br J Pharmacol* **2010**, *159* (4), 772–786. https://doi.org/10.1111/j.1476-5381.2009.00488.x.

(61) Králová, J.; Jurášek, M.; Mikšátková, L.; Marešová, A.; Fähnrich, J.; Cihlářová, P.; Drašar, P.; Bartůněk, P.; Král, V. Influence of Fluorophore and Linker Length on the Localization and Trafficking of Fluorescent Sterol Probes. *Sci Rep* **2020**, *10* (1). https://doi.org/10.1038/s41598-020-78085-9.

(62) Vernall, A. J.; Hill, S. J.; Kellam, B. The Evolving Small-Molecule Fluorescent-Conjugate Toolbox for Class A GPCRs. *Br J Pharmacol* **2014**, *171*, 1073–1084. https://doi.org/10.1111/bph.2014.171.issue-5.

(63)	Jacobson, K. A.; Uicena, D.; Padgett, W.; Kirk, K. L.; Daly, J. W. MOLECULAR PROBES FOR EXTRACELLULAR ADENOSINE RECEPTORS. *Biochem Pharmacol* **1987**, *36* (10), 1697–1707.

(64)	Macchia, M.; Salvetti, F.; Barontini, S.; Calvani, F.; Gesi, M.; Hamdan, M.; Lucacchini, A.; Pellegrini, A.; Soldani, P.; Martini, C. FLUORESCENT PROBES FOR ADENOSINE RECEPTORS: SYNTHESIS AND BIOLOGY OF N6-DANSYLAMINOALKYL-SUBSTITUTED NECA DERIVATIVES. *Bioorg Med Chem Lett* **1998**, *8*, 3223–3228.

(65)	Macchia, M.; Salvetti, F.; Bertini, S.; Bussolo, V. Di; Gattuso, L.; Gesi, M.; Hamdan, M.; Klotz, K.-N.; Laragione, T.; Lucacchini, A.; Minutolo, F.; Nencetti, S.; Papi, C.; Tuscano, D.; Martini, C. 7-Nitrobenzofurazan (NBD) Derivatives of 5 0-N-Ethylcarboxamidoadenosine (NECA) as New Fluorescent Probes for Human A 3 Adenosine Receptors. *Bioorg Med Chem Lett* **2001**, *11*, 3023–3026.

(66)	Middleton, R. J.; Briddon, S. J.; Cordeaux, Y.; Yates, A. S.; Dale, C. L.; George, M. W.; Baker, J. G.; Hill, S. J.; Kellam, B. New Fluorescent Adenosine A1-Receptor Agonists That Allow Quantification of Ligand-Receptor Interactions in Microdomains of Single Living Cells. *J Med Chem* **2007**, *50* (4), 782–793. https://doi.org/10.1021/jm061279i.

(67)	Dale, C. L.; Hill, S. J.; Kellam, B. New Potent, Short-Linker BODIPY-630/650™ Labelled Fluorescent Adenosine Receptor Agonists. *Medchemcomm* **2012**, *3* (3), 333–338. https://doi.org/10.1039/c2md00247g.

(68)	Stoddart, L. A.; Vernall, A. J.; Briddon, S. J.; Kellam, B.; Hill, S. J. Direct Visualisation of Internalization of the Adenosine A3 Receptor and Localization with Arrestin3 Using a Fluorescent Agonist. *Neuropharmacology* **2015**, *98*, 68–77. https://doi.org/10.1016/j.neuropharm.2015.04.013.

(69)	Briddon, S. J.; Middleton, R. J.; Cordeaux, Y.; Flavin, F. M.; Weinstein, J. A.; George, M. W.; Kellam, B.; Hill, S. J. Quantitative Analysis of the Formation and Diffusion of A 1-Adenosine Receptor-Antagonist Complexes in Single Living Cells. *PNAS* **2004**, *101*, 4673–4678.

(70)	Stoddart, L. A.; Vernall, A. J.; Denman, J. L.; Briddon, S. J.; Kellam, B.; Hill, S. J. Fragment Screening at Adenosine-A3 Receptors in Living Cells Using a Fluorescence-Based Binding Assay. *Chem Biol* **2012**, *19* (9), 1105–1115. https://doi.org/10.1016/j.chembiol.2012.07.014.

(71) Vernall, A. J.; Stoddart, L. A.; Briddon, S. J.; Ng, H. W.; Laughton, C. A.; Doughty, S. W.; Hill, S. J.; Kellam, B. Conversion of a Non-Selective Adenosine Receptor Antagonist into A 3-Selective High Affinity Fluorescent Probes Using Peptide-Based Linkers. *Org Biomol Chem* **2013**, *11* (34), 5673–5682. https://doi.org/10.1039/c3ob41221k.

(72) Comeo, E.; Trinh, P.; Nguyen, A. T.; Nowell, C. J.; Kindon, N. D.; Soave, M.; Stoddart, L. A.; White, J. M.; Hill, S. J.; Kellam, B.; Halls, M. L.; May, L. T.; Scammells, P. J. Development and Application of Subtype-Selective Fluorescent Antagonists for the Study of the Human Adenosine A1Receptor in Living Cells. *J Med Chem* **2021**, *64* (10), 6670–6695. https://doi.org/10.1021/acs.jmedchem.0c02067.

(73) Kozma, E.; Suresh Jayasekara, P.; Squarcialupi, L.; Paoletta, S.; Moro, S.; Federico, S.; Spalluto, G.; Jacobson, K. A. Fluorescent Ligands for Adenosine Receptors. *Bioorg Med Chem Lett* **2013**, *23* (1), 26–36. https://doi.org/10.1016/j.bmcl.2012.10.112.

(74) Comeo, E.; Goulding, J.; Lin, C. Y.; Groenen, M.; Woolard, J.; Kindon, N. D.; Harwood, C. R.; Platt, S.; Briddon, S. J.; Kilpatrick, L. E.; Scammells, P. J.; Hill, S. J.; Kellam, B. Ligand-Directed Labeling of the Adenosine A1 Receptor in Living Cells. *J Med Chem* **2024**, *67* (14), 12099–12117. https://doi.org/10.1021/acs.jmedchem.4c00835.

(75) Chandrasekera, P. C.; Wan, T. C.; Gizewski, E. T.; Auchampach, J. A.; Lasley, R. D. Adenosine A1 Receptors Heterodimerize with B1- and B2-Adrenergic Receptors Creating Novel Receptor Complexes with Altered G Protein Coupling and Signaling. *Cell Signal* **2013**, *25* (4), 736–742. https://doi.org/10.1016/j.cellsig.2012.12.022.

(76) Stoddart, L. A.; Kilpatrick, L. E.; Hill, S. J. NanoBRET Approaches to Study Ligand Binding to GPCRs and RTKs. *Trends Pharmacol Sci* **2018**, *39* (2), 136–147. https://doi.org/10.1016/j.tips.2017.10.006.

(77) Stoddart, L. A.; Johnstone, E. K. M.; Wheal, A. J.; Goulding, J.; Robers, M. B.; MacHleidt, T.; Wood, K. V.; Hill, S. J.; Pfleger, K. D. G. Application of BRET to Monitor Ligand Binding to GPCRs. *Nat Methods* **2015**, *12* (7), 661–663. https://doi.org/10.1038/nmeth.3398.

(78) Chalfie, M.; Tu, Y.; Euskirchen, G.; Ward, W. W.; Prasherf, D. C. Green Fluorescent Protein as a Marker for Gene Expression. *Science (1979)* **1994**, *263*, 802–805.

(79) Minoshima, M.; Reja, S. I.; Hashimoto, R.; Iijima, K.; Kikuchi, K. Hybrid Small-Molecule/Protein Fluorescent Probes. *Chem Rev* **2024**, *124* (10), 6198–6270. https://doi.org/10.1021/acs.chemrev.3c00549.

(80) Thorn, K. Genetically Encoded Fluorescent Tags. *Mol Biol Cell* **2017**, *28* (7), 848–857. https://doi.org/10.1091/mbc.E16-07-0504.

(81) Dreyer, R.; Pfukwa, R.; Barth, S.; Hunter, R.; Klumperman, B. The Evolution of SNAP-Tag Labels. *Biomacromolecules* **2023**, *24* (2), 517–530. https://doi.org/10.1021/acs.biomac.2c01238.

(82) Gautier, A.; Juillerat, A.; Heinis, C.; Corrêa, I. R.; Kindermann, M.; Beaufils, F.; Johnsson, K. An Engineered Protein Tag for Multiprotein Labeling in Living Cells. *Chem Biol* **2008**, *15* (2), 128–136. https://doi.org/10.1016/j.chembiol.2008.01.007.

(83) Los, G. V.; Encell, L. P.; McDougall, M. G.; Hartzell, D. D.; Karassina, N.; Zimprich, C.; Wood, M. G.; Learish, R.; Ohana, R. F.; Urh, M.; Simpson, D.; Mendez, J.; Zimmerman, K.; Otto, P.; Vidugiris, G.; Zhu, J.; Darzins, A.; Klaubert, D. H.; Bulleit, R. F.; Wood, K. V. HaloTag: A Novel Protein Labeling Technology for Cell Imaging and Protein Analysis. *ACS Chem Biol* **2008**, *3* (6), 373–382. https://doi.org/10.1021/cb800025k.

(84) Bonasio, R.; Carman, C. V.; Kim, E.; Sage, P. T.; Love, K. R.; Mempel, T. R.; Springer, T. A.; Von Andrian, U. H. Specific and Covalent Labeling of a Membrane Protein with Organic Fluorochromes and Quantum Dots. *Proc Natl Acad Sci U S A* **2007**, *104* (37), 14753–14758. https://doi.org/10.1073/pnas.0705201104.

(85) Hori, Y.; Nakaki, K.; Sato, M.; Mizukami, S.; Kikuchi, K. Development of Protein-Labeling Probes with a Redesigned Fluorogenic Switch Based on Intramolecular Association for No-Wash Live-Cell Imaging. *Angewandte Chemie - International Edition* **2012**, *51* (23), 5611–5614. https://doi.org/10.1002/anie.201200867.

(86) Gallagher, S. S.; Sable, J. E.; Sheetz, M. P.; Cornish, V. W. An in Vivo Covalent TMP-Tag Based on Proximity-Induced Reactivity. *ACS Chem Biol* **2009**, *4* (7), 547–556. https://doi.org/10.1021/cb900062k.

(87) Nonaka, H.; Tsukiji, S.; Ojida, A.; Hamachi, I. Non-Enzymatic Covalent Protein Labeling Using a Reactive Tag. *J Am Chem Soc* **2007**, *129* (51), 15777–15779. https://doi.org/10.1021/ja074176d.

(88) Amaike, K.; Tamura, T.; Hamachi, I. Recognition-Driven Chemical Labeling of Endogenous Proteins in Multi-Molecular Crowding in Live

Cells. *Chemical Communications* **2017**, *53* (88), 11972–11983. https://doi.org/10.1039/c7cc07177a.

(89)   Tamura, T.; Hamachi, I. Chemistry for Covalent Modification of Endogenous/Native Proteins: From Test Tubes to Complex Biological Systems. *J Am Chem Soc* **2019**, *141* (7), 2782–2799. https://doi.org/10.1021/jacs.8b11747.

(90)   Tsukiji, S.; Miyagawa, M.; Takaoka, Y.; Tamura, T.; Hamachi, I. Ligand-Directed Tosyl Chemistry for Protein Labeling in Vivo. *Nat Chem Biol* **2009**, *5* (5), 341–343. https://doi.org/10.1038/nchembio.157.

(91)   Fujishima, S. H.; Yasui, R.; Miki, T.; Ojida, A.; Hamachi, I. Ligand-Directed Acyl Imidazole Chemistry for Labeling of Membrane-Bound Proteins on Live Cells. *J Am Chem Soc* **2012**, *134* (9), 3961–3964. https://doi.org/10.1021/ja2108855.

(92)   Takaoka, Y.; Nishikawa, Y.; Hashimoto, Y.; Sasaki, K.; Hamachi, I. Ligand-Directed Dibromophenyl Benzoate Chemistry for Rapid and Selective Acylation of Intracellular Natural Proteins. *Chem Sci* **2015**, *6* (5), 3217–3224. https://doi.org/10.1039/c5sc00190k.

(93)   Hughes, C. C.; Yang, Y. L.; Liu, W. T.; Dorrestein, P. C.; La Clair, J. J.; Fenical, W. Marinopyrrole A Target Elucidation by Acyl Dye Transfer. *J Am Chem Soc* **2009**, *131* (34), 12094–12096. https://doi.org/10.1021/ja903149u.

(94)   Matsuo, K.; Nishikawa, Y.; Masuda, M.; Hamachi, I. Live-Cell Protein Sulfonylation Based on Proximity-driven N -Sulfonyl Pyridone Chemistry . *Angewandte Chemie* **2018**, *130* (3), 667–670. https://doi.org/10.1002/ange.201707972.

(95)   Tamura, T.; Ueda, T.; Goto, T.; Tsukidate, T.; Shapira, Y.; Nishikawa, Y.; Fujisawa, A.; Hamachi, I. Rapid Labelling and Covalent Inhibition of Intracellular Native Proteins Using Ligand-Directed N-Acyl-N-Alkyl Sulfonamide. *Nat Commun* **2018**, *9* (1). https://doi.org/10.1038/s41467-018-04343-0.

(96)   Xin, X.; Zhang, Y.; Gaetani, M.; Lundström, S. L.; Zubarev, R. A.; Zhou, Y.; Corkery, D. P.; Wu, Y. W. Ultrafast and Selective Labeling of Endogenous Proteins Using Affinity-Based Benzotriazole Chemistry. *Chem Sci* **2022**, *13* (24), 7240–7246. https://doi.org/10.1039/d1sc05974b.

(97)   Tsukiji, S.; Hamachi, I. Ligand-Directed Tosyl Chemistry for in Situ Native Protein Labeling and Engineering in Living Systems: From Basic

Properties to Applications. *Curr Opin Chem Biol* **2014**, *21*, 136–143. https://doi.org/10.1016/j.cbpa.2014.07.012.

(98)   Arttamangkul, S.; Plazek, A.; Platt, E. J.; Jin, H.; Murray, T. F.; Birdsong, W. T.; Rice, K. C.; Farrens, D. L.; Williams, J. T. Visualizing Endogenous Opioid Receptors in Living Neurons Using Ligand-Directed Chemistry. *Elife* **2019**, 49319. https://doi.org/10.7554/eLife.49319.001.

(99)   Kosar, M.; Sykes, D. A.; Viray, A. E. G.; Vitale, R. M.; Sarott, R. C.; Ganzoni, R. L.; Onion, D.; Tobias, J. M.; Leippe, P.; Ullmer, C.; Zirwes, E. A.; Guba, W.; Grether, U.; Frank, J. A.; Veprintsev, D. B.; Carreira, E. M. Platform Reagents Enable Synthesis of Ligand-Directed Covalent Probes: Study of Cannabinoid Receptor 2 in Live Cells. *J Am Chem Soc* **2023**, *145* (28), 15094–15108. https://doi.org/10.1021/jacs.2c13629.

(100)   Devaraj, N. K.; Finn, M. G. Introduction: ClickChemistry. *Chem Rev* **2021**, *121*, 6697–6698. https://doi.org/10.1021/acs.chemrev.0c00920.

(101)   Saxon, E.; Bertozzi, C. R. Cell Surface Engineering by a Modified Staudinger Reaction. *Science (1979)* **2000**, *287*, 2007–2009.

(102)   Hang, H. C.; Yu, C.; Kato, D. L.; Bertozzi, C. R. A Metabolic Labeling Approach toward Proteomic Analysis of Mucin-Type O-Linked Glycosylation. *Proc Natl Acad Sci U S A* **2003**, *100* (25), 14846–14851. https://doi.org/10.1073/pnas.2335201100.

(103)   Marter, K.; Kobler, O.; Erdmann, I.; Soleimanpour, E.; Landgraf, P.; Müller, A.; Abele, J.; Thomas, U.; Dieterich, D. C. Click Chemistry (CuAAC) and Detection of Tagged de Novo Synthesized Proteins in Drosophila. *Bio Protoc* **2019**, *9* (2). https://doi.org/10.21769/BioProtoc.3142.

(104)   Bednarek, C.; Wehl, I.; Jung, N.; Schepers, U.; Bräse, S. The Staudinger Ligation. *Chem Rev* **2020**, *120* (10), 4301–4354. https://doi.org/10.1021/acs.chemrev.9b00665.

(105)   Rostovtsev, V. V.; Green, L. G.; Fokin, V. V.; Sharpless, K. B. A Stepwise Huisgen Cycloaddition Process: Copper(I)-Catalyzed Regioselective "Ligation" of Azides and Terminal Alkynes. *Angewandte Chemie - International Edition* **2002**, *41* (14), 2596–2599. https://doi.org/10.1002/1521-3773(20020715)41:14<2596::AID-ANIE2596>3.0.CO;2-4.

(106)   Uttamapinant, C.; Sanchez, M. I.; Liu, D. S.; Yao, J. Z.; White, K. A.; Grecian, S.; Clarke, S.; Gee, K. R.; Ting, A. Y. Site-Specific Protein Labeling Using Prime and Chelation-Assisted Click Chemistry. *Nat Protoc* **2013**, *8* (8), 1620–1634. https://doi.org/10.1038/nprot.2013.096.

(107) Bird, R. E.; Lemmel, S. A.; Yu, X.; Zhou, Q. A. Bioorthogonal Chemistry and Its Applications. *Bioconjug Chem* **2021**, *32* (12), 2457–2479. https://doi.org/10.1021/acs.bioconjchem.1c00461.

(108) Agard, N. J.; Prescher, J. A.; Bertozzi, C. R. A Strain-Promoted [3 + 2] Azide-Alkyne Cycloaddition for Covalent Modification of Biomolecules in Living Systems. *J Am Chem Soc* **2004**, *126* (46), 15046–15047. https://doi.org/10.1021/ja044996f.

(109) Dommerholt, J.; Schmidt, S.; Temming, R.; Hendriks, L. J. A.; Rutjes, F. P. J. T.; Van Hest, J. C. M.; Lefeber, D. J.; Friedl, P.; Van Delft, F. L. Readily Accessible Bicyclononynes for Bioorthogonal Labeling and Three-Dimensional Imaging of Living Cells. *Angewandte Chemie - International Edition* **2010**, *49* (49), 9422–9425. https://doi.org/10.1002/anie.201003761.

(110) Knall, A. C.; Slugovc, C. Inverse Electron Demand Diels-Alder (IEDDA)-Initiated Conjugation: A (High) Potential Click Chemistry Scheme. *Chem Soc Rev* **2013**, *42* (12), 5131–5142. https://doi.org/10.1039/c3cs60049a.

(111) Karver, M. R.; Weissleder, R.; Hilderbrand, S. A. Synthesis and Evaluation of a Series of 1,2,4,5-Tetrazines for Bioorthogonal Conjugation. *Bioconjug Chem* **2011**, *22* (11), 2263–2270. https://doi.org/10.1021/bc200295y.

(112) Beerkens, B. L. H.; Koç, Ç.; Liu, R.; Florea, B. I.; Le Dévédec, S. E.; Heitman, L. H.; Ijzerman, A. P.; Van Der Es, D. A Chemical Biological Approach to Study G Protein-Coupled Receptors: Labeling the Adenosine A1Receptor Using an Electrophilic Covalent Probe. *ACS Chem Biol* **2022**, *17* (11), 3131–3139. https://doi.org/10.1021/acschembio.2c00589.

(113) Stoddart, L. A.; Kindon, N. D.; Otun, O.; Harwood, C. R.; Patera, F.; Veprintsev, D. B.; Woolard, J.; Briddon, S. J.; Franks, H. A.; Hill, S. J.; Kellam, B. Ligand-Directed Covalent Labelling of a GPCR with a Fluorescent Tag in Live Cells. *Commun Biol* **2020**, *3* (1). https://doi.org/10.1038/s42003-020-01451-w.

(114) Shah, S. J.; Voors, A. A.; McMurray, J. J. V.; Kitzman, D. W.; Viethen, T.; Bomfim Wirtz, A.; Huang, E.; Pap, A. F.; Solomon, S. D. Effect of Neladenoson Bialanate on Exercise Capacity among Patients with Heart Failure with Preserved Ejection Fraction: A Randomized Clinical Trial. *JAMA - Journal of the American Medical Association* **2019**, *321* (21), 2101–2112. https://doi.org/10.1001/jama.2019.6717.

(115) Pang, P. S.; Mehra, M.; Maggioni, A. P.; Filippatos, G.; Middlebrooks, J.; Turlapaty, P.; Kazei, D.; Gheorghiade, M. Rationale, Design, and Results

from RENO-DEFEND 1: A Randomized, Dose-Finding Study of the Selective A1 Adenosine Antagonist SLV320 in Patients Hospitalized with Acute Heart Failure. *Am Heart J* **2011**, *161* (6). https://doi.org/10.1016/j.ahj.2011.03.004.

(116) Ensor, C. R.; Russell, S. D. Tonapofylline: A Selective Adenosine-1 Receptor Antagonist for the Treatment of Heart Failure. *Expert Opin Pharmacother* **2010**, *11* (14), 2405–2415. https://doi.org/10.1517/14656566.2010.514605.

(117) Comeo, E.; Kindon, N. D.; Soave, M.; Stoddart, L. A.; Kilpatrick, L. E.; Scammells, P. J.; Hill, S. J.; Kellam, B. Subtype-Selective Fluorescent Ligands as Pharmacological Research Tools for the Human Adenosine A2A Receptor. *J Med Chem* **2020**, *63* (5), 2656–2672. https://doi.org/10.1021/acs.jmedchem.9b01856.

(118) Soave, M.; Kellam, B.; Woolard, J.; Briddon, S. J.; Hill, S. J. NanoBiT Complementation to Monitor Agonist-Induced Adenosine A1 Receptor Internalization. *SLAS Discovery* **2020**, *25* (2), 186–194. https://doi.org/10.1177/2472555219880475.

(119) Dale, N. C.; Johnstone, E. K. M.; White, C. W.; Pfleger, K. D. G. NanoBRET: The Bright Future of Proximity-Based Assays. *Front Bioeng Biotechnol* **2019**, *7* (MAR). https://doi.org/10.3389/fbioe.2019.00056.

(120) Vogel, S. S.; Thaler, christopher; Koushik, S. V. Fanciful FRET. *Sci. STKE* **2006**.

(121) Patera, F.; Mistry, S. J.; Kindon, N. D.; Comeo, E.; Goulding, J.; Kellam, B.; Kilpatrick, L. E.; Franks, H.; Hill, S. J. A Novel and Selective Fluorescent Ligand for the Study of Adenosine A2B Receptors. *Pharmacol Res Perspect* **2024**, *12* (4). https://doi.org/10.1002/prp2.1223.

(122) Chen, W.; YOUNIS, M. H.; Zhao, Z.; Cai, W. Recent Biomedical Advances Enabled by HaloTag Technology. *Biocell* **2022**, *46* (6). https://doi.org/10.32604/biocell.2022.018197.

(123) Fang, H.; Peng, B.; Ong, S. Y.; Wu, Q.; Li, L.; Yao, S. Q. Recent Advances in Activity-Based Probes (ABPs) and Affinity-Based Probes (AfBPs) for Profiling of Enzymes. *Chem Sci* **2021**, *12* (24), 8288–8310. https://doi.org/10.1039/d1sc01359a.

(124) Taliani, S.; Da Pozzo, E.; Bellandi, M.; Bendinelli, S.; Pugliesi, I.; Simorini, F.; La Motta, C.; Salerno, S.; Marini, A. M.; Da Settimo, F.; Cosimelli, B.; Greco, G.; Novellino, E.; Martini, C. Novel Irreversible Fluorescent Probes Targeting the 18 KDa Translocator Protein: Synthesis and Biological

Characterization. *J Med Chem* **2010**, *53* (10), 4085–4093.
https://doi.org/10.1021/jm100100q.

(125) Ojima, K.; Shiraiwa, K.; Soga, K.; Doura, T.; Takato, M.; Komatsu, K.;
Yuzaki, M.; Hamachi, I.; Kiyonaka, S. Ligand-Directed Two-Step Labeling
to Quantify Neuronal Glutamate Receptor Trafficking. *Nat Commun* **2021**,
12 (1). https://doi.org/10.1038/s41467-021-21082-x.

(126) Kiesman, W. F.; Zhao, J.; Conlon, P. R.; Dowling, J. E.; Petter, R. C.;
Lutterodt, F.; Jin, X.; Smits, G.; Fure, M.; Jayaraj, A.; Kim, J.; Sullivan, G.;
Linden, J. Potent and Orally Bioavailable 8-Bicyclo[2.2.2]Octylxanthines
as Adenosine A1 Receptor Antagonists. *J Med Chem* **2006**, *49* (24), 7119–
7131. https://doi.org/10.1021/jm0605381.

(127) Glukhova, A.; Thal, D. M.; Nguyen, A. T.; Vecchio, E. A.; Jörg, M.;
Scammells, P. J.; May, L. T.; Sexton, P. M.; Christopoulos, A. Structure of
the Adenosine A1 Receptor Reveals the Basis for Subtype Selectivity. *Cell*
2017, *168* (5), 867-877.e13. https://doi.org/10.1016/j.cell.2017.01.042.

(128) Vernall, A. J.; Stoddart, L. A.; Briddon, S. J.; Hill, S. J.; Kellam, B. Highly
Potent and Selective Fluorescent Antagonists of the Human Adenosine
A3 Receptor Based on the 1,2,4-Triazolo[4,3-a]Quinoxalin-1-One
Scaffold. *J Med Chem* **2012**, *55* (4), 1771–1782.
https://doi.org/10.1021/jm201722y.

(129) Schembri, L. S.; Stoddart, L. A.; Briddon, S. J.; Kellam, B.; Canals, M.;
Graham, B.; Scammells, P. J. Synthesis, Biological Evaluation, and Utility
of Fluorescent Ligands Targeting the μ-Opioid Receptor. *J Med Chem*
2015, *58* (24), 9754–9767.
https://doi.org/10.1021/acs.jmedchem.5b01664.

(130) Kiesman, W. F.; Zhao, J.; Conlon, P. R.; Petter, R. C.; Jin, X.; Smits, G.;
Lutterodt, F.; Sullivan, G. W.; Linden, J. Norbornyllactone-Substituted
Xanthines as Adenosine A1 Receptor Antagonists. *Bioorg Med Chem*
2006, *14* (11), 3654–3661. https://doi.org/10.1016/j.bmc.2006.01.021.

(131) Dunetz, J. R.; Xiang, Y.; Baldwin, A.; Ringling, J. General and Scalable
Amide Bond Formation with Epimerization-Prone Substrates Using T3P
and Pyridine. *Org Lett* **2011**, *13* (19), 5048–5051.
https://doi.org/10.1021/ol201875q.

(132) Li, P.; Xu, J. C. 2-Bromo-1-Ethyl Pyridinium Tetrafluoroborate (BEP): A
Powerful Coupling Reagent for N-Methylated Peptide Synthesis. *Balli and
F. Kersting, Liebigs Ann. Chem* **2000**, *29* (3), 204–205.

(133) Ghosh, A. K.; Shahabi, D. Synthesis of Amide Derivatives for Electron Deficient Amines and Functionalized Carboxylic Acids Using EDC and DMAP and a Catalytic Amount of HOBt as the Coupling Reagents. *Tetrahedron Lett* **2021**, *63*. https://doi.org/10.1016/j.tetlet.2020.152719.

(134) Beutner, G. L.; Young, I. S.; Davies, M. L.; Hickey, M. R.; Park, H.; Stevens, J. M.; Ye, Q. TCFH-NMI: Direct Access to N-Acyl Imidazoliums for Challenging Amide Bond Formations. *Org Lett* **2018**, *20* (14), 4218–4222. https://doi.org/10.1021/acs.orglett.8b01591.

(135) Brittain, W. D. G.; Cobb, S. L. Carboxylic Acid Deoxyfluorination and One-Pot Amide Bond Formation Using Pentafluoropyridine (PFP). *Org Lett* **2021**, *23* (15), 5793–5798. https://doi.org/10.1021/acs.orglett.1c01953.

(136) Hall, M. P.; Unch, J.; Binkowski, B. F.; Valley, M. P.; Butler, B. L.; Wood, M. G.; Otto, P.; Zimmerman, K.; Vidugiris, G.; MacHleidt, T.; Robers, M. B.; Benink, H. A.; Eggers, C. T.; Slater, M. R.; Meisenheimer, P. L.; Klaubert, D. H.; Fan, F.; Encell, L. P.; Wood, K. V. Engineered Luciferase Reporter from a Deep Sea Shrimp Utilizing a Novel Imidazopyrazinone Substrate. *ACS Chem Biol* **2012**, *7* (11), 1848–1857. https://doi.org/10.1021/cb3002478.

(137) Machleidt, T.; Woodroofe, C. C.; Schwinn, M. K.; Méndez, J.; Robers, M. B.; Zimmerman, K.; Otto, P.; Daniels, D. L.; Kirkland, T. A.; Wood, K. V. NanoBRET-A Novel BRET Platform for the Analysis of Protein-Protein Interactions. *ACS Chem Biol* **2015**, *10* (8), 1797–1804. https://doi.org/10.1021/acschembio.5b00143.

(138) Iqbal, A.; Arslan, S.; Okumus, B.; Wilson, T. J.; Giraud, G.; Norman, D. G.; Ha, T.; Lilley, D. M. J. Orientation Dependence in Fluorescent Energy Transfer between Cy3 and Cy5 Terminally Attached to Double-Stranded Nucleic Acids. *Proc Natl Acad Sci U S A* **2008**, *105* (32), 11176–11181. https://doi.org/10.1073/pnas.0801707105.

(139) Grime, R. L.; Goulding, J.; Uddin, R.; Stoddart, L. A.; Hill, S. J.; Poyner, D. R.; Briddon, S. J.; Wheatley, M. Single Molecule Binding of a Ligand to a G-Protein-Coupled Receptor in Real Time Using Fluorescence Correlation Spectroscopy, Rendered Possible by Nano-Encapsulation in Styrene Maleic Acid Lipid Particles. *Nanoscale* **2020**, *12* (21), 11518–11525. https://doi.org/10.1039/d0nr01060j.

(140) Cooper, S. L.; Wragg, E. S.; Pannucci, P.; Soave, M.; Hill, S. J.; Woolard, J. Regionally Selective Cardiovascular Responses to Adenosine A2A and A2B Receptor Activation. *FASEB Journal* **2022**, *36* (4). https://doi.org/10.1096/fj.202101945R.

(141) Kielkopf, C. L.; Bauer, W.; Urbatsch, I. L. Sodium Dodecyl Sulfate-Polyacrylamide Gel Electrophoresis of Proteins. *Cold Spring Harb Protoc* **2021**, *2021* (12), 494–504. https://doi.org/10.1101/pdb.prot102228.

(142) Schmidt, T. G. M.; Batz, L.; Bonet, L.; Carl, U.; Holzapfel, G.; Kiem, K.; Matulewicz, K.; Niermeier, D.; Schuchardt, I.; Stanar, K. Development of the Twin-Strep-Tag® and Its Application for Purification of Recombinant Proteins from Cell Culture Supernatants. *Protein Expr Purif* **2013**, *92* (1), 54–61. https://doi.org/10.1016/j.pep.2013.08.021.

(143) Schmidt, T. G. M.; Rgen Koepke, J.; Frank, R.; Skerra, A. Molecular Interaction Between the Strep-Tag Affinity Peptide and Its Cognate Target, Streptavidin. *J. Mol. Biol* **1996**, *255*, 753–766.

(144) Voss, S.; Skerra, A. Mutagenesis of a Flexible Loop in Streptavidin Leads to Higher Affinity for the Strep-Tag II Peptide and Improved Performance in Recombinant Protein Purification. *Protein Eng* **1997**, *10* (8), 975–982.

(145) Miljus, T.; Sykes, D. A.; Harwood, C. R.; Vuckovic, Z.; Veprintsev, D. B. GPCR Solubilization and Quality Control. In *Expression, Purification, and Structural Biology of Membrane Proteins*; Camilo Perez, Timm Maier, Eds.; Humana Press Inc., 2020; Vol. 2127, pp 105–127. https://doi.org/10.1007/978-1-0716-0373-4_8.

(146) Jones, J.; Nivitchanyong, T.; Giblin, C.; Ciccarone, V.; Judd, D.; Gorfien, S.; Krag, S. S.; Betenbaugh, M. J. Optimization of Tetracycline-Responsive Recombinant Protein Production and Effect on Cell Growth and ER Stress in Mammalian Cells. *Biotechnol Bioeng* **2005**, *91* (6), 722–732. https://doi.org/10.1002/bit.20566.

(147) Moss, S. M.; Jayasekara, P. S.; Paoletta, S.; Gao, Z. G.; Jacobson, K. A. Structure-Based Design of Reactive Nucleosides for Site-Specific Modification of the A2A Adenosine Receptor. *ACS Med Chem Lett* **2014**, *5* (9), 1043–1048. https://doi.org/10.1021/ml5002486.

(148) Escriche, M.; Burgueño, J.; Ciruela, F.; Canela, E. I.; Mallol, J.; Enrich, C.; Lluís, C.; Franco, R. Ligand-Induced Caveolae-Mediated Internalization of A1 Adenosine Receptors: Morphological Evidence of Endosomal Sorting and Receptor Recycling. *Exp Cell Res* **2003**, *285* (1), 72–90. https://doi.org/10.1016/S0014-4827(02)00090-3.

(149) Vendite, D.; Sanz, J. M.; Lopez-Alanon, D. M.; Vacas, J.; Andres, A.; Ros1', M. Desensitization of Adenosine A1 Receptor-Mediated Inhibition of Adenylyl Cyclase in Cerebellar Granule Cells. *Neurochem Res* **1998**, *23* (2), 211–218.

(150) Saura, C. A.; Mallol, J.; Canela, E. I.; Lluis, C.; Franco, R. Adenosine Deaminase and A 1 Adenosine Receptors Internalize Together Following Agonist-Induced Receptor Desensitization*. *J Biol Chem* **1998**, *273* (28), 17610–17617.

(151) Coelho, J. E.; Rebola, N.; Fragata, I.; Ribeiro, J. A.; De Mendonça, A.; Cunha, R. A. Hypoxia-Induced Desensitization and Internalization of Adenosine A 1 Receptors in the Rat Hippocampus. *Neuroscience* **2006**, *138* (4), 1195–1203. https://doi.org/10.1016/j.neuroscience.2005.12.012.

(152) Dixon, A. S.; Schwinn, M. K.; Hall, M. P.; Zimmerman, K.; Otto, P.; Lubben, T. H.; Butler, B. L.; Binkowski, B. F.; MacHleidt, T.; Kirkland, T. A.; Wood, M. G.; Eggers, C. T.; Encell, L. P.; Wood, K. V. NanoLuc Complementation Reporter Optimized for Accurate Measurement of Protein Interactions in Cells. *ACS Chem Biol* **2016**, *11* (2), 400–408. https://doi.org/10.1021/acschembio.5b00753.

(153) Michnick, S. W.; Ear, P. H.; Manderson, E. N.; Remy, I.; Stefan, E. Universal Strategies in Research and Drug Discovery Based on Protein-Fragment Complementation Assays. *Nat Rev Drug Discov* **2007**, *6* (7), 569–582. https://doi.org/10.1038/nrd2311.

(154) Schwinn, M. K.; Machleidt, T.; Zimmerman, K.; Eggers, C. T.; Dixon, A. S.; Hurst, R.; Hall, M. P.; Encell, L. P.; Binkowski, B. F.; Wood, K. V. CRISPR-Mediated Tagging of Endogenous Proteins with a Luminescent Peptide. *ACS Chem Biol* **2018**, *13* (2), 467–474. https://doi.org/10.1021/acschembio.7b00549.

(155) Yang, X.; Van Veldhoven, J. P. D.; Offringa, J.; Kuiper, B. J.; Lenselink, E. B.; Heitman, L. H.; Van Der Es, D.; Ijzerman, A. P. Development of Covalent Ligands for G Protein-Coupled Receptors: A Case for the Human Adenosine A3 Receptor. *J Med Chem* **2019**, *62* (7), 3539–3552. https://doi.org/10.1021/acs.jmedchem.8b02026.

(156) Goulding, J.; May, L. T.; Hill, S. J. Characterisation of Endogenous A2A and A2B Receptor-Mediated Cyclic AMP Responses in HEK 293 Cells Using the GloSensor™ Biosensor: Evidence for an Allosteric Mechanism of Action for the A2B-Selective Antagonist PSB 603. *Biochem Pharmacol* **2018**, *147*, 55–66. https://doi.org/10.1016/j.bcp.2017.10.013.

(157) Bouzo-Lorenzo, M.; Stoddart, L. A.; Xia, L.; IJzerman, A. P.; Heitman, L. H.; Briddon, S. J.; Hill, S. J. A Live Cell NanoBRET Binding Assay Allows the Study of Ligand-Binding Kinetics to the Adenosine A3 Receptor. *Purinergic*

Signal **2019**, *15* (2), 139–153. https://doi.org/10.1007/s11302-019-09650-9.

(158)   Hill, S. J.; Kilpatrick, L. E. Kinetic Analysis of Fluorescent Ligand Binding to Cell Surface Receptors: Insights into Conformational Changes and Allosterism in Living Cells. *Br J Pharmacol* **2023**, *181* (21), 4091–4102. https://doi.org/10.1111/bph.16185.

(159)   Jarmoskaite, I.; Alsadhan, I.; Vaidyanathan, P. P.; Herschlag, D. How to Measure and Evaluate Binding Affinities. *Elife* **2020**, *9*, 1–34. https://doi.org/10.7554/ELIFE.57264.

(160)   Sykes, D. A.; Stoddart, L. A.; Kilpatrick, L. E.; Hill, S. J. Binding Kinetics of Ligands Acting at GPCRs. *Mol Cell Endocrinol* **2019**, *485*, 9–19. https://doi.org/10.1016/j.mce.2019.01.018.

(161)   Ren, T.; Zhu, X.; Jusko, N. M.; Krzyzanski, W.; Jusko, W. J. Pharmacodynamic Model of Slow Reversible Binding and Its Applications in Pharmacokinetic/Pharmacodynamic Modeling: Review and Tutorial. *J Pharmacokinet Pharmacodyn* **2022**, *49* (5), 493–510. https://doi.org/10.1007/s10928-022-09822-y.

(162)   Shiraiwa, K.; Cheng, R.; Nonaka, H.; Tamura, T.; Hamachi, I. Chemical Tools for Endogenous Protein Labeling and Profiling. *Cell Chem Biol* **2020**, *27* (8), 970–985. https://doi.org/10.1016/j.chembiol.2020.06.016.

(163)   Zhao, H.; He, Y.; Lo, Y.; Song, H.; Lu, J. Fluorescent Probes Based on Bioorthogonal Reactions: Construction Strategies and Applications. *TrAC - Trends in Analytical Chemistry* **2023**, *169*. https://doi.org/10.1016/j.trac.2023.117388.

(164)   Baskin, J. M.; Prescher, J. A.; Laughlin, S. T.; Agard, N. J.; Chang, P. V; Miller, I. A.; Lo, A.; Codelli, J. A.; Bertozzi, C. R. Copper-Free Click Chemistry for Dynamic in Vivo Imaging. *PNAS* **2007**, *104* (43), 16793–16797.

(165)   Blackman, M. L.; Royzen, M.; Fox, J. M. Tetrazine Ligation: Fast Bioconjugation Based on Inverse-Electron-Demand Diels-Alder Reactivity. *J Am Chem Soc* **2008**, *130* (41), 13518–13519. https://doi.org/10.1021/ja8053805.

(166)   Chen, X.; Wu, Y. W. Selective Chemical Labeling of Proteins. *Org Biomol Chem* **2016**, *14* (24), 5417–5439. https://doi.org/10.1039/c6ob00126b.

(167) Devaraj, N. K.; Weissleder, R.; Hilderbrand, S. A. Tetrazine-Based Cycloadditions: Application to Pretargeted Live Cell Imaging. *Bioconjug Chem* **2008**, *19* (12), 2297–2299. https://doi.org/10.1021/bc8004446.

(168) Seliger, B.; Kiessling, R. The Two Sides of HER2/Neu: Immune Escape versus Surveillance. *Trends Mol Med* **2013**, *19* (11), 677–684. https://doi.org/10.1016/j.molmed.2013.08.003.

(169) Swirski, F. K.; Berger, C. R.; Figueiredo, J. L.; Mempel, T. R.; von Andrian, U. H.; Pittet, M. J.; Weissleder, R. A Near-Infrared Cell Tracker Reagent for Multiscopic in Vivo Imaging and Quantification of Leukocyte Immune Responses. *PLoS One* **2007**, *2* (10). https://doi.org/10.1371/journal.pone.0001075.

(170) Sun, E. Y.; Josephson, L.; Weissleder, R. "Clickable" Nanoparticles for Targeted Imaging. *Mol Imaging* **2006**, *5* (2), 7290.2006.00013. https://doi.org/10.2310/7290.2006.00013.

(171) Foster, R. A. A.; Willis, M. C. Tandem Inverse-Electron-Demand Hetero-/Retro-Diels-Alder Reactions for Aromatic Nitrogen Heterocycle Synthesis. *Chem Soc Rev* **2013**, *42* (1), 63–76. https://doi.org/10.1039/c2cs35316d.

(172) Oliveira, B. L.; Guo, Z.; Bernardes, G. J. L. Inverse Electron Demand Diels-Alder Reactions in Chemical Biology. *Chem Soc Rev* **2017**, *46* (16), 4895–4950. https://doi.org/10.1039/c7cs00184c.

(173) Soenen, D. R.; Zimpleman, J. M.; Boger, D. L. Synthesis and Inverse Electron Demand Diels-Alder Reactions of 3,6-Bis(3,4-Dimethoxybenzoyl)-1,2,4,5-Tetrazine. *Journal of Organic Chemistry* **2003**, *68* (9), 3593–3598. https://doi.org/10.1021/jo020713v.

(174) Adhikari, K.; Vanermen, M.; Da Silva, G.; Van den Wyngaert, T.; Augustyns, K.; Elvas, F. Trans-Cyclooctene—a Swiss Army Knife for Bioorthogonal Chemistry: Exploring the Synthesis, Reactivity, and Applications in Biomedical Breakthroughs. *EJNMMI Radiopharm Chem* **2024**, *9* (47). https://doi.org/10.1186/s41181-024-00275-x.

(175) Taylor, M. T.; Blackman, M. L.; Dmitrenko, O.; Fox, J. M. Design and Synthesis of Highly Reactive Dienophiles for the Tetrazine-Trans-Cyclooctene Ligation. *J Am Chem Soc* **2011**, *133* (25), 9646–9649. https://doi.org/10.1021/ja201844c.

(176) Darko, A.; Wallace, S.; Dmitrenko, O.; Machovina, M. M.; Mehl, R. A.; Chin, J. W.; Fox, J. M. Conformationally Strained Trans-Cyclooctene with

Improved Stability and Excellent Reactivity in Tetrazine Ligation. *Chem Sci* **2014**, *5* (10), 3770–3776. https://doi.org/10.1039/c4sc01348d.

(177) Luu, T.; Gristwood, K.; Knight, J. C.; Jörg, M. Click Chemistry: Reaction Rates and Their Suitability for Biomedical Applications. *Bioconjug Chem* **2024**, *35* (6), 715–731. https://doi.org/10.1021/acs.bioconjchem.4c00084.

(178) Svatunek, D.; Wilkovitsch, M.; Hartmann, L.; Houk, K. N.; Mikula, H. Uncovering the Key Role of Distortion in Bioorthogonal Tetrazine Tools That Defy the Reactivity/Stability Trade-Off. *J Am Chem Soc* **2022**, *144* (18), 8171–8177. https://doi.org/10.1021/jacs.2c01056.

(179) Cheng, H. C. The Power Issue: Determination of K B or K i from IC 50 A Closer Look at the Cheng-Prusoff Equation, the Schild Plot and Related Power Equations. *J Pharmacol Toxicol Methods* **2001**, *46* (2), 61–71.

(180) Gómez-Santacana, X.; Boutonnet, M.; Martínez-Juvés, C.; Cimadevila, M.; Catena, J.; Moutin, E.; Roux, T.; Trinquet, E.; Lamarque, L.; Perroy, J.; Prézeau, L.; Zwier, J. M.; Pin, J.-P.; Llebaria, A. A Modular Click Ligand-Directed Approach to Label Endogenous Dopamine D1 Receptors in Live Cells. *Commun Chem* **2025**, *8* (1), 113. https://doi.org/10.1038/s42004-025-01504-3.

(181) Weiskirchen, S.; Schröder, S. K.; Buhl, E. M.; Weiskirchen, R. A Beginner's Guide to Cell Culture: Practical Advice for Preventing Needless Problems. *Cells* **2023**, *12* (5). https://doi.org/10.3390/cells12050682.

(182) Rossin, R.; Van Den Bosch, S. M.; Ten Hoeve, W.; Carvelli, M.; Versteegen, R. M.; Lub, J.; Robillard, M. S. Highly Reactive Trans-Cyclooctene Tags with Improved Stability for Diels-Alder Chemistry in Living Systems. *Bioconjug Chem* **2013**, *24* (7), 1210–1217. https://doi.org/10.1021/bc400153y.

(183) Béquignat, J. B.; Ty, N.; Rondon, A.; Taiariol, L.; Degoul, F.; Canitrot, D.; Quintana, M.; Navarro-Teulon, I.; Miot-Noirault, E.; Boucheix, C.; Chezal, J. M.; Moreau, E. Optimization of IEDDA Bioorthogonal System: Efficient Process to Improve Trans-Cyclooctene/Tetrazine Interaction. *Eur J Med Chem* **2020**, *203*. https://doi.org/10.1016/j.ejmech.2020.112574.

(184) Rossin, R.; Verkerk, P. R.; Van Den Bosch, S. M.; Vulders, R. C. M.; Verel, I.; Lub, J.; Robillard, M. S. In Vivo Chemistry for Pretargeted Tumor Imaging in Live Mice. *Angewandte Chemie - International Edition* **2010**, *49* (19), 3375–3378. https://doi.org/10.1002/anie.200906294.

(185) Shcheslavskiy, V. I.; Shirmanova, M. V.; Yashin, K. S.; Rück, A. C.; Skala, M. C.; Becker, W. Fluorescence Lifetime Imaging Techniques—A Review on Principles, Applications and Clinical Relevance. *J Biophotonics* **2025**. https://doi.org/10.1002/jbio.202400450.

(186) Datta, R.; Heaster, T. M.; Sharick, J. T.; Gillette, A. A.; Skala, M. C. Fluorescence Lifetime Imaging Microscopy: Fundamentals and Advances in Instrumentation, Analysis, and Applications. *J Biomed Opt* **2020**, *25* (07), 1. https://doi.org/10.1117/1.jbo.25.7.071203.

(187) De Los Santos, C.; Chang, C. W.; Mycek, M. A.; Cardullo, R. A. FRAP, FLIM, and FRET: Detection and Analysis of Cellular Dynamics on a Molecular Scale Using Fluorescence Microscopy. *Mol Reprod Dev* **2015**, *82* (7–8), 587–604. https://doi.org/10.1002/mrd.22501.

(188) Okamoto, K.; Sako, Y. Recent Advances in FRET for the Study of Protein Interactions and Dynamics. *Curr Opin Struct Biol* **2017**, *46*, 16–23. https://doi.org/10.1016/j.sbi.2017.03.003.

(189) Sakamoto, S.; Hamachi, I. Ligand-Directed Chemistry for Protein Labeling for Affinity-Based Protein Analysis. *Isr J Chem* **2023**, *63* (3–4). https://doi.org/10.1002/ijch.202200077.

(190) Beerkens, B. L. H.; IJzerman, A. P.; Heitman, L. H.; van der Es, D. Covalent Functionalization of G Protein-Coupled Receptors by Small Molecular Probes. *RSC Chem Biol* **2025**, *6* (4), 525–538. https://doi.org/10.1039/d4cb00294f.

(191) Ongini, E.; Dionisotti, S.; Gessi, S.; Irenius, E.; Fredholm, B. B. Comparison of CGS 15943, ZM 241385 and SCH 58261 as Antagonists at Human Adenosine Receptors. *Naunyn Schmiedebergs Arch Pharmacol* **1999**, *359*, 7–10.

(192) Perchey, R. T.; Tonini, L.; Tosolini, M.; Fournié, J. J.; Lopez, F.; Besson, A.; Pont, F. PTMselect: Optimization of Protein Modifications Discovery by Mass Spectrometry. *Sci Rep* **2019**, *9* (1). https://doi.org/10.1038/s41598-019-40873-3.

(193) Doll, S.; Burlingame, A. L. Mass Spectrometry-Based Detection and Assignment of Protein Posttranslational Modifications. *ACS Chem Biol* **2015**, *10* (1), 63–71. https://doi.org/10.1021/cb500904b.

(194) Chen, G.; Pramanik, B. N. Application of LC/MS to Proteomics Studies: Current Status and Future Prospects. *Drug Discov Today* **2009**, *14* (9–10), 465–471. https://doi.org/10.1016/j.drudis.2009.02.007.

(195) Olsen, J. V.; Ong, S. E.; Mann, M. Trypsin Cleaves Exclusively C-Terminal to Arginine and Lysine Residues. *Molecular and Cellular Proteomics* **2004**, *3* (6), 608–614. https://doi.org/10.1074/mcp.T400003-MCP200.

(196) Tsiatsiani, L.; Heck, A. J. R. Proteomics beyond Trypsin. *FEBS Journal* **2015**, *282* (14), 2612–2626. https://doi.org/10.1111/febs.13287.

(197) Swaney, D. L.; Wenger, C. D.; Coon, J. J. Value of Using Multiple Proteases for Large-Scale Mass Spectrometry-Based Proteomics. *J Proteome Res* **2010**, *9* (3), 1323–1329. https://doi.org/10.1021/pr900863u.

(198) Gilmore, J. M.; Kettenbach, A. N.; Gerber, S. A. Increasing Phosphoproteomic Coverage through Sequential Digestion by Complementary Proteases. *Anal Bioanal Chem* **2012**, *402* (2), 711–720. https://doi.org/10.1007/s00216-011-5466-5.

(199) Köcher, T.; Pichler, P.; Swart, R.; Mechtler, K. Quality Control in LC-MS/MS. *Proteomics* **2011**, *11* (6), 1026–1030. https://doi.org/10.1002/pmic.201000578.

(200) Simpson, R. J. SYPRO Orange Fluorescent Staining of Protein Gels. *Cold Spring Harb Protoc* **2010**, *5* (4). https://doi.org/10.1101/pdb.prot5414.

(201) Telford, W. G. Flow Cytometry and Cell Sorting. *Front Med (Lausanne)* **2023**, *10*. https://doi.org/10.3389/fmed.2023.1287884.

(202) Majumdar, S.; Guha, T.; Barman, F.; Kundu, R. A Basic Method for Hoechst (33258) Staining of Nuclei from Whole Root Tissues of Oryza Sativa. *National Academy Science Letters* **2020**, *43* (4), 389–392. https://doi.org/10.1007/s40009-019-00865-3.

(203) Roy, A. Membrane Preparation and Solubilization. In *Methods in Enzymology*; Shukla, A. K., Ed.; Academic Press Inc., 2015; Vol. 557, pp 45–56. https://doi.org/10.1016/bs.mie.2014.11.044.

(204) Ellenbogen, K. A.; O'Neill, G.; Prystowsky, E. N.; Camm, J. A.; Meng, L.; Lieu, H. D.; Jerling, M.; Shreeniwas, R.; Belardinelli, L.; Wolff, A. A. Trial to Evaluate the Management of Paroxysmal Supraventricular Tachycardia during an Electrophysiology Study with Tecadenoson. *Circulation* **2005**, *111* (24), 3202–3208. https://doi.org/10.1161/CIRCULATIONAHA.104.510982.

(205) Lefton, K. B.; Wu, Y.; Dai, Y.; Okuda, T.; Zhang, Y.; Yen, A.; Rurak, G. M.; Walsh, S.; Manno, R.; Myagmar, B. E.; Dougherty, J. D.; Samineni, V. K.; Simpson, P. C.; Papouin, T. Norepinephrine Signals through Astrocytes to

Modulate Synapses. *Science (1979)* **2025**, *388* (6748), 776–783. https://doi.org/10.1126/science.adq5480.

(206) Chen, A. B.; Duque, M.; Rymbek, A.; Dhanasekar, M.; Wang, V. M.; Mi, X.; Tocquer, L.; Narayan, S.; Legorreta, E. M.; Eddison, M.; Yu, G.; Wyart, C.; Prober, D. A.; Engert, F.; Ahrens, M. B. Norepinephrine Changes Behavioral State through Astroglial Purinergic Signaling. *Science (1979)* **2025**, *388* (6748), 769–775. https://doi.org/10.1126/science.adq5233.

(207) Federico, S.; Lassiani, L.; Spalluto, G. Chemical Probes for the Adenosine Receptors. *Pharmaceuticals* **2019**, *12* (4). https://doi.org/10.3390/ph12040168.

(208) Boichenko, I.; Deiss, S.; Bär, K.; Hartmann, M. D.; Hernandez Alvarez, B. A FRET-Based Assay for the Identification and Characterization of Cereblon Ligands. *J Med Chem* **2016**, *59* (2), 770–774. https://doi.org/10.1021/acs.jmedchem.5b01735.

(209) Adhikari, K.; Dewulf, J.; Vangestel, C.; Van der Veken, P.; Stroobants, S.; Elvas, F.; Augustyns, K. Characterization of Structurally Diverse 18F-Labeled d-TCO Derivatives as a PET Probe for Bioorthogonal Pretargeted Imaging. *ACS Omega* **2023**, *8* (41), 38252–38262. https://doi.org/10.1021/acsomega.3c04597.

(210) Biedka, S.; Schmidt, B. F.; Frey, N. M.; Boothman, S. M.; Minden, J. S.; Lucas, A. Reversible Click Chemistry Tag for Universal Proteome Sample Preparation for Top-Down and Bottom-Up Analysis. *J Proteome Res* **2021**, *20* (10), 4787–4800. https://doi.org/10.1021/acs.jproteome.1c00443.

(211) Biedka, S.; Alkam, D.; Washam, C. L.; Yablonska, S.; Storey, A.; Byrum, S. D.; Minden, J. S. One-Pot Method for Preparing DNA, RNA, and Protein for Multiomics Analysis. *Commun Biol* **2024**, *7* (1). https://doi.org/10.1038/s42003-024-05993-1.

(212) Chai, Z.; Li, C. In-Cell 19F NMR of Proteins: Recent Progress and Future Opportunities. *Chemistry - A European Journal* **2024**, *30* (23). https://doi.org/10.1002/chem.202303988.

(213) Marsh, E. N. G.; Suzuki, Y. Using 19F NMR to Probe Biological Interactions of Proteins and Peptides. *ACS Chem Biol* **2014**, *9* (6), 1242–1250. https://doi.org/10.1021/cb500111u.

(214) Reddi, R. N.; Rogel, A.; Gabizon, R.; Rawale, D. G.; Harish, B.; Marom, S.; Tivon, B.; Arbel, Y. S.; Gurwicz, N.; Oren, R.; David, K.; Liu, J.; Duberstein, S.; Itkin, M.; Malitsky, S.; Barr, H.; Katz, B. Z.; Herishanu, Y.; Shachar, I.; Shulman, Z.; London, N. Sulfamate Acetamides as Self-Immolative

Electrophiles for Covalent Ligand-Directed Release Chemistry. *J Am Chem Soc* **2023**, *145* (6), 3346–3360. https://doi.org/10.1021/jacs.2c08853.